

C^1 Continuous Methods in Computational Gradient Elasticity

C^1 -stetige Methoden in der nummerischen Gradientenelastizität

Der Technischen Fakultät der
Universität Erlangen-Nürnberg

zur Erlangung des Grades

DOKTOR-INGENIEUR

vorgelegt von

Paul Edelbert Fischer

Erlangen - 2011

Als Dissertation genehmigt von
der Technischen Fakultät der
Universität Erlangen-Nürnberg

Tag der Einreichung: 29.11.2010
Tag der Promotion: 01.06.2011
Dekan: Prof. Dr.-Ing. habil. R. German
Berichterstatter: Prof. Dr.-Ing. habil. P. Steinmann
JP Dr.-Ing. J. Mergheim
Prof. N. Sukumar

Schriftenreihe Technische Mechanik
Band 6 · 2011

Paul Fischer

**C^1 Continuous Methods in Computational
Gradient Elasticity**

Herausgeber: Prof. Dr.-Ing. habil. Paul Steinmann
Prof. Dr.-Ing. habil. Kai Willner

Erlangen 2011

Impressum

Prof. Dr.-Ing. habil. Paul Steinmann
Prof. Dr.-Ing. habil. Kai Willner
Lehrstuhl für Technische Mechanik
Universität Erlangen-Nürnberg
Egerlandstrasse 5
91058 Erlangen
Tel: +49 (0)9131 85 28502
Fax: +49 (0)9131 85 28503

ISSN 2190-023X

© Paul Fischer

Alle Rechte, insbesondere das der Übersetzung in fremde Sprachen, vorbehalten. Ohne Genehmigung des Autors ist es nicht gestattet, dieses Heft ganz oder teilweise auf photomechanischem, elektronischem oder sonstigem Wege zu vervielfältigen.

Vorwort

Diese Arbeit entstand während meiner Tätigkeit als Stipendiat am Lehrstuhl für Technische Mechanik der Universität Kaiserslautern und meiner Zeit als wissenschaftlicher Mitarbeiter des Lehrstuhls für Technische Mechanik an der Friedrich-Alexander-Universität Erlangen-Nürnberg. Ich bedanke mich beim Land Rheinland-Pfalz, das mir durch seine RLP Graduate School "Engineering Materials and Processes" den Einstieg in die hier vorliegende Arbeit ermöglicht hat und der DFG für die weitere Finanzierung.

Mein besonderer Dank gilt meinem Doktorvater, Herrn Professor Paul Steinmann, ohne ihn wäre diese Arbeit nie zustandegekommen. Dabei danke ich ihm besonders für seine Geduld und die vielen Freiheiten, die er mir bei der Gestaltung meiner Arbeit gelassen hat. Recht herzlich danke ich Frau JP Julia Mergheim für die vielen fachlichen Diskussionen und kritischen Fragestellungen, die wesentlich zu meinem Verständniss und damit maßgeblich zur Verbesserung der hier vorliegenden Arbeit beigetragen haben. Insbesondere danke ich ihr für die Unterstützung, bei der Veröffentlichung meiner Ideen. Vielen Dank auch für die Übernahme des Zweitgutachtens dieser Arbeit. Zusätzlich danke ich Herrn Professor Natarajan Sukumar für die Übernahme des Drittgutachtens und sein Interesse an dieser Arbeit.

Ich bedanke mich bei meinen Kollegen für die gute Atmosphäre am Lehrstuhl in Kaiserslautern und auch später in Erlangen. Die vielen fachlichen Diskussionen haben mir den Anfang erheblich erleichtert und geholfen, mein Wissen stetig zu vergrößern. Auch die gemeinsamen privaten Aktivitäten haben wesentlich zu einem gutem Arbeitsumfeld beigetragen. An dieser Stelle möchte ich im Besonderem Holger Meier für das Korrekturlesen danken. Ausserdem danke ich Markus Klassen, dass er mir durch seine Diplomarbeit den Weg zur IGA erleichtert hat.

Für die Unterstützung und den persönlichen Rückhalt danke ich meiner Familie und meinen Freunden. An dieser Stelle möchte ich mich bei Karin und Andreas bedanken, durch euch haben meine Familie und ich uns schnell in Erlangen eingelebt. Im Besonderem möchte ich meiner Frau Eva danken, die mir besonders in den letzten Monaten meiner Arbeit den Rücken freigehalten hat und es geschafft hat, mich immer wieder aufs Neue zu motivieren. Auch danke ich meiner Tochter Lotte, dass sie mir jeden Tag wieder verdeutlicht, was im Leben wirklich wichtig ist und meiner zweiten Tochter Frieda, die in der Zeit zwischen Einreichen und der Prüfung für einige Aufregung gesorgt hat.

Erlangen, im Juli 2011

Paul Fischer

Für Eva, Lotte und Frieda

Contents

Index	1
1 Introduction	3
1.1 Outline	4
2 Basics of continuum mechanics	7
2.1 Kinematics	7
2.2 Boltzmann continuum	9
2.2.1 Boundary value problem	9
2.3 Strain gradient continuum	10
2.3.1 Boundary value problem	10
2.4 Constitutive modeling	11
2.4.1 Compressible Neo-Hookean model	12
2.4.2 Gradient continuum material models	12
2.5 Linear gradient elasticity	13
3 Galerkin Method	15
3.1 Geometry approximation	15
3.1.1 Lagrange interpolation	16
3.2 Approximation of the deformation map	16
3.2.1 Hermite interpolation	17
3.3 Boltzmann continuum: Discretization and linearization	17
3.3.1 Discrete weak equations	18
3.3.2 Linearized discrete weak equations	18
3.4 Gradient continuum: Discretization and linearization	18
3.4.1 Discrete weak equations	19
3.4.2 Linearized discrete weak equations	19
3.4.3 Computation of the Hessian	19
3.4.4 Application of boundary conditions	20
4 Bernstein-Bézier patches	21
4.1 Polynomial spline descriptions	22
4.1.1 Lagrange interpolation	22
4.1.2 Hermite interpolation	23
4.1.3 Bernstein polynomials	24
4.2 Bernstein-Bézier patches	26
4.2.1 Basics	27
4.2.2 Control mesh	27
4.3 Derivatives and continuity conditions	29
4.3.1 Derivatives values at the vertices of a simplex	29

4.3.2	Normal derivatives	32
5	Finite elements	35
5.1	Introduction to Hermite finite element descriptions	35
5.2	C^* finite elements	37
5.2.1	Hermite triangle	37
5.2.2	Zienkiewicz triangle	38
5.2.3	Morley triangle	39
5.2.4	Adini-Clough-Melosh rectangle	40
5.3	Subparametric C^1 elements	42
5.3.1	Argyris element	42
5.3.2	Bell element	43
5.3.3	Hsieh-Clough-Tocher (HCT) element	43
5.3.4	Reduced form of the HCT element	45
5.3.5	Powell-Sabin split elements	46
5.4	Isoparametric C^1 elements	51
5.4.1	Geometry approximation for isoparametric C^1 elements	52
5.4.2	C^1 continuous mappings	52
5.4.3	Hermite interpolation	55
5.4.4	The Bogner-Fox-Schmidt element	55
5.4.5	Mesh construction for the isoparametric Bogner-Fox-Schmidt element	56
6	Isogeometric Analysis	63
6.1	B-splines	64
6.1.1	B-spline curves	64
6.1.2	B-spline geometries	66
6.1.3	Multi-patch domains	68
6.2	Non-Uniform Rational B-Splines (NURBS)	68
6.2.1	NURBS curves	70
6.2.2	NURBS geometries	70
6.2.3	Multi-patch domains	71
6.3	Application to gradient continua	71
6.3.1	Gradient boundary conditions	72
6.3.2	Symmetry boundary conditions	74
6.3.3	Strategies of mesh refinement	75
7	Natural Element Method	77
7.1	Voronoi diagrams and Delaunay tessellations	78
7.2	C^0 natural neighbor functions	79
7.2.1	Thiessens interpolant	81
7.2.2	Laplace interpolant	81
7.2.3	Sibson interpolant	82
7.3	C^1 natural neighbor functions	83
7.3.1	Farins C^1 interpolant	84
7.4	Application of the natural element method to gradient elasticity	86

7.4.1	α -shapes for non-convex domains	86
7.4.2	Numerical integration	87
7.4.3	Additional bubble functions	87
8	Computational examples for gradient elasticity	91
8.1	Linear gradient elasticity	92
8.1.1	L-shaped domain	92
8.1.2	Thick hollow cylinder under external pressure	94
8.2	Gradient elasticity at finite strains	103
8.2.1	Inhomogeneous compression test	103
8.2.2	Plate with hole example	106
8.2.3	Cracked specimen	109
8.3	Conclusions	112
9	The Bogner-Fox-Schmidt element with incompressible material behavior	115
9.1	The principle of volumetric locking	115
9.2	Three-field formulation	116
9.2.1	Weak form of the equation	117
9.2.2	Incompressible Neo-Hookean model	117
9.2.3	Volumetric part of the internal energy	118
9.3	Incompressible material behavior: Discretization and linearization	119
9.3.1	Pressure approximation	119
9.3.2	Discrete weak equations	119
9.3.3	Linearized discrete weak equations	120
9.4	The BFS element in a mixed formulation	120
9.5	Numerical validation for the Boltzmann continuum	121
9.6	Numerical validation for the strain gradient continuum	126
10	Cahn-Hilliard equation	129
10.1	Introduction	129
10.2	Governing equations	130
10.3	Decomposition of the diffusion equation	132
10.4	Weak form of the Cahn-Hilliard equation	132
10.5	Time integration	132
10.6	Stiffness matrices	133
10.7	Periodic boundary conditions	134
10.8	Computational results	134
11	Conclusion	139
11.1	Summary	139
11.2	Main contribution	139
11.3	Outlook	140
A	Notation	143
B	Strain gradient elasticity	145

C Isoparametric C^1-continuous triangular elements	147
C.1 Construction of the shape of the triangles	147
C.2 Numerical examples	149
C.3 Conclusion	150

Kurzfassung

Die vorliegende Arbeit beinhaltet die Präsentation und den Vergleich verschiedener C^1 stetiger numerischer Methoden. Dies sind mehrere C^1 stetige finite Elemente sowie die “Isogeometric Analysis” (IGA) und die Methode der natürlichen Elemente (NEM). Als Gemeinsamkeit der Methoden kann die Tatsache angesehen werden, dass alle genutzten numerischen Verfahren direkt oder indirekt auf der Bernstein-Bézier Darstellung von polynomialen Splines beruhen.

Das Hauptziel dieser Arbeit liegt dabei auf der Untersuchung der Anwendbarkeit der Methoden auf die Gradientenelastizität. Hierfür werden die oben genannten Verfahren anhand von relevanten numerischen Beispielen verglichen. Als Fehlermaß werden die Sobolev-Normen L^2 , H^1 und H^2 genutzt. Diese Fehlernormen werden mit Hilfe von analytischen oder numerischen Referenzlösungen berechnet. In dieser Arbeit wird erstmals ein umfassender Vergleich der oben genannten Methoden präsentiert. Zudem werden die IGA und einige der präsentierten finiten Elemente erstmals auf die Gradientenelastizität angewendet.

Bei der Anwendung der Methode der finiten Elemente werden unterschiedliche Verbesserungsvorschläge präsentiert. Zum einen wird gezeigt, dass eine einfache Verbesserung der linearen Geometrieapproximation für die subparametrischen C^1 Elemente sowohl den absoluten Fehler, als auch die Konvergenzraten wesentlich beeinflussen kann. Für die Netzgenerierung von isoparametrischen C^1 Elementen wird ein neuer linearer Optimierungsalgorithmus vorgeschlagen, der die numerischen Ergebnisse signifikant verbessert.

Als Zusatzanwendung wird die Cahn-Hilliard Gleichung mit Hilfe der NEM diskretisiert. Dazu werden sowohl die C^0 stetigen Sibson-Interpolationsfunktionen als auch Farins C^1 stetige Interpolierende verwendet. Mit Hilfe letzterer kann die partielle Differentialgleichung vierter Ordnung direkt gelöst werden. Für die Anwendung der C^0 stetigen Funktionen wird eine Aufspaltung der PDE in zwei gekoppelte Gleichungen durchgeführt. Hierbei kann anhand eines numerischen Beispiels gezeigt werden, dass die direkte Berechnung mit Hilfe von C^1 stetigen Ansatzfunktionen schneller konvergiert.

Schlagwörter: Generalisierte Kontinua, Gradientenelastizität, Cahn-Hilliard Gleichung, Hermite Elemente, Methode der natürlichen Elemente (NEM), Isogeometric Analysis (IGA), isoparametrische C^1 Elemente, Netzgenerierung, Simulation

Abstract

This thesis contains the presentation and the comparison of different C^1 continuous numerical methods. These are a couple of C^1 continuous finite elements, the isogeometric analysis (IGA) and the natural element method (NEM). They all have in common that their shape functions are directly or indirectly related to the Bernstein-Bézier representation of polynomial splines.

The major goal of this work is the examination of the applicability of those methods to strain gradient elasticity. Therefore different problems occurring within the application of the methods are presented and demonstrated at relevant numerical benchmark tests. The errors are measured by the use of the L^2 , H^1 and H^2 Sobolev norms. These norms are computed by the use of analytical and numerical reference solutions. Within this thesis, a comprehensive comparison of the above mentioned numerical methods is presented. Furthermore, the IGA as well as some of the presented elements were applied to gradient elasticity for the first time.

For the application of the finite element method, several ideas for the improvement are proposed. It is demonstrated that a simple enhancement of the linear geometry approximation of the subparametric C^1 elements improves the absolute error as well as the rate of convergence. Furthermore, for the mesh construction of the isoparametric C^1 elements a new linear mesh optimization algorithm is proposed. This algorithm again improves the performance of the elements, significantly.

A complementary application is the Cahn-Hilliard equation. It is discretized by the use of the NEM. Therefore, the C^0 continuous Sibson interpolants as well as Farin's C^1 interpolant are used to find the solution of the fourth order partial differential equation. For the application of the C^0 continuous functions, a split of the PDE into a set of two coupled equations is used. By the use of a numerical example, it is demonstrated that the direct C^1 continuous approach converges faster.

Keywords: generalized continua, gradient elasticity, Cahn-Hilliard equation, Hermite elements, natural element method (NEM), isogeometric analysis (IGA), isoparametric C^1 elements, mesh generation, simulation

1 Introduction

The modeling of materials displaying size effects is an issue of great interest. Size effects depend on the microstructure of the material and can be observed when the size of the specimen is sufficiently small, i.e., approximately the size of the microstructure. At this length scale specimens with similar shape but different dimensions show different mechanical behavior. Size effects have been observed for a wide variety of materials such as concrete [23], metals [102] and composites [186, 237], just to mention a few. Within the classical Boltzmann theory such effects cannot be captured, since the theory does not contain an internal length scale. Therefore, the extension of the standard continuum mechanics is necessary.

Extensions to the generalized continuum theory are originated in the pioneering work of the Cosserats [65], where additional rotational degrees of freedom are introduced on a micro level. The new potential of this generalization was recognized by Hellinger [121] but the ideas were not picked up again until to the early sixties. Some of these works, with special emphasis on the continuum description are the publications of Mindlin and Thiersten [162], Mindlin [159–161] Koiter [143, 144], Toupin [204, 205] and Eringen [89]. An excellent review on the history of generalized continua, including all relevant references of the last 100 years is presented by Maugin in [153].

Within these theories, our interest is on the application of strain gradient elasticity when the micro deformation coincides with the gradient of macroscopic displacements, compare to [160] and [204]. In gradient elasticity the strain energy becomes a function of the strain and its derivative, and thus the stresses depend on higher-order derivatives of the displacements. The simplest format of strain gradient elasticity was introduced by Altan and Aifantis [10], who included the Laplacian of the strains together with one additional material parameter, that describes the internal material length scale, into the constitutive law. It was shown in [2], [3] and [237] that this theory of gradient elasticity can adequately model size effects. A recent survey on the applicability of gradient continua is presented in [4] and an overview on the current state of ongoing research is collected in [154].

The introduction of higher order gradients of the strains into the constitutive law leads to a partial differential equation of higher order. The numerical solution of this governing equation in the context of a Galerkin method requires a higher regularity of the interpolation scheme, i.e. for the proposed first order strain gradient method global C^1 -continuity has to be ensured. Within the C^1 continuous finite element method, the increase of complexity is either caused by a high number of degrees of freedom per element, as in the Argyris [15] or Bell element [29], or the structure of the element is complicated, cf. the Hsieh-Clough-Tocher triangle [63] or the Powell-Sabin-split element [172].

For this reason the application of C^1 -continuous finite elements to gradient elasticity is considered only in few works: In [234] the results obtained with two different C^1 -continuous finite elements are compared to the results from a formulation based on the

micromorphic theory. The first application of a three-dimensional element with C^1 -continuity to gradient elasticity is presented in [167]. In [99] the performance of three different C^1 -continuous finite elements and the C^1 Natural Element Method (NEM) was analyzed for nonlinear gradient elasticity. In [17] advantage was taken of the inherently higher continuity of meshfree interpolation functions, and linear gradient elasticity was modeled with the Element Free Galerkin Method (EFG). In [203] a meshless local Petrov Galerkin scheme is presented. Additionally, the isogeometric analysis for the application to gradient elasticity is firstly used in [96]. By the construction of the shape functions from NURBS the C^1 continuity in an isoparametric setting is easily achieved.

Furthermore, in gradient plasticity, C^1 continuous polynomials are applied to approximate the plastic strain measure in [78, 79] and [232, 233]. To discretize the displacement field, a nonconforming C^1 was used in [224] for the investigation of crack tip fields in gradient plasticity. Within a finite element framework, the Bell triangle [15] and the BFS element [169] are applied to gradient plasticity in [232].

Due to the increased numerical complexity of C^1 methods, many efforts have been undertaken to find alternative approaches to simulate gradient elasticity without the requirements of C^1 continuous interpolations. Therefore implicit methods [18, 19], mixed formulations [12] and micromorphic continuum formulations with Lagrange multipliers [187] or penalty parameters [122, 140, 141] have been developed. However, these alternatives involve drawbacks, e.g. incompatibilities of the different approximation fields resulting in locking and unphysical results. Moreover, a high number of degrees of freedom has to be used for the additional approximation fields resulting in a poor behavior of the mixed formulations in comparison to C^1 continuous finite elements, see [167, 234, 235].

The goal of this thesis is the systematic investigation of several locally defined C^1 continuous methods for the application to gradient continua in two dimensions, namely the C^1 finite element method, chapter 5, the isogeometric analysis, chapter 6, as well as the natural element method chapter 7. The comparison of the method is based on the Sobolev norms L^2 , H^1 and H^2 , where the error is related to the global number of degrees of freedom, see chapter 8.

Within the work, three major problems arose. First, for the representation of the shape functions of the subparametric C^1 continuous elements, see section 5.3, a feasible parameterization of the polynomial spaces on the simplices is necessary to get a unified representation of the finite element shape functions. Therefore the Bézier representation is introduced in chapter 4. Secondly, the existing mesh construction schemes, for the subparametric as well as the isoparametric C^1 continuous finite elements had to be improved, see chapter 5 and 8. Furthermore, new benchmark problems, for the evaluation of the different numerical methods had to be developed, i.e. see subsection 8.2.1.

1.1 Outline

The eleven chapters of this thesis are organized as follows. Chapter 2 provides the necessary kinematic quantities, for both, the classical as well as the strain gradient continuum. This is supplemented by the introduction of the principle of the minimization of the total

potential energy, as well as the derivation of the resulting equations. Furthermore, two sets of material models are introduced. This is followed by chapter 3, where the discretization and linearization of the equations of the classical and non-classical continua are provided. Therefore, the geometry approximation is explained, followed by the introduction of the discrete deformation map.

For an efficient and stable treatment of the C^1 continuous methods, the reformulation of the polynomials in the Bézier representation is absolutely necessary. Within chapter 4, the basic principles of the polynomial coefficients of the Bernstein polynomials, the so called control points and their relation to the global shape function derivative values are explained.

Up to now, a complete overview and comparison of the basic C^1 continuous finite elements is still missing. Therefore, three different types of elements for the application to gradient continuum problems are presented, nonconforming C^* elements, section 5.1, subparametric C^1 elements, section 5.3, and isoparametric C^1 elements, see section 5.4 and chapter C.

The basic settings of the isogeometric analysis are introduced in chapter 6. Furthermore, additional difficulties arising within the numerical treatment of gradient elasticity, like the application of gradient and symmetry boundary conditions are discussed in section 6.3.

The last considered numerical method is the NEM, see chapter 7. It combines the advantages of a finite element method with those of a meshfree approximation scheme. These are the interpolation property of the shape functions at the boundary, as well as a the fully algorithmic treatment of the computation of the shape functions. A detailed description of the method is presented, together with the proposition of a new integration scheme and the discussion on the introduction of additional degrees of freedom.

Chapter 8 presents the effects of the gradient material parameters as well as a comprehensive comparison of the numerical schemes, introduced within the previous chapters. In a first numerical example, the effects of the internal length scale are illustrated, see subsection 8.1.1. The comparison of the numerical results for the different discretization schemes starts with the thick hollow cylinder example. It is one of the few examples, with known analytical solution. The results are presented in subsection 8.1.2. Therefore the L^2 , H^1 and energy norm errors are computed, based on the analytical solution. Within this numerical analysis, it is pointed out that the usual linear interpolation of the geometry results in severe errors due to the poor approximation of the geometry. The results can be significantly improved, if a linear, area preserving approximation of the boundary is used.

The second part of the chapter, i.e. section 8.2 deals with the comparison of the performance at finite strains. To get rid of the influence of the geometry within the numerical validation, a new benchmark test is introduced for the application to gradient elasticity in subsection 8.2.1. It is followed by the plate with hole example in subsection 8.2.2. Thereby, the performance of the different mesh construction algorithms for the BFS element, as presented in subsection 5.4.5, are studied. The chapter closes with a short discussion of the limits of the numerical methods, presented by the computation of a cracked specimen, see subsection 8.2.3.

By the numerical analysis of chapter 8, the BFS element has shown to be the best fi-

nite element. Therefore, a short investigation of its behavior for nearly incompressible materials is accomplished in chapter 9. Thereby locking behavior of the elements is revealed. This motivates the development of several new mixed finite elements, based on the original BFS element. Their improvement of the numerical behavior is demonstrated in section 9.5.

In chapter 10, the Cahn-Hilliard equation is treated with the use of the natural element method. This is for the demonstration of the wide variety of applications for C^1 continuous numerical methods. Here, a comparison of an operator split and the use of the C^0 NEM as well as the direct evaluation with C^1 continuous shape functions is compared, revealing the superiority of the C^1 continuous solutions.

The main part of the thesis closes with a short discussion of the results and an outlook to possible future work in chapter 11.

2 Basics of continuum mechanics

In this chapter, the basic principles and notations, necessary for the modeling of classical and strain gradient hyperelastic continua are presented. Therefore, the underlying kinematic quantities as well as the basic equations, necessary for the application of a Galerkin method are introduced.

For a more detailed description of the classical continuum theory, the interested reader is referred to the monographs of Truesdell and Noll [209], Marsden and Hughes [152] or Altenbach and Altenbach [11]. Excellent introductions to the topic of generalized continua can be found in the publications of Mindlin [161], Eringen [88] for the linear theory and Forest and Cardona [105] or Kirchner and Steinmann [140, 141] for the finite strain framework. Some more recent contributions, considering the topic of strain gradient elasticity are given by Sunyk and Steinmann [202] or Fischer et al. [96–100].

Starting with the introduction of the kinematic quantities necessary for both, the Boltzmann and Mindlin continuum in section 2.1, a description of the boundary value problem of classical (Boltzmann) hyperelasticity is presented in section 2.2. Subsequently, the theory of the Mindlin continuum is explained in section 2.3. Therein the additional dependency on the strain gradient is introduced. Although, the focus is on the nonlinear theory, it is necessary to introduce the linear settings in order to be able to compare the results to the existing analytical solutions. Therefore, the chapter closes with a short review on the linear theory of gradient and classical continua in section 2.5.

2.1 Kinematics

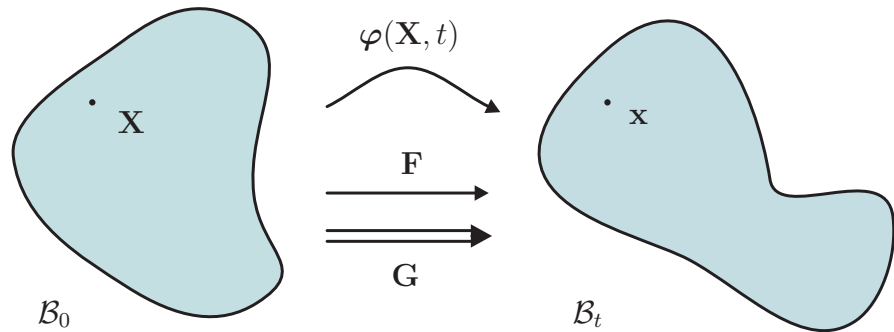


Figure 2.1: Deformation map of a body \mathcal{B}_0 , dependent on the additional quantity \mathbf{G} .

A body \mathcal{B} is considered to be a collection of physical particles. Let \mathbf{X} denote a particle in the initial configuration $\mathcal{B}_0 \subset \mathbb{R}^n$. $n \in \mathbb{N}$ denotes the dimension of the problem. The

outer normal to the boundary $\partial\mathcal{B}_0$ of the body is denoted by \mathbf{N} .

The deformation map to the deformed body \mathcal{B}_t is defined by the time dependent vector field of the nonlinear spatial deformation map

$$\begin{aligned}\varphi : \mathcal{B}_0 \times \mathbb{R}^+ &\rightarrow \mathcal{B}_t \\ \varphi(\mathbf{X}, t) &= \mathbf{x},\end{aligned}\tag{2.1}$$

where \mathbf{x} denotes the spatial position of the particle \mathbf{X} at time t .

The displacement \mathbf{u} of the body is characterized by the vector field,

$$\begin{aligned}\mathbf{u} : \mathcal{B}_0 \times \mathbb{R}^+ &\rightarrow \mathbb{R}^n \\ \mathbf{u}(\mathbf{X}, t) &= \varphi(\mathbf{X}, t) - \mathbf{X},\end{aligned}\tag{2.2}$$

and the deformation gradient is defined to be the spatial derivative of φ ,

$$\mathbf{F}(\mathbf{X}, t) := \nabla_{\mathbf{x}} \varphi(\mathbf{X}, t).\tag{2.3}$$

\mathbf{F} maps line elements $d\mathbf{X}$ on the referential tangent space $T\mathcal{B}_0$ to the spatial tangent elements $T\mathcal{B}_t$. Its determinant, the Jacobian

$$J := \det(\mathbf{F}) \geq 0,\tag{2.4}$$

is describing the volume change at a point \mathbf{X} , i.e. volume elements dV are transformed by J via the relation

$$dv = J dV.\tag{2.5}$$

To make sure, not to have unphysical self-penetration and that the deformation map is one-to-one, J has to be strictly positive.

The Nansons's formula is introduced in order to describe the change of infinitesimal area elements

$$d\mathbf{a} = J \mathbf{F}^{-T} \cdot d\mathbf{A}.\tag{2.6}$$

As a measure for the homogeneity of the strain, the strain gradient

$$\mathbf{G} := \nabla_{\mathbf{x}} \mathbf{F} = \nabla_{\mathbf{x}}^2 \varphi\tag{2.7}$$

representing the spatial change of the deformation gradient \mathbf{F} ¹ is introduced. It is necessary for the introduction of the additional size effect occurring in the generalization of the classical continuum to a strain gradient continuum.

Remark 2.1 (Strain measures) *The natural deformation measure for problems in the material configuration is the deformation gradient \mathbf{F} , as defined in (2.3). However, in order to define rotational invariant material models, it is convenient to introduce a strain measure without any influence of rigid body rotations. Thus, the right Cauchy-Green tensor*

$$\mathbf{C} := \mathbf{F}^T \mathbf{F}\tag{2.8}$$

is introduced. The independence of \mathbf{C} of any rigid body rotations is a consequence of the polar decomposition of \mathbf{F} ,

$$\mathbf{C} = \mathbf{F}^T \mathbf{F} = \mathbf{U}^T \mathbf{R}^T \mathbf{R} \mathbf{U} = \mathbf{U}^2.\tag{2.9}$$

¹ $\nabla_{\mathbf{x}}^2$ is defined to be the Hessian of φ , i.e. $(\nabla_{\mathbf{x}}^2 \varphi)_{ijk} = \varphi_{i,jk}$.

2.2 Boltzmann continuum

As basis for the strain gradient continuum theory of section 2.3 and the mixed displacement pressure formulation, applied in chapter 9.2.3, the fundamental equations of classical continuum theory are shortly reviewed within this section.

2.2.1 Boundary value problem

In this contribution, the basic equations are all based on the principle of stationary potential energy. Therefore, the existence of an energy functional Π for both, the stresses and the loads is assumed. By only considering dead loading as boundary conditions, together with the quasistatic case, the total potential $\Pi(\varphi)$ of the classical Boltzmann continuum can be expressed by the sum of the internal and external parts of the potential energy, $\Pi_{int}(\varphi)$ and $\Pi_{ext}(\varphi)$.

The internal potential energy is solely dependent on the stored mechanical energy, i.e.

$$\Pi_{int} := \int_{\mathcal{B}_0} W(\mathbf{F}) \, dV, \quad (2.10)$$

where the energy density $W = W(\mathbf{F})$ is only dependent on the deformation gradient. The external energy Π_{ext} is governed by the bulk and boundary terms by means of

$$\Pi_{ext} := - \int_{\mathcal{B}_0} \mathbf{b} \cdot \varphi \, dV - \int_{\partial \mathcal{B}_0} \mathbf{t}^P \cdot \varphi \, dA. \quad (2.11)$$

The vectorial quantities \mathbf{b} and \mathbf{t}^P in (2.11) are denoting the spatial body force and the boundary tractions. At the state of equilibrium, the variational derivative of the total potential energy $\Pi(\varphi, \mathbf{F})$ has to vanish, resulting in the weak form of the Euler-Lagrange equations, i.e.

$$\delta \Pi(\varphi, \mathbf{F}) = 0. \quad (2.12)$$

Making use of the definitions given in (2.10) and (2.11), equation (2.12) results in

$$\delta \Pi = \int_{\mathcal{B}_0} [\mathbf{P} : \delta \mathbf{F} - \mathbf{b} \cdot \delta \varphi] \, dV - \int_{\partial \mathcal{B}_0} \mathbf{t}^P \cdot \delta \varphi \, dA = 0. \quad (2.13)$$

Here \mathbf{P} denotes the 1. Piola-Kirchhoff stress tensor, which is defined as

$$\mathbf{P} := \frac{\partial W}{\partial \mathbf{F}}. \quad (2.14)$$

\mathbf{P} is energy conjugated to the deformation gradient, i.e. the rate of change of the energy density $W(\mathbf{F})$ can be expressed by

$$\dot{W} = \mathbf{P} : \dot{\mathbf{F}}. \quad (2.15)$$

Equation (2.13) together with the Dirichlet and Neumann boundary conditions

$$\varphi = \bar{\varphi} \quad \text{on } \partial \mathcal{B}_0^\varphi \quad \text{and} \quad \mathbf{P} \cdot \mathbf{N} = \bar{\mathbf{t}}^P \quad \text{on } \partial \mathcal{B}_0^P, \quad (2.16)$$

describes the weak form of the boundary value problem.

The dependence of the internal energy density on the deformation gradient will be discussed later in section 2.4.

To transform the weak boundary value problem to its strong form, integration by parts has to be applied to the first term of (2.13), resulting in

$$\int_{\mathcal{B}_0} [\text{Div}(\mathbf{P}) + \mathbf{b}] \cdot \delta \boldsymbol{\varphi} \, dV = 0. \quad (2.17)$$

Thus, the local form of the boundary value problem for quasi-static elasticity can be stated to be

$$\text{Div}(\mathbf{P}) = -\mathbf{b} \quad \text{in } \mathcal{B}_0, \quad (2.18)$$

which has to satisfy the boundary conditions (2.16) to represent the strong form of the boundary value problem.

2.3 Strain gradient continuum

The boundary value problem as introduced in subsection 2.2.1 is not capable of capturing size effects. Therefore, the classical model has to be extended. The simplest additional assumption is the dependence of the internal energy density on the strain gradient

$$\mathbf{G} := \nabla_{\mathbf{x}} \mathbf{F} = \nabla_{\mathbf{x}}^2 \boldsymbol{\varphi}, \quad (2.19)$$

representing the spatial change of the deformation gradient \mathbf{F} . Thus, in contrast to the Boltzmann continuum (see section 2.2), the free energy density of the gradient continuum is not solely dependent on \mathbf{F} but also on \mathbf{G} , i.e.

$$W := W(\mathbf{F}, \mathbf{G}). \quad (2.20)$$

2.3.1 Boundary value problem

The internal energy of the system is given as $\Pi^{int} = \int_{\mathcal{B}_0} W(\mathbf{F}, \mathbf{G}) \, dV$. Its variation can be written as

$$\delta \Pi^{int} = \int_{\mathcal{B}_0} \left[\frac{\partial W}{\partial \mathbf{F}} : \delta \mathbf{F} + \frac{\partial W}{\partial \mathbf{G}} : \delta \mathbf{G} \right] \, dV = \int_{\mathcal{B}_0} [\mathbf{P} : \delta \mathbf{F} + \mathbf{Q} : \delta \mathbf{G}] \, dV. \quad (2.21)$$

Therein, the Piola stress is denoted by \mathbf{P} and is thermodynamically conjugated to the deformation gradient \mathbf{F} , while \mathbf{Q} , the so-called double stress, is thermodynamically conjugate to the strain gradient \mathbf{G} and defined by

$$\mathbf{Q} := \frac{\partial W}{\partial \mathbf{G}}. \quad (2.22)$$

By applying the Gauss theorem twice and by the use of the surface divergence theorem, the variation of the internal energy (2.21) can be transformed into the expression

$$\delta \Pi^{int} = \int_{\mathcal{B}_0} [[\nabla_{\mathbf{x}} \cdot [\nabla_{\mathbf{x}} \cdot \mathbf{Q} - \mathbf{P}]] : \delta \boldsymbol{\varphi}] \, dV + \int_{\partial \mathcal{B}_0} [\mathbf{t}^P \cdot \delta \boldsymbol{\varphi} - \mathbf{t}^Q \cdot \nabla_{\mathbf{x}}^N \delta \boldsymbol{\varphi}] \, dA, \quad (2.23)$$

whereby the tractions \mathbf{t}^P and the double tractions \mathbf{t}^Q are defined as

$$\mathbf{t}^P := [\mathbf{P} - \nabla_{\mathbf{x}} \cdot \mathbf{Q}] \cdot \mathbf{N} + [\nabla_{\mathbf{x}}^S \cdot \mathbf{N}] \mathbf{Q} : [\mathbf{N} \otimes \mathbf{N}] - \nabla_{\mathbf{x}}^S \cdot [\mathbf{Q} \cdot \mathbf{N}]^T \quad (2.24)$$

$$\mathbf{t}^Q := \mathbf{Q} : [\mathbf{N} \otimes \mathbf{N}]. \quad (2.25)$$

Here, smooth boundaries are assumed. A more detailed and more general description of the derivation of the equations is presented in appendix B. The variation of the external energy $\delta\Pi^{ext}$ is given in terms of the prescribed tractions and body forces \mathbf{b} by

$$\delta\Pi^{ext} = - \int_{B_0} \mathbf{b} \cdot \delta\varphi \, dV - \int_{\partial B_0^P} \bar{\mathbf{t}}^P \cdot \delta\varphi \, dA + \int_{\partial B_0^Q} \bar{\mathbf{t}}^Q \cdot \nabla_{\mathbf{x}}^N \delta\varphi \, dA, \quad (2.26)$$

whereby its structure is a direct consequence of (2.23). The expressions $\bar{\mathbf{t}}^P$ and $\bar{\mathbf{t}}^Q$ are the independent prescribed tractions on the boundaries ∂B_0^P and ∂B_0^Q , respectively. The variation of the total potential energy has to vanish and follows from (2.23) and (2.26) as

$$\begin{aligned} \delta\Pi = & \int_{B_0} [\mathbf{P} : \delta\mathbf{F} + \mathbf{Q} : \delta\mathbf{G} - \mathbf{b} \cdot \delta\varphi] \, dV \\ & - \int_{\partial B_0^P} \bar{\mathbf{t}}^P \cdot \delta\varphi \, dA + \int_{\partial B_0^Q} \bar{\mathbf{t}}^Q \cdot \nabla_{\mathbf{x}}^N \delta\varphi \, dA = 0. \end{aligned} \quad (2.27)$$

Assuming the solution to be four times partially differentiable, the weak form (2.27) is equivalent to the fourth order local form of the balance equation,

$$\nabla_{\mathbf{x}} \cdot (\nabla_{\mathbf{x}} \cdot \mathbf{Q} - \mathbf{P}) = \mathbf{b}, \quad (2.28)$$

subject to the following boundary conditions

$$\varphi = \bar{\varphi} \quad \text{on } \partial B_0^P \quad (2.29)$$

$$\nabla_{\mathbf{x}}^N \varphi = \nabla_{\mathbf{x}}^N \bar{\varphi} \quad \text{on } \partial B_0^Q \quad (2.30)$$

$$\mathbf{t}^P = \bar{\mathbf{t}}^P \quad \text{on } \partial B_0^P \quad (2.31)$$

$$\mathbf{t}^Q = \bar{\mathbf{t}}^Q \quad \text{on } \partial B_0^Q. \quad (2.32)$$

The two types of independent boundaries have the properties $\partial B_0^P \cap \partial B_0^Q = \partial B_0^Q \cap \partial B_0^F = \emptyset$ and $\partial B_0^P \cup \partial B_0^Q = \partial B_0^Q \cup \partial B_0^F = \partial B_0$.

Remark 2.2 Due to the use of the second gradient of the deformation map within the constitutive modeling, an internal length scale of the underlying microstructure of the material can be introduced. However it lacks of capturing size effects for homogeneous strain states, i.e. there will be no size effect observed for the patch test where $\mathbf{F} \equiv \mathbf{const.}$

2.4 Constitutive modeling

To be able to solve the presented systems of equations, the relation of the free energy density with respect to the strain measures \mathbf{F} and \mathbf{G} have to be known. In this subsection, the stresses and tangent operators are illustrated for one simple selected model. Further formulations of the free energy density, especially for the modeling of polymer materials are due to Flory [103, 104], Treloar [206–208], Ogden [165] and Gent [109]. However, many others have worked on that topic, i.e. [16, 157, 158] and more recently [85] or [145].

2.4.1 Compressible Neo-Hookean model

The aim of this work is not on the introduction of new material models. Therefore, only the Neo-Hookean model in its two different versions is applied. At this place, only the compressible Neo-Hookean model is explained. It is described by the strain energy density

$$W(\mathbf{F}) = \frac{1}{2}\lambda \ln^2 J + \frac{1}{2}\mu[\mathbf{F} : \mathbf{F} - n - 2 \ln J], \quad (2.33)$$

where n denotes the spatial dimension of the problem. The model is governed by the two coefficients μ and λ , the Lamé parameters. The corresponding 1. Piola stress of the compressible Neo-Hookean model is given by

$$\mathbf{P} = \frac{\partial W}{\partial \mathbf{F}} = \lambda \ln J \mathbf{F}^{-T} + \mu [\mathbf{F} - \mathbf{F}^{-T}]. \quad (2.34)$$

and the corresponding tangent operator is derived to

$$\mathbb{A} := \frac{\partial \mathbf{P}^T}{\partial \mathbf{F}} = [\mu - \lambda \ln J] \mathbf{F}^{-1} \bar{\otimes} \mathbf{F}^{-T} + \lambda \mathbf{F}^{-1} \otimes \mathbf{F}^{-T} + \mu \mathbf{I}_2 \otimes \mathbf{I}_2. \quad (2.35)$$

In (2.35) the tensor \mathbf{I}_2 denotes the second order identity tensor.

Remark 2.3 (Rotational invariance of the Neo-Hookean model.) As discussed in remark 2.1, it should be possible to reformulate a material model in terms of the right Cauchy-Green tensor. Within the Neo-Hookean model, by simply considering $J = \sqrt{\det \mathbf{C}}$ and $\mathbf{F} : \mathbf{F} = \text{tr } \mathbf{C}$ in (2.33), the reformulation with respect to the second Piola stress tensor is possible.

2.4.2 Gradient continuum material models

For the construction of the internal free energy, an additive split is assumed,

$$W(\mathbf{F}, \mathbf{G}) := W^{\mathbf{F}}(\mathbf{F}) + W^{\mathbf{G}}(\mathbf{G}). \quad (2.36)$$

Therefore, the setup of the material models for the classical strain energy density $W^{\mathbf{F}}$ is completely independent of the description of $W^{\mathbf{G}}$. For the strain energy density $W^{\mathbf{F}}$, the Neo-Hookean model can be used. In case of the strain gradient energy, a quadratic relation of the strain energy is assumed. It is of the form

$$W^{\mathbf{G}}(\mathbf{G}) := \mu l^2 \mathbf{G} \cdot \mathbf{G} + \frac{1}{2}\lambda l^2 [\mathbf{I}_2 : \mathbf{G}] \cdot [\mathbf{I}_2 : \mathbf{G}], \quad (2.37)$$

which is similar to the model presented by Altan and Aifantis [10] for the linear elastic case. Its major advantage is that only one additional material parameter is introduced, i.e. l , related to the internal length scale. In most of our examples, the relation is reduced to

$$W^{\mathbf{G}}(\mathbf{G}) := \mu l^2 \mathbf{G} \cdot \mathbf{G}. \quad (2.38)$$

The double stresses \mathbf{Q} , corresponding to (2.37) is given by

$$\mathbf{Q} = 2\mu l^2 \mathbf{G} + \lambda l^2 \mathbb{I}_4 : \mathbf{G}, \quad (2.39)$$

where \mathbb{I}_4 denotes the fourth order identity tensor, characterized by $\mathbb{I}_4 : \mathbf{A} = \mathbf{A}$, for any second order tensor \mathbf{A} .

The double stress corresponding to (2.38) is given by

$$\mathbf{Q} = \mu l^2 \mathbf{G}, \quad (2.40)$$

being a direct consequence of (2.39).

The sixth order tangent operator \mathbb{B} , corresponding (2.39) can be derived to

$$\mathbb{B} = \frac{\partial \mathbf{Q}^T}{\partial \mathbf{G}} = 2\mu l^2 \mathbb{M} + \lambda l^2 \mathbb{N} \quad (2.41)$$

where the sixth order tensor \mathbb{M} and \mathbb{N} are defined by

$$(\mathbb{M})_{ijklmn} = \delta_{il}\delta_{jm}\delta_{kn} \quad (2.42)$$

and

$$(\mathbb{N})_{ijklmn} = \delta_{in}\delta_{kl}\delta_{mj}, \quad (2.43)$$

respectively.

2.5 Linear gradient elasticity

Here, the general framework of linear elasticity with microstructure is presented briefly. For a more detailed description, the interested reader is referred to Mindlin [160]. At first, we want to introduce the relevant kinematic quantities. \mathbf{u} denotes the displacement field and $\boldsymbol{\epsilon}$ denotes the symmetric part of the displacement gradient, $\boldsymbol{\epsilon} := \frac{1}{2} [\nabla_x \mathbf{u} + (\nabla_x \mathbf{u})^T]$, i.e. $\epsilon_{ij} = \frac{1}{2} [u_{i,j} + u_{j,i}]$. The strain gradient $\boldsymbol{\kappa}$ is defined to be the gradient of $\boldsymbol{\epsilon}$.

$$\boldsymbol{\kappa} := \nabla_x \boldsymbol{\epsilon}. \quad (2.44)$$

Here, $\kappa_{ijk} := \epsilon_{ijk} = \frac{1}{2} [u_{i,jk} + u_{j,ik}]$ is symmetric in the first two components. In general, the energy density could consist of any possible quadratic combinations of $\boldsymbol{\epsilon}$ and $\boldsymbol{\kappa}$. By restriction to isotropic material behavior, the strain energy density $W := W(\boldsymbol{\epsilon}, \boldsymbol{\kappa})$ reduces to

$$\begin{aligned} W(\boldsymbol{\epsilon}, \boldsymbol{\kappa}) &= \frac{1}{2} \lambda \epsilon_{ii} \epsilon_{jj} + \mu \epsilon_{ij} \epsilon_{ij} \\ &\quad + a_1 \kappa_{iik} \kappa_{kjj} + a_2 \kappa_{iik} \kappa_{jjk} + a_3 \kappa_{kii} \kappa_{kjj} + a_4 \kappa_{ijk} \kappa_{ijk} + a_5 \kappa_{ijk} \kappa_{kji}. \end{aligned} \quad (2.45)$$

Using the Altan and Aifantis model [10], $a_1 = a_3 = a_5 = 0$, $a_2 = \frac{1}{2} l^2 \lambda$ and $a_4 = l^2 \mu$, (2.45) can be rewritten in the following form

$$W(\boldsymbol{\epsilon}, \boldsymbol{\kappa}) = \mu [\boldsymbol{\epsilon} : \boldsymbol{\epsilon} + l^2 \nabla_x \boldsymbol{\epsilon} : \nabla_x \boldsymbol{\epsilon}] + \frac{1}{2} \lambda [(\text{tr } \boldsymbol{\epsilon})^2 + l^2 \nabla_x \text{tr } \boldsymbol{\epsilon} \cdot \nabla_x \text{tr } \boldsymbol{\epsilon}]. \quad (2.46)$$

Resulting in the following expressions for the stress

$$\boldsymbol{\sigma} = 2\mu \boldsymbol{\epsilon} + \lambda \text{tr}(\boldsymbol{\epsilon}) \mathbf{I}_2, \quad (2.47)$$

and double stress tensors

$$\boldsymbol{\tau} = 2\mu l^2 \boldsymbol{\kappa} + \lambda l^2 [\mathbf{I}_2 : \boldsymbol{\kappa}] \cdot [\mathbf{I}_2 : \boldsymbol{\kappa}]. \quad (2.48)$$

3 Galerkin Method

For the solution of the partial differential equations of chapter 2 analytical solutions are only known for a few special problems. Therefore, numerical solution schemes are absolutely necessary. In this text, we restrict ourselves to the Bubnov-Galerkin method. Thereby, the weak form of the equations is solved in a finite dimensional subspace. Additionally, the testfunctions and the deformation map are approximated by the same set of functions.

Within this chapter, the general framework for the approximation of the geometry, as well as the approximation of the unknown displacement field, is presented in section 3.1 and 3.2. This is followed by the discretization, as well as the linearization of both, the classical Boltzmann continuum, presented in section 3.3, and the Gradient continuum, see section 3.4. Due to the use of generalized coordinates, the linearized equations are not restricted to only one of the numerical methods, presented in this thesis. Therefore, they can be used for the application to all of them.

3.1 Geometry approximation

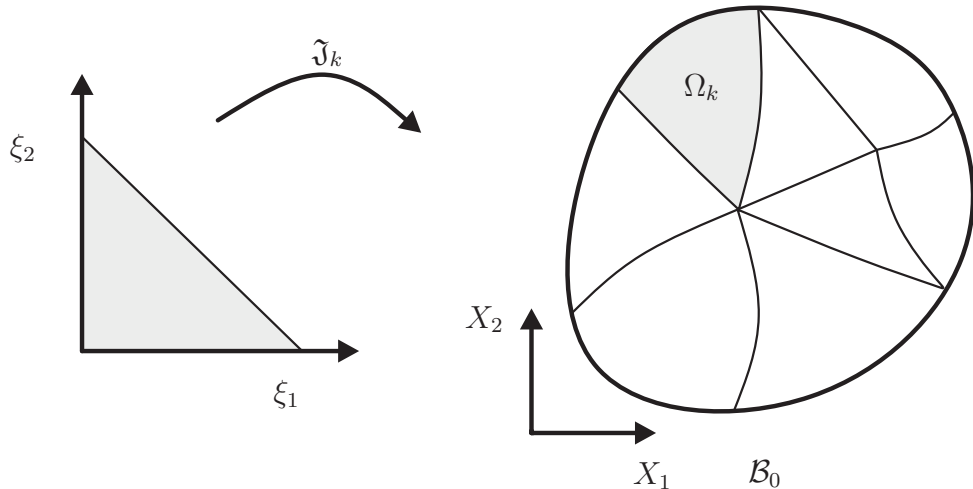


Figure 3.1: Mapping \mathfrak{J}_k from the reference to the physical element, used for the geometry description.

Let \mathcal{B}_0 be the domain for the boundary value problem. Typically, the domain is subdivided into a set of m subdomains Ω_k . For the finite element method, these subdomains Ω_k are called elements. From the definition of a reference element Ω_ξ , an element Ω_k is defined to be the image of the one-to-one map \mathfrak{J}_k , mapping the reference element Ω_ξ to the physical space \mathcal{B}_0 ,

$$\mathfrak{J}_k : \Omega_\xi \rightarrow \Omega_k \subset \mathcal{B}_0. \quad (3.1)$$

For example, a 2D triangular reference element is usually defined by

$$\Omega_{\xi} := \{\boldsymbol{\xi} \mid \xi_i \geq 0 \cap \xi_1 + \xi_2 \leq 1\} \quad (3.2)$$

and a quadrilateral element by

$$\Omega_{\xi} := \{\boldsymbol{\xi} \mid -1 \leq \xi_i \leq 1\}. \quad (3.3)$$

An illustration of these definitions is presented in figure 3.1.

In terms of the generalized coordinates \mathbf{Y}_I and an appropriate set of functions $\Xi_I : \Omega_{\xi} \rightarrow \mathbb{R}^n$, the dependence of a point $\mathbf{X} \in \Omega_k \subset \mathcal{B}_0$ on the local coordinate system is given by

$$\mathbf{X}(\boldsymbol{\xi}) = \sum_I \mathbf{Y}_I \Xi_I(\boldsymbol{\xi}). \quad (3.4)$$

This expression can be used for all of the numerical methods discussed in the following chapters. However, in subsections 3.1.1 a well known example is presented for sake of clarity.

3.1.1 Lagrange interpolation

The simplest case for the construction of finite elements is a Lagrange interpolation. Therefore the generalized coordinates coincide with the nodal positions, i.e. (3.4) can be rewritten as

$$\mathbf{X}(\boldsymbol{\xi}) = \sum_I \mathbf{X}_I N_I(\boldsymbol{\xi}) \text{ with } \boldsymbol{\xi} \in \Omega_{\xi}. \quad (3.5)$$

Here, N_I denotes the polynomial shape functions fulfilling the interpolation property

$$N_I(\boldsymbol{\xi}_J) = \delta_{IJ}. \quad (3.6)$$

at the element nodes $\boldsymbol{\xi}_J$ in the reference coordinate system. This implies the interpolation property of the geometry, i.e. $\mathbf{X}(\boldsymbol{\xi}_I) = \mathbf{X}_I$.

Remark 3.1 (linear interpolation) *A special case of the Lagrange interpolation is the linear approximation of the geometry. This simple approximation is used for the subparametric C^1 continuous finite elements. This is due to the fact that for a linear map from the reference to the spatial element, the degree of a polynomial is preserved. Therefore the shape functions are still polynomial functions on the physical reference domain \mathcal{B}_0 . This is in general not the case for arbitrary, higher order isoparametric finite elements.*

3.2 Approximation of the deformation map

The approximated displacement field \mathbf{u}^h is given in terms of nodal variables, denoted by \mathbf{a}_L and associated shape functions Ψ_L . By the additional use of (3.4), the approximation of the deformation map is thus obtained in terms of the ansatz functions as

$$\boldsymbol{\varphi}^h = \mathbf{X}^h + \mathbf{u}^h = \sum_I \mathbf{Y}_I \Xi_I + \sum_L \mathbf{a}_L \Psi_L. \quad (3.7)$$

For the approximation of the variation $\delta \varphi$, the first summand of (3.7) vanishes, and

$$\delta \varphi^h = \sum_L \delta \mathbf{a}_L \Psi_L \quad (3.8)$$

does not depend explicitly on the approximation of the geometry. If in (3.7) the same functions are used for the approximation of the geometry as well as for the variation of the deformation map, the isoparametric concept is applied. If the approximation of the displacement is of higher order, the subparametric principle is used. Those two principles are utilized within this contribution. The third possibility of a better geometry approximation than the approximation of the deformation is called superparametric, but it is mainly restricted to contact problems [229] and therefore not considered within this work.

3.2.1 Hermite interpolation

The generalized nodal variables \mathbf{a}_L do not necessarily represent nodal displacements. In terms of a Hermite interpolation, (3.8) can additionally include nodal derivatives of the variables. For sake of clarity, the equivalent approximation of the variation of the deformation map for a Hermite interpolation is introduced by

$$\delta \varphi^h = \sum_{\mathcal{I}} \delta \varphi_I N_I + \sum_{\mathcal{J}} \delta \mathbf{F}_J \cdot \mathbf{M}_J + \sum_{\mathcal{K}} \delta \mathbf{G}_K : \mathbf{L}_K. \quad (3.9)$$

N_I , \mathbf{M}_J and \mathbf{L}_K are scalar, vector and tensor valued ansatz functions. The functions are related to the interpolated nodal values at the (possibly non-equal) nodal points $\mathbf{X}_I \in \mathcal{I}$, $\mathbf{X}_J \in \mathcal{J}$ and $\mathbf{X}_K \in \mathcal{K}$. Equation (3.9) contains $\delta \varphi_I$, which are the nodal variations of the deformation map φ , the quantities $\delta \mathbf{F}_J$ represent the nodal variations of the deformation gradient, whereas $\delta \mathbf{G}_K$ refer to the variations of the second derivatives of $\delta \varphi$. A more detailed description will follow in subsection 5.4.3.

Remark 3.2 (Hermite interpolation for the geometry approximation) *Generally, it is as well possible to introduce a Hermite interpolation of the geometry. However, the restriction is that the interpolation property, especially for the gradient values is difficult to realize. Therefore, in this case, the Hermite shape functions are related to a reference coordinate system. A detailed description needs some of the results of chapter 4 and will follow in section 5.4.*

3.3 Boltzmann continuum: Discretization and linearization

Using the notations of sections 3.1 and 3.2, the discrete equations for the Boltzmann continuum are recapitulated briefly. Since all our computations have been done in the material configuration, we omit any expressions in the spatial description of the problem. The interested reader is referred to the textbooks of Bonet and Wood [43] or Wriggers [222].

3.3.1 Discrete weak equations

To be able to solve (2.13), i.e. the weak form of the boundary value problem introduced in section 2.2.1, the test functions $\delta \varphi$ are reduced to a finite subset of the space $H^1(\mathcal{B}_0)$, spaned by the set of shape functions Ψ_I . Thus, the discrete set of residuals are introduced by

$$\mathbf{R}_I(\varphi^h) := \int_{\mathcal{B}_0} \mathbf{P}(\varphi^h) \cdot \nabla_{\mathbf{x}} \Psi_I \, dV - \int_{\partial \mathcal{B}_0^P} \bar{\mathbf{t}}^P \Psi_I \, dA - \int_{\mathcal{B}_0} \mathbf{b} \Psi_I \, dV. \quad (3.10)$$

3.3.2 Linearized discrete weak equations

For the efficient solving of

$$\mathbf{R}_I(\varphi^h) = \mathbf{0}, \quad (3.11)$$

a Newton-Raphson scheme is used. To this end, the linearization of the residuals is needed

$$\mathbf{R}_I^{k+1} = \mathbf{R}_I^k + \Delta \mathbf{R}_I \doteq \mathbf{0}, \quad (3.12)$$

whereby the iteration increment $\Delta \mathbf{R}_I$ is given by

$$\Delta \mathbf{R}_I = \frac{\partial \mathbf{R}_I}{\partial \mathbf{a}_J} \cdot \Delta \mathbf{a}_J = \mathbf{K}_{IJ} \cdot \Delta \mathbf{a}_J \quad (3.13)$$

and the incremental update $\Delta \mathbf{a}_j$ of the nodal variables is calculated by solving

$$\mathbf{K}_{IJ} \cdot \Delta \mathbf{a}_J = -\mathbf{R}_I^k. \quad (3.14)$$

Here, the tangent stiffness matrix \mathbf{K} is given by

$$\mathbf{K}_{IJ} = \int_{\mathcal{B}_0^h} \nabla_{\mathbf{x}} \Psi_I \cdot \frac{\partial \mathbf{P}^T}{\partial \mathbf{F}} \cdot \nabla_{\mathbf{x}} \Psi_J \, dV, \quad (3.15)$$

and is clearly symmetric, if \mathbf{P} derives from a potential.

3.4 Gradient continuum: Discretization and linearization

To solve the governing equations of gradient elasticity numerically, an appropriate discretization scheme has to be derived. Due to the occurring second order derivatives of the variation of the deformation map, introduced in (2.21), i.e. $\delta \mathbf{G} = \nabla_{\mathbf{x}}^2 \delta \varphi$, the variation $\delta \varphi$ of the deformation map φ needs to be in $H^2(\mathcal{B}_0)$, requiring C^1 continuous formulations. Thus, in the following, appropriate C^1 continuous discretization schemes are derived. In this section the general formulation of the discretized equations is stated and the specification of the particular schemes is given subsequently.

3.4.1 Discrete weak equations

For the gradient continuum, the weak formulation is already introduced in section 2.3.1. The discretization of (2.21) by means of (3.8) gives the following expressions for the residuals,

$$\begin{aligned} \mathbf{R}_I(\boldsymbol{\varphi}^h) := & \int_{\mathcal{B}_0} [\mathbf{P}(\boldsymbol{\varphi}^h) \cdot \nabla_{\mathbf{x}} \Psi_I + \mathbf{Q}(\boldsymbol{\varphi}^h) : \nabla_{\mathbf{x}}^2 \Psi_I] \, dV \\ & - \int_{\partial \mathcal{B}_0^P} \bar{\mathbf{t}}^P \Psi_I \, dA + \int_{\partial \mathcal{B}_0^Q} \bar{\mathbf{t}}^Q \nabla_{\mathbf{x}}^N \Psi_I \, dA - \int_{\mathcal{B}_0} \mathbf{b} \Psi_I \, dV = 0. \end{aligned} \quad (3.16)$$

3.4.2 Linearized discrete weak equations

Similar to section 3.3.2, the linearization of the residuals is introduced, leading to the slightly more complicated stiffness matrix

$$\begin{aligned} \mathbf{K}_{IJ} = & \int_{\mathcal{B}_0} \nabla_{\mathbf{x}} \Psi_I \cdot \frac{\partial \mathbf{P}^T}{\partial \mathbf{F}} \cdot \nabla_{\mathbf{x}} \Psi_J \, dV + \int_{\mathcal{B}_0} \nabla_{\mathbf{x}} \Psi_I \cdot \frac{\partial \mathbf{P}^T}{\partial \mathbf{G}} : \nabla_{\mathbf{x}}^2 \Psi_J \, dV \\ & + \int_{\mathcal{B}_0} \nabla_{\mathbf{x}}^2 \Psi_I : \frac{\partial \mathbf{Q}^T}{\partial \mathbf{F}} \cdot \nabla_{\mathbf{x}} \Psi_J \, dV + \int_{\mathcal{B}_0} \nabla_{\mathbf{x}}^2 \Psi_I : \frac{\partial \mathbf{Q}^T}{\partial \mathbf{G}} : \nabla_{\mathbf{x}}^2 \Psi_J \, dV. \end{aligned} \quad (3.17)$$

Remark 3.3 (Additive split of the internal energy) *For the special case, where an additive split of the internal free energy is possible, i.e.*

$$W(\mathbf{F}, \mathbf{G}) = W^F(\mathbf{F}) + W^G(\mathbf{G}), \quad (3.18)$$

the linearization (3.17) reduces to

$$\mathbf{K}_{IJ} = \int_{\mathcal{B}_0} \nabla_{\mathbf{x}} \Psi_I \cdot \frac{\partial \mathbf{P}^T}{\partial \mathbf{F}} \cdot \nabla_{\mathbf{x}} \Psi_J + \nabla_{\mathbf{x}}^2 \Psi_I : \frac{\partial \mathbf{Q}^T}{\partial \mathbf{G}} : \nabla_{\mathbf{x}}^2 \Psi_J \, dV. \quad (3.19)$$

since in this case $\partial \mathbf{P}^T / \partial \mathbf{G} = \mathbf{0}$ and additionally $\partial \mathbf{Q}^T / \partial \mathbf{F} = \mathbf{0}$.

3.4.3 Computation of the Hessian

In order to obtain the second derivative of the shape functions $\partial^2 \Xi_I / \partial \mathbf{X}^2$, one has to consider the following equations. Let

$$\mathbf{J} := \frac{\partial \mathbf{X}}{\partial \boldsymbol{\xi}}$$

denote the Jacobi mapping. The second derivative is then determined by means of the following applications of the chain rule

$$\begin{aligned} \frac{\partial^2 \Xi_I}{\partial \mathbf{X}^2} &= \partial \left(\frac{\partial \Xi_I}{\partial \boldsymbol{\xi}} \cdot \frac{\partial \boldsymbol{\xi}}{\partial \mathbf{X}} \right) / \partial \mathbf{X} = \partial \left(\frac{\partial \Xi_I}{\partial \boldsymbol{\xi}} \cdot \mathbf{J}^{-1} \right) / \partial \mathbf{X} \\ &= \mathbf{J}^{-T} \cdot \frac{\partial^2 \Xi_I}{\partial \boldsymbol{\xi}^2} \cdot \mathbf{J}^{-1} + \frac{\partial \Xi_I}{\partial \boldsymbol{\xi}} \cdot \frac{\partial \mathbf{J}^{-1}}{\partial \mathbf{J}} : \frac{\partial^2 \mathbf{X}}{\partial \boldsymbol{\xi}^2} \cdot \mathbf{J}^{-1}. \end{aligned} \quad (3.20)$$

In case of a linear approximation of the geometry, it is obvious, that the second part of (3.20) is zero, due to $\partial^2 \mathbf{X} / \partial \boldsymbol{\xi}^2 = \mathbf{0}$.

3.4.4 Application of boundary conditions

For the application of essential boundary conditions along a straight boundary line, the influence of a set of four possible boundary conditions on the nodal values is given in table 3.1.

	u_n	u_t	$\partial_n u_n$	$\partial_n u_t$	$\partial_t u_n$	$\partial_t u_t$	$\partial_n^2 u_n$	$\partial_n^2 u_t$	$\partial_t^2 u_n$	$\partial_t^2 u_t$	$\partial_{nt}^2 u_n$	$\partial_{nt}^2 u_t$
1.	0	0	—	—	0	0	—	—	0	0	—	—
2.	u_n	u_t	—	—	0	0	—	—	0	0	—	—
3.	0	—	—	—	0	—	—	—	0	—	—	—
4.	0	—	—	0	0	—	0	—	0	—	—	0

Table 3.1: Imposition of different boundary conditions. 1. homogeneous displacements, 2. constant displacements, 3. fixed normal direction 4. boundary is symmetry axis of the problem.

4 Bernstein-Bézier patches

This chapter is designated to introduce the necessary fundamentals of the polynomial representations for a simple and efficient treatment of finite elements with higher order of continuity. For the description of classical C^0 -continuous elements, Lagrange polynomials have established themselves due to their interpolation property at the nodes and easy construction of the shape functions. However, when Hermite elements are involved, i.e. when directional derivatives are appearing, different approaches for the description of the shape functions have to be used. In most of the finite elements, the shape functions with the directional derivatives are used in a linear subparametric setting. In this case a linear subdivision of the geometry into triangles or quadrilaterals is combined with the use of shape functions of higher polynomial order. The major advantage within this linear approximation of the geometry is that the shape functions do not lose their polynomial structure on the physical element and therefore ensuring C^1 continuity is an easy task. The use of C^1 continuous piecewise polynomial functions on triangles goes back to Clough and Tocher [63] and Argyris [15] for the two dimensional case and Alfeld [5] or Worsey et al. [221] for the extension to three dimensions.

The main difficulty for the practical use of Hermite finite elements is the increased complexity within the construction of the shape functions. This is mainly caused by the fact that primal function values and its gradients behave differently under affine transformations. Therefore, several problems occur within the mapping of the reference to the physical element. In the earlier attempts, the monomial coefficients were specified by the setup of a coefficient matrix on the physical elements. The resulting system of equations can either be solved analytically or numerically. Even so, the numerical solution is provided by the computer, some aspects have to be considered. At first, a numerical solution can be costly, especially with increasing order of polynomials. Furthermore, one has to deal with the inversion of a Vandermonde-like system of equations. This is likely to be badly conditioned, thus reducing the accuracy of the finite element method itself, see [108]. Therefore the analytical solution of the problem is extremely important. Its computation gets really complicated if the wrong polynomial function basis is used for the construction of the shape functions.

In our opinion, the best parameterization is the use of the Bézier representation of polynomial splines. Therefore, the continuity of the piecewise polynomial splines on n dimensional simplices can directly be related to the geometrical positions of the control points (here, the coefficients of the Bernstein polynomials) in the $n + 1$ dimensional space. This is due to the fact that they combine the (linear) geometry approximation and the (higher order) approximation of the unknown scalar field. This principle will be explained in subsection 4.2.1.

The use of control points was initiated by de Casteljau [80] for the construction of piecewisely polynomial surfaces and has been intensively studied in the field of computer graphics, i.e. see the works of Dahmen [74], Böhm et al. [42] and Farin [93, 95] or even more extensively in the monographs of Prautzsch and Böhm [174]. An example for the use

of the monomial description to the construction of Hermite finite element shape functions is presented in the work of El-Zafrany and Cookson [83, 84]. A relation between the 1d Hermite interpolation and Bézier curves can be found in [77].

In case of dimension $n \geq 2$, it has to be distinguished between the bipolynomials, used in tensor product spaces and the Bernstein-Bézier patches for the construction of polynomial splines on simplices (triangles in the two dimensional case). In this chapter, the main focus is on the properties of the Bernstein-Bézier patches.

This chapter is structured as follows, in section 4.1, the three major classes of polynomial spaces are introduced and shortly compared to each other. It is followed by the introduction of the Bézier representation of polynomials on simplices in section 4.2 and a review on the basic relations of the control points and the related continuity properties in section 4.3. These results are necessary for the application of the two dimensional finite elements of chapter 5 as well as the construction of the smooth natural neighbor interpolants of chapter 7. Furthermore, the Bernstein-Bézier representation is highly related to the B-spline functions, introduced in chapter 6.

4.1 Polynomial spline descriptions

For the construction of finite element shape functions in the one dimensional case, mainly two types of polynomial representations have been established in the field of the finite element method. These are the Lagrange and Hermite interpolations. Here, the Bernstein-Bézier representation is presented. The use of the control points combines several of the advantages of both, the Hermite and Lagrange representation.

4.1.1 Lagrange interpolation

The usual set of polynomials for the construction of the finite element shape functions are the Lagrange polynomials. They are defined to be interpolating at a given set of points $\mathcal{P} := \{\mathbf{X}_1, \dots, \mathbf{X}_{k+1}\}$ where k denotes the degree of the polynomial,

$$N_K(\mathbf{X}) = \frac{\prod_{I \neq K} (\mathbf{X} - \mathbf{X}_I)}{\prod_{I \neq K} \mathbf{X}_K - \mathbf{X}_I}. \quad (4.1)$$

The major advantages of the Lagrange polynomials are the simple construction of the polynomial basis functions as well as the fact that an affine transformation of the geometry is performed by the application of the deformation to the nodal points.

An one dimensional example for Lagrange polynomials for an equidistant nodal distribution is presented in figure 4.1. As revealed by figure 4.1, the values of the derivatives do not show any specific structure. Therefore, Lagrange interpolation is not usefull for the application to Hermite finite elements, being one of the major disadvantages of the method. Additionally, with increasing polynomial order, the representation is loosing its stability, i.e. small errors in the positions of the nodal points can lead to completely different polynomial functions.

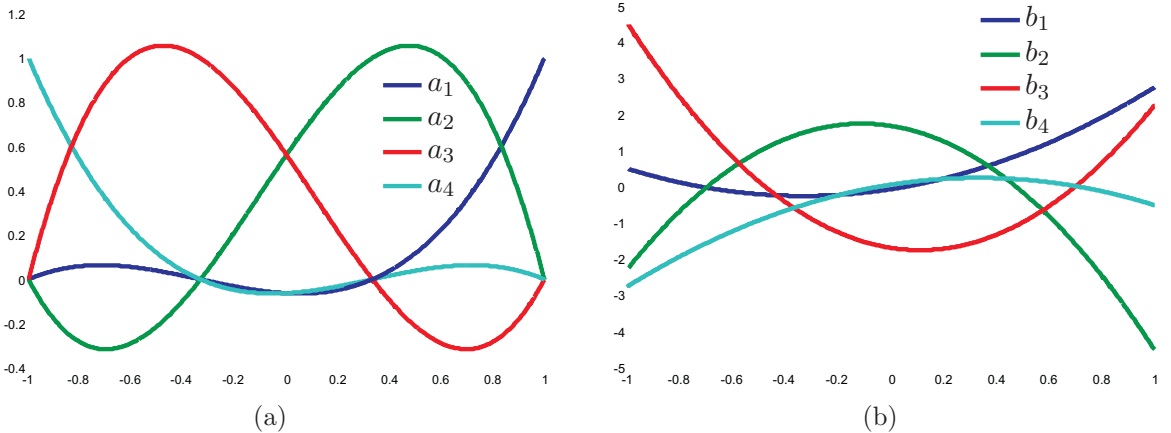


Figure 4.1: (a) Cubic Lagrange polynomial on the domain $[-1, 1]$. The functions a_i , $1 \leq i \leq 4$ are corresponding to the nodal points $[1, 1/3, -1/3, -1]$. (b) The b_i are the derivative values of a_i .

4.1.2 Hermite interpolation

Additionally to the primal unknowns, within a Hermite interpolation scheme, directional degrees of freedom are involved in the shape function description. The best known example are the C^1 continuous finite elements, based on the cubic Hermite polynomials which are illustrated in figure 4.2. For the presented one dimensional case, the length of the physical element is influencing the shape functions on the reference element. For higher dimensional elements, one of the major difficulties is that the shape functions on the physical element are again related to the element size but even worse, dependent on the geometry of the physical element as well. Therefore, extensions to higher dimensions based on tensor product spaces are favorite approaches. Therein, the principle of 1d Hermite polynomials is used for each dimension, separately. The most famous finite element of this kind is the Bogner-Fox-Schmidt (BFS) element. Moreover, B-spline finite elements and the isogeometric analysis are based on this principle as well. A detailed instruction for the use of the BFS element will be given in subsection 5.4.4. B-splines are discussed in chapter 6.

Nevertheless, Hermite interpolation is not restricted to tensor product spaces. Piecewise polynomial splines defined on simplices are well known as well, but show some additional difficulties due to the strong relation of the shape functions and the element geometry. The global construction of the shape functions on simplices can be done by means of a coefficient matrix \mathbf{A} , resulting in the following linear system of equations:

$$\underbrace{\begin{pmatrix} 1 & X_1 & Y_1 & X_1^2 & Y_1^2 & X_1Y_1 & \dots \\ 1 & X_2 & y_2 & X_2^2 & Y_2^2 & X_2Y_2 & \dots \\ \vdots & & & & & & \\ 0 & 1 & 0 & 2X_1 & 0 & Y_1 & \dots \\ \vdots & & & & & \ddots & \end{pmatrix}}_{\mathbf{A}} \begin{pmatrix} a_1 \\ a_2 \\ a_3 \\ \vdots \end{pmatrix} = \delta_{ij}. \quad (4.2)$$

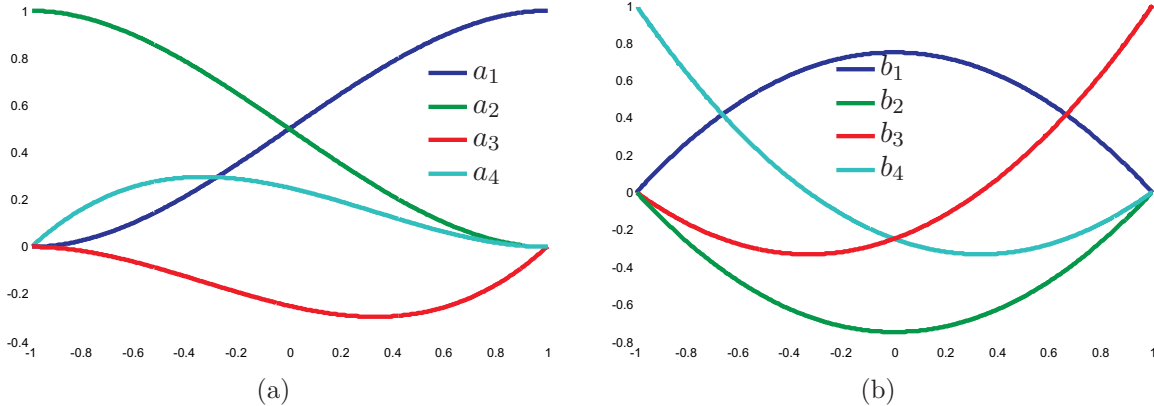


Figure 4.2: (a) Cubic Hermite polynomials on the interval $[-1, 1]$, a_1 and a_2 the interpolatory functions at the boundaries and a_3 and a_4 interpolate for the derivatives. (b) b_i the derivatives of the cubic Hermite polynomials, a_i .

Here, $(X_1, Y_1), \dots, (X_m, Y_m)$ are the nodal positions, at which the shape function values are defined, the δ_{ij} is indicating that only one value at the nodes is non-zero. In the first two rows of (4.2), the entries are the monomials, neccessary for the description of the primal unknowns, whereas the third row is including the derivatives of the monomials with respect to the coordinate system.

The equation system of (4.2) can either be solved numerically as proposed in [239] or once analytically which is realized in [32] for the Argyris element or in [34] for the HCT element. Due to the appearance of higher order polynomials, the coefficient matrix \mathbf{A} is likely to be badly conditioned for irregular meshes. Therefore and for reasons of efficiency, the analytical derivation should be preferred. However, solving of equation systems of this kind is complex and any modifications of the element are extremely difficult. Therefore, the theory of Bernstein-Bézier polynomials is used to transform the abstract system of equations to simple geometric constraints, necessary to construct the shape functions and achieve the desired continuity inside the macroelements.

4.1.3 Bernstein polynomials

The key to achieve a better methodology for the construction of Hermite pointwise interpolating shape functions with arbitrary order of continuity are the Bernstein polynomials. The 1d Bernstein polynomials are defined by the use of barycentric coordinates. At a point λ , $0 \leq \lambda_i \leq 1$, The Bernstein polynomials of degree $k \in \mathbb{N}$ are the summands of the multinomial expansion of

$$1 = [\lambda_1 + \lambda_2]^k = \sum_{i=0}^k \binom{k}{i} \lambda_1^i \lambda_2^{k-i}. \quad (4.3)$$

In (4.3), $\binom{k}{i}$ represents the binomial coefficient. The four cubic Bernstein polynomials are presented in figure 4.3(a). Within figure 4.3(b) it is apparent that the derivatives of the Bernstein polynomials show some kind of structure, allowing the construction of higher

order continuity. Additionally, similar to the Lagrange polynomials, affine transformations of a geometry, defined by the coefficients of the Bernstein polynomials, are realized by the application of the transformation to the coefficients of the Bernstein polynomials.

The extension of the Bernstein polynomial to an $n = m - 1$ dimensional simplex can be

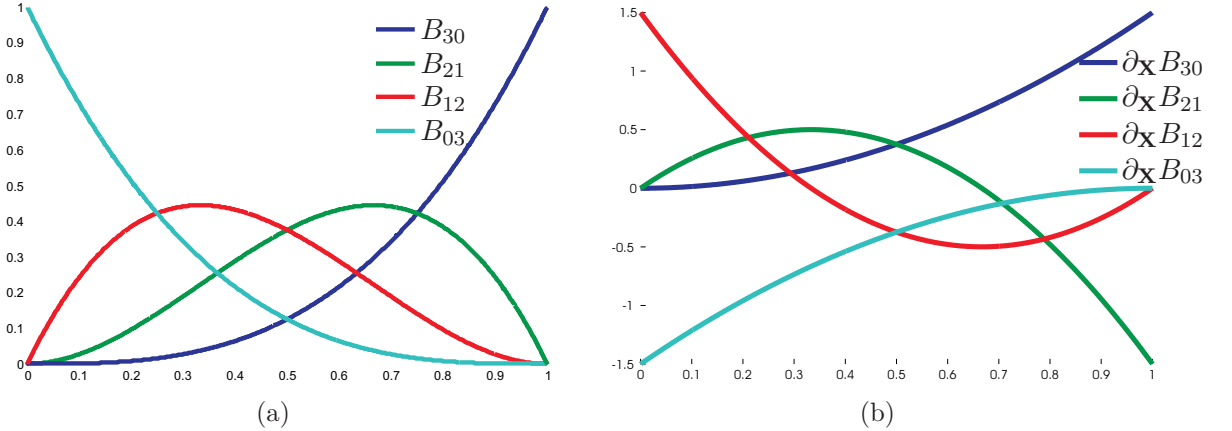


Figure 4.3: (a) Bernstein polynomials on the interval $[0, 1]$ and (b) their derivatives.

done analogously by the multinomial expansion

$$1 = (\lambda_1 + \lambda_2 + \dots + \lambda_m)^k. \quad (4.4)$$

For the mathematical description of the higher dimensional Bernstein polynomials, the following definition is introduced:

A m -variate Bernstein polynomial B_α^k of degree $k := |\boldsymbol{\alpha}|$ is defined as

$$B_\alpha^k := \frac{k!}{\alpha!} \boldsymbol{\lambda}^\alpha = \frac{k!}{\alpha!} [\lambda_1]^{\alpha_1} [\lambda_2]^{\alpha_2} \dots [\lambda_m]^{\alpha_m}, \quad (4.5)$$

based on the definitions for the use of a multi-index $\boldsymbol{\alpha} \in \mathbb{N}^m$:

$$|\boldsymbol{\alpha}| = \sum_{i=1}^m \alpha_i, \quad \alpha! = \prod_{i=1}^m \alpha_i \quad \text{and} \quad \boldsymbol{\lambda}^\alpha = \prod_{i=1}^m [\lambda_i]^{\alpha_i}. \quad (4.6)$$

Additionally, the notation \mathcal{A}_k for the index sets of all possible vectors $\boldsymbol{\alpha}$ describing the m -variate Bernstein polynomials is introduced,

$$\mathcal{A}_k := \{\boldsymbol{\alpha} \in \mathbb{N}^m : |\boldsymbol{\alpha}| = k\}. \quad (4.7)$$

The Bernstein polynomials have the following useful properties:

linear independence: Any linear combination of the Bernstein polynomials can only be zero, if all coefficients are vanishing, i.e.

$$\sum_{\alpha \in \mathcal{A}} b_\alpha B_\alpha^k(\boldsymbol{\lambda}) = 0 \iff b_\alpha = 0 \quad \forall \boldsymbol{\alpha} \in \mathcal{A}_k. \quad (4.8)$$

positivity: For all points $\boldsymbol{\lambda}$, conformal to the condition $0 < \lambda_i < 1$, the Bernstein polynomial is strictly positive: $B_\alpha^k(\boldsymbol{\lambda}) > 0$.

interpolating at the vertices: At the points $\lambda_i = 1$, the function value of the polynomial curve

$$c(\boldsymbol{\lambda}) := \sum_{\beta} c_{\beta} B_{\beta}^k \quad (4.9)$$

is given by c_{β} , with $\beta_i = k$.

partition of unity: The summation over all Bernstein polynomials equals one,

$$\sum_{\alpha \in \mathcal{A}_k} B_{\alpha}^k(\boldsymbol{\lambda}) = 1, \quad \forall \boldsymbol{\lambda} \in \mathbb{R}^m. \quad (4.10)$$

This property is a direct result of the definition due to the multinomial expansion, see (4.4).

4.2 Bernstein-Bézier patches

A polynomial spline on a linear triangulation described by the coefficients of the Bernstein polynomials is called the Bézier representation of the spline or Bézier spline¹. By the use of the Bézier representation, a Bernstein-Bézier patch is the image of the polynomial function on the reference simplex. Within this section, the properties of the Bernstein-Bézier patches, necessary for the construction of the finite element shape functions occurring in chapter 5 are recapitulated. Therefore, the control point description is introduced. Due to the fact that within the control points, both, the map from a reference to the physical element, as well as the definition of the function are combined, the abstract problem of the construction of Hermite finite element shape functions is transformed into a purely geometric problem.

The use of the Bézier representation has three major advantages. As already mentioned, the control point description is invariant against affine transformations. This means that if the control points are used for the definition of a geometry, any affine transformation of the geometry is accomplished by the application of the transformation to the control points. Second, the introduction of control points is leading to an intuitive definition of a polynomial function due to the relation of the control polygon to the resulting curve. Furthermore, its computation is numerically more stable since de Casteljau's algorithm [80] can be used.

Remark 4.1 (Equivalence of Bézier and monomial representation:) A direct result of the linear independence of the Bernstein polynomials is that each polynomial curve has its Bézier representation. The completeness is a simple counting argument.

¹Please note that a Bézier spline is not the same as a B-spline (Box-spline). Even so they are closely related to each other.

4.2.1 Basics

A Bernstein-Bézier patch $\mathbf{c}(\boldsymbol{\lambda})$ is a polynomial curve in the Bézier representation, defined on a simplex by

$$\mathbf{c}(\boldsymbol{\lambda}) := \sum_{\alpha} \mathbf{c}_{\alpha} B_{\alpha}^k(\boldsymbol{\lambda}), \quad (4.11)$$

where the coefficients \mathbf{c}_{α} are called the control points. In case of the finite element analysis, the description of the physical element, as well as the approximation of an unknown scalar or vector valued field are defined by polynomials on the reference element. By the use of control points, the mapping of the reference to the physical element as well as the construction of a scalar valued shape function is combined in one vector. For the shape function on an n dimensional simplex, the first n dimensions are related to the approximation of the physical element whereas the last dimension describes a scalar valued shape function on the element itself. The control points for the definition of a linear triangle are presented in figure 4.4.

In this contribution, the Bézier representation is used for the application to subparametric finite elements. Therefore the first n dimensions of the control point coordinates, denoted by $\bar{\mathbf{c}}_{\alpha} \in \mathbb{R}^n$ are equidistantly distributed on the physical element. The remaining value, responsible for the shape function on the physical element are denoted by b_{α} and the unknown scalar or vector valued field, given as polynomial function on the simplex is denoted

$$\mathbf{b}(\boldsymbol{\lambda}) := \sum_{\alpha} \mathbf{b}_{\alpha} B_{\alpha}^k(\boldsymbol{\lambda}). \quad (4.12)$$

The whole control point set is now defined by

$$\mathbf{c}_{\alpha} := \begin{pmatrix} \bar{\mathbf{c}}_{\alpha} \\ b_{\alpha} \end{pmatrix}. \quad (4.13)$$

In case of a linear geometry approximation, the coordinates $\bar{\mathbf{c}}_{\alpha}$ are uniquely defined by the vertex coordinates of the linear elements. Let $\mathbf{X}_1, \mathbf{X}_2, \dots, \mathbf{X}_{n+1} \in \mathbb{R}^n$ denote the vertices of the simplex, then the first n dimensions $\bar{\mathbf{c}}_{\alpha}$ are directly given by the relation

$$\bar{\mathbf{c}}_{\alpha} = \sum_{j=1}^{n+1} \frac{\alpha_j}{k} \mathbf{X}_j, \quad (4.14)$$

compare figure 4.4 for $n = 2$ and $k = 3$. This definition seems to be odd but by the combination of the approximation of the physical element as well as the construction of scalar valued shape functions it is possible to identify certain relations of the control points which are necessary for the construction of globally C^1 continuous finite element functions.

4.2.2 Control mesh

Introducing the vectors

$$\mathbf{e}_i \in \mathbb{R}^m \text{ with } (\mathbf{e}_i)_j := \delta_{ij}, \quad (4.15)$$

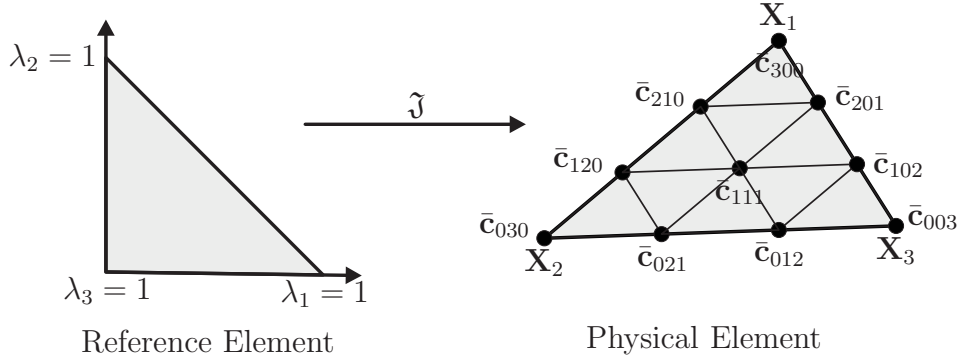


Figure 4.4: Mapping of the reference to the physical element. The control point distribution for the geometry description is given by equation (4.14).

the control mesh is the piecewise linear function, defined by each set of m control points \mathbf{c}_α , which satisfies the pairwise relation for their multiindices $\boldsymbol{\alpha}_a$, $a, b = 1, \dots, m$

$$\boldsymbol{\alpha}_a - \mathbf{e}_i = \boldsymbol{\alpha}_b - \mathbf{e}_j. \quad (4.16)$$

For the bivariate case, the piecewise linear function, connecting the control points is called the control polygon, compare to figures 4.5 and 4.8. The control polygons for the quintic Bernstein polynomials on the interval $[0, 1]$ is presented in figure 4.5(a). It is nicely seen that at the boundaries, the tangent of the curve coincides with the control polygon. Additionally, the control polygon of the quartic polynomial of the derivatives can observed, revealing a periodic structure, as well, see 4.5(b).

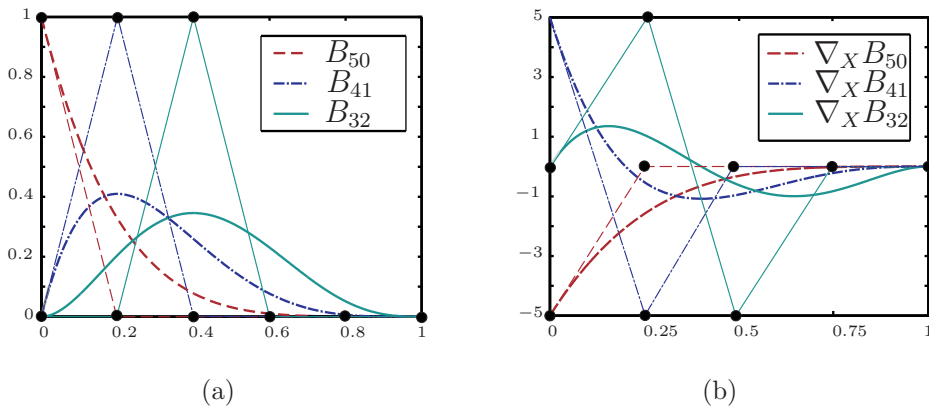


Figure 4.5: Bivariate Bernstein polynomials together with their control polygons. (a): Quintic Bernstein polynomials. (b): Derivatives of the quintic Bernstein polynomials. The remaining polynomials are omitted for reasons of symmetry.

4.3 Derivatives and continuity conditions

Within this chapter, the derivatives of the Bernstein-Bézier patches on the physical domain are related to the control point positions. Therefore, the construction of the finite element shape functions can easily be accomplished. Based on these results, the necessary geometric relations of the control mesh of two neighboring patches for the desired C^1 continuity are presented. They are extremely useful for the description of the macro elements, where only continuity conditions, but no primal or gradient values have to be satisfied.

4.3.1 Derivatives values at the vertices of a simplex

Within this chapter, the derivative values of the Bernstein-Bézier patches on the physical simplex are derived. The positions of the vertices of the simplex are denoted \mathbf{X}_I . Using the definition of the control points, it holds that $\mathbf{X}_I = \bar{\mathbf{c}}_{\alpha_I}$, $\alpha_I := k\delta_{IJ}$ and k the order of the Bernstein polynomials.

The derivative of a Bernstein-Bézier patch $\mathbf{b}(\boldsymbol{\lambda})$ with respect to the local coordinate system is given by

$$\frac{\partial \mathbf{b}(\boldsymbol{\lambda})}{\partial \lambda_i} = \sum_{\boldsymbol{\alpha}} b_{\boldsymbol{\alpha}} \alpha_i B_{\boldsymbol{\alpha}-\mathbf{e}_i}^{k-1}, \quad (4.17)$$

where \mathbf{e}_i is defined as in (4.15) and the polynomials $B_{\boldsymbol{\alpha}-\mathbf{e}_i}^{k-1}$ with $\min(\boldsymbol{\alpha} - \mathbf{e}_i) < 0$ are defined to be zero.

For sake of clarity, in the following part of this section, we restrict ourselves to the two dimensional case, although the principles could be extended to the arbitrary dimensional case. Here, the definitions for the triangle, as presented in figure 4.6 are used. Therein the vertices are denoted by \mathbf{X}_I and the edge vectors are defined $\mathbf{E}_I = \mathbf{X}_{I+1} - \mathbf{X}_I$.

In the first part of this section, we consider $\mathbf{b}(\boldsymbol{\lambda})$ to be a vector valued function on the simplex, in the sense of (3.9). First, we explain the construction of vector valued shape functions \mathbf{M}_J , fulfilling $\nabla_{\mathbf{X}} \mathbf{M}_J = \mathbf{I}_2$. Introducing the vector $\bar{\boldsymbol{\lambda}} := (\lambda_2, \lambda_3)$ and making use of (4.17) together with the relation $\lambda_1 = 1 - \lambda_2 - \lambda_3$, the derivative of the Bernstein-Bézier patch $\mathbf{b}(\boldsymbol{\lambda})$ at the vertex $\lambda_1 = 1$ is given by

$$\frac{\partial \mathbf{b}(\boldsymbol{\lambda})}{\partial \bar{\boldsymbol{\lambda}}} \Big|_{\lambda_1=1} = k (\mathbf{b}_{(k-1)10} - \mathbf{b}_{k00}, \mathbf{b}_{(k-1)01} - \mathbf{b}_{k00}). \quad (4.18)$$

By application of the chain rule, the derivative with respect to the local coordinates is stated as

$$\frac{\partial \mathbf{b}(\boldsymbol{\lambda})}{\partial \mathbf{X}} \Big|_{\lambda_1=1} = k (\mathbf{b}_{(k-1)10} - \mathbf{b}_{k00}, \mathbf{b}_{(k-1)01} - \mathbf{b}_{k00}) \cdot \left(\frac{\partial \mathbf{X}}{\partial \bar{\boldsymbol{\lambda}}} \right)^{-1} \quad (4.19)$$

and therefore, an interpolation relation at the vertices ($\partial \mathbf{b}(\boldsymbol{\lambda}) / \partial \mathbf{X} = \delta_{ij}$) for vector valued control points $\mathbf{b}_{\boldsymbol{\alpha}}$ is achieved for

$$\begin{aligned} \mathbf{b}_{(k-1)10} - \mathbf{b}_{k00} &= \frac{1}{k} [\mathbf{X}_2 - \mathbf{X}_1] = \frac{1}{k} \mathbf{E}_1 \quad \text{and} \\ \mathbf{b}_{(k-1)01} - \mathbf{b}_{k00} &= \frac{1}{k} [\mathbf{X}_3 - \mathbf{X}_1] = -\frac{1}{k} \mathbf{E}_3. \end{aligned} \quad (4.20)$$

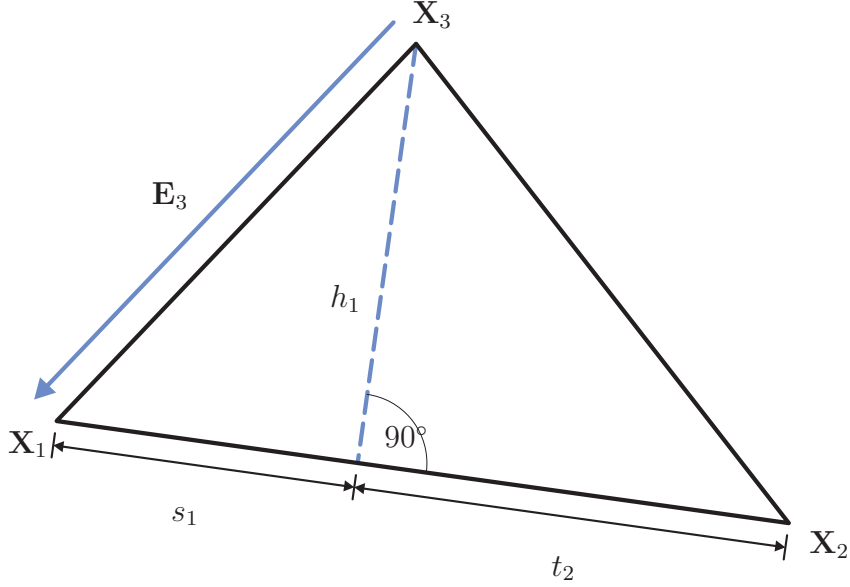


Figure 4.6: Description of the relevant geometric properties of the triangle.

By the use of the definition of the control point values $\bar{\mathbf{c}}$, (4.14), (4.20) can be transformed to the relation

$$\begin{aligned} \mathbf{b}_{(k-1)10} - \mathbf{b}_{k00} &= \bar{\mathbf{c}}_{(k-1)10} - \bar{\mathbf{c}}_{k00} \quad \text{and} \\ \mathbf{b}_{(k-1)01} - \mathbf{b}_{k00} &= \bar{\mathbf{c}}_{(k-1)01} - \bar{\mathbf{c}}_{k00}, \end{aligned} \quad (4.21)$$

and therefore, the values of the derivative are only related to the control points.

A similar result can be achieved for the second order derivative. The results can be used for the construction of the tensor valued shape functions \mathbf{L}_K occurring in (3.9). Here, the results will be presented componentwise, and therefore, a scalar valued field $b(\boldsymbol{\lambda})$ is considered. Straightforward computations lead to

$$\begin{aligned} \frac{\partial^2 b(\boldsymbol{\lambda})}{\partial \boldsymbol{\lambda}^2} &= \\ k(k-1) \left(\begin{array}{cc} b_{k00} - 2b_{(k-1)10} + b_{(k-2)20} & b_{k00} - b_{(k-1)10} - b_{(k-1)01} + b_{(k-2)11} \\ sym. & b_{k00} - 2b_{(k-1)01} + b_{(k-2)02} \end{array} \right). \end{aligned} \quad (4.22)$$

Due to the linear relation between the barycentric coordinates and the physical coordinate system, the second derivative with respect to \mathbf{X} is given by

$$\frac{\partial^2 b(\boldsymbol{\lambda})}{\partial \mathbf{X}^2} = k[k-1] \left(\frac{\partial \mathbf{X}}{\partial \boldsymbol{\lambda}} \right)^{-T} \cdot \frac{\partial^2 b(\boldsymbol{\lambda})}{\partial \boldsymbol{\lambda}^2} \cdot \left(\frac{\partial \mathbf{X}}{\partial \boldsymbol{\lambda}} \right)^{-1}, \quad (4.23)$$

motivating the following definition

$$\mathbf{V}_{ij} = -\frac{1}{2} [\mathbf{E}_i \otimes \mathbf{E}_j + \mathbf{E}_j \otimes \mathbf{E}_i]. \quad (4.24)$$

with $i \in \{1, 3\}$, since

$$\left(\frac{\partial \mathbf{X}}{\partial \boldsymbol{\lambda}} \right)^{-T} \cdot \mathbf{V}_{ij} \cdot \left(\frac{\partial \mathbf{X}}{\partial \boldsymbol{\lambda}} \right)^{-1} = \left(\begin{array}{cc} \delta_{1i}\delta_{1j} & \frac{1}{2}(\delta_{1i}\delta_{2j} + \delta_{1i}\delta_{2j}) \\ \frac{1}{2}(\delta_{1i}\delta_{2j} + \delta_{1i}\delta_{2j}) & \delta_{2i}\delta_{2j} \end{array} \right). \quad (4.25)$$

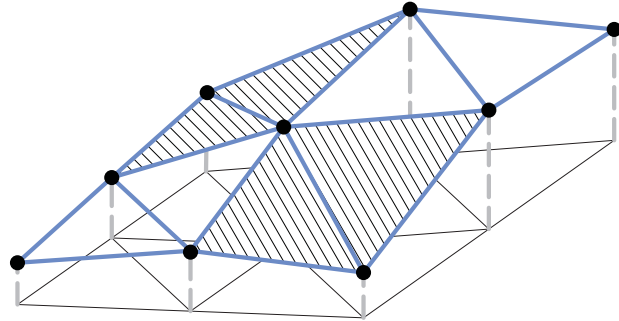


Figure 4.7: Control polygon for a trivariate quadratic Bernstein-Bézier patch. C^1 continuity is achieved, if the shaded surfaces are coplanar and the quadrilateral projections are congruent.

The result of equation (4.25) is the desired property for interpolation shape functions in terms of the second derivative. This means that the coefficients in the matrix of (4.22) have to be chosen such that they are equal to $\frac{1}{k[1-k]} \mathbf{V}_{ij}$.

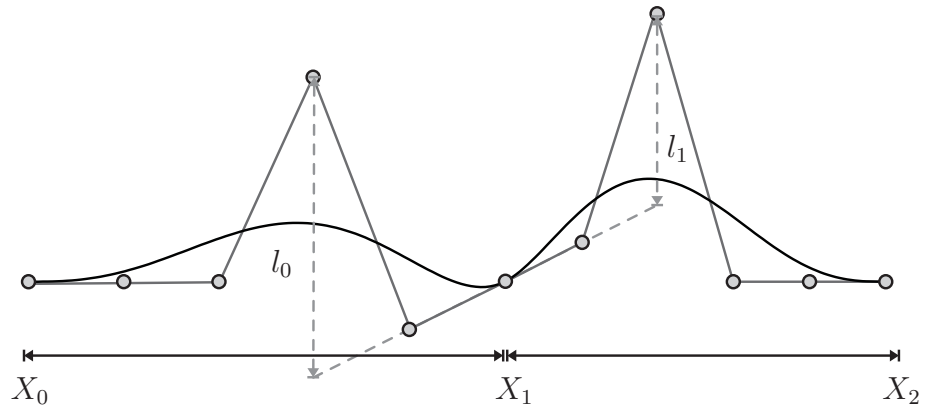


Figure 4.8: Control polygon for a bivariate quintic Bernstein-Bézier patch.

The one dimensional case Considering only one dimension, simple computations result in the derivatives of the Bernstein-Bézier patches at the node X_1 which is characterized by the local coordinate $\lambda_1 = 1$

$$\left. \frac{\partial b(\boldsymbol{\lambda})}{\partial \lambda_2} \right|_{\lambda_1=1} = k[b_{[k-1]1} - b_{k0}], \quad (4.26)$$

and the value of the derivative with respect to the physical coordinates X is therefore given by

$$\frac{\partial b(\boldsymbol{\lambda})}{\partial X} \Big|_{\lambda_1=1} = \frac{k}{[X_2 - X_1]} [b_{[k-1]1} - b_{k0}]. \quad (4.27)$$

In terms of the two dimensional control points \mathbf{c}_α , (4.27) can be rewritten by

$$\frac{\partial b(\boldsymbol{\lambda})}{\partial X} \Big|_{\lambda_1=1} = \frac{(\mathbf{c}_{[k-1]1})_2 - (\mathbf{c}_{k0})_2}{(\mathbf{c}_{[k-1]1})_1 - (\mathbf{c}_{k0})_1}. \quad (4.28)$$

A direct consequence of (4.28) and the intercept theorems is that the first derivative across a shared point is continuous if the control points in its direct neighborhood are coplanar, compare to figure 4.8. Note, that this result does not depend on the degree of the polynomial.

The value of the second derivative w.r.t. λ_2 is given by

$$\frac{\partial^2 b(\boldsymbol{\lambda})}{\partial \lambda_2^2} \Big|_{\lambda_1=1} = k[k-1][b_{k0} - 2b_{[k-1]1} + b_{[k-2]2}], \quad (4.29)$$

i.e. the second derivative is zero at the point X_1 if the control points \mathbf{c}_α with $k-\alpha_1 \leq 2$ are coplanar. For a continuous second derivative only the difference $l_1 = b_{[k-2]2} - [b_{k0} - 2b_{[k-1]1}]$ is of interest, compare to figure 4.8. When a new patch is introduced on $[X_0, X_1]$ with $l_0 = b_{2[k-2]} - [b_{0k} - 2b_{1[k-1]}]$ it can be shown that the following equation holds

$$\frac{[l_0]}{[l_1]} = \frac{[X_1 - X_0]^2}{[X_2 - X_1]^2} \quad (4.30)$$

if the function is globally C^2 -continuous at the shared point X_1 .

A geometric interpretation of this C^2 continuity condition based on the control points is possible as well. The interested reader is referred to Stärks theorem, introduced in [192]. Geometric conditions for the even higher order continuity can be found in [173].

4.3.2 Normal derivatives

It is possible to define the normal derivatives along the edges in a similar recursive relation as for the one dimensional case. Therefore, the normal vector in the nodal coordinate system $\boldsymbol{\lambda}$ has to be derived. Without loss of generality, this is demonstrated for edge \mathbf{E}_1 , opposite to \mathbf{X}_3 .

To find the values λ_1 and λ_2 of the orthogonal projection of the point \mathbf{X}_3 to the opposite edge, the values s_1 and t_1 as defined by

$$s_1 = \frac{\mathbf{E}_1 \cdot \mathbf{E}_3}{\|\mathbf{E}_1\|^2} \text{ and } t_1 = \frac{\mathbf{E}_2 \cdot \mathbf{E}_1}{\|\mathbf{E}_1\|^2}, \quad (4.31)$$

are necessary. A geometric description of s_1 and t_1 is given in figure 4.6. By use of the definition (4.31), the normal vector is given by

$$\mathbf{N} = \frac{1}{h_1} (-s_1, -t_1, 1), \quad (4.32)$$

where h_1 is the distance of the point \mathbf{X}_3 to the line crossing \mathbf{X}_1 and \mathbf{X}_2 or simply $h_1 = \|\mathbf{X}_3 - s_1\mathbf{X}_1 - t_1\mathbf{X}_2\|$.

By application of the chain rule and the use of (4.17), the derivative of a Bernstein polynomial B_{α}^k along the edge \mathbf{E}_1 is given by

$$\nabla_{\mathbf{x}}^N B_{\alpha}^k = \frac{k}{h_1} [B_{\alpha-\mathbf{e}_1}^{k-1}, B_{\alpha-\mathbf{e}_2}^{k-1}, B_{\alpha-\mathbf{e}_3}^{k-1}] \cdot [-s_1, -t_1, 1], \quad (4.33)$$

where $B_{\alpha}^{k-1} := 0$ for $\min_j(\alpha_j) < 0$. For sake of clarity, the results of (4.33) for a quintic patch, restricted to the boundary $\lambda_3 = 0$ are illustrated.

$$\begin{aligned} \nabla_{\mathbf{x}}^N B_{500}^5 &= -\frac{5}{h_1} [s_1 B_{400}^4] & \nabla_{\mathbf{x}}^N B_{401}^5 &= \frac{5}{h_1} [B_{400}^4] \\ \nabla_{\mathbf{x}}^N B_{410}^5 &= -\frac{5}{h_1} [s_1 B_{310}^4 + t_1 B_{400}^4] & \nabla_{\mathbf{x}}^N B_{311}^5 &= \frac{5}{h_1} [B_{310}^4] \\ \nabla_{\mathbf{x}}^N B_{320}^5 &= -\frac{5}{h_1} [s_1 B_{220}^4 + t_1 B_{310}^4] & \nabla_{\mathbf{x}}^N B_{221}^5 &= \frac{5}{h_1} [B_{220}^4] \\ \nabla_{\mathbf{x}}^N B_{230}^5 &= -\frac{5}{h_1} [s_1 B_{130}^4 + t_1 B_{220}^4] & \nabla_{\mathbf{x}}^N B_{131}^5 &= \frac{5}{h_1} [B_{130}^4] \\ \nabla_{\mathbf{x}}^N B_{140}^5 &= -\frac{5}{h_1} [s_1 B_{040}^4 + t_1 B_{130}^4] & \nabla_{\mathbf{x}}^N B_{041}^5 &= \frac{5}{h_1} [B_{040}^4] \\ \nabla_{\mathbf{x}}^N B_{050}^5 &= -\frac{5}{h_1} [t_1 B_{040}^4]. \end{aligned} \quad (4.34)$$

Going back to the general case, but motivated by the results of (4.34) the normal derivative of the Bézier polynomials is a Bézier function of degree $k - 1$ showing the following relation to the original control point values b_{α}^n

$$\nabla_{\mathbf{x}}^N b^k \Big|_{(\lambda_3=0)} = \frac{k}{h_1} \sum_{i=0}^{k-1} [b_{i[k-1-i]1}^k - s_1 b_{[i+1][k-1-i]0}^k - t_1 b_{[i][k-i]0}^k] B_{i,k-1-i,0}^{k-1}. \quad (4.35)$$

By simple geometric relations, the term

$$\frac{k}{h_1} [b_{i[k-1-i]1}^k - s_1 b_{[i+1][k-1-i]0}^k - t_1 b_{[i][k-i]0}^k] \quad (4.36)$$

can be identified to be the slope of the control polygon, in the direction perpendicular to the boundary of the physical triangle. By this derivation, the geometric description of Farin [95] or Böhm [42] is proven. It claims that the connection between two adjacent triangles is C^1 continuous if the control mesh triangles of the different elements having a common edge are coplanar. See figure 4.7 for the illustration of this property.

The reformulation of (4.36) states that the Bézier coefficients $b_{\alpha_1, \alpha_2, 0}^{k-1}$ describing the Bézier spline of the normal derivative along the edge $\lambda_3 = 0$ are given by

$$b_{\alpha_1, \alpha_2, 0}^{k-1} = b_{\alpha_1, \alpha_2, 1}^k - s_1 b_{\alpha_1+1, \alpha_2, 0}^k - t_1 b_{\alpha_1, \alpha_2+1, 0}^k, \quad (4.37)$$

being the slope of the surface in the direction of the normal vector, defined by the complete control points $\mathbf{c}_{\alpha_1, \alpha_2, 1}$, $\mathbf{c}_{\alpha_1+1, \alpha_2, 0}$ and $\mathbf{c}_{\alpha_1, \alpha_2+1, 0}$.

5 Finite elements

The finite element method is the most common method for solving partial differential equations, numerically. This chapter is dedicated to present the framework of finite elements for the solution of fourth order partial differential equations like gradient elasticity. A nice introduction to the classical finite element method for the application to second order problems together with the presentation of the early history can be found in Hahn [119]. For an excellent overview on the mathematical background, the interested reader is referred to Strang and Fix [196], Ciarlet [59] or Braes [46]. More applied introductions can be found in Wriggers [222] or Großmann [118].

Even though there is plenty of literature on C^0 continuous finite element formulations, very few of them treat C^1 continuous elements in a sufficient way. A nice introduction to finite elements for solving fourth order partial differential equation can be found in Ciarlet and Lions [60] or Zienkiewicz [239]. A comprehensive overview on C^1 finite elements is presented in Brenner [48] for the mathematical point of view and Farin [93] or Prautzsch et al. [174] for the application to computergraphics.

This chapter is structured as follows. The basic principles, necessary for the C^1 continuous finite element analysis are presented in section 5.1. In section 5.2, some non-conforming (not globally C^1 continuous) elements are revisited. This is followed by the presentation of the subparametric C^1 elements in section 5.3. The chapter closes with the description of isoparametric C^1 continuous elements, see section 5.4. Additionally, for the Bogner-Fox-Schmidt element several mesh construction algorithms, based on a linear reference mesh are presented in subsection 5.4.1.

5.1 Introduction to Hermite finite element descriptions

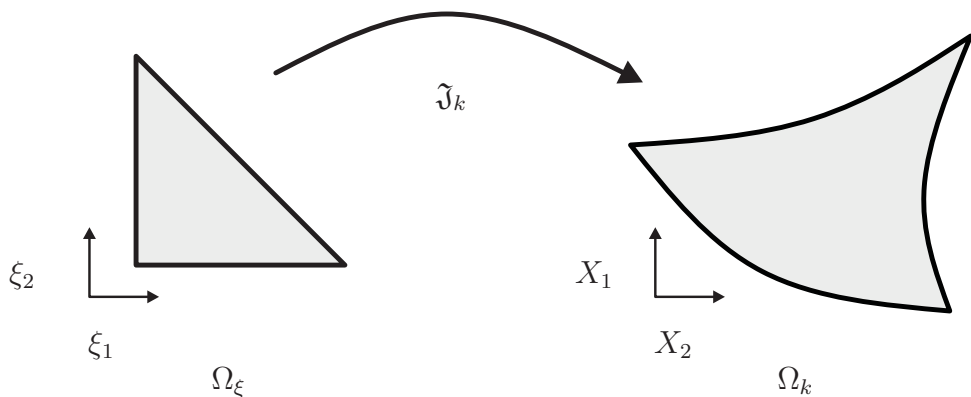


Figure 5.1: Jacobi mapping \mathfrak{J}_k of the reference element Ω_ξ in the reference coordinate system ξ to the physical element Ω_k in the physical space X .

Hermite finite elements are elements with derivative degrees of freedom within the de-

scription of the element. Therein the main difficulty is that the shape function values and their derivatives behave differently under affine transformations. This becomes apparent by observation of the bijective Jacobi mapping \mathfrak{J}_k of the reference element Ω_ξ to the physical element Ω_k , compare to figure 5.1. It is introduced as

$$\begin{aligned}\mathfrak{J}_k : \Omega_\xi &\rightarrow \Omega_k \subset \mathcal{B}_0 \\ \mathfrak{J}_k(\xi) &= \mathbf{X},\end{aligned}\tag{5.1}$$

and its inverse

$$\begin{aligned}\mathfrak{J}_k^{-1} : \Omega_k &\rightarrow \Omega_\xi \\ \mathfrak{J}_k^{-1}(\mathbf{X}) &= \xi.\end{aligned}\tag{5.2}$$

By the study of the relation between the element shape function $N_I(\xi)$ defined on the reference domain and its counterpart $\bar{N}_I(\mathbf{X})$ on the physical domain, defined by

$$\bar{N}_I(\mathbf{X}) := N_I(\mathfrak{J}_k^{-1}(\mathbf{X})),\tag{5.3}$$

and analyzing the shape function gradients $\nabla_{\mathbf{x}} \bar{N}_I(\mathbf{X})$ on the physical and $\nabla_\xi N_I(\xi)$ on the local element coordinate system, i.e. by

$$\nabla_{\mathbf{x}} \bar{N}_I(\mathbf{X}) = \nabla_\xi N_I(\mathfrak{J}_k^{-1}(\mathbf{X})) \cdot \frac{d\mathfrak{J}_k^{-1}(\mathbf{X})}{d\mathbf{x}}\tag{5.4}$$

it is obvious that in contrast to the function values, the interpolation property of the derivative values are in general either fulfilled on the reference or the spatial domain. Therefore, in contrast to the C^0 continuous shape functions, the shape function construction is highly related to the physical element and can not be restricted to the reference element.

Additional problems are occurring due to the fact that by the multiplication with the gradient $\nabla_{\mathbf{x}} \mathfrak{J}_k^{-1}$, the run of the gradient curve is not necessarily unique by simply describing the $k - 1$ normal derivative values at the element edges, since $\nabla_\xi N_I \cdot \nabla_{\mathbf{x}} \mathfrak{J}_k^{-1}$ is in general not a polynomial function. Even worse, a closer look at the shape function derivatives along the element boundaries of two neighboring elements at their common edge reveals that the type of function can even be different.

In principal, there are two strategies to solve this problem. By the use of subparametric

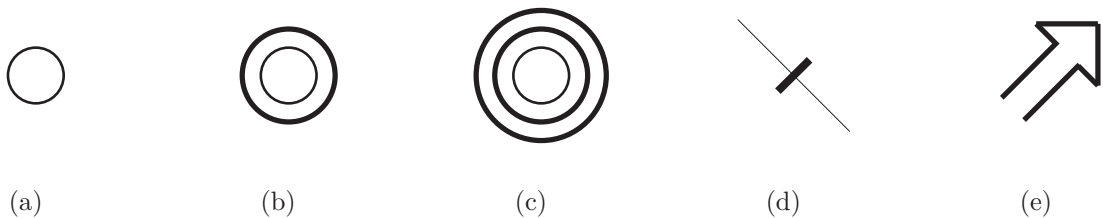


Figure 5.2: Symbols, used to represent the element degrees of freedom: (a): primal unknown; (b): first derivatives; (c): second derivatives; (d): normal derivative; (e): mixed second derivative.

elements, the Jacobi mapping \mathfrak{J}_k and its inverse both are an affine linear functions and are

therefore only representing a coordinate transformation. In this case, the derivatives with respect to the physical coordinate system is still polynomial and C^1 continuity is achieved by a unique prescription of the normal derivative for two neighboring elements. This subparametric representation is used in sections 5.2 and 5.3. Second the use of isoparametric C^1 continuous elements works with an intermediate configuration, necessary for the globally C^1 continuous construction of the shape functions. Therefore, C^1 continuous functions are defined on a linear subparametric configuration, which is mapped C^1 continuously to the physical configurations \mathcal{B}_0 and \mathcal{B}_t . A detailed description of the method will be presented in section 5.4.

Within the following sections of the chapter, the symbols, presented in figure 5.2 are used within the schematic representation for the types of degrees of freedom that are used for the description of the different elements.

5.2 C^* finite elements

By C^* elements¹, we denote finite elements which are constructed including gradient degrees of freedom but which are not fully C^1 . Due to the large number of possibilities, within this contribution we restricted ourselves to the elements, presented in figure 5.3. With the exception of the Morley triangle, only complete first order derivatives are occurring as gradient degrees of freedom. Therefore, the construction of the shape function is not very challenging. But still, the use of the Bernstein-Bézier patches simplifies their formulation.

5.2.1 Hermite triangle

The simplest Hermite element is the Hermite triangle, see figure 5.3(a). Therefore the 10 degrees of freedom of the cubic polynomial space, forming the element, are prescribed by the nodal unknowns and the first derivatives at the corner nodes plus the coefficient of the internal bubble function. The shape functions, in terms of the Bernstein polynomials at node \mathbf{X}_1 are a direct consequence of (4.19) and (4.20) and given by

$$\begin{aligned} N_1 &= B_{300} + B_{210} + B_{201} \\ \mathbf{M}_1 &= \frac{1}{3} [\mathbf{E}_1 B_{210} - \mathbf{E}_3 B_{201}] . \end{aligned} \tag{5.5}$$

The additional internal bubble function N_b is simply the remaining Bernstein polynomial

$$N_b = B_{111}. \tag{5.6}$$

The construction of the shape function for the nodes $I = 2, 3$ is done analogously by cyclic permutation of the indices in equation (5.5). Unfortunately, it turns out that the additional internal degree for the bubble function weakens the structure and the results were not convergent any more when applied to gradient elasticity. This motivates the relation of the internal function to the corner functions N_I and M_I , as done for the Zienkiewicz triangle.

¹The expression is due to the publication of Bigdely and Kelly [35, 36].

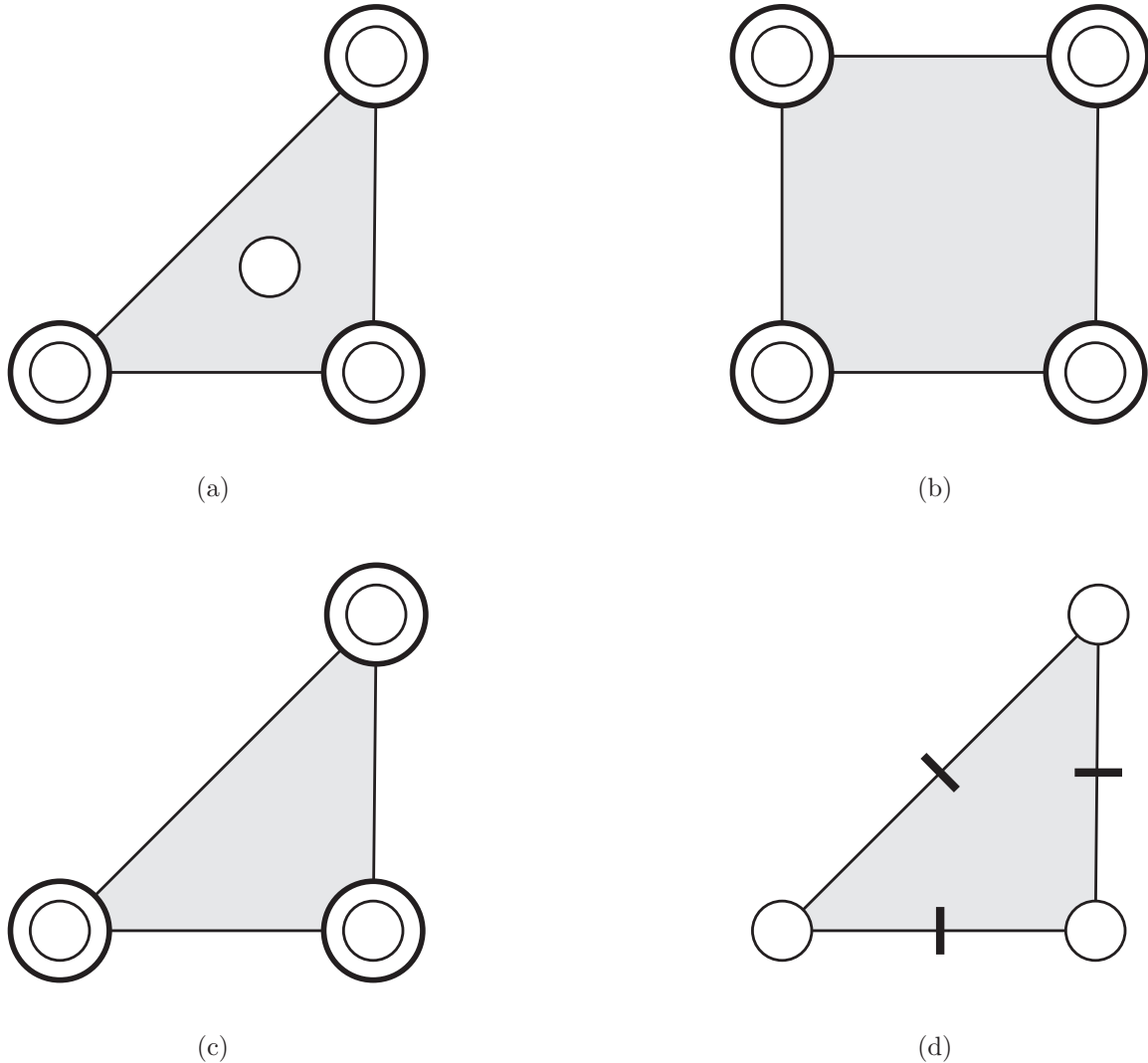


Figure 5.3: C^* elements, used in this thesis. (a) Hermite triangle, (b) Adini element (c) Zienkiewicz triangle (d) Morley triangle

5.2.2 Zienkiewicz triangle

The Zienkiewicz triangle is similar to the Hermite triangle of subsection 5.2.1 but without an internal bubble function N_b , compare to (5.5). There are several variations, how the internal bubble function $\lambda_1\lambda_2\lambda_3$ can be linked to the degrees of freedom at the element edges. Bazeley et al. [24] proposes to use the quadratic polynomials together with the cubic functions $\lambda_1^2\lambda_2$, $\lambda_2^2\lambda_3$ and $\lambda_3^2\lambda_1$. However, it fails the patch test for general meshes, see Bergan [30]. Nevertheless the formulation is successfully used for practical applications by Cheung et al. [57]. In Bergan [30] a new set of cubic polynomials is proposed to overcome the failure of the patch test. However, that formulation fails the patch test as well. This is demonstrated in Specht [191] together with the proposal of a new set of shape functions. Therein quartic polynomial are used to define the shape functions. In Zienkiewicz et al. [238] even rational functions are introduced.

The two propositions of Bazeley et al. [24] and Specht [191] are used for the computation of crack tip fields in strain gradient plasticity by Xia and Hutchinson [224] but with only moderate results.

Therefore, within this publication, the link of the internal function has been done analogously to the construction of Farin's C^1 interpolant [94], proposed for natural element shape functions. By this choice, the shape functions are derived as

$$\begin{aligned} N_1 &= B_{300} + B_{210} + B_{201} + \frac{1}{3}B_{111} \\ \mathbf{M}_1 &= \frac{1}{3} \left[\mathbf{E}_1 B_{210} - \mathbf{E}_3 B_{201} + \frac{1}{4} [\mathbf{E}_1 - \mathbf{E}_3] B_{111} \right]. \end{aligned} \quad (5.7)$$

Unfortunately, despite the good performance of this combination within Farin's C^1 interpolant, the convergence of the Zienkiewicz triangle in the version of (5.7) is not satisfying our demands on economic finite element descriptions.

5.2.3 Morley triangle

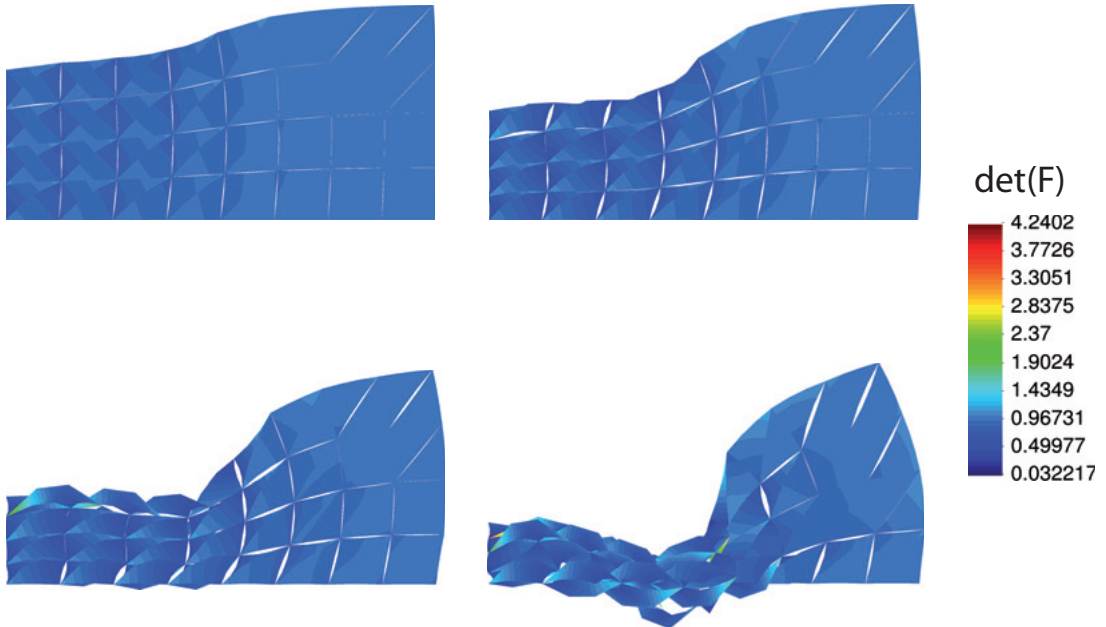


Figure 5.4: Behavior of the Morley element under pressure loading and large deformation within a finite strain setting.

The last triangular element of this section is the Morley triangle [164]. Its shape functions are constructed by the quadratic polynomials, and thus, the Morley triangle is the element with the lowest possible number of degrees of freedom for the application to fourth order partial differential equations. It can be proven mathematically, that the element converges for linear plate bending problems, even so, the finite element shape functions are not even C^0 continuous on the domain \mathcal{B}_0 .

As illustrated in figure 5.3(d), the degrees of freedom are the primal unknowns at the vertices and the normal derivatives at the center of the edges. Therefore, the discontinuity

of the displacement field is due to the fact that there are only two degrees of freedom to describe the quadratic behavior of the shape functions along the edges. In the case of a linear analysis, the convergence is due to the fact that the strains are fulfilling the equilibrium conditions in an integral sense. The extension of the Morley triangle to higher order polynomial functions are the Fraeijs de Veubeke elements [106], which are not taken into account within this contribution.

The shape functions of the Morley triangle are derived as

$$\begin{aligned} N_1 &= B_{200} + \frac{1}{2} [s_3 B_{110} + [s_3 + t_1] B_{011} + t_1 B_{101}] \\ M_1 &= h_1 [B_{011} + B_{101}] \end{aligned} \quad (5.8)$$

where M_1 is related to the midpoint of edge \mathbf{E}_1 , $[\mathbf{X}_1 + \mathbf{X}_2] / 2$.

Here, the element is applied to linear and non-linear gradient elasticity. In the latter case, the element completely fails under large deformations, see figure 5.4 where a constant pressure is applied at the top of the block. Due to the nonlinear material behavior, the element overlap is causing self-penetration of the structure even though the determinant of the deformation gradient $\det \mathbf{F}$ is strictly positive. For a detailed description of the geometry, boundary conditions and material parameters, the reader is referred to subsection 8.2.1.

5.2.4 Adini-Clough-Melosh rectangle

The Adini rectangle was first described in a subparametric setting by Adini and Clough [1] and Melosh [156]. On each element, the polynomial space is the same as for the cubic Serendipity elements. The element degrees of freedom are defined by the nodal degrees and nodal derivatives to prescribe the 12 element degrees of freedom, see figure 5.3(b). A similar element is developed by Zienkiewicz [238] and the same functional space is used by Bigdely and Kelly [35, 36] to introduce the class of C^* elements. Their motivation to use the gradients in the description of the elements is to lower the global number of degrees of freedom. This works due to the fact that each degree of freedom occurring in the C^* element description is shared by four elements at a node. In the classical C^0 element, the nodes at the edges are only occurring in two elements. Within the C^* elements, the element description is additionally extended to subparametric bilinear geometry descriptions, making the element usage much more flexible.

The element shape functions result after careful computation in

$$\begin{aligned} N_1 &= B_{30}^1 B_{30}^2 + B_{30}^1 B_{21}^2 + B_{21}^1 B_{30}^2 + \frac{8}{9} B_{21}^1 B_{21}^2 + \frac{1}{9} [B_{12}^1 B_{21}^2 + B_{21}^1 B_{12}^2] \text{ and} \\ \mathbf{M}_1 &= \frac{1}{3} \left[\mathbf{E}_1 B_{21}^1 \left[B_{30}^2 + \frac{2}{3} B_{21}^2 + \frac{1}{3} B_{12}^2 \right] - \mathbf{E}_4 B_{21}^2 \left[B_{30}^1 + \frac{2}{3} B_{21}^1 + \frac{1}{3} B_{12}^1 \right] \right], \end{aligned} \quad (5.9)$$

where B_α^i denotes the bivariate Bernstein polynomial B_α of degree 3 in the coordinate direction ξ_i . Once again, the remaining shape functions are results of cyclic permutations.

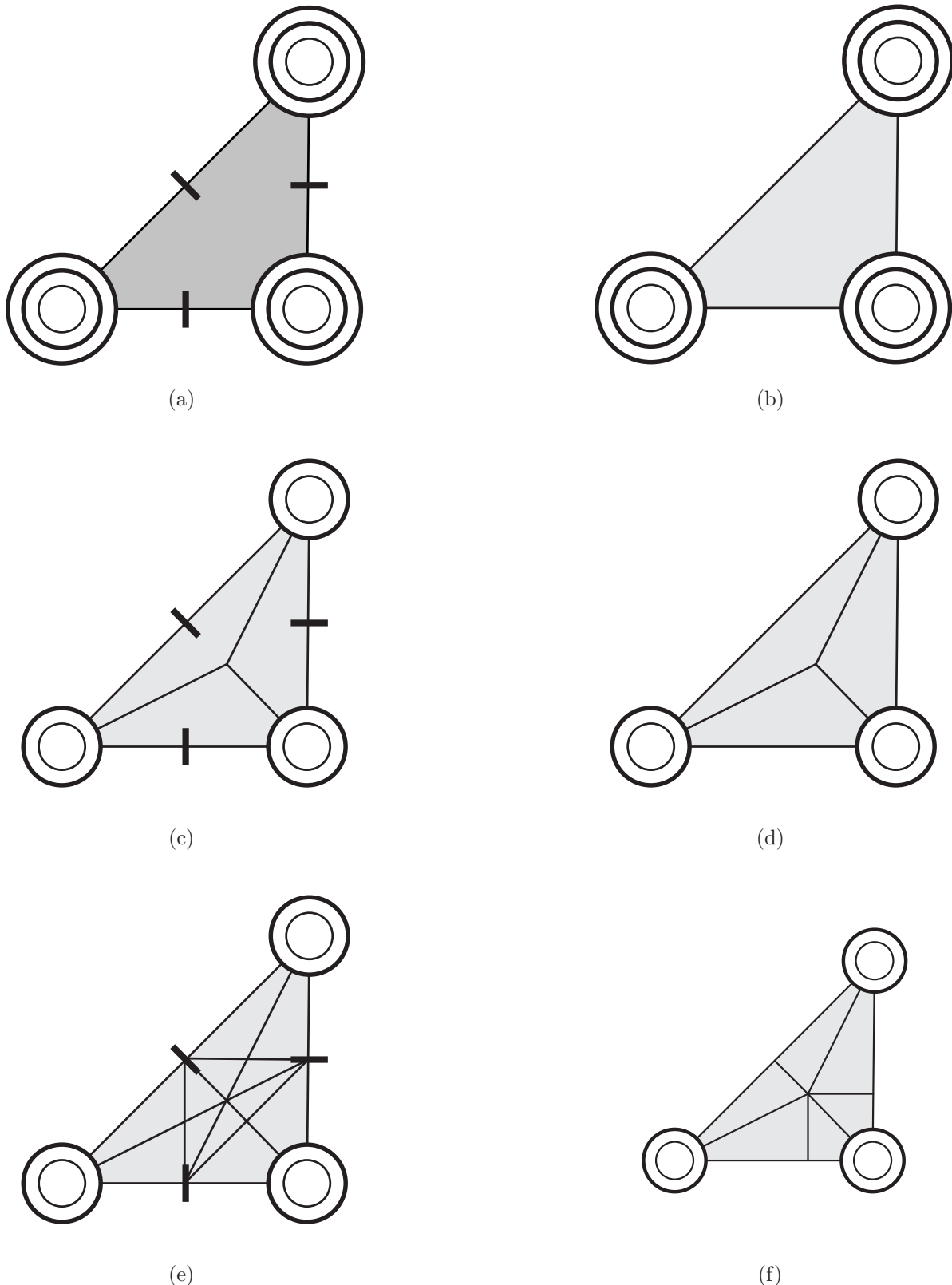


Figure 5.5: Subparametric C^1 elements, used in this thesis. (a) Argyris element, (b) Bell element (c) Hsieh-Clough-Tocher (HCT) element (d) reduced HCT element (e) Powell-Sabin-12 split triangle (f) Powell-Sabin-6 split triangle

5.3 Subparametric C^1 elements

In terms of fully C^1 -continuous elements, the subparametric approach is the most common. This is due to the fact that the nodal degrees of freedom are described by the derivative of the approximated value with respect to the physical coordinate system. Otherwise some sort of intermediate configuration would have to be used.

In the subparametric approach, the reference configuration is approximated linearly, whereas the polynomial shape functions on the elements are constructed in such a way that the resulting piecewise polynomial function is C^1 continuous.

For the description of the element, one can either incorporate a high number of degrees of freedom, cf. the Argyris element [15] with 21 degrees for each interpolation field. Or alternatively one has to use macroelements like the HCT [63] or PS [172] elements. For the application to non-polynomial domain, an interpolation of the domain boundary may lead to significant numerical errors, i.e. see Fischer et al. [97] or chapter 8.

In the following part, the simplest elements for each of the three classes of elements are described. Each of the elements can be extended to an arbitrary high number of degrees of freedom, where for the shift of polynomial degree k to $k+1$ only one additional normal derivative degree is introduced at the element edges.

5.3.1 Argyris element

The Argyris element [15] is the C^1 element of lowest possible order, if fully polynomial shape functions are used. Even so, the element has been developed in 1968, explicit derivations of the shape functions can first be found in Bernadou [32] in 1982 or even more recently by Dasgupta et al. [75] in 1990.

The element shape functions are constructed by the 21 parameters of the function space of the quintic polynomials in two dimension. The degrees of freedom are the function values and the values of the derivatives up to second order at the three element vertices, leading to 18 equations. The remaining three values are determined by means of the normal derivatives at the center of the edges. The resulting elementwise polynomial functions for the approximation are then globally C^1 continuous.

The Argyris element is used in a subparametric concept, i.e. the geometry is approximated linearly whereas the displacements are approximated by C^1 continuous piecewise quintic polynomial splines. The geometric properties of the Bézier patches are used for the recursive construction of the shape functions.

The coefficients with $\max(\alpha) \geq 3$ are uniquely defined by the values of the shape functions at the vertices of the triangle, i.e. compare to section 4.3 and equations (4.19) and (4.22) of the previous chapters. At the vertex \mathbf{X}_1 the coefficients of the shape functions N_1 , interpolating the primal unknown are given by

$$N_1 = B_{500} + B_{410} + B_{401} + B_{320} + B_{302} + B_{311} + s_1 B_{221} - t_3 B_{212}. \quad (5.10)$$

Additionally, the shape functions interpolating the gradient values at the vertices \mathbf{M}_1 together with the mid edge derivative \tilde{M}_1 shape function at $[\mathbf{X}_1 + \mathbf{X}_2]/2$ are resulting in

$$\begin{aligned}\mathbf{M}_1 &= \frac{1}{5} \left[\mathbf{E}_1 B_{410} - \mathbf{E}_3 B_{401} + 2\mathbf{E}_1 B_{320} - 2\mathbf{E}_3 B_{302} + [\mathbf{E}_1 - \mathbf{E}_3] B_{311} \right. \\ &\quad \left. + \frac{7s_1\mathbf{E}_1 - 5\mathbf{E}_2}{6} B_{221} + \frac{-7t_3\mathbf{E}_3 + 5\mathbf{E}_2}{6} B_{212} \right] \\ \tilde{M}_1 &= \frac{1}{5} \left[\frac{8}{3} h_1 B_{221} \right]\end{aligned}\tag{5.11}$$

and \mathbf{L}_1 is derived as

$$\begin{aligned}\mathbf{L}_1 &= \frac{1}{20} \left[\mathbf{V}_{11} B_{320} + \mathbf{V}_{33} B_{302} - \mathbf{V}_{13} B_{311} \right. \\ &\quad \left. + \frac{1}{3} [s_1 \mathbf{V}_{11} - 2\mathbf{V}_{12}] B_{221} + \frac{1}{3} [t_3 \mathbf{V}_{33} - 2\mathbf{V}_{23}] B_{212} \right].\end{aligned}\tag{5.12}$$

Here, the definition of \mathbf{V}_{IJ} as presented in (4.24) is used.

5.3.2 Bell element

The Bell element [29] is the reduced form of the Argyris element (subsection 5.3.1). Similar to the Argyris element, the shape functions are composed of the quintic polynomials. The only difference is that the normal edge derivative is replaced by the condition that the normal derivatives are cubic polynomials instead of quartic. The resulting shape functions are only different for the coefficients of B_{122} , B_{212} and B_{221} and the shape functions are derived as:

$$\begin{aligned}N_1 &= B_{500} + B_{410} + B_{401} + B_{320} + B_{302} + B_{311} + s_1 B_{221} + t_3 B_{212} \\ \mathbf{M}_1 &= \frac{1}{5} \left[\mathbf{E}_1 B_{410} - \mathbf{E}_3 B_{401} + 2\mathbf{E}_1 B_{320} - 2\mathbf{E}_3 B_{302} + [\mathbf{E}_1 - \mathbf{E}_3] B_{311} \right. \\ &\quad \left. + \left[2s_1\mathbf{E}_1 - \frac{1}{2} [\mathbf{E}_3 + t_1\mathbf{E}_1] \right] B_{221} - \left[2t_3\mathbf{E}_3 - \frac{1}{2} [\mathbf{E}_1 + s_3\mathbf{E}_1] \right] B_{212} \right] \\ \mathbf{L}_1 &= \frac{1}{20} \left[\mathbf{V}_{11} B_{320} + \mathbf{V}_{33} B_{302} - \mathbf{V}_{13} B_{311} \right. \\ &\quad \left. + \left[s_1 \mathbf{V}_{11} - \frac{2}{3} [\mathbf{V}_{31} + t_1 \mathbf{V}_{11}] \right] B_{221} + \left[t_3 \mathbf{V}_{33} - \frac{2}{3} [\mathbf{V}_{31} + s_3 \mathbf{V}_{33}] \right] B_{212} \right].\end{aligned}\tag{5.13}$$

By comparison of (5.10) with (5.13) it is revealed that the shape functions N_I are equal for the Argyris and the Bell element. For the shape functions \mathbf{M}_I and \mathbf{L}_I , only the coefficients of B_{122} , B_{212} and B_{221} are different.

5.3.3 Hsieh-Clough-Tocher (HCT) element

The introduction of the HCT element is due to [63] and the first analytical representation of the shape functions are presented in [34] in terms of barycentric coordinates or in [92] for the Bernstein-Bézier representation. Its first application to gradient elastic problems is given in [97] and [99]. The degrees of freedom for the HCT element are the displacements

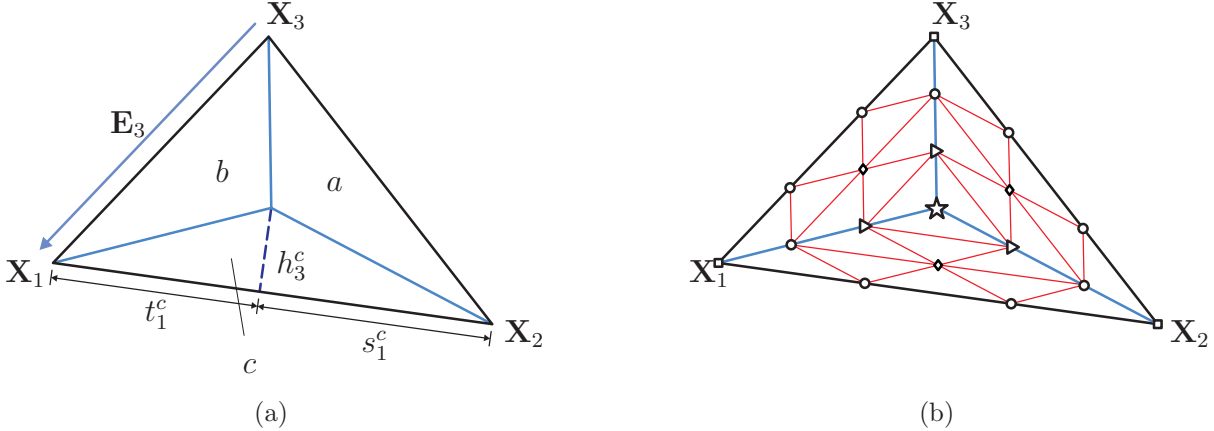


Figure 5.6: (a) Geometrical properties used for the HCT element; (b) Recursive construction of the shape functions.

and their derivatives at the vertices of the triangle. Again, the normal derivatives are described at the center of the edges. Contrary to the first two elements, investigated in this section, the HCT element is a macro element, i.e. it is composed of subelements with piecewise polynomial shape functions. The HCT element is split into three subtriangles which all share a common vertex $\bar{\mathbf{X}}$ in the interior of the macro triangle. This point can be chosen arbitrarily. Here, we choose $\bar{\mathbf{X}}$ to be the barycenter of the triangle, i.e. $\bar{\mathbf{X}} = \frac{1}{3} \sum_{i=1}^3 \mathbf{X}_i$, which is explicitly used in the construction of the shape functions.

The approximation space is built of the 10 cubic polynomials on each subtriangle. The requirement of C^1 continuity of the displacement field inside the element reduces the total number of degrees of freedom to 12.

To present the element shape functions, the following definitions are used. The mini triangles opposing to node \mathbf{X}_1 with the vertices \mathbf{X}_2 , \mathbf{X}_3 and $\bar{\mathbf{X}}$ is called triangle a . Triangle b is defined by \mathbf{X}_3 , \mathbf{X}_1 and $\bar{\mathbf{X}}$, etc.. The quantities for each subtriangle are defined as in subsection 4.3.1 and denoted \bullet^\diamond , with $\diamond \in \{a, b, c\}$.

The recursive construction of the element shape functions is illustrated in figure 5.6(b). First, the values \square are due to the nodal function values. The control point coefficients \circ are given by the nodal gradients. At last, the normal derivatives at the edges yields the values of \diamond . Subsequently, the remaining values are given by the C^1 continuity requirement and a direct consequence of the results of section 4.3. The \triangleright values are on the same plane as \circ and \diamond and \star is placed on one plane with the values \triangleright .

The shape functions related to node \mathbf{X}_1 on element c are resulting in

$$N_1 = B_{300} + B_{210} + B_{201} + s_1^c B_{111} + \frac{1}{3} [1 + s_1^c + t_1^c] B_{102} + \frac{1}{3} s_1^c B_{012} + \frac{1}{9} [1 + 2s_1^c + 2t_1^c] B_{003} \quad (5.14)$$

for the interpolating value at the node and

$$\begin{aligned} \mathbf{M}_1 = & \frac{1}{3} \left[\mathbf{E}_1^c B_{210} - \mathbf{E}_3^c B_{201} + \frac{1}{2} [s_1^c \mathbf{E}_1^c - \mathbf{E}_2^c] B_{111} \right. \\ & + \frac{1}{3} \left[\frac{1}{2} [s_1^c \mathbf{E}_1^c - t_1^b \mathbf{E}_1^b - \mathbf{E}_2^c + \mathbf{E}_3^b] + \mathbf{E}_2^b \right] B_{102} + \frac{1}{6} [s_1^c \mathbf{E}_1^c - \mathbf{E}_2^c] B_{012} \\ & \left. + \frac{1}{9} [s_1^c \mathbf{E}_1^c - t_1^b \mathbf{E}_1^b + \mathbf{E}_3^b - \mathbf{E}_2^c + \mathbf{E}_2^b] B_{003} \right] \end{aligned} \quad (5.15)$$

together with

$$\tilde{\mathbf{M}}_1 = \frac{1}{3} \left[2h_1^c B_{111} + \frac{2}{3} h_1^c B_{102} + \frac{2}{3} h_1^c B_{012} + \frac{4}{9} h_1^c B_{003} \right]. \quad (5.16)$$

for the shape functions, interpolating the gradient values. On element b , the shape functions are given by:

$$\begin{aligned} N_1 = & B_{030} + B_{021} + B_{120} + t_1^b B_{111} + \frac{1}{3} [1 + s_1^c + t_1^b] B_{012} \\ & + \frac{1}{3} t_1^b B_{102} + \frac{1}{9} [1 + 2s_1^c + 2t_1^b] B_{003} \\ \mathbf{M}_1 = & \frac{1}{3} \left[-\mathbf{E}_3^c B_{021} - \mathbf{E}_1^b B_{120} - \frac{1}{2} [t_1^b \mathbf{E}_1^b - \mathbf{E}_3^b] B_{111} \right. \\ & + \frac{1}{3} \left[\frac{1}{2} [s_1^c \mathbf{E}_1^c - t_1^b \mathbf{E}_1^b + \mathbf{E}_3^b - \mathbf{E}_2^c] + \mathbf{E}_2^b \right] B_{012} + \frac{1}{6} [\mathbf{E}_3^b - t_1^b \mathbf{E}_1^b] B_{102} \\ & \left. + \frac{1}{9} [s_1^c \mathbf{E}_1^c - t_1^b \mathbf{E}_1^b + \mathbf{E}_3^b - \mathbf{E}_2^c + \mathbf{E}_2^b] B_{003} \right] \\ \tilde{\mathbf{M}}_1 = & \left[\frac{2}{9} h_1^c B_{102} + \frac{4}{27} h_1^c B_{003} \right] \end{aligned} \quad (5.17)$$

and on triangle a , opposite to the node:

$$\begin{aligned} N_1 = & \frac{1}{3} t_1^b B_{012} + \frac{1}{9} [1 + 2s_1^c + 2t_1^b] B_{003} \\ \mathbf{M}_1 = & B_{012} + \frac{1}{27} [s_1^c \mathbf{E}_1^c - \mathbf{E}_2^c + \mathbf{E}_3^b - t_1^b \mathbf{E}_1^b + \mathbf{E}_2^b] B_{003} \\ \tilde{\mathbf{M}}_1 = & \left[\frac{2}{9} h_1^c B_{012} + \frac{4}{27} h_1^c B_{003} \right] \end{aligned} \quad (5.18)$$

As obviously revealed by figure 5.6(b), there are only 19 different coefficients for the shape functions of each element that have to be stored. The remaining 11 are condensed out by the C^0 continuity condition inside the element.

5.3.4 Reduced form of the HCT element

Similar to the reduction of the Argyris element the HCT element can be reduced such that the normal derivative is a linear instead of a quadratic function. Here, the coefficients are explicitly given for each of the subelements, compare figure 5.6(a). For the construction, the same procedure as presented in subsection 5.3.3 is used. Simply the values marked \diamond in figure 5.6(b) are directly related to the coefficient values of the full HCT element and

due this equality, the function N_1 is omitted. On subelement c , the shape function \mathbf{M}_1 results in:

$$\begin{aligned}\mathbf{M}_1 = & \frac{1}{3} \left[\mathbf{E}_1^c B_{210} - \mathbf{E}_3^c B_{201} + \frac{1}{2} [[2 - 3s_1^c] \mathbf{E}_1^c - \mathbf{E}_2^c] B_{111} \right. \\ & + \frac{1}{3} \left[\frac{1}{2} [s_1^c \mathbf{E}_1^c - t_1^b \mathbf{E}_1^b - \mathbf{E}_2^c + \mathbf{E}_3^b] + \mathbf{E}_2^b \right] B_{102} + \frac{1}{6} [s_1^c \mathbf{E}_1^c - \mathbf{E}_2^c] B_{012} \\ & \left. + \frac{1}{9} [s_1^c \mathbf{E}_1^c - t_1^b \mathbf{E}_1^b + \mathbf{E}_3^b - \mathbf{E}_2^c + \mathbf{E}_2^b] B_{003} \right].\end{aligned}\quad (5.19)$$

Similar expressions are given on subelement b :

$$\begin{aligned}\mathbf{M}_1 = & \frac{1}{3} \left[-\mathbf{E}_3^c B_{021} - \mathbf{E}_1^b B_{120} - \frac{1}{2} [[2 - 3t_1^b] \mathbf{E}_1^b - \mathbf{E}_3^b] B_{111} \right. \\ & + \frac{1}{3} \left[\frac{1}{2} [s_1^c \mathbf{E}_1^c - t_1^b \mathbf{E}_1^b + \mathbf{E}_3^b - \mathbf{E}_2^c] + \mathbf{E}_2^b \right] B_{012} + \frac{1}{6} [\mathbf{E}_3^b - t_1^b \mathbf{E}_1^b] B_{102} \\ & \left. + \frac{1}{9} [s_1^c \mathbf{E}_1^c - t_1^b \mathbf{E}_1^b + \mathbf{E}_3^b - \mathbf{E}_2^c + \mathbf{E}_2^b] B_{003} \right].\end{aligned}\quad (5.20)$$

On subelement a , the part opposite to the node, the values are given by:

$$\mathbf{M}_1 = B_{012} + \frac{1}{27} [s_1^c \mathbf{E}_1^c - \mathbf{E}_2^c + \mathbf{E}_3^b - t_1^b \mathbf{E}_1^b + \mathbf{E}_2^b] B_{003}. \quad (5.21)$$

5.3.5 Powell-Sabin split elements

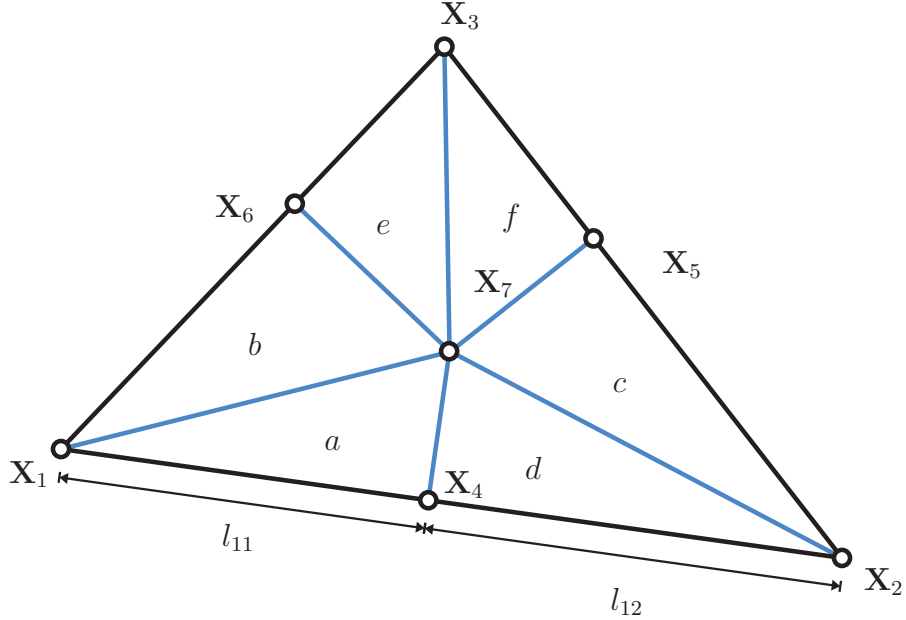


Figure 5.7: Geometry description of the PS-6 element with labeling for the subelements.

The lowest possible order for the construction of C^1 continuous piecewise polynomial functions is $k = 2$, i.e. the use of quadratic functions, resulting in constant values for the strain

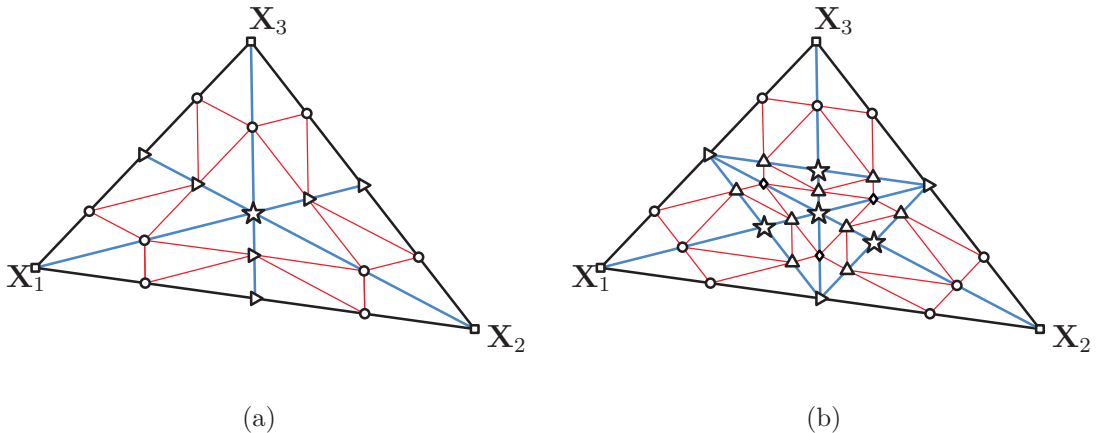


Figure 5.8: (a): Schematic representation of the PS-6 element construction, and (b): Schematic representation of the PS-12 element construction.

gradient \mathbf{G} . These elements are combined in the class of Powell-Sabin macroelements, firstly formulated by Powell and Sabin [172]. This class of elements can be separated into two different parts, classified by the number of subelements. In the minimal case, 6 subelements are used. Unfortunately, this description is restricted and not applicable on general meshes, motivating the split into 12 subelements. In general, the degrees of freedom of both splits are defined by the nodal values and nodal gradients at the vertices of the macroelement. For the PS-12 element, an additional value of the mid-normal derivative can be introduced as additional degree of freedom.

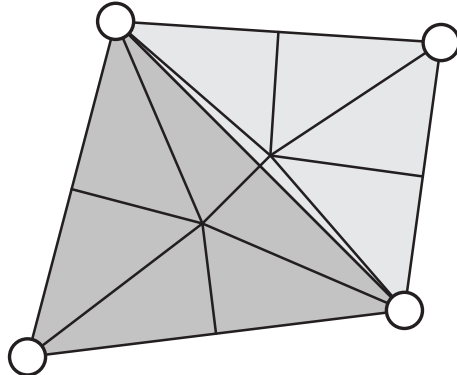
The first application for the solution of fourth order problems is due to [194] where the elements are used to solve the biharmonic equation. In [195], an application to the Cahn-Hilliard equation is presented. The first application to gradient elasticity is performed in [98].

As mentioned above, only the twelve split element is in general applicable to arbitrary

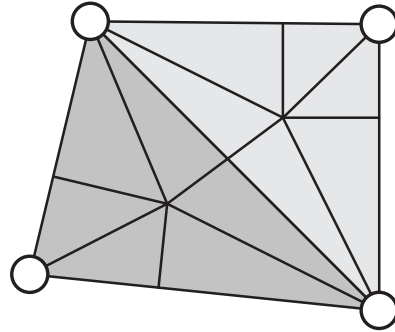
	B_{200}	B_{020}	B_{002}	B_{110}	B_{011}	B_{101}	B_{020}	B_{002}	B_{110}	B_{011}	B_{101}
a	1	g_1	λ_1	1	g_1	1	$\frac{1}{2}g_1 \mathbf{E}_1^a$	$-\frac{1}{2}\lambda_1 \mathbf{E}_2^a$	$\frac{1}{2}\mathbf{E}_1^a$	$-\frac{1}{2}g_1 \mathbf{E}_2^a$	$-\frac{1}{2}\mathbf{E}_2^a$
b	1	λ_1	h_3	1	h_3	1	$\frac{1}{2}\lambda_1 \mathbf{E}_1^b$	$-\frac{1}{2}f_3 \mathbf{E}_3^b$	$\frac{1}{2}\mathbf{E}_1^b$	$\frac{1}{2}f_3 \mathbf{E}_1^b$	$-\frac{1}{2}\mathbf{E}_3^b$
c	0	0	λ_1	0	0	0	0	$\frac{1}{2}\lambda_1 \mathbf{E}_1^b$	0	0	0
d	0	λ_1	g_1	0	g_1	0	$\frac{1}{2}\lambda_1 \mathbf{E}_1^b$	$\frac{1}{2}g_1 \mathbf{E}_1^a$	0	$-\frac{1}{2}g_1 \mathbf{E}_2^a$	0
e	0	h_3	λ_1	0	h_3	0	$-\frac{1}{2}f_3 \mathbf{E}_3^b$	$\frac{1}{2}\lambda_1 \mathbf{E}_1^b$	0	$\frac{1}{2}f_3 \mathbf{E}_1^b$	0
f	0	λ_1	0	0	0	0	$\frac{1}{2}\lambda_1 \mathbf{E}_1^b$	0	0	0	0

Table 5.1: Left: Shape function coefficients for N_1 on the different subtriangles and Right: Shape function coefficients for M_1 . The coefficients of $B_{200} = 0$ on all of the subtriangles.

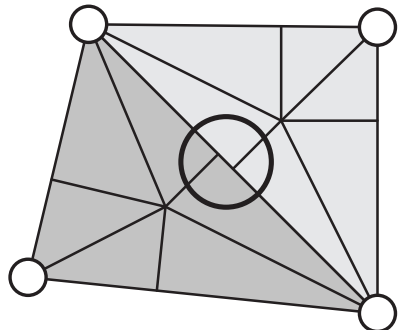
shaped meshes. In case of the PS-6 element, the minimal restriction is that inside each element there has to exist a unique point, such that the direct line, connecting that point to the corresponding points of the neighboring elements intersects the shared edge, see figure 5.9(b). Since this intersection line is necessary for the construction of the PS-6 subelements, it is desirable to use the circumcircle center as interior point. In this case, the mid side normals are connections of the points of the two adjacent triangles. Thus,



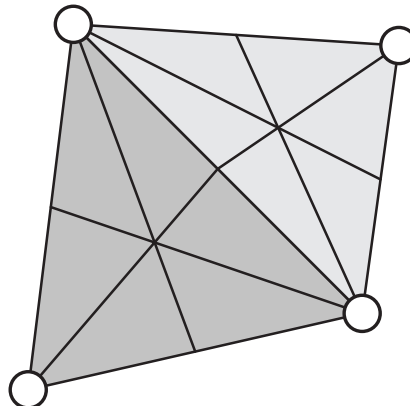
(a)



(b)



(c)



(d)

Figure 5.9: (a): The usual mode of use of the PS-6 element, the inner point is the circumcircle center. Here the problem with the occurrence of skinny subtriangles is visible (b): Alternatively, where the barycenter can be used. Therefore, the neighboring element is influencing the split. (c): To get a nonconforming element with linear distribution of the normal derivative, the intersection of the element is performed such that the lines are perpendicular to the element edges. (d): C^0 form of the PS-6 element.

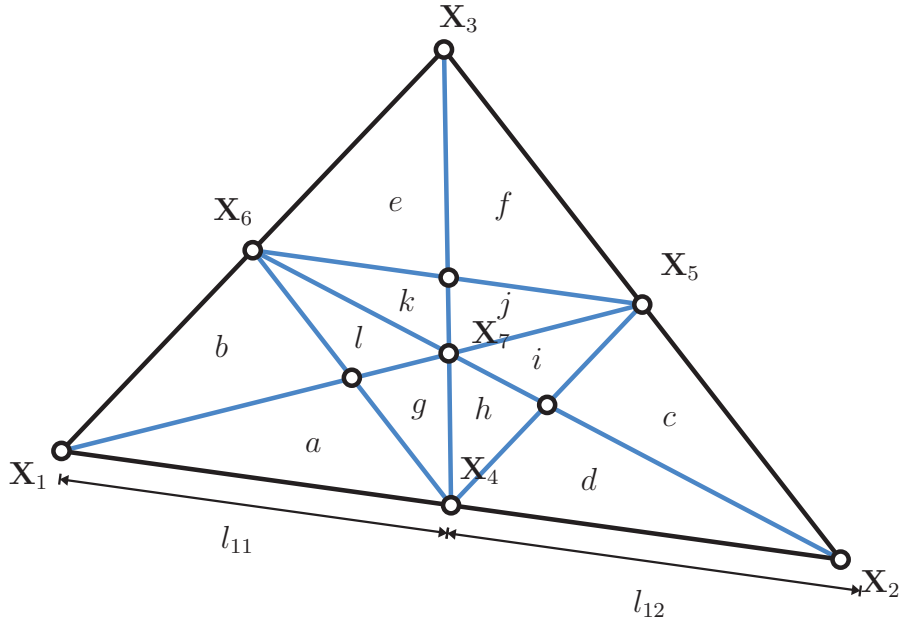


Figure 5.10: Geometry description for the PS-12 macroelement. The geometry is directly given due to the choice of the centroid and the centerpoints of the element edges.

the subelements can be defined without the knowledge of the neighboring triangles, compare figure 5.9(a). A heuristic criterion that this split can be used is that the maximum angle of the element has to be smaller than 75° in order to avoid skinny subtriangles, see [92].

Within this thesis, the barycenter is used for all the splits. This is requiring additional effort in the preprocessing step in order to compute the intersection of the line, connecting the barycenter of two neighboring triangles with the common edge. In the following, this version is denoted C^1 -continuous PS-6 element. To overcome the problem of the additional computation of the intersection point, two different versions of the PS-6 element are introduced. Within the two variations, only the intersection of the edges is varied. In the first version, called C^0 -continuous PS-6 element, the elements are intersected at the midpoints of the edges, 5.9(d). The result is a C^0 continuous interpolation, with possible jumps in the normal derivatives along the element edges. Unfortunately, the element does not show a reliable convergence behavior when applied to gradient elasticity, see chapter 8.

The second alternative is the use of the orthogonal projection of the barycenter to the element edge. In this case, the normal derivative of the shape functions are equal along the whole edge. The only problem is that the function values itself and its tangent derivatives are discontinuous. This is not very much of a problem, since due to the fixed nodal positions, the average of the values is equal on both sides. The principle is similar to that of the Morley triangle as presented in section 5.2.3, but reveals a more stable behavior when applied to nonlinear problems. Fortunately, the jumps in the stresses are not significant, i.e. see figure 8.8.

To derive the shape function values of the PS-6 element, the following additional def-

	B_{200}	B_{020}	B_{002}	B_{110}	B_{011}	B_{101}
a	1	$\frac{1}{2}$	$\frac{1}{8}[2 + 3g_1 + 3f_3]$	1	$\frac{1}{4}[1 + 3g_1]$	1
b	1	$\frac{1}{8}[2 + 3g_1 + 3f_3]$	$\frac{1}{2}$	1	$\frac{1}{4}[1 + 3f_3]$	1
c	0	0	$\frac{3}{8}g_1$	0	0	0
d	0	$\frac{3}{8}g_1$	$\frac{1}{2}$	0	$\frac{3}{4}g_1$	0
e	0	$\frac{3}{8}f_3$	0	0	0	0
f	0	$\frac{1}{2}$	$\frac{3}{8}f_3$	0	$\frac{3}{4}f_3$	0
g	$\frac{1}{2}$	$\frac{1}{3}[g_1 + f_3]$	$\frac{1}{8}[2 + 3g_1 + 3f_3]$	g_1	$\frac{1}{2}[g_1 + f_3]$	$\frac{1}{4}[1 + 3g_1]$
h	$\frac{1}{2}$	$\frac{3}{8}g_1$	$\frac{1}{3}[g_1 + f_3]$	$\frac{3}{4}g_1$	$\frac{1}{2}g_1$	0
i	0	$\frac{1}{3}[g_1 + f_3]$	$\frac{3}{8}g_1$	0	$\frac{1}{2}g_1$	0
j	0	$\frac{3}{8}f_3$	$\frac{1}{3}[g_1 + f_3]$	0	$\frac{1}{2}f_3$	$\frac{3}{4}f_3$
k	$\frac{1}{2}$	$\frac{1}{3}[g_1 + f_3]$	$\frac{3}{8}f_3$	f_3	$\frac{1}{2}f_3$	$\frac{3}{4}f_3$
l	$\frac{1}{2}$	$\frac{1}{8}[2 + 3g_1 + 3f_3]$	$\frac{1}{3}[g_1 + f_3]$	$\frac{1}{4}[1 + 3f_3]$	$\frac{1}{2}[g_1 + f_3]$	f_3

Table 5.2: Shape function N_1 of the $PS - 12$ split element.

	B_{200}	B_{020}	B_{002}	B_{110}	B_{011}	B_{101}
a	0	$\frac{1}{4}\mathbf{E}_1^a$	$\frac{1}{16}[c_1\mathbf{E}_1^a - d_3\mathbf{E}_3^a]$	$\frac{1}{2}\mathbf{E}_1^a$	$\frac{1}{8}[3g_1\mathbf{E}_1^a - \mathbf{E}_3^a]$	$-\frac{1}{2}\bar{\mathbf{E}}_3^a$
b	0	$\frac{1}{16}[c_1\mathbf{E}_1^a - d_3\mathbf{E}_3^a]$	$-\frac{1}{4}\mathbf{E}_3^b$	$\frac{1}{2}\mathbf{E}_1^b$	$\frac{1}{8}[\mathbf{E}_1^b - 3f_3\mathbf{E}_3^b]$	$-\frac{1}{2}\bar{\mathbf{E}}_3^b$
c	0	0	$\frac{3}{16}g_1\mathbf{E}_1^a$	0	0	0
d	0	$\frac{3}{16}g_1\mathbf{E}_1^a$	$\frac{1}{4}\mathbf{E}_1^a$	0	$\frac{3}{8}g_1\mathbf{E}_1^a$	0
e	0	$-\frac{1}{4}\mathbf{E}_3^b$	$\frac{3}{16}f_3\mathbf{E}_3^b$	0	$-\frac{3}{8}f_3\mathbf{E}_3^b$	0
f	0	$-\frac{3}{16}f_3\mathbf{E}_3^b$	0	0	0	0
g	$\frac{1}{4}\mathbf{E}_1^a$	$\frac{1}{6}[g_1\mathbf{E}_1^a - f_3\mathbf{E}_3^b]$	$\frac{1}{16}[c_1\mathbf{E}_1^a - d_3\mathbf{E}_3^a]$	$\frac{1}{2}g_1\mathbf{E}_1^a$	$\frac{1}{4}[g_1\mathbf{E}_1^a - f_3\mathbf{E}_3^b]$	$\frac{1}{8}\bar{\mathbf{E}}_1^a$
h	$\frac{1}{4}\mathbf{E}_1^a$	$\frac{3}{16}g_1\mathbf{E}_1^a$	$\frac{1}{6}[g_1\mathbf{E}_1^a - f_3\mathbf{E}_3^b]$	$\frac{3}{8}g_1\mathbf{E}_1^a$	$\frac{1}{4}g_1\mathbf{E}_1^a$	$\frac{1}{2}g_1\mathbf{E}_1^a$
i	0	$\frac{1}{6}[g_1\mathbf{E}_1^a - f_3\mathbf{E}_3^b]$	$\frac{3}{16}g_1\mathbf{E}_1^a$	0	$\frac{1}{4}g_1\mathbf{E}_1^a$	0
j	0	$-\frac{3}{16}f_3\mathbf{E}_3^b$	$\frac{1}{6}[g_1\mathbf{E}_1^a - f_3\mathbf{E}_3^b]$	0	$-\frac{1}{4}f_3\mathbf{E}_3^b$	0
k	$-\frac{1}{4}f_3\mathbf{E}_3^b$	$\frac{1}{6}[g_1\mathbf{E}_1^a - f_3\mathbf{E}_3^b]$	$-\frac{3}{16}f_3\mathbf{E}_3^b$	$-\frac{1}{2}f_3\mathbf{E}_3^b$	$-\frac{1}{4}f_3\mathbf{E}_3^b$	$-\frac{3}{16}f_3\mathbf{E}_3^b$
l	$-\frac{1}{4}f_3\mathbf{E}_3^b$	$-\frac{1}{8}\bar{\mathbf{E}}_3^b$	$\frac{1}{6}[g_1\mathbf{E}_1^a - f_3\mathbf{E}_3^b]$	$\frac{1}{8}\bar{\mathbf{E}}_3^b$	$\frac{1}{4}[g_1\mathbf{E}_1^a - f_3\mathbf{E}_3^b]$	$-\frac{1}{2}f_3\mathbf{E}_3^b$

Table 5.3: Shape functions of the $PS - 12$ split elements. The abbreviations $c_1 = 3g_1 - 1$, $d_3 = 3f_3 - 1$, $\bar{\mathbf{E}}_1^a = 3g_1\mathbf{E}_1^a - \mathbf{E}_3^a$ and $\bar{\mathbf{E}}_3^b = 3f_3\mathbf{E}_3^b - \mathbf{E}_1^b$ have been used.

initions have to be considered corresponding with figure 5.7. The numeration of the elements is always starting from one of the macrovertices and continuing in anti clockwise direction. Additionally introducing the the quantities $f_i := l_{i1}/\|\mathbf{X}_{i+1} - \mathbf{X}_i\|$ and $g_i := l_{i2}/\|\mathbf{X}_{i-1} - \mathbf{X}_i\|$ and $\boldsymbol{\lambda} := (\lambda_1, \lambda_2, \lambda_3)$ to be the vector of the barycentric coordinates of the center point \mathbf{X}_7 of the macroelement. Within this contribution, the special case of $\lambda_1 = \lambda_2 = \lambda_3 = 1/3$ results from the use of the barycenter. The principle for the construction of the finite element shape functions is presented in figure 5.8(a). The values of the Bernstein polynomials, \square and \circ , related to the vertices of the element are direct results of (4.20), the definition of the edge vectors \mathbf{E}_i^j , $j \in \{a, \dots, f\}$ and the interpolation property of the Bernstein polynomials. The values \triangleright at the boundary are results of (4.28), i.e. the condition that the control point of the onedimensional case have to be coplanar to achieve C^1 continuity and the remaining values \diamond are given by relation (4.36). By a similar argument, the value \star is given by coplanarity condition with the values \circ at its direct neighborhood. The complete expression of the shape functions for the elements can be found in table 5.1.

For the PS-12 split, the definition of the macroelements is never varied. The definition of the macroelement and subelements is presented in figure 5.10. The split is always performed by the use of the barycenter and straight lines, the bisection of the element edges by \mathbf{X}_4 , \mathbf{X}_5 and \mathbf{X}_6 together with the use of the straight lines, connection those three points. The schematical construction of the shape functions is presented in figure 5.8(b). Again, the values \square and \circ , related to the vertices of the element are direct results of (4.20) and the coefficients \triangleright are related to their neighboring coefficients by the coplanarity condition. Only the additional value \diamond is occurring, being related to the mid-normal interpolation property of the shape functions. The explicit representation of the shape function N_1 is given in table 5.2 and the coefficients of \mathbf{M}_1 can be found in table 5.3. The remaining functions can be obtained by cyclic permutations.

The results of table 5.2 and table 5.3 are related to the version of the PS-12 split element, with additional normal derivative. For the remaining shape function, the coefficient values, related \square and \circ are zero and the value \diamond , corresponding to the edge \mathbf{E}_1 is related to the vector $\mathbf{D} := \mathbf{X}_7 - \mathbf{X}_4$ by $\diamond = \frac{1}{2} [\mathbf{D} \cdot \mathbf{E}_1^\perp] / \|\mathbf{E}_1\|^2$. Here, \mathbf{E}_1^\perp is the vector given by

$$\mathbf{E}_1^\perp \cdot \mathbf{E}_1 = 0 \quad \text{and} \quad \|\mathbf{E}_1^\perp\|_2 = \|\mathbf{E}_1\|_2. \quad (5.22)$$

The remaining values for the description of the shape functions are direct results of the above mentioned geometric relations and left to the reader.

5.4 Isoparametric C^1 elements

The subparametric C^1 continuous elements as presented in the previous section 5.3 have many advantages such as being simple and they can be used very flexibly on arbitrary triangulations². However, they have one big drawback which is the poor approximation of the geometry. This linear geometry description can lead to a severe restriction within the convergence behavior of the elements, see Fischer et al. [100]. A more detailed discussion

²Of course, there are similar restrictions like for the standard elements that skinny triangles or those with high maximal angle are resulting in poor performance.

of this problem is presented in chapter 8. To get rid of this problem, isoparametric C^1 elements are necessary. At this point, we want to present the principle of isoparametric C^1 continuous finite elements and point out the additional problems occurring within the construction of a C^1 continuous function on the reference domain \mathcal{B}_0 . These problems are the main reason that only little work has been done in the field of isoparametric C^1 elements. In principle, the quadrilateral Bogner-Fox-Schmidt element [41] is the only element really used in an isoparametric setting and applied to computational analysis. Some examples are the works of Petera et al. [169], Bradley et al. [45] or more recently Zervos and coworkers [167, 234] and Fischer et al. [99].

5.4.1 Geometry approximation for isoparametric C^1 elements

Usually, the state of the art in computational mechanics is the use of isoparametric finite elements. However, for C^1 continuous elements, linear subparametric approximation schemes are still the most common approach. This is even more surprising since the linear approximation of the geometry is severely influencing the performance of the elements. In Fischer et al. [100], it is pointed out that the convergence of the different subparametric elements is mainly influenced by the geometry approximation rather than the polynomial order of the shape function. A more detailed investigation of this effect is presented in chapter 8. Due to this reason, isoparametric meshes with the ability of a better approximation of the boundary are necessary.

In contrast to existing approaches, where the geometry is described globally, we want to explain the principle of a local, fully C^1 continuous isoparametric approximation of the geometry. Although, only the isoparametric BFS element is considered in subsection 5.4.4, the description of the principles of isoparametric elements is described very general, to be applicable to the use of isoparametric triangular elements as presented in the appendix C.

5.4.2 C^1 continuous mappings

To achieve a C^1 continuous mapping, the simplest way is to define a global reference mesh, which is mapped C^1 continuously to the isoparametric geometry representation globally. Then the C^1 continuity of the deformation map is a consequence of the C^1 continuity of both, the map from the reference to the mesh of the undeformed and the deformed configuration.

A second, more complex but additionally more flexible possibility is to define the map locally, such that for each pair of elements it is ensured that the map of an intermediate configuration to the physical space is C^1 continuous. This idea is presented in figure 5.11 for a pair of triangular elements. If $\mathbf{X}(\xi)$ and $\mathbf{x}(\xi)$ both are C^1 continuous and one-to-one, then this is clearly also the case for the deformation map $\varphi = \mathbf{x}(\xi) \circ \mathbf{X}(\xi)^{-1}$.

To define the C^1 continuous relations $\mathbf{X}(\xi)$ and $\mathbf{x}(\xi)$, we make use of the Bernstein-Bézier representation of a triangular patch and similar for the Bézier representation of the tensor product spaces involved in the description of the Bogner-Fox-Schmidt element. The advantage is that for the proof of C^1 continuity only the shape of the two elements is of importance.

It is well known, how to construct C^1 continuous finite element shape functions for linear

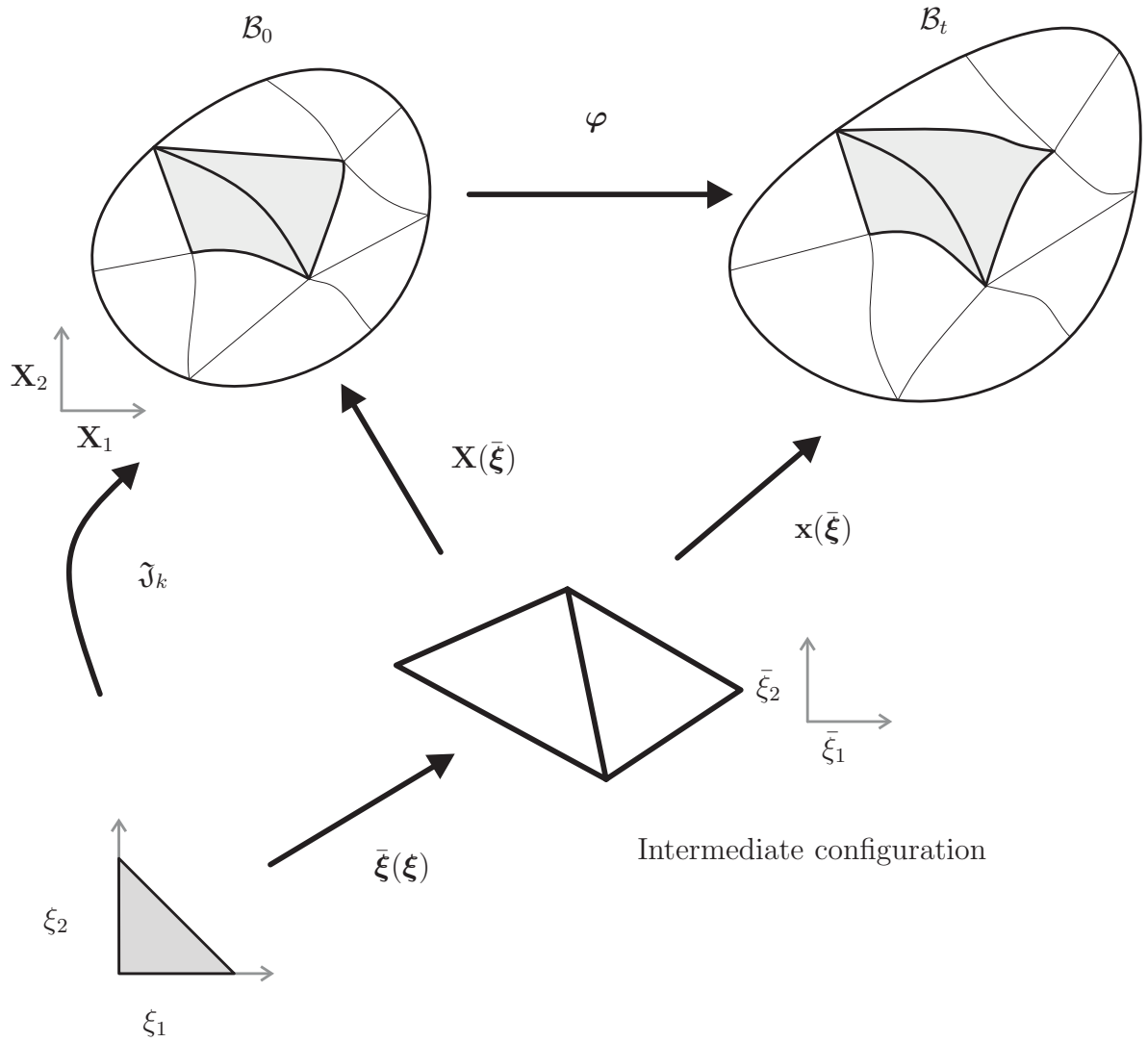


Figure 5.11: Mapping of two triangular elements to the material configuration \mathcal{B}_0 and the spatial configuration \mathcal{B}_t . By providing one-to-one C^1 continuous mappings from the intermediate configuration ξ to the reference and spatial configurations \mathcal{B}_0 and \mathcal{B}_t , φ is C^1 continuous as well.

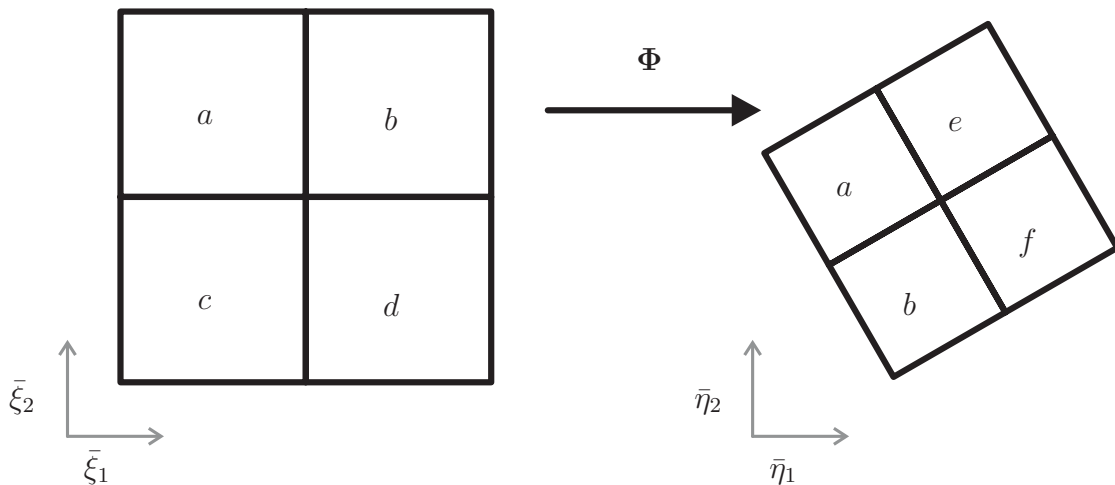


Figure 5.12: Demonstration for the C^1 continuity of a function within the map of one to the other intermediate configuration.

subparametric elements. Here, the basic idea is that for each set of elements at a common node, an intermediate configuration can be defined and the map of the intermediate to physical configuration is constructed C^1 continuously.

To proof that the shape functions are C^1 continuous on any possible reference configuration, we need the control point representation of the geometry as well as the unknown shape function. Therefore, recall (4.13), i.e. the definition of the control points

$$\mathbf{c}_\alpha := \begin{pmatrix} \bar{\mathbf{c}}_\alpha \\ b_\alpha \end{pmatrix}. \quad (5.23)$$

The control points \mathbf{c}_α include the geometry description, by the values $\bar{\mathbf{c}}_\alpha$, as well as the definition of the shape function coefficients, b_α . By the statement that the shape of the elements has to be equal in any intermediate configuration $\bar{\xi}$, the transformation Φ between two intermediate configurations $\bar{\xi}$ and $\bar{\eta}$ has to be an angle preserving linear mapping. A schematic picture of Φ is presented in figure 5.12. The shifting of the shape functions from one configuration to the other is done by the simple application of Φ to the vectors $\bar{\mathbf{c}}_\alpha$. Therefore, the shape functions defined by the control points on the pair of elements a and b in the $\bar{\xi}$ intermediate configuration is still C^1 continuous in the $\bar{\eta}$ configuration if the control points are transformed by the corresponding deformation map Φ extended to three dimensions by simply leaving the third dimension of the control point values.

Since we are not interested in the description of the intermediate configuration, the first two entries of the three dimensional control points, which describe the map of the reference to the intermediate element are of no importance. For the unique description of \mathfrak{J}_k , the mapping the reference to the physical domain, only the additional entries in the control point vector are necessary.

In case of the BFS element, we assume that all elements are square shaped. Therefore, no

further information on the element shape has to be remembered within the construction of the geometry. In case of a triangular elements, the shape can be described by the knowledge of the element angles.

Similar to the description of the subparametric finite elements, the design of the shape functions is prescribed by the interpolation property of the function values and additional derivative degrees of freedom. The only difference is that the derivative degrees of freedom are not related to the physical domain, but to the intermediate configuration coordinate system $\bar{\xi}$.

5.4.3 Hermite interpolation

Here, the Hermite interpolation of the geometry is introduced. As discussed in the previous subsection, the main problem is the definition of a common tangent in the reference configuration. Therefore, in many cases a whole reference mesh is created and mapped to the physical domain, for example see [107] or [169]. A similar approach is the use of the isoparametric analysis, where the local coordinate system of the isoparametric patches are similar to the reference mesh.

Here a more general approach in which the reference mesh is defined locally for each nodal point is adopted. Therefore (3.4) can be rewritten by

$$\mathbf{X}(\bar{\xi}) = \sum_{\mathcal{I}} \mathbf{X}_I N_I(\bar{\xi}) + \sum_{\mathcal{J}} \mathbf{F}_J \cdot \mathbf{M}_J(\bar{\xi}) + \sum_{\mathcal{K}} \mathbf{G}_K : \mathbf{L}_K(\bar{\xi}). \quad (5.24)$$

In contrast to (3.5), but similar to (3.9), the shape functions are classified into N_I , \mathbf{M}_J and \mathbf{L}_K which are scalar, vector and tensor valued functions. Let $\bar{\xi}_O$ denote the nodes in the reference configuration for which the shape function values are defined. In the following, the set of nodes, where the primal unknown is described will be denoted by the index set \mathcal{I} , the nodal set of the prescribed derivatives is given by \mathcal{J} and the set of nodes for the given Hessian is called \mathcal{K} . The shape functions are then characterized by the following extended interpolation property

$$\begin{aligned} N_I(\bar{\xi}_O) &= \delta_{IO}, & \mathbf{M}_J(\bar{\xi}_O) &= \mathbf{0}, & \mathbf{L}_K(\bar{\xi}_O) &= \mathbf{0} & \text{for } O \in \mathcal{I} \\ \nabla_{\bar{\xi}} N_I(\bar{\xi}_O) &= \mathbf{0}, & \nabla_{\bar{\xi}} \mathbf{M}_J(\bar{\xi}_O) &= \delta_{JO} \mathbf{I}_2, & \nabla_{\bar{\xi}} \mathbf{L}_K(\bar{\xi}_O) &= \mathbf{0} & \text{for } O \in \mathcal{J} \\ \nabla_{\bar{\xi}}^2 N_I(\bar{\xi}_O) &= \mathbf{0}, & \nabla_{\bar{\xi}}^2 \mathbf{M}_J(\bar{\xi}_O) &= \mathbf{0}, & \nabla_{\bar{\xi}}^2 \mathbf{L}_K(\bar{\xi}_O) &= \delta_{KO} \mathbb{G} & \text{for } O \in \mathcal{K}, \end{aligned} \quad (5.25)$$

with $(\mathbb{G})_{ijkl} := \frac{1}{2} [\delta_{ik} \delta_{jl} + \delta_{il} \delta_{kj}]$.

5.4.4 The Bogner-Fox-Schmidt element

The only presented isoparametric element is the bicubic Bogner-Fox-Schmidt element. The necessary 16 degrees of freedom are the primal unknowns, the first derivatives and the mixed second derivative in the direction of the element edges. It shows good convergence behavior, but has one major drawback, which is that a linear subparametric mesh is restricted to parallelograms with exactly four elements per internal node. Definitely, the good performance of the elements as well as the severe geometric restriction have influenced its enhancement to an isoparametric setting.

To construct the element shape functions on the intermediate configuration $\bar{\xi}$, we want

to use the Bézier representation of the bipolynomials. Therefore, the usual reference coordinate system ξ is replaced by two sets of barycentric coordinates. The ξ_1 coordinate is replaced by the 1d barycentric coordinates λ_1, λ_2 and ξ_2 by $\bar{\lambda}_1, \bar{\lambda}_2$. The corresponding bivariate cubic Bernstein polynomials are denoted B_α and \bar{B}_α . Thus, the Hermite shape functions on the intermediate configuration at the node $\bar{\xi}_1$ are given by

$$\begin{aligned} N_1 &= [B_{30} + B_{21}] [\bar{B}_{30} + \bar{B}_{21}] \\ \mathbf{M}_1 &= \frac{1}{3} [\mathbf{E}_1 B_{21} [\bar{B}_{30} + \bar{B}_{21}] - \mathbf{E}_4 [B_{30} + B_{21}] \bar{B}_{21}] \\ L_1 &= \frac{1}{6} \mathbf{E}_1 \cdot \mathbf{A} \cdot \mathbf{E}_2 B_{21} \bar{B}_{21}, \end{aligned} \quad (5.26)$$

with $\mathbf{A} := \begin{bmatrix} 0 & 1 \\ 1 & 0 \end{bmatrix}$. The remaining shape functions at the other vertices are a direct result of (5.26) and are obtained by cyclic permutations of the indices.

5.4.5 Mesh construction for the isoparametric Bogner-Fox-Schmidt element

In the following, three options for the construction of isoparametric C^1 continuous meshes are compared. Additionally to the review of the Petera-Pittmann algorithm [169] in subsection 5.4.5.1, a direct construction algorithm is presented in subsection 5.4.5.2 together with a new $\bar{\mathbf{G}}$ algorithm for the construction of smooth C^1 meshes. The latter two have been published in [99]. A first impression on the behavior of the different algorithms is given in figure 5.13.

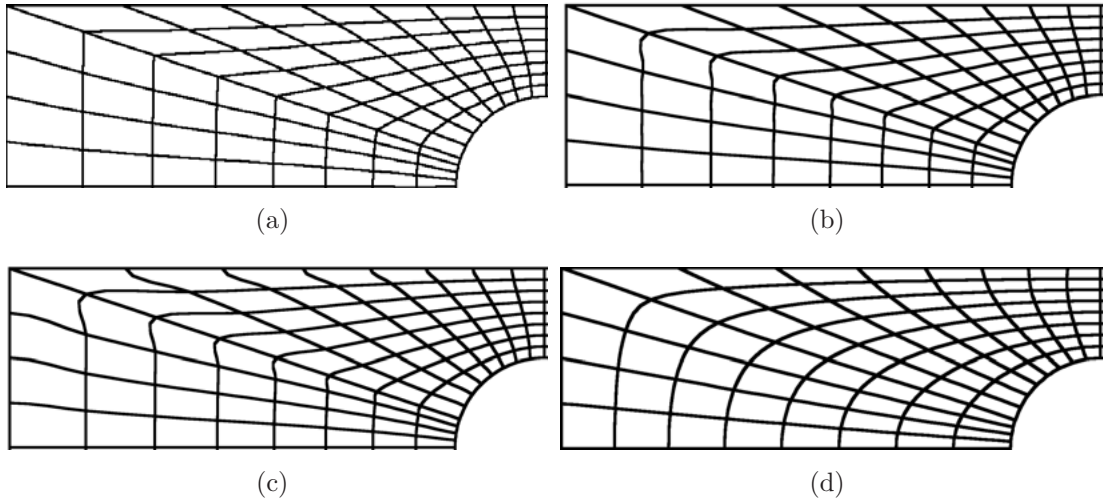


Figure 5.13: (a): Original bilinear mesh, (b): Mesh constructed by Petera-Pittmann algorithm, (c): Mesh, designed with the algorithm of subsection 5.4.5.2, (d): Mesh with $\bar{\mathbf{G}}$ optimization of subsection 5.4.5.3.

5.4.5.1 Petera-Pittmann algorithm

The Petera-Pittmann algorithm [169], introduces the problem of the creation of isoparametric geometries, based on a bilinear reference mesh. Let us denote the bilinear reference

geometry by

$$\mathbf{X}^b = \sum_K \mathbf{X}_k N_K, \quad (5.27)$$

whereas for an isoparametric approximation of the geometry, the notation based on generalized coordinates is used, i.e.

$$\mathbf{X}^h = \sum_J \mathbf{Y}_J \Xi_J. \quad (5.28)$$

The algorithm, proposed by Petera-Pittmann is described by the minimization of the functional

$$\bar{\Pi} := \frac{1}{2} \int_{\mathcal{B}_{\xi}} \|\mathbf{X}^h - \mathbf{X}^b\|^2 + \|\nabla_{\xi} \mathbf{X}^h - \nabla_{\xi} \mathbf{X}^b\|^2 + \|\partial_{\xi_1 \xi_2}^2 [\mathbf{X}^h - \mathbf{X}^b]\|^2 \, dV_{\xi} \quad (5.29)$$

with respect to the generalized coordinates \mathbf{Y}_J . (5.29) is a quadratic expression in terms of the generalized coordinates coefficients, thus resulting in a linear system of equations. In a standard procedure the residuals

$$\mathbf{R}_I = \int_{\mathcal{B}_{\xi}} \Xi_I [\mathbf{X}^h - \mathbf{X}^b] + \nabla_{\xi} \Xi_I \cdot [\nabla_{\xi} \mathbf{X}^h - \nabla_{\xi} \mathbf{X}^b] + \partial_{\xi_1 \xi_2}^2 \Xi_I [\partial_{\xi_1 \xi_2}^2 [\mathbf{X}^h - \mathbf{X}^b]] \, dV_{\xi} \quad (5.30)$$

and tangent stiffness matrix

$$\mathbf{K}_{IJ} = \int_{\mathcal{B}_{\xi}} \Xi_I \Xi_J + \partial_{\xi_1} \Xi_I \partial_{\xi_1} \Xi_J + \partial_{\xi_2} \Xi_I \partial_{\xi_2} \Xi_J + \partial_{\xi_1 \xi_2}^2 \Xi_I \partial_{\xi_1 \xi_2}^2 \Xi_J \, dV_{\xi} \quad (5.31)$$

are derived.

The major advantage of this mesh construction algorithm is that no geometry boundary conditions are necessary. Yet, the relation to the linear geometry can lead to poor quality meshes, i.e. compare with figure 5.13 and chapter 8.

5.4.5.2 Local mesh construction algorithm

A further option for the construction of isoparametric meshes is to define the tangent vectors for the mapping of the intermediate to the physical reference configuration by the nodal points of the bilinear finite elements. Let e_1, \dots, e_n , $n \leq 4$ denote the elements at the global node K . Without loss of generality, the elements are arranged in counter clockwise direction around the common node, which is the n -th node of each element, compare to figure 5.14 (right). Then the intermediate configuration coordinates $\bar{\xi}$ are simply achieved by a translation map. In the following, the physical mesh coordinates are given in terms of the nodal coordinates and derivatives with respect to the intermediate coordinate system $\bar{\xi}$.

Therefore, the edge vectors \mathbf{K}^i are constructed, compare figure 5.14. In this case of the element arrangements, the vectors \mathbf{K}^i are defined by

$$\begin{aligned} \mathbf{K}^1 &= \frac{1}{2} [\mathbf{X}_2^{e_1} - \mathbf{X}_4^{e_3}] \\ \mathbf{K}^2 &= \frac{1}{2} [\mathbf{X}_4^{e_1} - \mathbf{X}_2^{e_3}]. \end{aligned} \quad (5.32)$$

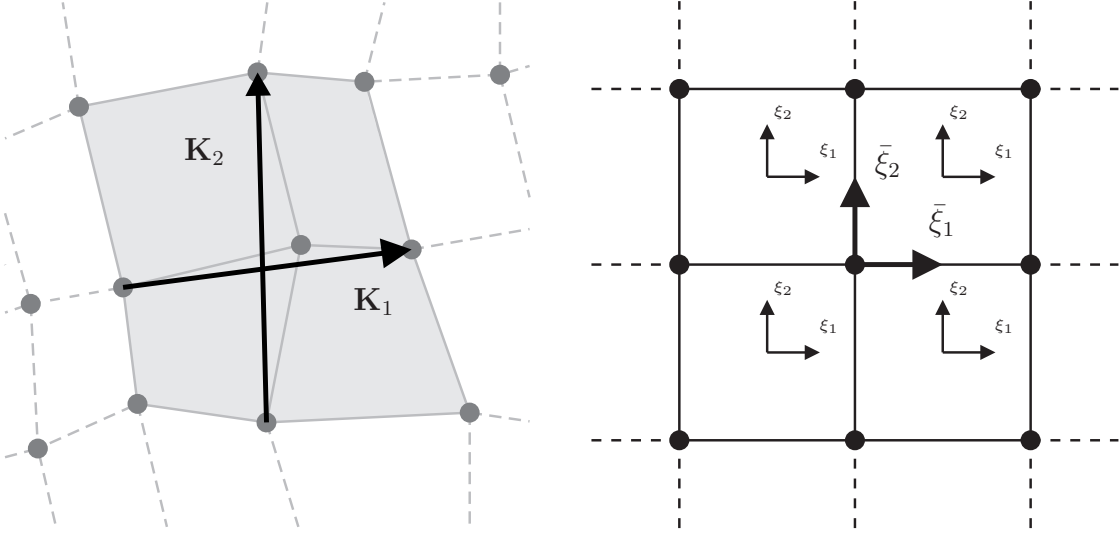


Figure 5.14: (Left): Edge vectors defined by the bilinear reference mesh at an internal node; (Right): Edge vectors defined by the bilinear reference mesh at a boundary node.

If there are only three elements at one node and the element at position 3 is missing, the coordinates can be replaced by the equivalent nodal coordinates $\mathbf{X}_1^{e_2} = \mathbf{X}_4^{e_3}$ and $\mathbf{X}_1^{e_4} = \mathbf{X}_2^{e_3}$. In case of only one or two elements at the node, the missing nodal positions are replaced by the node itself and the factor 1/2 is omitted.

Now, we obtain the isoparametric mesh by the nodal values of the bilinear mesh. Keeping the nodal values, solely the derivative expressions have to be defined.

$$\left| \frac{\partial \mathbf{X}}{\partial \xi_i} \right|_{\bar{\xi}=0} := \mathbf{K}^i \quad (5.33)$$

motivates the definition of the tensor \mathbf{D} with $D_{ij} = (\mathbf{K}^i)_j$ for the construction of the isoparametric geometry. The second derivative is set to be zero.

The geometry description can thus be done by the use of the shape functions (5.26) and is resulting in a Hermite description, given by the gradient values \mathbf{D} of the derivative with respect to the intermediate configuration, i.e.

$$\mathbf{X}^h := \sum_I \mathbf{X}^I N^I + \mathbf{D}^I \cdot \mathbf{M}^I + \mathbf{0L}^I. \quad (5.34)$$

Remark 5.1 (Application of gradient boundary values) *In order to get an easy description of boundary values, it can be desirable that the tangent vector for a nodal point can be perpendicular to the surface of the body. In this case, the mixed derivative $\partial_{\xi_1 \xi_2}^2$ is up to a constant factor equal to the mixed derivative in the normal and tangent direction ∂_{nt}^2 . This result is facilitating the application of relevant boundary conditions like symmetry boundary conditions, i.e. compare tabular 3.1.*

5.4.5.3 \bar{G} -optimization for finite elements

The shape functions of the isoparametric BFS element depend on the geometry of the neighboring elements. This can lead to numerical errors when "non-smooth" reference

meshes with differently oriented elements are used, e.g. see the mesh in figure 5.13 on the left hand side. When this mesh is used in a simulation, the largest error is observed along the diagonal, where the disturbance of the mesh

$$\bar{\mathbf{G}} := \frac{\partial^2 \mathbf{X}}{\partial \xi^2} \quad (5.35)$$

shows the highest values. This motivates the optimization of the mesh by minimizing the values $\bar{\mathbf{G}}$. Therefore, the following potential is defined

$$\bar{\Pi} = \frac{1}{2} \sum_{I=1}^K \int_{\Omega_\xi^I} \bar{\mathbf{G}} : \bar{\mathbf{G}} \, dV_\xi, \quad (5.36)$$

where dV_ξ is an area increment in the local coordinate system of each reference element Ω_ξ^I and K the total number of elements. This potential (5.36) has to be minimized with respect to the generalized coordinates, i.e. its variation $\delta \bar{\Pi}$ has to vanish

$$\delta \bar{\Pi} = \sum_{I=1}^K \int_{\Omega_\xi^I} \bar{\mathbf{G}} : \delta \bar{\mathbf{G}} \, dV_\xi = 0. \quad (5.37)$$

Due to the quadratic nature of the potential, the variation (5.37) is a bilinear form on $\bar{\mathbf{G}}$ and $\delta \mathbf{X}^h$. The resulting linear system of equation gives the necessary change $\Delta \mathbf{Y}^I$ of the geometry approximation

$$\Delta \mathbf{Y}^I = \bar{\mathbf{K}}_{IJ}^{-1} \bar{\mathbf{R}}_I, \quad (5.38)$$

Whereby the residual vector and the stiffness matrix are given by

$$\bar{\mathbf{R}}_I = \sum_{I=1}^K \int_{\Omega_\xi^I} \bar{\mathbf{G}} : \nabla_\xi^2 \Xi_I \, dV_\xi. \quad (5.39)$$

$$\bar{\mathbf{K}}_{IJ} = \sum_{I=1}^K \int_{\Omega_\xi^I} \nabla_\xi^2 \Xi_I : \nabla_\xi^2 \Xi_J \mathbf{I}_2 \, dV_\xi. \quad (5.40)$$

With the knowledge of the residuals and the stiffness matrix, it is necessary to define some boundary condition to be able to solve the minimization problem (5.37) uniquely. In our numerical examples the mesh construction of subsection 5.4.5.2 is used for the description of the boundary approximation. The remaining degrees of freedom are totally free to move.

Since (5.39) is linear, the equation can be solved in only one step, which is not very costly. The major advantage of this method in comparison to the direct mesh optimization as presented in subsection 5.4.5.2 or the algorithm of [169] is not only that the meshes are optically more beautiful, i.e. compare to figure 5.13 but additionally, the method is resulting in quantitatively superior results, see chapter 8 for details.

Remark 5.2 (Integration domain on the reference configuration) *The integration domain is set to be on the reference configuration for two reasons. First, we end up with a linear system of equations, which creates the adjusted mesh in simply one step. Otherwise, the change of the integration domain would have to be taken into account. Additionally, mesh refinement is usually done in the regions, where a better solution is desired and weighting with the physical domain would decrease the importance of the small elements.*

5.4.5.4 \bar{G} -optimization with locally refined meshes

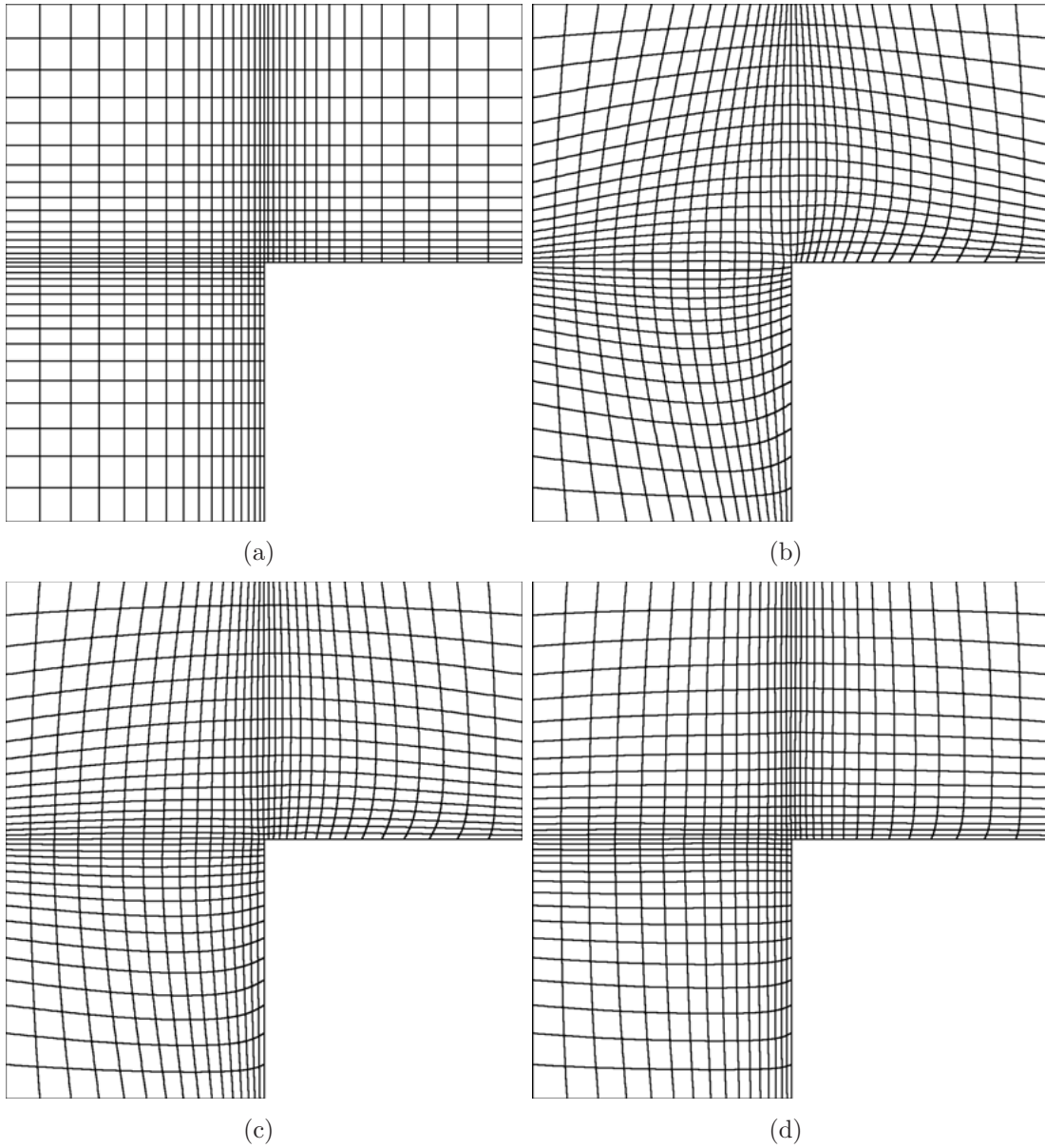


Figure 5.15: Comparison of the different mesh optimization procedures (a) Original mesh, (b) mesh optimized with the \bar{G} -optimization (c) volume control algorithm with $\kappa = 10000$ and (d) volume control algorithm with $\kappa = 100000$.

Unfortunately, every method has its disadvantages. Within the mesh optimization scheme, presented in subsection 5.4.5.3, sometimes mesh refinement can be annihilated. This is especially the case, if the nodal positions are not fixed, as done in most of our analysis. However, if these positions are fixed, the mesh optimization is very much restricted and optimal results can not be guaranteed.

Therefore, we propose to link the size of the elements, computed within the \bar{G} -optimization

procedure to the size of the bilinear reference geometry \mathbf{X}^b , introduced by

$$\tilde{\theta} := \int_{\Omega_\xi^I} \det(\nabla_\xi \mathbf{X}^b) \, dV_\xi. \quad (5.41)$$

Similar to a three-field variational principle for the treatment of incompressible materials, the quantities $\bar{\mathbf{F}} := \nabla_\xi \mathbf{X}$ together with the additional fields $\bar{\theta}$ and \bar{p} are introduced. The potential (5.36) is extended the three-field potential

$$\bar{\Pi} := \sum_{I=1}^K \int_{\Omega_\xi^I} \bar{\mathbf{G}} : \bar{\mathbf{G}} + \bar{p} [\det(\bar{\mathbf{F}}) - \bar{\theta}] + \frac{\kappa}{\tilde{\theta}^2} [\bar{\theta} - \tilde{\theta}]^2 \, dV_\xi. \quad (5.42)$$

The values κ in (5.42) enables to control the importance of the volume preservation, whereas the value $1/\tilde{\theta}^2$ is proposed, to link the volumetric term to the relative volume change and not to the absolute value of $\bar{\theta} - \tilde{\theta}$. The discrete residuals are therefore given by

$$\mathbf{R}_I^{\bar{\mathbf{G}}} = \sum_{I=1}^K \int_{\Omega_\xi^I} \bar{\mathbf{G}} : \nabla_\xi^2 \Xi_I \, dV_\xi + \sum_{I=1}^K \int_{\Omega_\xi^I} \bar{p} \det \bar{\mathbf{F}} \bar{\mathbf{F}}^{-t} \cdot \nabla_\xi \Xi_I \, dV_\xi \quad (5.43)$$

for the dependence on the change of the geometry description and the additional parts

$$R_J^{\bar{p}} = \sum_{I=1}^K \int_{\Omega_\xi^I} [\det \bar{\mathbf{F}} - \bar{\theta}] N_J \, dV_\xi \quad (5.44)$$

$$R_K^{\bar{\theta}} = \sum_{I=1}^K \int_{\Omega_\xi^I} \frac{\kappa}{\tilde{\theta}^2} [\bar{\theta} - \tilde{\theta}] N_K - p N_K \, dV_\xi. \quad (5.45)$$

The nonzero parts of the discrete stiffness matrix for the variation of (5.43) are derived to

$$\begin{aligned} \mathbf{K}_{IL}^{\bar{\mathbf{G}}, \bar{\mathbf{G}}} &= \sum_{I=1}^K \int_{\Omega_\xi^I} \nabla_\xi^2 \Xi_I : \nabla_\xi^2 \Xi_L \mathbf{I}^2 \, dV_\xi \\ &\quad + \sum_{I=1}^K \int_{\Omega_\xi^I} \bar{p} \det \bar{\mathbf{F}} \nabla_\xi \Xi_I \cdot [\bar{\mathbf{F}}^{-1} \otimes \bar{\mathbf{F}}^{-1} - \bar{\mathbf{F}}^{-1} \bar{\otimes} \bar{\mathbf{F}}^{-1}] \cdot \nabla_\xi \Xi_L \, dV_\xi \end{aligned} \quad (5.46)$$

and additionally

$$\mathbf{K}_{IM}^{\bar{\mathbf{G}}, \bar{p}} = \sum_{I=1}^K \int_{\mathcal{B}_\xi} \nabla_\xi \Xi_I \cdot \bar{\mathbf{F}}^{-1} \det \bar{\mathbf{F}} N_M \, dV_\xi. \quad (5.47)$$

The non-trivial linearizations of (5.44) and (5.45) are the transposed of (5.47) together with

$$K_{JN}^{\bar{p}, \bar{\theta}} = - \sum_{I=1}^K \int_{\Omega_\xi^I} N_J N_N \, dV_\xi \quad (5.48)$$

$$K_{KN}^{\bar{\theta}, \bar{\theta}} = \frac{\kappa}{\tilde{\theta}^2} \sum_{I=1}^K \int_{\Omega_\xi^I} N_K N_N \, dV_\xi. \quad (5.49)$$

In contrast to the original version, the potential $\bar{\Pi}$ is a non-quadratic functional of $\delta \bar{\mathbf{u}}$ and therefore, the problem can no longer be solved directly.

Remark 5.3 (static condensation) For a more effective computation, the complete problem of this subsection can be be rewritten as

$$\left[\bar{\mathbf{K}}^{\bar{\mathbf{u}}, \bar{\mathbf{u}}} - \bar{\mathbf{K}}^{\bar{\mathbf{u}}, p\theta} [\mathbf{K}^{p\theta, p\theta}]^{-1} \mathbf{K}^{p\theta, \bar{\mathbf{u}}} \right] \bar{\mathbf{u}} = \bar{\mathbf{R}}^{\bar{\mathbf{u}}} - \mathbf{K}^{\bar{\mathbf{u}}, p\theta} [\bar{\mathbf{K}}^{p\theta, p\theta}]^{-1} \mathbf{R}^{p\theta}. \quad (5.50)$$

and the increment $\delta\mathbf{p}$ and $\delta\theta$ computed in a second step by

$$\mathbf{u}_p = [\mathbf{K}^{p\theta p\theta}]^{-1} [\mathbf{R}^{p\theta} - K^{p\theta \mathbf{u}} \mathbf{u}_u]. \quad (5.51)$$

Additionally, by the above prescribed procedure, the condition number of the stiffness matrix is stabilized.

6 Isogeometric Analysis

The isogeometric analysis is defined to be the use of Non-Uniform-Rational-B-Splines (NURBS) for the approximation of the geometry as well as the deformed configuration. Within this chapter, the concept of isogeometric analysis is introduced for the application to gradient elasticity. The major advantage is that the continuity of the ansatz functions (NURBS or B-splines) can easily be adjusted by the use of the Cox-deBoor algorithm. Therefore, a smooth approximation of the geometry is obtained easily. B-spline methods for the application to partial differential equations are rather old, i.e. see [179] or [127] for a comprehensive overview on the topic. However, the concept of isogeometric analysis, proposed by Hughes et al. in [129], enables the exact representation of the geometry for nearly all relevant mechanical components since they are often designed by a CAD program. In this pioneering paper the closest attention is paid to the exact representation of the geometry and the superior properties of the isogeometric analysis (IGA) during the different types of mesh refinement. A comparison of the p -method for finite elements with the k -method for the IGA is documented in [130]. A mathematical analysis of the isogeometric NURBS-based approach is performed in [25] and a study on refinement and continuity is presented in [67]. Further applications of this framework include, among others, the modeling of structural vibrations [68], fluid-structure interaction [27] and patient-specific modeling in biomechanics [236].

For the improvement of the method, in [131] enhanced quadrature schemes for the integration of the rational functions are proposed. [215] discusses the application of inhomogeneous boundary conditions. [82] deals with shear locking for thin shell structures, [26] introduces the method of T-splines and [139] the use of trimmed CAD surfaces. Both methods are extensions of the original form of the isogeometric analysis for the modeling of more general geometries.

Furthermore, the IGA can successfully be applied to fourth order partial differential equations. The first publication of Auricchio et al. [20, 21] uses the stream function approach to create divergence free deformations. This is necessary to satisfy the incompressibility condition within a small strain analysis. In [112] the Cahn-Hilliard equation is solved by means of the isogeometric concept and in [136, 137] the isogeometric analysis is used for the application to the Kirchhoff-Love shell theory. The first application of the isogeometric analysis to gradient elasticity is due to Klassen [142] and Fischer et al. [96].

Additionally, an excellent introduction and overview of the topic of the isogeometric analysis is found in [66]. Since NURBS and B-splines are originated in the field of CAGD, the reader, interested in a detailed description of the basic principles of B-splines and NURBS is referred to the monographs of Prautzsch et al. [174], Farin [95], Lai et al. [149] or Piegl [170].

This chapter is structured as follows. In the first section 6.1, the basic principles of B-spline up to the construction of multi-patch B-spline geometries is introduced. This is extended to the rational case in section 6.2, where special problems occurring due to the non-polynomial shape functions are discussed. Further aspects, necessary for the appli-

cation of NURBS within the application to a Galerkin method to solve gradient elasticity are presented in section 6.3.

6.1 B-splines

B-splines are the fundament of the isogeometric analysis. 1d B-splines are very similar to the Bézier representation of polynomial curves. The name B-spline has been introduced by Schoenberg [181] and refers to a polynomial spline defined by a minimal set of control points. The difference to the Bernstein-Bézier representation is the following. Within the Bernstein-Bézier representation of a polynomial spline, a special alignment of the control points is enforced to create functions with higher order continuity. Those additional conditions restrict the possible position of the control points, and thus, not all degrees of freedom are really “free”. Within the B-spline representation, this dependency is cancelled out by the use of independent control points, only. In practice, the Bernstein polynomials are replaced by the use of the Cox-deBoor algorithm [69,76] for the evaluation of the basis functions. Therein the continuity is directly taken into account.

Within the field of B-splines or NURBS, one differs between patches and elements. This is mainly motivated by the definition of the function in the reference space. Since B-splines are used in a tensor product structure they are defined on rectangular domains. The complete domain on which the B-splines are constructed by the Cox-deBoor algorithm is defining the patch. An element is the part of the patch, on which the function is fully polynomial, compare to figure 6.1. For complicated geometries it is possible that one single patch is not sufficient. Therefore, additional care on positioning the control points has to be taken to obtain the desired continuity between the patches. This is similar to the conditions occurring within the isoparametric BFS element, see section 5.4.

6.1.1 B-spline curves

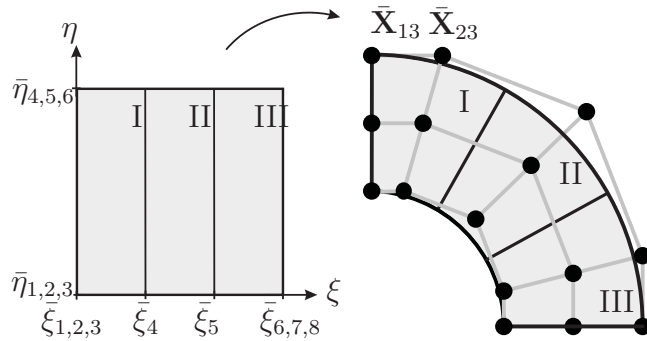


Figure 6.1: (Left): Knot vectors define the three quadratic elements ($p = 2$) for one patch in parameter space, note the multiplicity of the knots on the boundary; (Right): Control points and geometry of a quarter ring in the physical space. At both ends, symmetry boundary conditions are applied, by prescribing that the adjacent control points, e.g. \bar{X}_{13} and \bar{X}_{23} , have to stay on one line.

For the one-dimensional case, using the monotonically increasing knot vector $\mathbf{T} := [\bar{\xi}_1, \dots, \bar{\xi}_m]$,

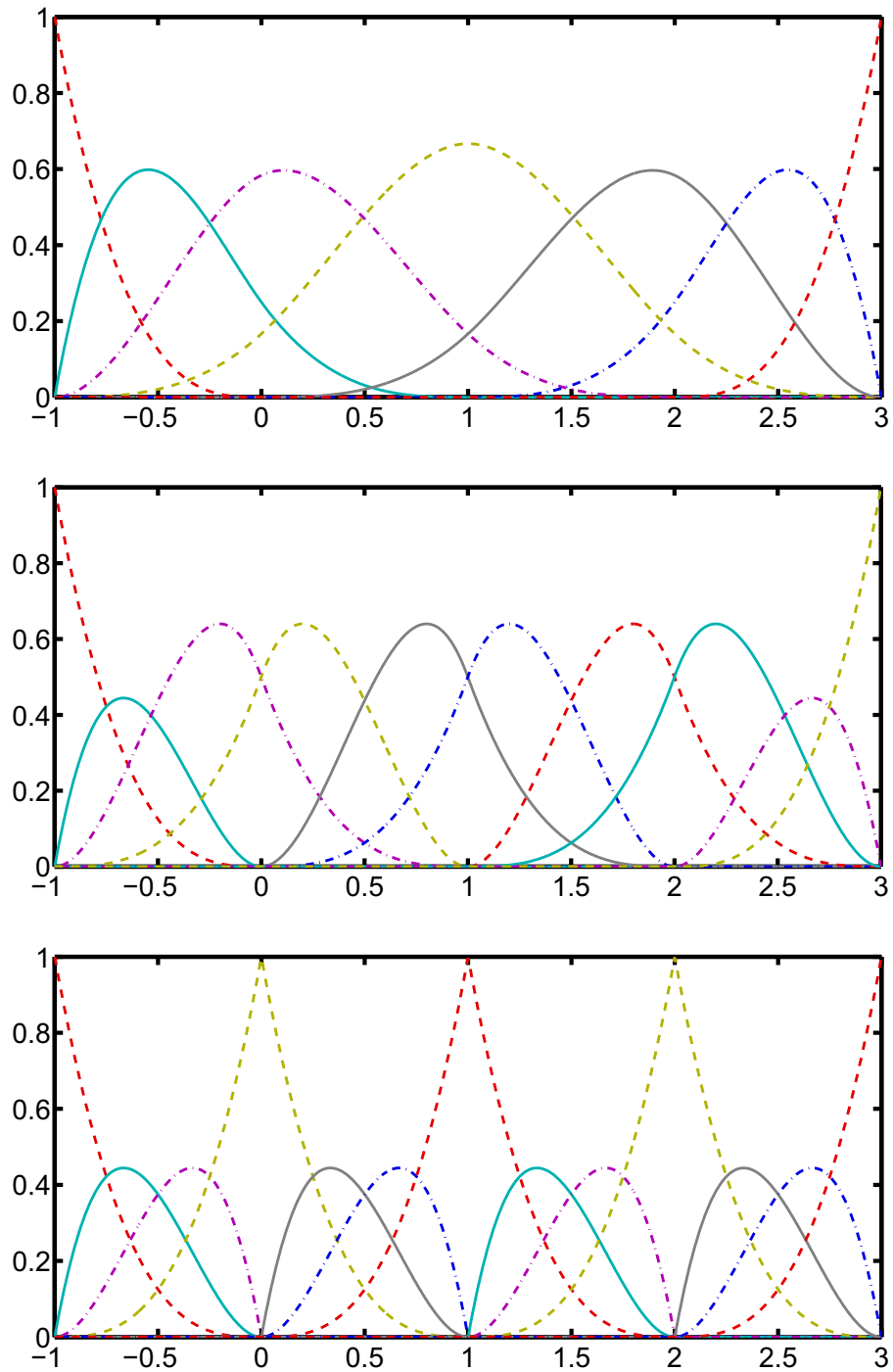


Figure 6.2: Cubic B-spline functions for different knot vectors: (Top): knot vector $\mathbf{T} = [-1, -1, -1, -1, 0, 1, 2, 3, 3, 3, 3]$ resulting in C^2 continuous B-spline functions; (Center): knot vector $\mathbf{T} = [-1, -1, -1, -1, 0, 0, 1, 1, 2, 2, 3, 3, 3, 3]$ resulting in C^1 continuous functions and (Bottom): knot vector $\mathbf{T} = [-1, -1, -1, -1, 0, 0, 0, 1, 1, 1, 2, 2, 2, 3, 3, 3, 3]$ only providing C^0 continuous B-splines.

the B-spline functions of degree p are defined recursively on the interval $[\bar{\xi}_1, \bar{\xi}_m]$ by

$$B_i^p(\xi) = \frac{(\xi - \bar{\xi}_i)B_i^{p-1}(\xi)}{\bar{\xi}_{i+p} - \bar{\xi}_i} + \frac{(\bar{\xi}_{i+p+1} - \xi)B_{i+1}^{p-1}(\xi)}{\bar{\xi}_{i+p+1} - \bar{\xi}_{i+1}}, \quad (6.1)$$

with $1 \leq i \leq n$, $n = m - p - 1$ the number of B-splines and m the number of entries in the knot vector. The initialization functions in (6.1) are the piecewise constants

$$B_i^0(\xi) = \begin{cases} 1 & \text{for } \bar{\xi}_i \leq \xi < \bar{\xi}_{i+1} \\ 0 & \text{otherwise.} \end{cases} \quad (6.2)$$

If some of the knots have a multiplicity higher than 1, the denominators in (6.1) may become zero. In this case, the B-splines are defined to be zero, i.e. $B_i^p := 0$ if $\bar{\xi}_{i+p} - \bar{\xi}_i = 0$. A knot vector \mathbf{T} is called open, if the multiplicity at both ends of \mathbf{T} is $p + 1$. B-splines defined by open knot vectors are interpolatory at the boundary of the domain.

A B-spline curve is described by the single B-spline functions (6.1) and prescribed control points $\bar{\mathbf{X}}_i$ as

$$\mathbf{c}(\xi) = \sum_{i=1}^n \bar{\mathbf{X}}_i B_i^p(\xi). \quad (6.3)$$

Similar to the Bézier representation of a polynomial spline (see chapter 4), the control points are not interpolatory.

6.1.2 B-spline geometries

Higher dimensional B-spline surfaces or bodies are created by the use of tensor products. For example, a 2d geometry of polynomial degree $p_1 \times p_2$ is given by

$$\mathbf{X}(\xi) = \sum_{i=1}^{n_1} \sum_{j=1}^{n_2} \bar{\mathbf{X}}_{ij} B_i^{p_1}(\xi) B_j^{p_2}(\eta). \quad (6.4)$$

and due to the isoparametric setting, the displacement field is approximated equally

$$\mathbf{u}(\xi) = \sum_{i=1}^{n_1} \sum_{j=1}^{n_2} \bar{\mathbf{u}}_{ij} B_i^{p_1}(\xi) B_j^{p_2}(\eta). \quad (6.5)$$

B-splines show several properties which are convenient for the application to a Galerkin scheme. These properties of the B-spline functions are

- non-negativity

$$B_i^p(\xi) \geq 0 \quad (6.6)$$

- compact support

$$\text{supp}(B_i^p) = [\bar{\xi}_i, \bar{\xi}_{i+p+1}] \quad (6.7)$$

- partition of unity

$$\sum_i B_i^p(\xi) = 1 \quad (6.8)$$

- B-splines are piecewise polynomial functions with continuity of C^{p-k} , where p is the polynomial degree and k the multiplicity of the knot.

However, if more than one patch is involved, additional strategies have to be developed to be able to treat higher order continuity. This is presented in the following subsection.

Derivatives at the boundary of the patch For the application of gradient boundary conditions and even more important, the connection of two B-spline patches, it is necessary to know the behavior of the derivatives of B-spline patches at their boundaries.

The derivative of a 1d B-spline curve $\mathbf{c}(\xi)$ with respect to the local coordinate system ξ can be expressed as a B-spline object of order $p - 1$. This is a direct result of the Cox-de Boor recursion formula (6.1),

$$\frac{d\mathbf{c}(\xi)}{d\xi} = \sum_{i=1}^{n-1} \frac{p}{\bar{\xi}_{i+p+1} - \bar{\xi}_{i+1}} [\bar{\mathbf{X}}_{i+1} - \bar{\mathbf{X}}_i] B_i^{p-1}. \quad (6.9)$$

By the introduction of $\bar{\mathbf{X}}_i^{d\xi} := \frac{p}{\bar{\xi}_{i+p+1} - \bar{\xi}_{i+1}} [\bar{\mathbf{X}}_{i+1} - \bar{\mathbf{X}}_i]$ (6.9) can be identified as the control points of a B-spline curve of degree $p - 1$, i.e.

$$\frac{d\mathbf{c}(\xi)}{d\xi} = \sum_{i=1}^{n-1} \bar{\mathbf{X}}_i^{d\xi} B_i^{p-1}. \quad (6.10)$$

For the multidimensional case, the derivatives of a B-spline function $\mathbf{X}(\xi)$ as given in (6.4) with respect to the local coordinates are simple results of the tensor product structure and given by

$$\begin{aligned} \frac{\partial \mathbf{X}}{\partial \xi}(\xi) &= \sum_{i=1}^{n_1-1} \sum_{j=1}^{n_2} \bar{\mathbf{X}}_{ij}^{d\xi} B_i^{p_1-1}(\xi) B_j^{p_2}(\eta) \\ \frac{\partial \mathbf{X}}{\partial \eta}(\xi) &= \sum_{i=1}^{n_1} \sum_{j=1}^{n_2-1} \bar{\mathbf{X}}_{ij}^{d\eta} B_i^{p_1}(\xi) B_j^{p_2-1}(\eta). \end{aligned} \quad (6.11)$$

where the quantities

$$\bar{\mathbf{X}}_{ij}^{d\xi} := \frac{p_1}{\bar{\xi}_{i+p_1+1} - \bar{\xi}_{i+1}} [\bar{\mathbf{X}}_{(i+1)j} - \bar{\mathbf{X}}_{ij}] \quad (6.12)$$

and

$$\bar{\mathbf{X}}_{ij}^{d\eta} := \frac{p_2}{\bar{\eta}_{j+p_2+1} - \bar{\eta}_{j+1}} [\bar{\mathbf{X}}_{i(j+1)} - \bar{\mathbf{X}}_{ij}] \quad (6.13)$$

are defined analogously to the 1d case (6.9).

At the boundary $\xi = \bar{\xi}_1$ of the patch, the derivatives can be reduced to

$$\frac{\partial \mathbf{X}}{\partial \xi}(\bar{\xi}_1, \eta) = \sum_{j=1}^{n_2} \bar{\mathbf{X}}_{1j}^{d\xi} B_j^{p_2}(\eta) \quad (6.14)$$

for the local direction perpendicular to the boundary and

$$\frac{\partial \mathbf{X}}{\partial \eta}(\bar{\xi}_1, \eta) = \sum_{j=1}^{n_2-1} \bar{\mathbf{X}}_{1j}^{d\eta} B_j^{p_2-1}(\eta), \quad (6.15)$$

in the direction parallel to the boundary. For the results given in (6.14) and (6.15), the openness of the knot vector is necessary, so that the summation over i drops out.

6.1.3 Multi-patch domains

Consider two B-spline patches with the coordinates \mathbf{X} and \mathbf{Y} . A sufficient condition for the construction of a C^1 continuous connection of the two patches is given by

$$\bar{\mathbf{X}}_{1j}^{d\xi} = \bar{\mathbf{Y}}_{(n_2-1)j}^{d\xi}. \quad (6.16)$$

Here, the linear independence of the B-splines and (6.14) is used. This condition can as well be described geometrically. Since C^1 continuity contains C^0 continuity, the control points along the common edge have to be equal, i.e.

$$\bar{\mathbf{X}}_{1j} = \bar{\mathbf{Y}}_{n_2j}. \quad (6.17)$$

Including definitions (6.12) and (6.13) in (6.16) we get

$$\frac{p_1}{\bar{\xi}_{p_1+2} - \bar{\xi}_2} [\bar{\mathbf{X}}_{(2)j} - \bar{\mathbf{X}}_{1j}] = \frac{q_1}{\bar{\xi}_{q_1+n_2} - \bar{\xi}_{n_2}} [\bar{\mathbf{X}}_{(n_2)j} - \bar{\mathbf{X}}_{[n_2-1]j}]. \quad (6.18)$$

(6.18) motivates the definition of $x_c := \frac{p_1}{\bar{\xi}_{p_1+2} - \bar{\xi}_2}$ and $y_c := \frac{q_1}{\bar{\xi}_{q_1+n_2} - \bar{\xi}_{n_2}}$ and the use of (6.17) to obtain

$$\bar{\mathbf{X}}_{1j} = \frac{x_c}{x_c + y_c} \bar{\mathbf{X}}_{2j} + \frac{y_c}{x_c + y_c} \bar{\mathbf{Y}}_{(n_2-1)j} = \bar{\mathbf{Y}}_{n_2j}. \quad (6.19)$$

A geometric interpretation of (6.19) is to claim that the control points have to be coplanar with constant ratio

$$||\bar{\mathbf{X}}_{1j} - \bar{\mathbf{X}}_{2j}|| / ||\bar{\mathbf{Y}}_{(n_2-1)j} - \bar{\mathbf{X}}_{n_2j}|| = \frac{y_c}{x_c}. \quad (6.20)$$

6.2 Non-Uniform Rational B-Splines (NURBS)

Within this chapter, the extension of the B-splines, presented in the previous section 6.1 is extended to rational functions. This is necessary to extend the description of the geometry to be able to exactly represent conic sections, thus the ability to exactly represent circles and ellipses.

NURBS are related to the B-splines by the fact that the fraction for its representation is build of B-spline functions but additionally, the n -dimensional image of a NURBS function can be considered to be the projection of the image of a $n+1$ dimensional B-spline. This property is explained in subsection 6.2.3. Therein it is used for the construction of C^1 continuous multi-patch domains.

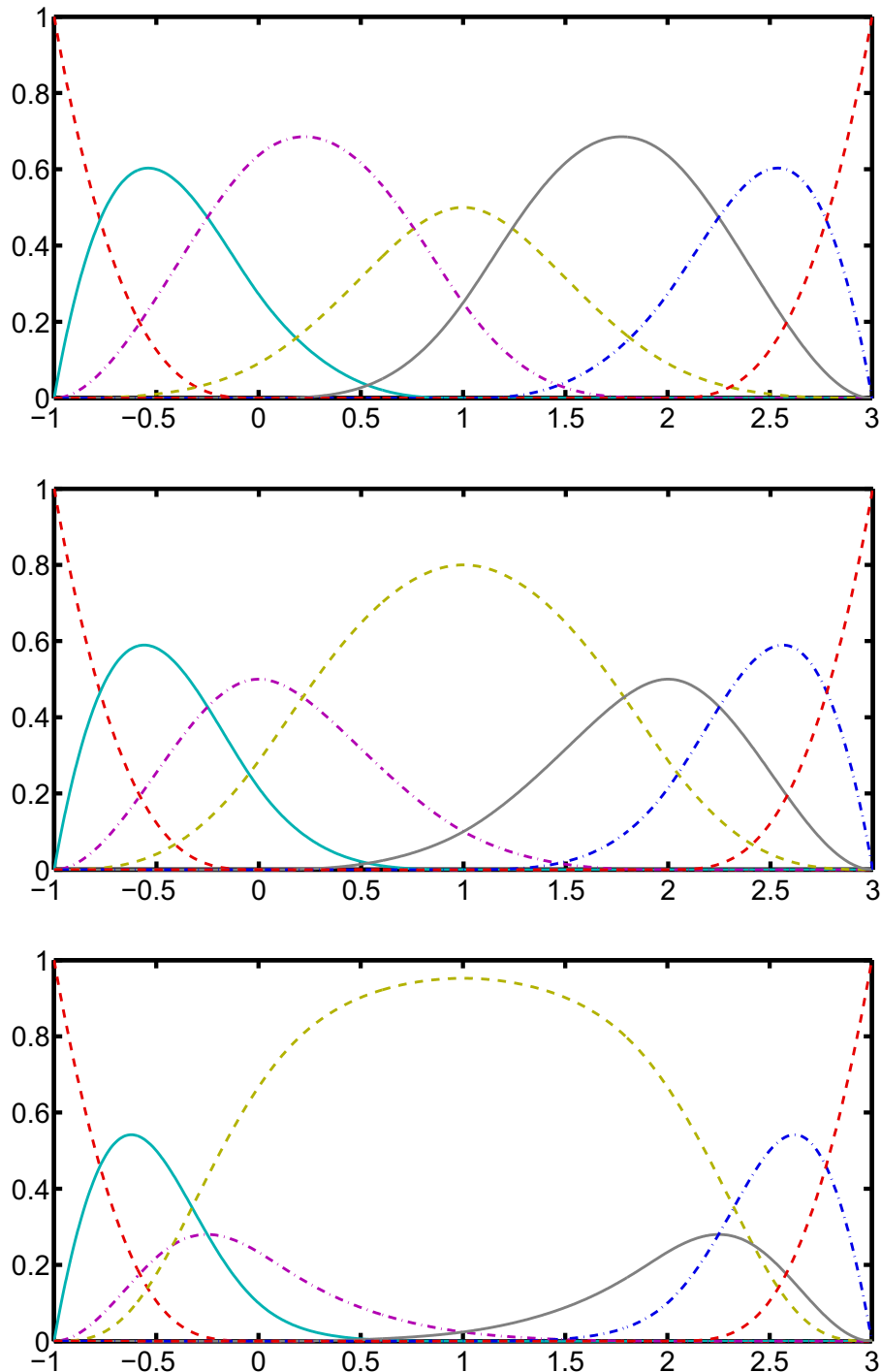


Figure 6.3: Cubic B-spline functions with knot vector $\mathbf{T} = [-1, -1, -1, -1, 0, 1, 2, 3, 3, 3]$ and weight factors $w_i = 1$ for $i \neq 5$ and different weight factor w_5 . (Top): $w_5 = 0.5$, (Center): $w_5 = 2$ and (Bottom): $w_5 = 10$.

6.2.1 NURBS curves

Rational B-splines of polynomial degree p are obtained by the B-spline functions and additional weight factors

$$R_i^p(\xi) := \frac{w_i B_i^p(\xi)}{\sum_{j=1}^n w_j B_j^p(\xi)}. \quad (6.21)$$

To be able to verify that the denominator is strictly positive, it is sufficient to postulate that the weight factors are strictly positive. That restriction is not necessary, but it simplifies the method and for nearly all engineering geometries, non-positive weight factors are not required.

The weights associated to the B-spline functions are only unique up to a constant factor, which is obvious by simply multiplying a constant factor c to all the weight factors occurring in (6.21).

6.2.2 NURBS geometries

In higher dimensions, NURBS functions are computed as the tensor product of the one-dimensional functions, i.e. in the two-dimensional case one obtains

$$N_{ij}(\xi) := \frac{w_{ij} B_i^{p_1}(\xi) B_j^{p_2}(\eta)}{\bar{w}(\xi)}, \quad (6.22)$$

where $\bar{w}(\xi) := \sum_{i=1}^{n_1} \sum_{j=1}^{n_2} w_{ij} B_i^{p_1}(\xi) B_j^{p_2}(\eta)$. Equation (6.22) does not describe a usual tensor product since the weights w_{ij} are not necessarily defined by the multiplication of the weights of the one-dimensional B-splines, i.e. in general $w_{ij} \neq w_i w_j$. More details on the construction of NURBS functions and their geometric properties is found in [170]. A NURBS geometry is described by the means of the NURBS functions (6.22) and prescribed control points $\bar{\mathbf{X}}_{ij}$ as

$$\mathbf{X}(\xi) = \sum_{i=1}^{n_1} \sum_{j=1}^{n_2} \bar{\mathbf{X}}_{ij} N_{ij}(\xi). \quad (6.23)$$

Similarly, the discrete displacement field can be approximated by

$$\mathbf{u}(\xi) = \sum_{i=1}^{n_1} \sum_{j=1}^{n_2} \bar{\mathbf{u}}_{ij} N_{ij}(\xi). \quad (6.24)$$

At the vertices of the geometry the control points are made interpolatory by using open knot vectors, which concurrently reduces the continuity at this points to C^0 . The areas, in which the shape functions N_{ij} are derived by the Cox-de Boor algorithm, are denoted as patches. The knot vector separates the patches into elements. Inside each element, the NURBS functions are fully rational. The continuity between certain elements of the same patch is of the order C^{p-k} , with k being the multiplicity of the knot.

6.2.3 Multi-patch domains

For NURBS-multi-patch domains, the C^1 continuity between two patches with parallel local coordinates is achieved, if the derivatives at the boundary of both patches are equal. In general, the condition is rather complex to verify if no tensor product structure is underlying at those two boundaries. This gets obvious, if the derivatives at the boundary of the patch are computed, see subsection 6.3.1.

An alternative is to use the property, that an n -dimensional NURBS function can be considered to be the projection of an $n+1$ -dimensional B-spline function to an n -dimensional hyperplane. This is based on the homogeneous control point coordinates $\tilde{\mathbf{X}}_i \in \mathbb{R}^{n+1}$ where $(\tilde{\mathbf{X}}_i)_k := w_i (\bar{\mathbf{X}}_i)_k$ for $k \leq n$ and $(\tilde{\mathbf{X}}_i)_{n+1} := w_i$. Since the projection is preserving the continuity of a function, for the connection of two NURBS patches it is sufficient to know the procedure for the connection of two B-spline patches. This has already been described in subsection 6.1.3.

For the result in terms of the classical control point coordinates, we introduce the two patches \mathbf{X} and \mathbf{Y} . By the results of subsection 6.1.3, equation (6.19) we know the dependence

$$w_{1j}^X = \frac{x_c}{x_c + y_c} w_{2j}^X + \frac{y_c}{x_c + y_c} w_{(n_2-1)j}^Y = w_{n_2j}^Y, \quad (6.25)$$

of the boundary weights on the weight factors inside the patches. Using this result to substitute the w_{1j}^X and $w_{n_2j}^Y$ in the relation for the homogeneous control points results in

$$\bar{\mathbf{X}}_{1j} = \frac{x_c w_{1j}^X}{x_c w_{2j}^X + y_c w_{(n_2-1)j}^Y} \bar{\mathbf{X}}_{2j} + \frac{y_c w_{(n_2-1)j}^Y}{x_c w_{2j}^X + y_c w_{(n_2-1)j}^Y} \bar{\mathbf{Y}}_{(n_2-1)j} = \bar{\mathbf{Y}}_{n_2j}. \quad (6.26)$$

Based on this result we claim that the classical control points have to be colinear as well. The only difference to the B-spline case is that the positions of the control points at the boundary of the patches are not only dependent on the knot vector (compare to subsection 6.1.3), but additionally on the weight factors. A simple example of an L-shaped geometry consistent of three cubic patches of one element is presented in figure 6.4. The control points \circ are dependent on the neighboring points \bullet . A special case occurs at the reentrant corner, where the nine control points are determined by only four independent values. The control point \square is dependent on the values of the neighboring \circ s. The additional phantom control point \blacksquare is introduced for practical reasons in the implementation.

6.3 Application to gradient continua

At this point, all necessary properties of B-splines and NURBS are presented for their application to the discrete equations, established in chapter 3. However, especially with the focus on the application to gradient continua, where C^1 continuity of the shape functions is necessary, there are some additional aspects to be considered. The first is the application of gradient boundary conditions, presented in subsection 6.3.1. Additionally, the application of symmetry boundary conditions is discussed in subsection 6.3.2. The chapter closes with a short remark on the strategies of mesh refinement in subsection 6.3.3.

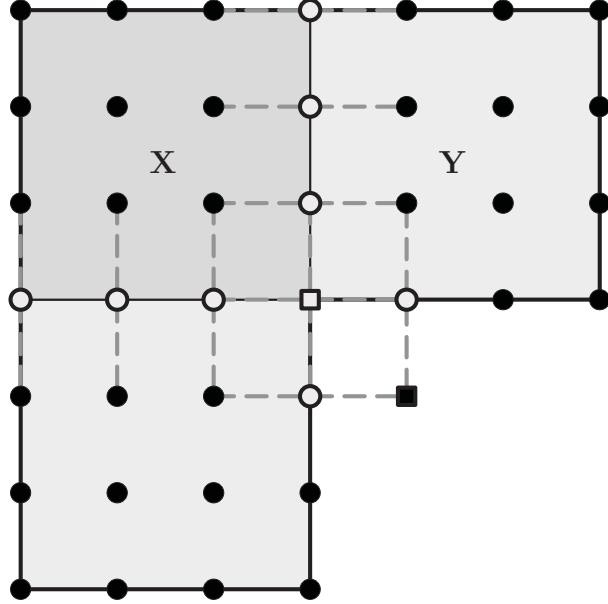


Figure 6.4: Control points for the L-shape domain consistent of three single element patches.

6.3.1 Gradient boundary conditions

In the following it is pointed out that the exact application of boundary conditions on the displacement gradient is difficult or in certain cases even impossible in the framework of the isogeometric analysis. In gradient elasticity, the specification of the normal gradient of the displacement field $\nabla_{\mathbf{n}}\mathbf{u}$, with \mathbf{n} being the normal vector, is, e.g. necessary to realize symmetry conditions. To deduce reasons for these difficulties, we consider the NURBS derivatives at the boundary of a patch defined by an open knot vector. Evaluating the derivatives of the displacement field \mathbf{u} , compare equation (6.24), with respect to the reference coordinate system at the boundary of the domain, i.e. for $\xi = \bar{\xi}_1$, results after careful calculations in

$$\partial_{\xi}\mathbf{u}(\bar{\xi}_1, \eta) = \bar{p}_1 \frac{\bar{w}_2(\eta)}{\bar{w}_1(\eta)} \sum_{j=1}^{n_2} [R_{2j}(\eta)\bar{\mathbf{u}}_{2j} - R_{1j}(\eta)\bar{\mathbf{u}}_{1j}] \quad (6.27)$$

$$\partial_{\eta}\mathbf{u}(\bar{\xi}_1, \eta) = \frac{1}{\bar{w}_1(\eta)} [\tilde{\mathbf{u}}(\eta) - \partial_{\eta}\bar{w}_1(\eta)\mathbf{u}(\bar{\xi}_1, \eta)] \quad (6.28)$$

whereby the tensor product like structure motivates the definitions

$$\bar{w}_i(\eta) := \sum_{j=1}^{n_2} w_{ij} B_j^{p_2}(\eta) \quad (6.29)$$

$$R_{ij}(\eta) := \frac{w_{ij} B_j^{p_2}(\eta)}{\bar{w}_i} \quad (6.30)$$

with the use of the following abbreviations

$$\bar{p}_1 = \frac{p_1}{\bar{\xi}_{(p_1+2)} - \bar{\xi}_2} \quad \tilde{p}_{2j} = \frac{p_2}{\bar{\eta}_{(j+p_2)} - \bar{\eta}_j} \quad (6.31)$$

$$\tilde{\mathbf{u}} = \sum_{j=2}^{n_2} \tilde{p}_{2j} [w_{1j} \bar{\mathbf{u}}_{1j} - w_{1(j-1)} \bar{\mathbf{u}}_{1(j-1)}] B_j^{p_2-1}(\eta). \quad (6.32)$$

In (6.28), the displacements at the boundary $\mathbf{u}(\bar{\xi}_1, \eta)$ are evaluated by means of (6.5), and the required partial derivative $\partial_\eta \bar{w}_i$ is obtained as

$$\partial_\eta \bar{w}_1(\eta) = \sum_{j=2}^{n_2} \tilde{p}_{2j} [w_{1j} - w_{1(j-1)}] B_j^{p_2-1}(\eta). \quad (6.33)$$

It is desirable that boundary conditions on the displacements and the normal gradients can be applied independently of each other. For arbitrary NURBS geometries, this is usually not possible due to the following reasons:

Consider the simplest case by assuming $\partial_\xi \mathbf{X} = c_n(\eta) \mathbf{n}$, with $c_n(\eta)$ being a scaling function related to $\|\partial_\xi \mathbf{X}\|$. Then the normal derivative of the displacements is given as $\nabla_{\mathbf{n}} \mathbf{u} = 1/c_n(\eta) \partial_\xi \mathbf{u}$. The definition of this derivative with respect to the local coordinate, as given in (6.27), contains the sum of the rational functions R_{1j} and R_{2j} , weighted with the control point displacements $\bar{\mathbf{u}}_{1j}$ and $\bar{\mathbf{u}}_{2j}$. Therefore, the rational functions are in general linearly independent to some extend¹. The exact specification of the displacement gradient is then only possible for a very limited number of values for $\bar{\mathbf{u}}_{1j}$ and $\bar{\mathbf{u}}_{2j}$, i.e. when displacements are prescribed for $\bar{\mathbf{u}}_{1j}$, the additional definition of the normal displacement gradient can in general only be accomplished in a least square sense.

This problem is solved if the geometry has a tensor product structure, at least close to the boundary. That means $w_{2j} = c_w w_{1j}$, with c_w being a constant, and entails $R_{1j} = R_{2j}$ for all $1 \leq j \leq n$. Equation (6.27) simplifies to

$$\partial_\xi \mathbf{u}(\bar{\xi}_1, \eta) = \bar{p} \sum_{j=1}^n R_{1j}(\eta) [\bar{\mathbf{u}}_{2j} - \bar{\mathbf{u}}_{1j}], \quad (6.34)$$

which allows to prescribe e.g. homogeneous gradient boundary conditions by requiring that the displacements in η -direction $(\bar{\mathbf{u}}_{1j})_2$ and $(\bar{\mathbf{u}}_{2j})_2$ are equal.

Difficulties to apply gradient boundary conditions occur also if the rational functions R_{1j} and R_{2j} are equal but $\partial_\xi \mathbf{X} \neq c_n(\eta) \mathbf{n}$. Then the normal gradient of the displacements is derived as

$$\nabla_{\mathbf{n}} \mathbf{u} = -\frac{\partial_\eta \mathbf{X} \cdot \partial_\eta \mathbf{X}}{\det \mathbf{J} \|\partial_\eta \mathbf{X}\|} \partial_\xi \mathbf{u} + \frac{\partial_\eta \mathbf{X} \cdot \partial_\xi \mathbf{X}}{\det \mathbf{J} \|\partial_\eta \mathbf{X}\|} \partial_\eta \mathbf{u}, \quad (6.35)$$

with the Jacobian $\mathbf{J} := \nabla_\xi \mathbf{X}$. Assuming the simplest case of a constant Jacobian $\mathbf{J} \equiv \text{const.}$, (6.35) reduces to

$$\partial_{\mathbf{n}} \mathbf{u} = c_1 \partial_\xi \mathbf{u} - c_2 \partial_\eta \mathbf{u} \quad (6.36)$$

¹The sets R_{1j} and R_{2j} can never be completely linearly independent due to their partition of unity property, a result of the restriction to positive weight factors.

with c_1 and c_2 being constants. Again, the functions in both summands in (6.36) are in general linearly independent to some extend and the admissible sets of coefficients $\{\bar{\mathbf{u}}_{1j}, \dots, \bar{\mathbf{u}}_{2n}\}$ is underlying severe restrictions.

For these reasons, we consider in the following and especially in the numerical examples only geometries, defined by a tensor product structure with $w_{1j} = c_w w_{2j}$ and $\partial_\xi \mathbf{X} = c_n(\eta) \mathbf{n}$ at the boundary with prescribed normal derivatives.

6.3.2 Symmetry boundary conditions

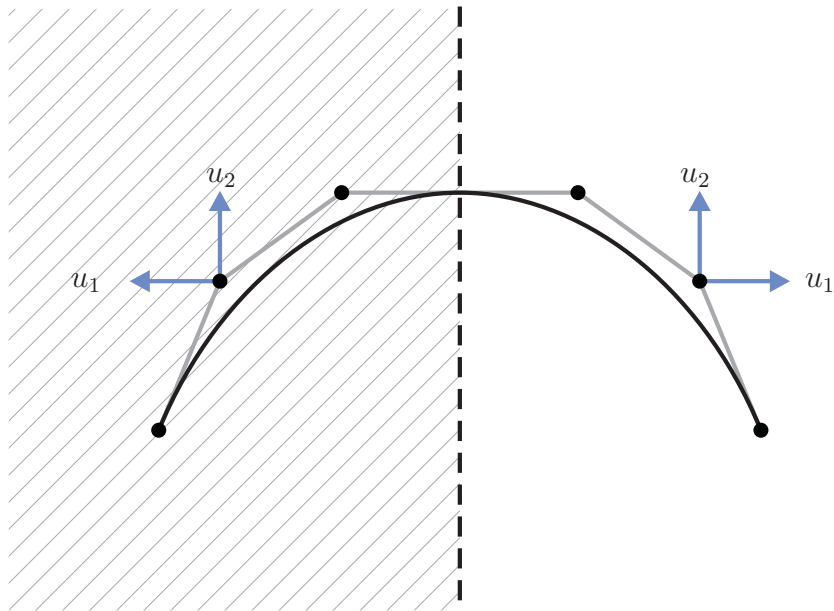


Figure 6.5: One possibility to apply symmetry boundary conditions. The full geometry is approximated and the control points are moved symmetrically.

For the application of symmetry boundary conditions to strain gradient continua, it is not sufficient to fix the geometry along the symmetry axis. At least the first derivative has to be continuous, if the full geometry is approximated. Without loss of generality, we are considering the abscissa to be the symmetry axis, therefore

$$\mathbf{u}_y(x, y) = -\mathbf{u}_y(-x, y) \text{ and } \mathbf{u}_x(x, y) = -\mathbf{u}_x(-x, y), \quad (6.37)$$

are the necessary conditions for the symmetry of the displacement field $\mathbf{u} : \mathcal{B}_0 \rightarrow \mathbb{R}^2$. Additionally, (6.37) implies the following conditions on the derivatives of the function

$$\begin{aligned} u_{x,x}(x, y) &= u_{x,x}(-x) & \text{and} & \quad u_{y,x}(x, y) = -u_{y,x}(-x, y) \\ u_{x,y}(x, y) &= -u_{x,y}(-x) & \text{and} & \quad u_{y,y}(x, y) = u_{y,y}(-x, y). \end{aligned} \quad (6.38)$$

Equations (6.37) and (6.38) imply the following homogeneous boundary conditions on the displacement and its gradient

$$u_x(0, y) = 0 \text{ and } u_{x,y}(0, y) = 0, \quad (6.39)$$

where $u_{x,y}(0, y) = 0$ is a direct consequence of $u_x(0, y) = 0$ and is therefore easily achieved by fixing of the boundary control points to the symmetry axis. The constraint on the normal gradient is given by

$$u_{y,x}(0, y) = 0. \quad (6.40)$$

As already discussed in subsection 6.3.1, the application of gradient boundary conditions for arbitrary rational geometry descriptions can lead to severe problems. Therefore, at this point we only demonstrate the verification of (6.40) for a tensor product structure of the geometry, with local coordinates pointing in the tangential and normal direction of the boundary. In this case, (6.34) can be used and results in the constraint that the displacements of two rows of control points at the symmetry axis of the boundary are linked pairwisely in the direction, tangential to the symmetry axis.

Alternatively, the full geometry can be constructed by at least two patches and the continuity conditions between the patches can be used. Therefore, it is obvious that the control points opposite to each other can only be moved in similar directions, tangential to the symmetry boundary and contrary in the normal direction, see figure 6.5. This procedure implies equal conditions as for the direct imposition of the constraints as direct result of (6.26).

6.3.3 Strategies of mesh refinement

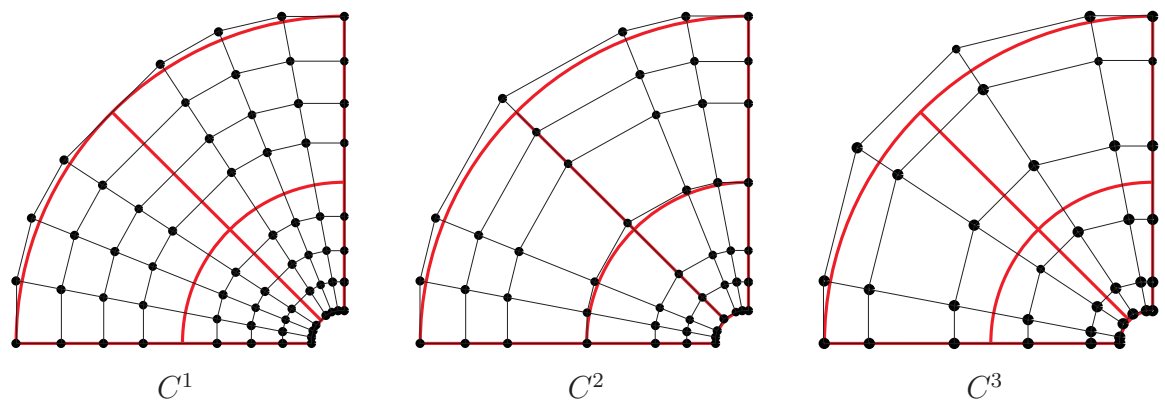


Figure 6.6: Control points and elements for a discretization with 2×2 element with $p = 4$ and different orders of continuity. They are refinement results of a quadratic geometry by (Left:) h -refinement followed by $2 \times p$ -refinement. (Center:) k -refinement followed by p -refinement or p -refinement, followed h -refinement and an additional p -refinement. (Right:) p -refinement followed by k -refinement which is equal to $2 \times p$ -refinement followed by h -refinement.

In contrast to the finite element method, where only p and h refinement is known, within isogeometric analysis three types of refinement can be identified. These are the classical h refinement, performed by the insertion of a knot $\bar{\xi}_*$ into the knot vector \mathbf{T} , i.e. $\mathbf{T}_* = [t_1, \dots, t_l, t_*, t_{l+1}, \dots]$ where $t_l \leq t_* < t_{l+1}$. The B-spline at the knot $\bar{\xi}_*$ is of continuity C^{p-1} . p -refinement is the increase of the polynomial degree of the function. Since the B-spline functions are only of continuity C^{p-k} with k being the multiplicity of the knots, the order

elevation or p -refinement makes an increase of the multiplicity necessary in order to keep the discontinuity at the $p - (k + 1)$ -th derivative. Since the p - and h - refinement strategies are not commutative, the k -refinement is introduced. For the k -refinement, first the p refinement and only then the h -refinement is performed, resulting in the highest possible continuity of the functions. A comparison of different strategies for the discretization of a hollow cylinder segment are presented in figure 6.6.

Remark 6.1 (Increase of continuity) *Even though, the p -refinement increases the polynomial degree, it is not increasing the order of continuity of the shape functions. This is due to the reason that the algorithms have to increase the multiplicity of the knot as well to verify that the span of the original functions is a subset of the span of the refined function. The other direction is possible. By h refinement, the continuity of the geometry can be decreased by the increase of multiplicity of the knots. Therefore, the choice of the initial geometry governs the continuity of the resulting shape functions, used within the Galerkin method for computation of the numerical solution.*

7 Natural Element Method

The natural element method (NEM) is a Galerkin method, whereby the shape functions are solely based on geometry, rather than explicit function representations. It is originated in the field of data interpolation. The original natural element interpolation is the Sibson interpolant, based on the first and second order Voronoi diagram, first presented by Sibson [188] in 1980 and supplemented with the Laplace interpolant by Belikov et. al. [28] not until 1997. The application of the interpolation function to a Galerkin scheme was first accomplished by Braun and Sambridge [47] in 1995. Since then, many improvements have been made to the method. Sukumar was the first to present an extensive investigation of the NEM applied to linear elasticity using the Sibson interpolant [199] and Laplace (non-Sibson) interpolant, [200]. The proof for the applicability to large strain analysis with a high number of degrees of freedom, together with a comparison of NEM and FEM has been presented by Calvo et. al. [53].

Since the NEM in its original form was only suitable for convex domains, several variations for the NEM have been introduced. These are the use of α -shapes [70, 72], the curve-voronoi disk criterion, where the boundary is explicitly represented by the medial axis of the geometry, [13, 71] or the constrained (C-)NEM, where a visibility criterion is introduced [227]. The latter has the advantage of being able to treat cracked domains. Further developments have been the extension of the method to higher continuity of the interpolation functions [94], first applied to the biharmonic equation and plate bending in [198] and applied to gradient elasticity in [99, 177]. Smooth interpolants with C^2 continuity were introduced by Hiyoshi et. al. in [124, 125] and [126] and have been recently applied in an isoparametric setting of the NEM by Gonzalez et al. [114].

A further extension of the natural element method are mixed formulations for the treatment of incompressible materials. The combination of the Sibson interpolant for the approximation of the displacement and Thiessen's interpolant for the pressure approximation, proposed by Sukumar [197] has shown not to satisfy the LBB-condition [49]. In [113], volumetric locking within different combinations of natural element based functions for the approximation of the displacement and the additional pressure field are investigated for the linear elastic case. In [228], the so called *b1-NEM* and *b2-NEM* is introduced, where the displacement is enriched by the introduction of bubble functions. Additional modifications, based on the bubble and Hermite natural neighbor interpolation can be found in [226].

Within the application of the natural element method, there are two problems, not occurring in the finite element method. One is the use of an effective, stable and accurate algorithm for the computation of the shape functions and the other, even more critical aspect, the numerical integration.

In the early works of Sukumar [199], Watson's algorithm [218] is used, failing at points on the Delaunay edges. Gonzalez et. al. [113, 115] have chosen Lasserre's algorithm [150], being especially suitable for the computation of 3d Sibson's interpolant. Detailed investigations of the stability of the computational algorithms are given in [123]. Within this

work, the stable Bowyer-Watson algorithm [44, 217], most efficient for the computation of Laplace's interpolant, has been applied. Many efforts have been made for the development of a stable and accurate integration scheme. In the early works, the Delaunay triangulation, necessary for the computation of the natural element shape functions, has been used for the alignment of the integration points and weight factors, e.g. [72, 198, 199] just to mention a few. More promising are nodal integration schemes, introduced for meshfree-Galerkin method in [55, 56] and adopted to the NEM by Yoo et al. [225]. A comparison of Gaussian integration on the Delaunay tessellation and stabilized nodal integration is given in Gonzalez et al. [115]. There it is demonstrated that integration schemes based on the Delaunay triangles or circle segments are not giving accurate results.

A comprehensive overview and introduction to the natural element method for computational mechanics can be found in [73]. Another overview, more related to data interpolation, but more detailed on higher order interpolants can be found in [37, 40]. An explicit computation of the derivatives of the Sibson interpolant is given in [171].

Additional fields, where natural element functions have been applied are, as already mentioned the data interpolation on highly unstructured data sets, i.e. see Bobach et al. [38, 40] for a comparison of the different possibilities. Due to their linear interpolation property at the boundary of the domain they are ideal shape functions for polygonal elements, extensively used by Sukumar [201] or similar works by Constantiniu et al. [64] and Bobach et al. [39], involving polygonal data interpolation on adaptive Delaunay tessellations.

In this chapter, the aspects of the natural element method, necessary for the application to a Galerkin method are provided. To demonstrate the advantages and disadvantages of the method the first part of this chapter is used for introduction of the C^1 -NEM shape functions. Therefore the underlying concept of Delaunay triangulations and Voronoi diagrams is introduced in section 7.1. This is followed by a brief recapitulation of the C^0 natural neighbor shape functions in section 7.2. The presentation of NEM shape functions is completed by the explanation, how the results of chapter 4 have to be applied to cubic combinations of Sibson's interpolant for the assembly of Farin's C^1 interpolant.

In section 7.4, special aspects, arising within the numerical computations are considered. The first aspect is the extension of the NEM to nonconvex domains, discussed in subsection 7.4.1. This is followed by the introduction of a Voronoi based integration scheme, see subsection 7.4.2. The chapter closes with the introduction of an enrichment of Farin's interpolant by additional bubble functions. Their influence on the performance of the C^1 -NEM is analyzed in subsection 7.4.3.

7.1 Voronoi diagrams and Delaunay tessellations

In this section, the basics for the construction of natural neighbor shape functions are introduced.

Definition 7.1 (Voronoi diagram) *Based on a set of points $\mathcal{N} := \{\mathbf{P}_1, \dots, \mathbf{P}_M\}$, $\mathbf{P}_I \in \mathbb{R}^n$, the Voronoi diagram is the unique subdivision of the space \mathbb{R}^n into M convex cells \mathcal{V}_I , called the Voronoi cells, by the definition,*

$$\mathcal{V}_I := \{\mathbf{X} \in \mathbb{R}^n | d(\mathbf{X}, \mathbf{P}_I) \leq d(\mathbf{X}, \mathbf{P}_J)\}. \quad (7.1)$$

This means a separation of \mathbb{R}^n into the sets of points, which are closer to the point \mathbf{P}_I than to any other point $\mathbf{P}_J \in \mathcal{N}$. The fragmentation for a set of nine points is illustrated in figure 7.1(b). In the following, we always assume that the Euclidean distance is used, but any distance function is possible. Especially for the application of periodic boundary conditions within the C^1 NEM, the modified distance on the space $\mathbb{R}/l_1\mathbb{R} \times \mathbb{R}/l_2\mathbb{R}$ for a periodic box of width l_1 and height l_2 is defined by

$$d(\mathbf{x}, \mathbf{y}) := \left[\sum_i [\min \{ |x_i - y_i|, l_i - |x_i - y_i| \}]^2 \right]^{\frac{1}{2}}, \quad (7.2)$$

resulting in a periodic subdivision of the box $[0, l_1] \times [0, l_2]$.

Definition 7.2 (Delaunay triangulation) A triangulation \mathcal{T} of the point set \mathcal{N} is called Delaunay triangulation, if the open (in the sense of an open set) circumcircles of the triangles contains none of the points $\mathbf{P}_I \in \mathcal{N}$, compare to figure 7.1(c).

The Delaunay triangulation is the triangulation with the largest minimum angle of any possible triangulation of \mathcal{N} . The Voronoi diagram and Delaunay triangulation are dual pairs, i.e. vertices of the Voronoi cells are the circumcenters of the Delaunay triangles. Additionally, the connection of the points \mathbf{P}_I and \mathbf{P}_J of two neighboring Voronoi cells are the edges of the Delaunay triangles.

Therefore, if the Delaunay triangulation is unique, it can be constructed by the connection of each pair of natural neighbors, defined by the following relation:

Definition 7.3 (Natural neighbors:) Two points \mathbf{P}_I and $\mathbf{P}_J \in \mathcal{N}$ are called natural neighbors, if $\mathcal{V}_I \cap \mathcal{V}_J \neq \emptyset$.

The uniqueness is related to the intersection of the Voronoi cells \mathcal{V}_I . If the non empty intersections include more than one point, the Delaunay triangulation is unique. The non-uniqueness states that at least two Delaunay triangles share the same circumcircle.

7.2 C^0 natural neighbor functions

In this section, the principle for the construction of the shape functions is briefly explained. The three basic interpolations are the Thiessen, the Laplace and the Sibson interpolants. Even though the Thiessen and Laplace interpolants will not be used further, they are recapitulated briefly for sake of completeness. The C^0 natural neighbor interpolants N_I are defined on the convex hull of \mathcal{N} , denoted as

$$\mathcal{B} := \text{conv}(\mathcal{N}), \quad (7.3)$$

which are all points in the set

$$\text{conv}(\mathcal{N}) := \{ \mathbf{X} | \mathbf{X} = \sum_{I=1}^M \lambda_I \mathbf{P}_I \text{ with } 0 \leq \lambda_I \leq 1 \}. \quad (7.4)$$

All interpolants have the following desirable properties:

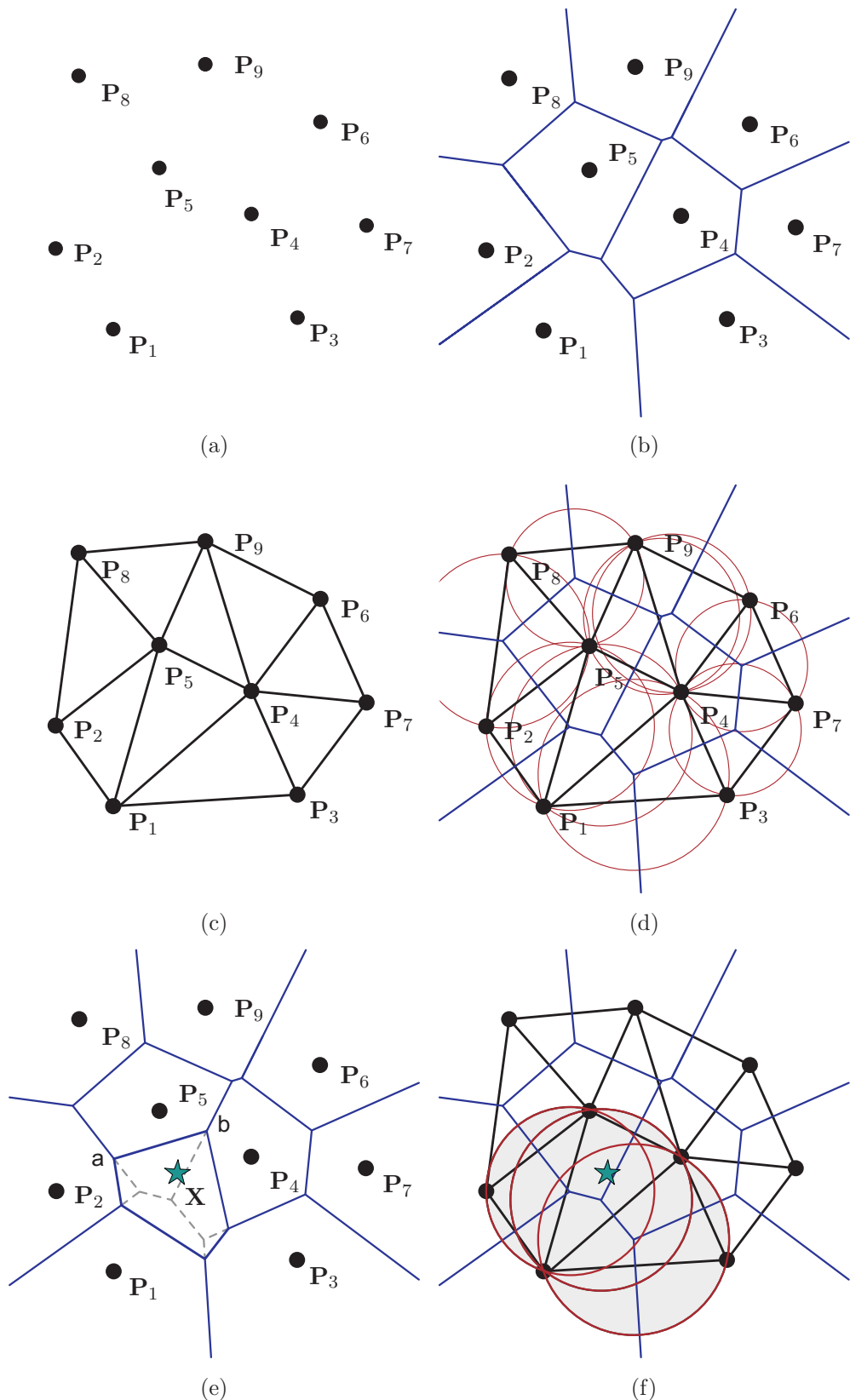


Figure 7.1: (a): Original set of points, (b): Voronoi diagram, (c): Delaunay triangulation, (d): Voronoi diagram, Delaunay triangulation and circumcircles, (e): Voronoi diagram of \bar{N} and (f): Natural neighbors of the point X .

- interpolation at the data site: $N_I(\mathbf{P}_J) = \delta_{IJ}$,
- non-negativity: $N_I(\mathbf{X}) \geq 0$ and
- partition of unity: $\sum_{I=1}^M N_I(\mathbf{X}) = 1$.

Apart from the Thiessen interpolant which is C^{-1} , the original natural neighbor interpolants are based on the following principle:

If the interpolation functions at the point $\mathbf{X} \in \mathcal{B}$ are to be evaluated, a new set of points $\bar{\mathcal{N}} := \mathcal{N} \cup \mathbf{X}$ is introduced. $\bar{\mathcal{V}}_J$ are the Voronoi cells of the new point set, see figure 7.1(e). The circumcircles of the Delaunay triangulation indicate, if the new point \mathbf{X} affects the original Voronoi cells, i.e. whether $\mathcal{V}_I = \bar{\mathcal{V}}_I$. It is changed, if \mathbf{X} lies within one of the circumcircles of the Delaunay triangles, including \mathbf{P}_I , compare to figure 7.1(f).

7.2.1 Thiessens interpolant

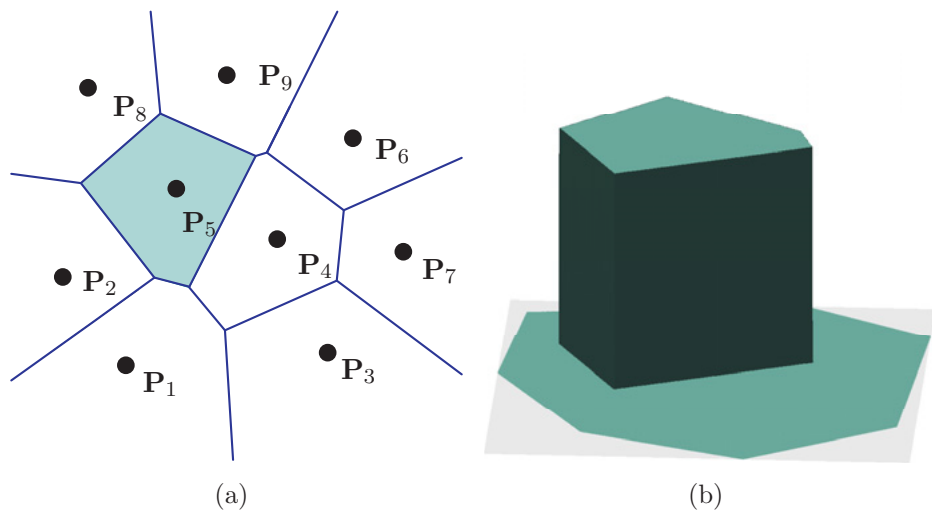


Figure 7.2: Thiessens interpolant: (a) Support of the interpolation function, (b) Interpolation function T_5 .

The Thiessens interpolant T_I is the simplest of all natural neighbor interpolants. The value of the function $T_I(\mathbf{X})$ is defined by simply deciding, whether the point is inside the Voronoi cell \mathcal{V}_I or not.

$$T_I(\mathbf{X}) := \begin{cases} 1 & \text{for } \mathbf{X} \in \mathcal{V}_I \\ 0 & \text{else.} \end{cases} \quad (7.5)$$

It has continuity C^{-1} and its major application to computational mechanics is for the approximation of an additional pressure field for mixed displacement pressure interpolation.

7.2.2 Laplace interpolant

Considering a point $\mathbf{X} \in \mathcal{B}$, the Laplace interpolant is solely based on the new Voronoi cell $\bar{\mathcal{V}}_X$ and the natural neighbors of \mathbf{X} . To derive the Laplace interpolant of the site \mathbf{P}_I

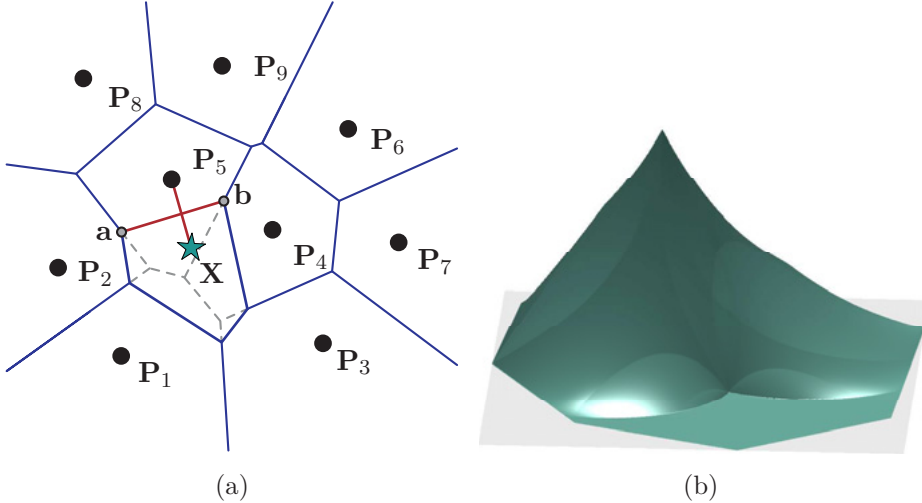


Figure 7.3: (a) Voronoi diagram and intersection of the Voronoi cells $\bar{\mathcal{V}}_5$ and $\bar{\mathcal{V}}_X$. (b) Interpolation function L_I .

at the point \mathbf{X} the quantities

$$\tilde{L}_I := \frac{A(\bar{\mathcal{V}}_I \cap \bar{\mathcal{V}}_X)}{d(\mathbf{P}_I, \mathbf{X})}, \quad (7.6)$$

are necessary for the construction of the shape functions. In (7.6), A denotes the $n - 1$ -dimensional size of the intersection of the Voronoi cells. This is equivalent to the length $d(\mathbf{a}, \mathbf{b})$, compare to figure 7.3.

The interpolation and partition of unity property is achieved by dividing \tilde{L}_I by the sum of all \tilde{L}_J ,

$$L_I(\mathbf{X}) := \frac{\tilde{L}_I(\mathbf{X})}{\sum_{J=1}^L \tilde{L}_J}. \quad (7.7)$$

It is C^∞ everywhere apart from the boundaries of the circumcircles of the Delaunay triangles.

7.2.3 Sibson interpolant

The last interpolation method considered in this context is the Sibson interpolant. It is the original method for the computation of the Voronoi diagram based shape functions. Again consider the new set $\bar{\mathcal{N}} := \mathcal{N} \cup \mathbf{X}$, where $\mathbf{X} \in \text{conv}(\mathbf{N})$ and $\bar{\mathcal{V}}_1, \dots, \bar{\mathcal{V}}_L$ and $\bar{\mathcal{V}}_X$ the Voronoi cells, the Sibson interpolant is defined by

$$S_I(\mathbf{X}) := \frac{A(\mathcal{V}_I \cap \bar{\mathcal{V}}_X)}{A(\bar{\mathcal{V}}_X)}. \quad (7.8)$$

Continuity of Sibson's interpolant: The support of Sibson's interpolant S_I is the union of all circumcircles of the Delaunay triangles T_J , including \mathbf{P}_I . It is of continuity C^∞ everywhere apart from the boundaries of the domains. There it is only C^1 and C^0 at the sites $\mathbf{P}_K \in \mathcal{N}$.

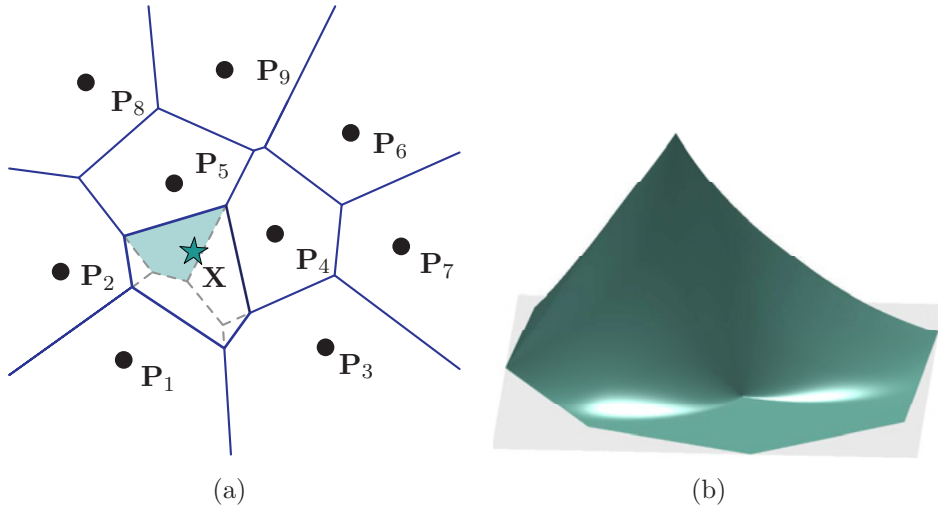


Figure 7.4: (a) Overlap of the original Voronoi cell \mathcal{V}_5 and $\bar{\mathcal{V}}_X$. (b) Sibson interpolant S_5 .

Remark 7.1 (Interpolation at the boundary of the convex hull) The Laplace and Sibson shape function, are only defined at the interior of the convex hull \mathcal{N} . This is due to the fact that only for interior points the Voronoi cell $\bar{\mathcal{V}}_X$ is a bounded subset of \mathbb{R}^n . Otherwise, the numerator of (7.6) and (7.7) or (7.8) would be equal to infinity. However, it makes sense to define the value at a point X_b on the boundary by

$$\mathbf{S}_I(\mathbf{X}_b) := \lim_{\mathbf{X}_n \rightarrow \mathbf{X}_b} S_I(\mathbf{X}_n). \quad (7.9)$$

The same is valid for the Laplace interpolant $L_I(\mathbf{X}_b)$.

Remark 7.2 (Alternative description of Sibson interpolant) An alternative description of the Sibson interpolant is accomplished by introducing the second order Voronoi diagram of $\bar{\mathcal{N}}$,

$$\bar{\mathcal{V}}_{IJ} := \{\mathbf{X} \in \mathbb{R}^d : d(\mathbf{X}, \mathbf{P}_I) \leq d(\mathbf{X}, \mathbf{P}_J) \leq d(\mathbf{X}, \mathbf{P}_K), J \neq I \neq K\}. \quad (7.10)$$

Now, the Sibson interpolant is given by:

$$S_I = \frac{A(\bar{\mathcal{V}}_{\mathbf{X}I})}{A(\bigcup_J \bar{\mathcal{V}}_{\mathbf{X}J})} \quad (7.11)$$

7.3 C^1 natural neighbor functions

The first method, introduced to construct C^1 continuous function, based on the Sibson's natural neighbor interpolant is due to Sibson [188]. Unfortunately, it is not suited for application to computational mechanics, since the smooth interpolation is related to the data points but an explicit expression of interpolating functions can not be extracted. To design C^1 continuous natural neighbor interpolations, applicable to Galerkin methods, at least two alternatives exist. One approach introduced by Farin [94] is embedding the smooth Sibson's interpolant into a Bernstein-Bézier patch. This technique works only with

the use of Sibson's interpolant due to the necessity of C^1 continuity anywhere, apart from the nodes. Additionally, since the underlying principle is the smoothing of the interpolant at the nodal points, it is not suitable for smoothing the functions at the boundary of the support and thus, only C^1 continuity is possible. Another approach, introduced by Hioshi and Sugihara [124, 125] makes use of power Voronoi diagrams, being able of smoothing the function anywhere, not only at the nodes. With this method it is even possible to construct functions of order C^2 and higher.

In this text, Farin's method has been selected since its principles are closely related to the subparametric C^* and C^1 continuous finite elements, introduced in sections 5.2 and 5.3.

7.3.1 Farin's C^1 interpolant

Farin's interpolant utilizes of the fact that natural neighbor shape functions can be considered as generalized barycentric coordinates. Considering a point $\mathbf{X} \in \mathcal{B}_0$ with m nonzero natural neighbor interpolants, $\Lambda = (\lambda_1, \dots, \lambda_m)$, compare figure 7.5(a). These nonzero in-

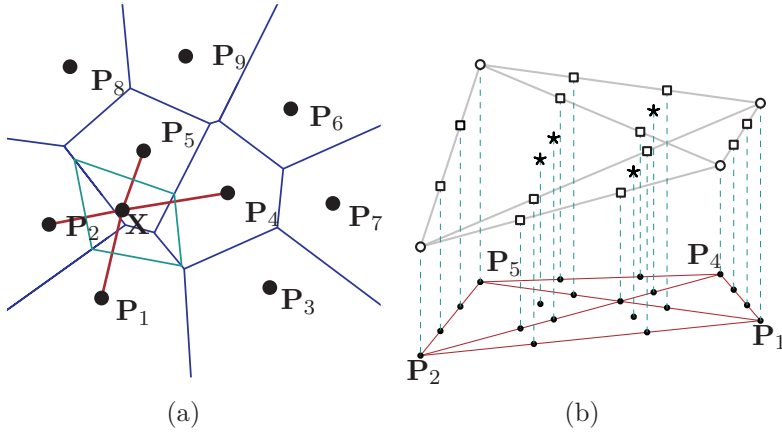


Figure 7.5: (a): Local neighbors of the point X ; (b): The Sibson's interpolant, considered as projection of the 3d space to the plane.

terpolation functions are regarded to be barycentric coordinates of an $m - 1$ -dimensional simplex, see figure 7.5(b). By embedding the natural neighbor interpolants in a cubic Bernstein-Bézier polynomial,

$$\bar{F} = \sum_{|\alpha|=3} b_\alpha \mathbf{B}_\alpha(\Lambda), \quad (7.12)$$

the results of chapter 4 can be used. To obtain the prescribed function and derivative values at the nodes, the Bézier ordinates b_α are defined recursively. The ordinates $\{b_\alpha | \max(\alpha) = 3\}$, marked by \circ in figure 7.5(b) are defined by the function values at the vertices. The Bézier ordinates denoted by \square , $\{b_\alpha | \max(\alpha) = 2\}$ are uniquely defined by the prescribed derivatives in the direction of the vertices of the simplex.

The remaining Bézier ordinates

$$\{b_\alpha | \max \alpha = 1\} \quad (7.13)$$

are neither influencing the function values at the vertices nor contribute to the vertex derivatives. They are related to the vertex values such that the resulting functions fulfills the property of quadratic completeness¹. Finally, the C^1 NEM shape functions are

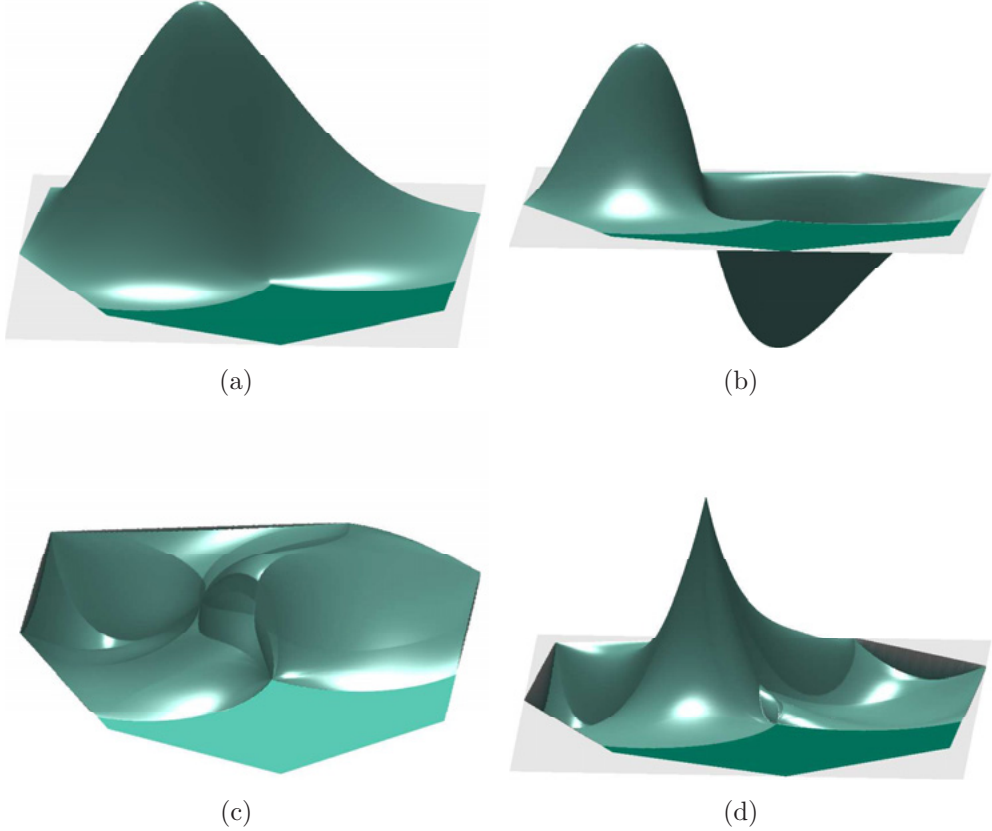


Figure 7.6: Sibsons interpolant (a) $N_5(\mathbf{X})$, (b) $(\mathbf{M}_5)_2(\mathbf{X})$ and the derivatives with respect to X_2 . (c) $\partial_{X_2}N_4(\mathbf{X})$ and (d) $\partial_{X_2}(\mathbf{M}_5)_2(\mathbf{X})$.

expressed by the following combination of the cubic Bézier polynomial of the Sibson's interpolant by

$$N^I(\mathbf{X}) = [\Lambda^I]^3 + \sum_{\alpha_I^2} B_{\alpha}(\Lambda) + \frac{1}{3} \sum_{\alpha_I^1} B_{\alpha}(\Lambda) \quad (7.14)$$

$$\mathbf{M}^I(\mathbf{X}) = \sum_{\alpha_I^2} [\mathbf{P}_J - \mathbf{P}_I] B_{\alpha}(\Lambda) + \frac{1}{4} \sum_{\alpha_I^1} [\mathbf{P}_J + \mathbf{P}_K - 2\mathbf{P}_I] B_{\alpha}(\Lambda) \quad (7.15)$$

where the following definition is used $\alpha_I^k := \{\alpha : \alpha_I = k \text{ and } \max_{J \neq I}(\alpha_J) = 1\}$.

¹Quadratic completeness means that the natural neighbor interpolation function reproduces any given quadratic function exactly, by prescribing the interpolation values at the nodal points.

7.4 Application of the natural element method to gradient elasticity

At this point, any of the natural neighbor functions can be used for the approximation of the discrete displacement introduced in section 3.2 for the solution of the elasticity problem, see section 3.3. Farin's C^1 interpolant can additionally be applied to the discrete equations of gradient elasticity as defined in section 3.4. The advantage of the C^1 NEM is that the degrees of freedom are restricted to the field values and their first derivatives at each node. No additional edge normal derivatives or second order derivatives are needed to obtain C^1 continuity. Yet the drawback of the NEM is its high computational cost for the construction of the shape functions. The identification of the shape functions at each point of calculation as well as the construction and derivation of the different areas is more expensive than the evaluation of polynomials within the finite element method. Further aspects, necessary to be explained the method in more details, are discussed in the following subsections. In general the natural element functions are defined on the convex hull of the point set \mathcal{N} and thus without further extensions, it would only be applicable to convex domains. Therefore, in section 7.4.1, α -shapes are introduced. Further difficulties are arising within the integration of the discretized equations, necessary for the computation of the residual vectors and the stiffness matrix. A description of the problem and a comparison of two different alternatives are presented in subsection 7.4.2. The current section on the application of the natural element method to gradient elasticity closes with a discussion of a possible enrichment of Farin's C^1 interpolant in subsection 7.4.3.

7.4.1 α -shapes for non-convex domains

One problem for the natural element method is that its shape functions are defined on the convex hull of the domain. Simply removing parts of the convex hull of the set \mathcal{N} after the shape function construction is not suitable for two reasons. In the first place, the natural element functions would loose their linear interpolatory character along the boundary and second, it is possible that the shape functions related to nodes opposing a gap in the geometry are influencing the displacement at the opposing side, leading to false results of the computation. There are at least three different methods to treat non-convex domains. Within this contribution, the α -shape method has been chosen.

The α -shape method is based on using a subset of the Delaunay-triangulation for the construction of the shape functions. Its introduction to the natural element method is due to Cueto et al. [70].

If the Boyer-Watson algorithm [44, 217] is applied, the construction of the NEM shape functions is solely related to the Delaunay tessellation. The principle of the α -shapes is that only a subset of the Delaunay triangulation is considered within the algorithm. The major advantage is that the method is easily implemented. Furthermore, if the used subset of the Delaunay tessellation is given by the restriction of the maximal size of the circumcircles, the linear interpolation at the boundary of the domain is remaining.

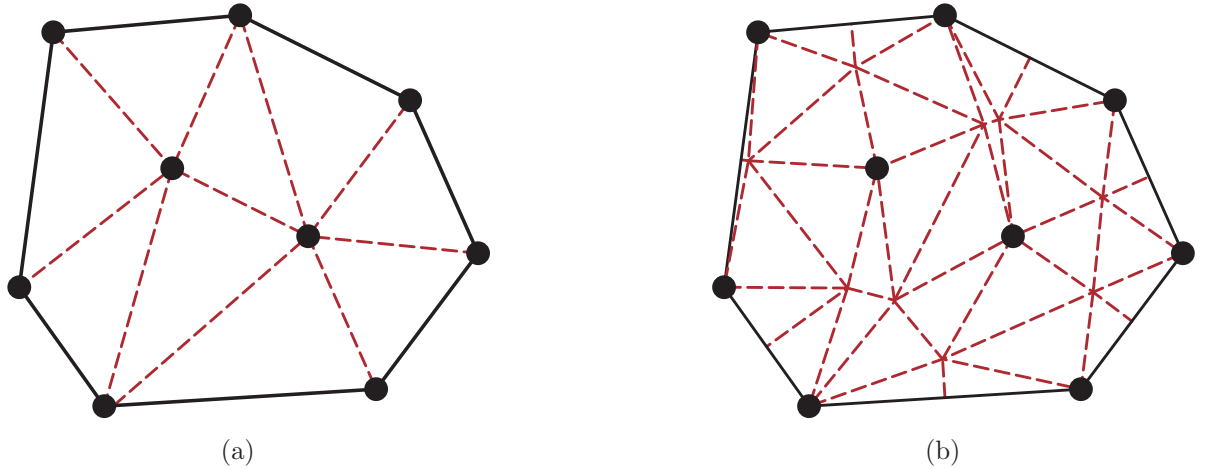


Figure 7.7: (a): The Delaunay triangulation, often used for numerical integration. (b): New triangulation of the domain based on the Voronoi cells and the data points.

7.4.2 Numerical integration

For the numerical integration of the shape functions, Gauss integration on the Delaunay triangulation, see figure 7.7(a) or 7.8(a), is not a sufficient procedure for the treatment of natural neighbor interpolants. A simple example for the insufficiency of the procedure is given by the application to a hollow cylinder under external pressure. The geometry, boundary conditions and material parameters are equal to those of subsection 8.1.2. Figure 7.9 (left) displays the displacement error of the Delaunay based integration. It is visible that for a uniform distribution of the interpolation points, the computation provides non-symmetric results. This effect can only be explained by the non-symmetric intersection of the domain into integration cells, caused by the non uniqueness of the Delaunay triangulation. In the figure 7.9 (right), the Voronoi cell based integration is used. Therefore the Voronoi cells \mathcal{V}_I are separated into triangles, by the connection of the edges of a cell \mathcal{V}_I to the corresponding point $\mathbf{X}_I \in \mathcal{N}$, compare to figure 7.7(b) and 7.8(b). In contrast to the Delaunay triangulation, the Voronoi cells are always unique and therefore, by the symmetry of the point set, it follows, that the distribution of the integration triangles is symmetric as well.

7.4.3 Additional bubble functions

Within this subsection, the influence of an enrichment of Farin's interpolant by additional bubble functions degrees of freedom is investigated. Within the description of Farin's interpolant (7.14), the bubble functions are the functions denoted by B_α with $\alpha \in \alpha_I^1$. As already mentioned in subsection 7.3.1, they neither influence the primal function value at any node I , nor the derivative values at this node. Due to this property, additional degrees of freedom related to the bubble functions are not wanted within the original purpose of data interpolation. Therefore, those components are directly related to the nodal values by the objective of quadratic completeness. Yet, in the field of computational mechanics, the condensation of additional degrees of freedom can impair the performance

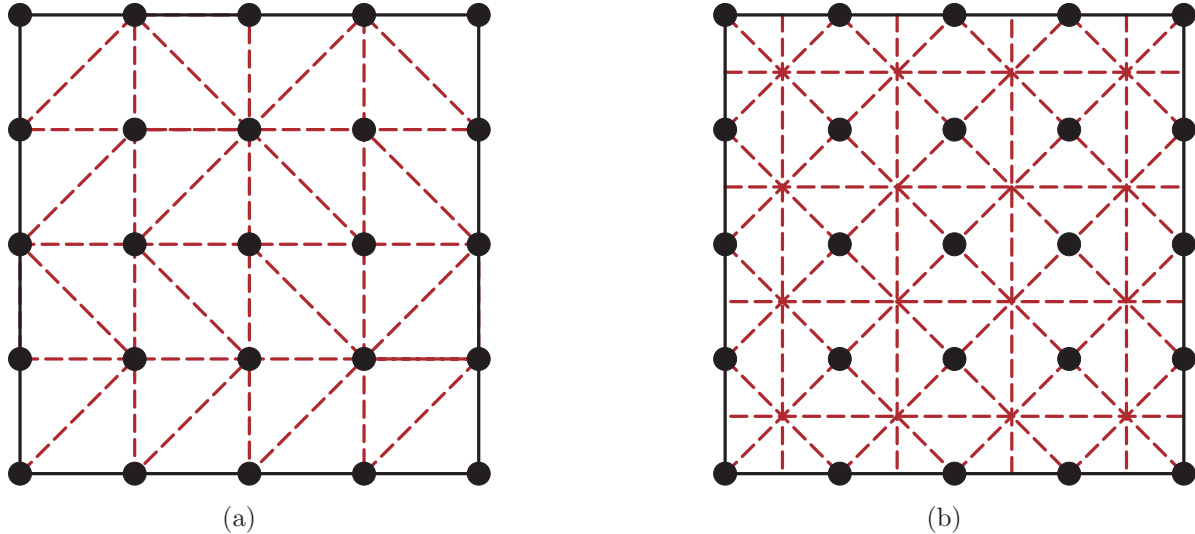


Figure 7.8: (a): The Delaunay triangulation, often used for numerical integration. (b): New triangulation of the domain based on the Voronoi cells and the data points.

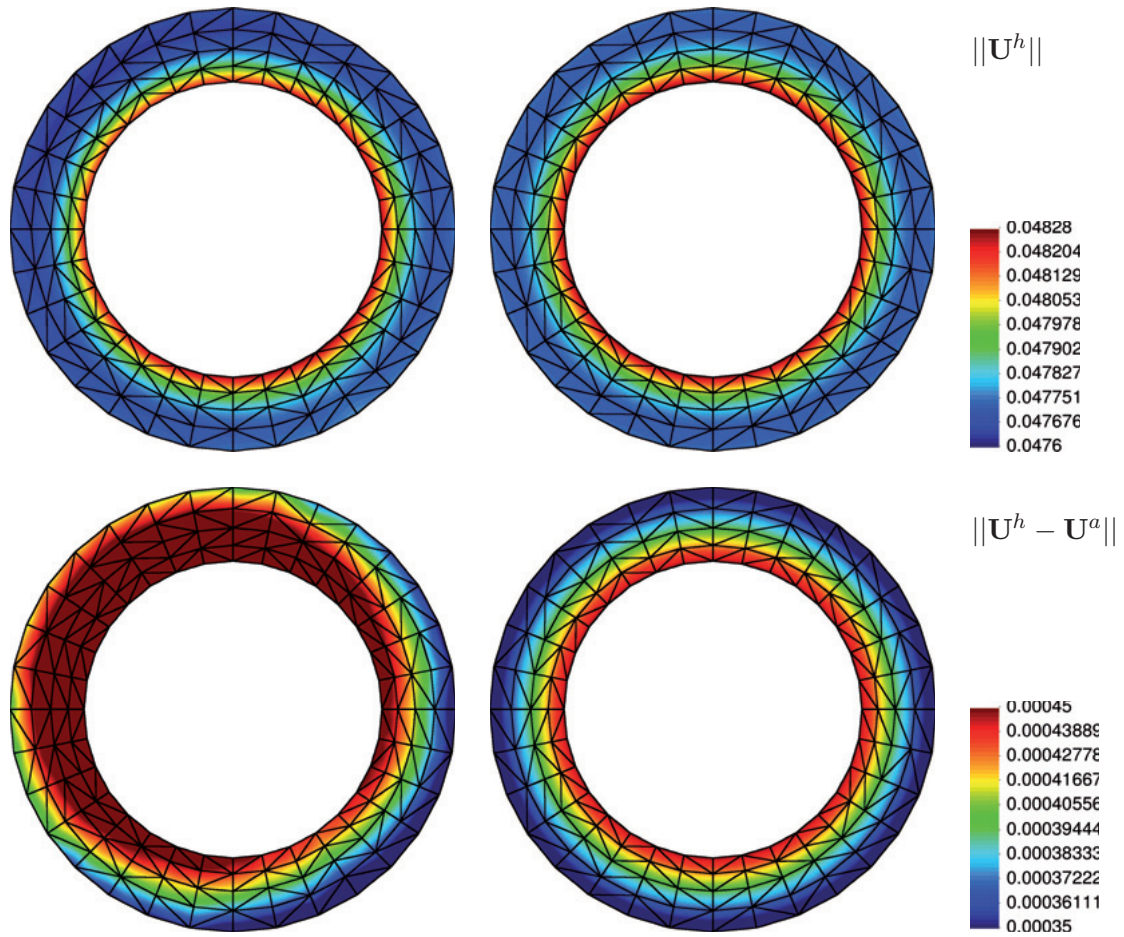


Figure 7.9: Error distribution, cased by the two different integration schemes. In contrast to the Delaunay based results (left), the Voronoi based integration preserves the symmetry of the results (right).

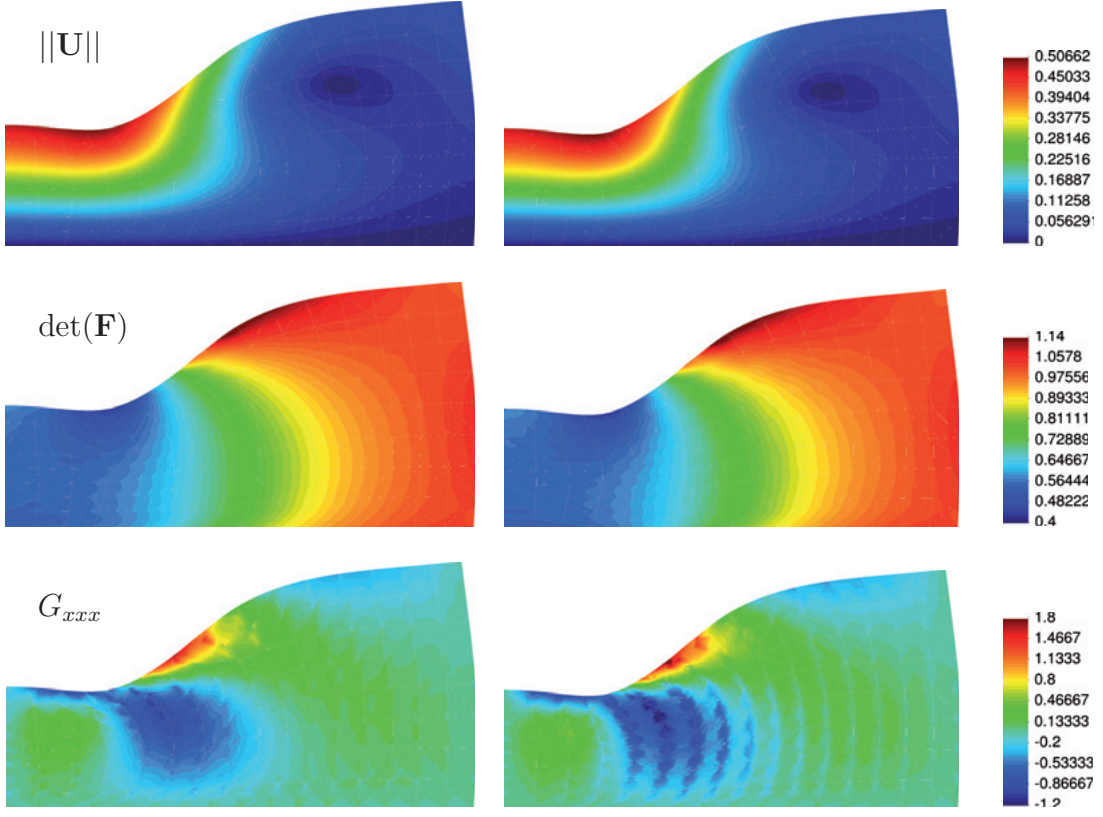


Figure 7.10: Contour plot of selected values of the inhomogeneous compression test. Left: Values computed with C^1 NEM without bubble functions. Right. Values computed with C^1 NEM and bubble functions, $a = 0.5$.

of a method. In [98] as well as chapter 8 the HCT element in its complete form is compared to its reduced form. Motivated by the superior behavior of the HCT element in its complete form, the influence of the introduction of additional bubble function degrees of freedom on the quality of the solution is investigated at this point. Since the H^1 and H^2 norms of these additional functions are possibly very small, we introduce a measure, explaining whether a bubble function B_α , $\alpha \in \alpha_I^1$ is included.

The bubble functions are all functions, given by the product $6S_ISJS_K$, $I \neq J \neq K \neq I$ with S_\circ the Sibson interpolants. Here a condition is used which is linked to the support of the Sibson interpolant. The first restriction is to claim that at least two points, $\mathbf{X}_I \neq \mathbf{X}_J \in \mathcal{N}$ are natural neighbors. Let us denote the common Delaunay triangles by T_a and T_b , \mathbf{c}_a , r_a and \mathbf{c}_b , r_b the corresponding circumcenters and circumcircle radii. We state that the additional degree of freedom of the product $6S_ISJS_K$ is used if there exists a Delaunay triangle T_c , including \mathbf{X}_K with

$$\min_{i \in \{a,b\}} (d(\mathbf{c}_i, \mathbf{c}_c) - 0.5[r_i + r_c]) \leq 0. \quad (7.16)$$

In figure 7.10, the contour plots of selected results for the inhomogeneous compression test are compared for the classical Farin's interpolant and the enriched approximation scheme. The geometry and material parameters are coinciding with those of the inhomogeneous

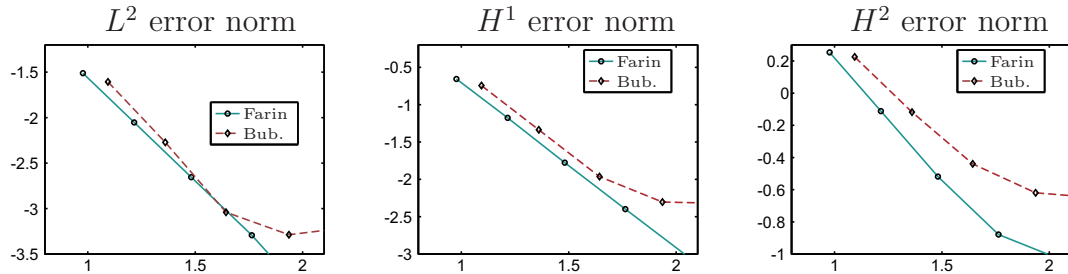


Figure 7.11: Convergence rates for the Farin's interpolant and the C^1 NEM with additional bubble function. The diagrams are logarithmic, showing the error with respect to the total number of degrees of freedom.

compression test in subsection 8.2.1. Even so the error is slightly better for the same number of nodes it is not better for the same number of degrees of freedom. Thus, the additional degrees of freedom are not worth consideration, see figure 7.11. The strange behavior at the end of the curves is due to errors in numerical integration. Especially for the method, where additional degrees of freedom are incorporated, improved integration schemes are necessary. Here a 16 point scheme as described in Lyness and Jespersen [151] has been applied on the Voronoi cell based triangulation as presented in subsection 7.4.2.

8 Computational examples for gradient elasticity

In the field of computational analysis of gradient continua, only little work has been done for a systematic comparison of the performance of different numerical methods. Some exceptions are the work of Xia and Hutchinson [224], where different non-conforming C^* elements have been applied to the numerical treatment of gradient plasticity at crack-tip fields. Up to our knowledge, systematic comparisons can only be found in the [234] where the maximal displacement and strain errors for the C^1 continuous Bell and isoparametric BFS element are compared to different mixed finite element formulations. The only extension to three dimensions is found in [167], where the three dimensional BFS element is used. This chapter is mainly based on the results, presented in the following publications [96, 97, 99] and [98] and gives a systematic comparison for a large variety of different C^1 continuous approximation schemes. These are the comparison of the finite elements, presented in chapter 5 as well as the isogeometric analysis, introduced in chapter 6 and the natural element method, see chapter 7. For a qualified judgment of the results, the rates of convergence within the relevant L^2 , H^1 and H^2 error norms¹ are computed. Within the first sections, involving linear gradient elasticity, the computation of the error norms is based on an analytical solution. For the numerical analysis, carried out in section 8.2, the error norms are based on a numerical reference solution.

A numerical reference solution is almost never exact and thus some part of the computed error is caused by the reference solution. Unfortunately, it is not possible to know exactly, how much of the error is a result of the numerical reference solution and which part is caused by the coarser mesh. During this work, at least two indicators have been identified to judge if an insufficient numerical reference solution significantly influences the error norms. Our first indicator is to use the contour plot of the difference between the local and reference field variables. Usually, within these plots, the coarse mesh is recognizable by the error distribution, but no hint on the reference mesh can be observed. If this is not the case anymore, something is wrong with the reference solution.

The second error indicator relies on regular meshes with nested homogeneous mesh refinement. Therefore the convergence diagrams in the double logarithmic representation are observed to be very close to a straight line. This is the case, as long as the reference solution is much closer to the analytic solution than to the coarse solutions in the convergence diagrams. If this is not the case anymore, changes within the rates of convergence were observed. Results, for which we could identify one of the above mentioned indicators, have been sorted out and the reference solution has been replaced by a more accurate one. A similar result to the second indicator is obtained if numerical inaccuracies (e.g. calculation of shape functions, numerical integration) prevent further convergence. Fortunately, we could differentiate between a bad reference solution and the range of accuracy of the numerical scheme by the fact that for the wrong reference solution, the error first

¹The interested reader is referred to [9] for a detailed description of the underlying fundamentals of functional analysis.

decreases and then increases again, if further mesh refinement is applied. In contrast to that observation, the error remains constant under further mesh refinement, if the limit of accuracy of the numerical scheme is reached.

This chapter is separated into two parts. In the first part (section 8.1) linear gradient elasticity is treated. Therefore, in a first example, the effect of the internal length scale is presented. In the second example, the thick hollow cylinder (THC) problem is treated. The THC example is chosen, since here an analytical solution exists [234]. In the second part of the chapter, three different numerical examples have been investigated in a finite strain framework, see section 8.2.

8.1 Linear gradient elasticity

8.1.1 L-shaped domain

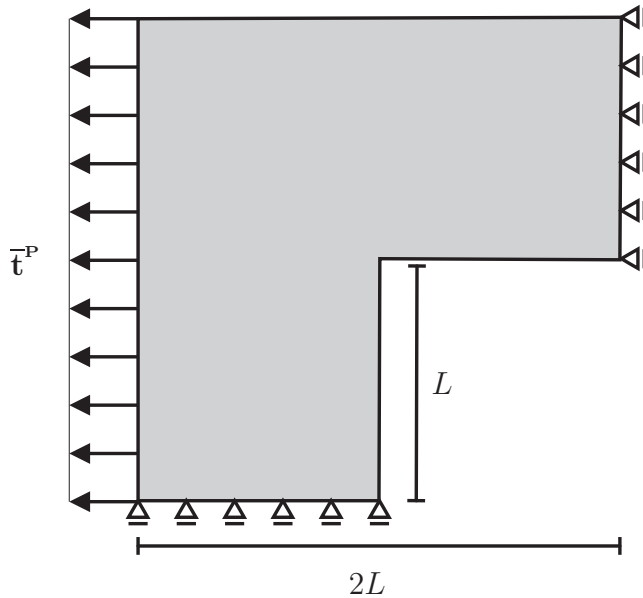


Figure 8.1: Geometry and loading description for the L-shaped domain.

The L-shape domain example was chosen due to several reasons. At first, it is an optimal example to analyze the influence of the internal length scale. Furthermore, the combination of several patches in gradient elasticity is demonstrated.

For the numerical computation, the isogeometric analysis is used. The geometry is composed of three quadratical patches, which are combined C^1 continuously as described in subsection 6.2.3. Each patch is uniformly separated into 10×10 elements and the cubic B-splines involved in the computation have C^2 continuity inside the patch.

For the computation, the Lamé parameters $\lambda = 7000$ and $\mu = 3000$, together with the four values (a): $l = 10L$, (b): $l = 5/16L$, (c) $l = 5/32768L$ and (d) $l = 0L$ are used for

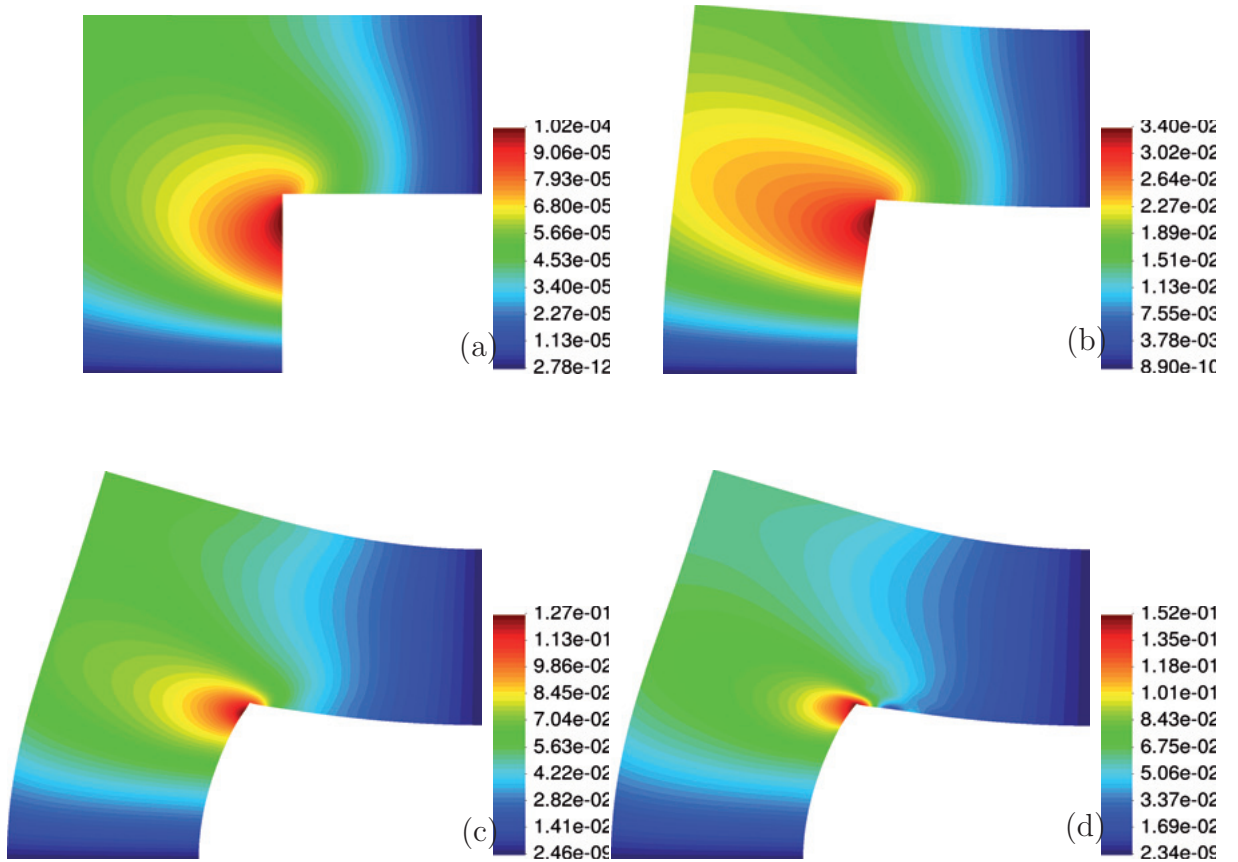


Figure 8.2: Local distribution of ϵ_{xy} , for different values of the internal length parameter. (a): $l = 10L$, (b): $l = 5/16L$, (c) $l = 5/32768$ and (d) $l = 0$. The deformation is multiplied by the factor 5.

the linear gradient elastic model with $a_2 = \frac{1}{2}l^2\lambda$ and $a_4 = l^2\mu$.

The geometry and loading description for the L-shaped domain are presented in figure 8.1. The value of the surface tension is $\bar{\tau}^P = -100$.

In figure 8.2, the values of ϵ_{xy} are presented. First of all, the values are continuous and thus, we can state that the connection of the three patches is working. Furthermore, the smoothing of the strains, caused by the application of gradient elasticity is nicely visible. Within the limit case for $l \rightarrow \infty$ a completely homogeneous strain state would be achieved.

The second figure 8.3 demonstrates the distribution of the strain gradient component κ_{xyx} . The jump of the strain gradients due to the restriction to C^1 continuity at the boundary of the patches is nicely visible. Furthermore, for the low values of the internal length scale l , the value of the strain gradient is strongly localizing.

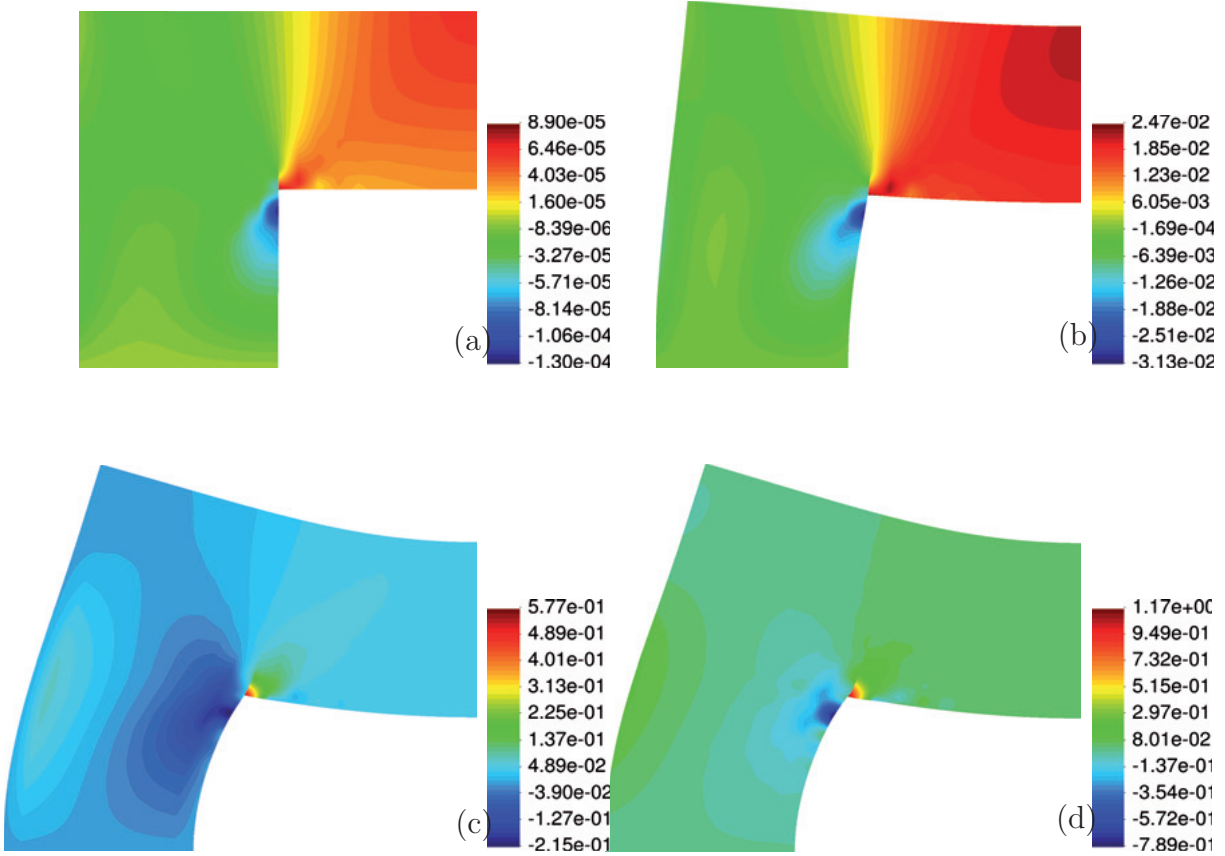


Figure 8.3: Local distribution of the strain gradient component κ_{xyx} , for different values of the internal length parameter. (a): $l = 10L$, (b): $l = 5/16L$, (c) $l = 5/32768$ and (d) $l = 0$. The deformation is multiplied by the factor 5.

8.1.2 Thick hollow cylinder under external pressure

In order to make a qualified judgment on the performance and applicability of a numerical method, it is inevitable to compare the numerical result to an analytical solution. One possibility for the application of gradient elasticity is the thick hollow cylinder example, presented in Zervos et al. [234]. Due to the complicated structure of the analytical solution, it is not rewritten at this place. A brief description of the geometry and boundary conditions is given in figure 8.4. In our first investigation, the linear elastic model as presented in subsection 2.5 with the material parameters $E = 10.000$ and $\mu = 0.3$, together with $a_4 = l^2\mu$, $l = 0.1$ is chosen. The values a_i for $i \neq 4$ are set to zero. A boundary pressure of $\bar{\mathbf{t}}^P = 2000$ is applied.

In the first comparison of the numerical methods, the subparametric elements are used. Therein it can be demonstrated that the linear geometry approximation is leading to severe restrictions of the convergence of the elements. At first, a linear interpolation of the boundary is used, see figure 8.5, (right). The convergence results for this type of approximation are presented in the first row of diagrams in figure 8.6. It can be observed that there is no visible difference for any of the elements. This fact is not coinciding with our expected result, claiming that a higher polynomial order of the (quintic) Argyris element would show superior results to the (quadratic) Powell-Sabin 12-split element. This is only

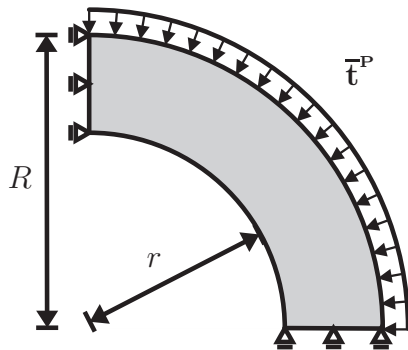


Figure 8.4: Geometry of the thick hollow cylinder example. The external loading is the constant pressure on the outer boundary. Symmetry boundary conditions are used.

the case for the H^2 error norm, but similar results would be expected for the L^2 and H^1 norms as well. There are two possibilities to explain this result. Either the continuity of the weak solution is restricted, and therefore, the assumptions for an optimal convergence are violated or the effect is caused by the poor approximation of the boundary. Due to the C^∞ structure of the analytical solution only the latter can be taken into account for the explanation of this effect.

Since the whole finite element method is based on the least square fit of the discrete numerical solution to the real analytical solution, a least square fit should be considered for the approximation at the boundary as well. Here, due to the special geometry, an area preserving approximation of the cylinder is considered. Therefore, the nodal positions at the boundary are placed such that the area within the linear polygon is equal to the area of the circle, which should be approximated. The linear approximation is illustrated in figure 8.5, (left). Dramatically different rates of convergence can be investigated in the diagrams, presented in the bottom row of figure 8.6. Within those new results, all conforming elements show better results than for the linear interpolation in both, the rates of convergence and the level of the absolute error. Only the Morley element shows better results for the linear interpolation together with similar rates of convergence.

In figure 8.7, the convergence diagrams for the linear subparametric elements, presented in chapter 5 are combined. This result is supplemented with a tabular of the rates of convergence, computed by a least square fit to the diagrams in table 8.1.

Within those results, there are at least three aspects worth mentioning. Not really surprising is the result that neither the Hermite triangle nor the PS-6 (C^0) element are really suitable for the application to strain gradient continua. Additionally it is interesting to investigate the result of the reduced forms of the Argyris, HCT and PS-12 elements. While the result for the reduced HCT element is dramatically inferior to the original element, the reduced form of the PS-12 element is only slightly different when compared to the total number of degrees of freedom. But due to the lower number of integration points for the same number of degree of freedom, in practice, it is better than the reduced ver-

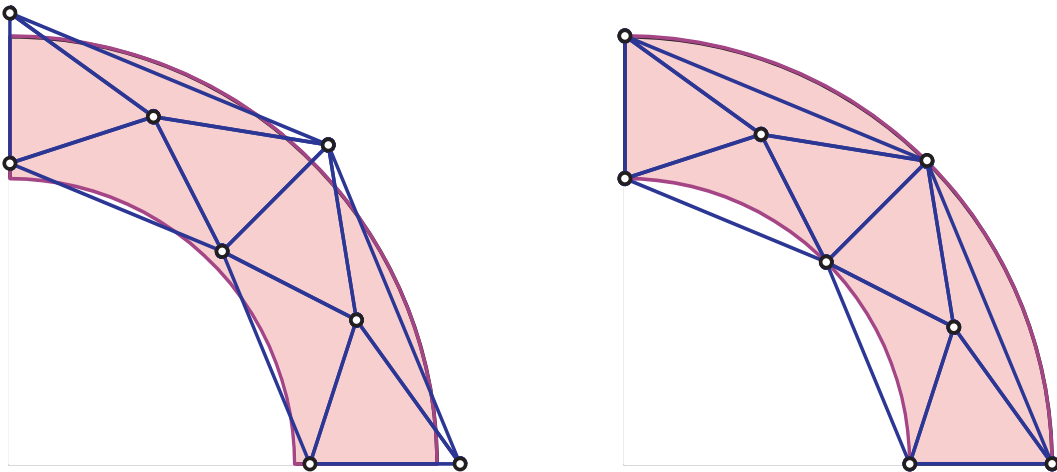


Figure 8.5: Two possible linear approximations of the boundary. (Left): Area preserving approximation of the boundary and (Right): Linear interpolation

sion. Within the comparison, the most surprising result is that for the Bell element not only be behavior in comparison with the total number of degrees of freedom is better but additionally, the same discretization with a lower number of degrees of freedom is closer to the analytical solution than for the Argyris element in its full version. An explanation for this result would be that the Argyris element is closer to the solution with a piecewise linear boundary but that does not necessarily coincide with the distance to the analytical solution of the circular domain.

In case of the comparison of the PS-6 (C^1), PS-6 (C^0) and PS-6 (d) element, it is worth to mention that even so, all three show similar convergence behavior, the local error distribution of the PS-6 (C^1) and PS-6 (d) elements is different from that of the PS-6 (C^0) element, see figure 8.8. Furthermore, the performance of the PS-6 (C^0) element is bounded. Due to a structural error within the element description, at a certain degree of accuracy, further convergence is not possible anymore, compare to figure 8.7. Even so, it seems that for this example, the element is slightly better than the other PS-6 versions but a qualified prediction of the moment of stagnation is not possible. For the comparison of the PS-6 (C^1) and PS-6 (d) elements, it is worth mentioning that the PS-6 (d) element can be defined independently of its neighboring elements. We recommend to use this version in case of linear gradient elastic computations.

The second application of this example is the investigation of the effects of the different algorithms for the approximation of the geometry of the isoparametric BFS element, described in subsection 5.4.5. The results for a very coarse discretization of 4×2 elements is presented in figure 8.9. Even so, the geometries are quite similar in its shape, the local error distributions as well as the integral error norms are differing significantly from each other. The local error distribution is presented in figure 8.10, whereas the convergence diagrams for the L^2 and H^1 errors can be found in figure 8.11. To the convergence diagrams, additionally the results for the HCT element with the optimal approximation is added. Therefore it is visible, that only the $\bar{\mathbf{G}}$ -optimization is showing superior results to the linear subparametric elements and thus, special care has to be taken for the isoparametric C^1 -continuous approximation of the geometry.

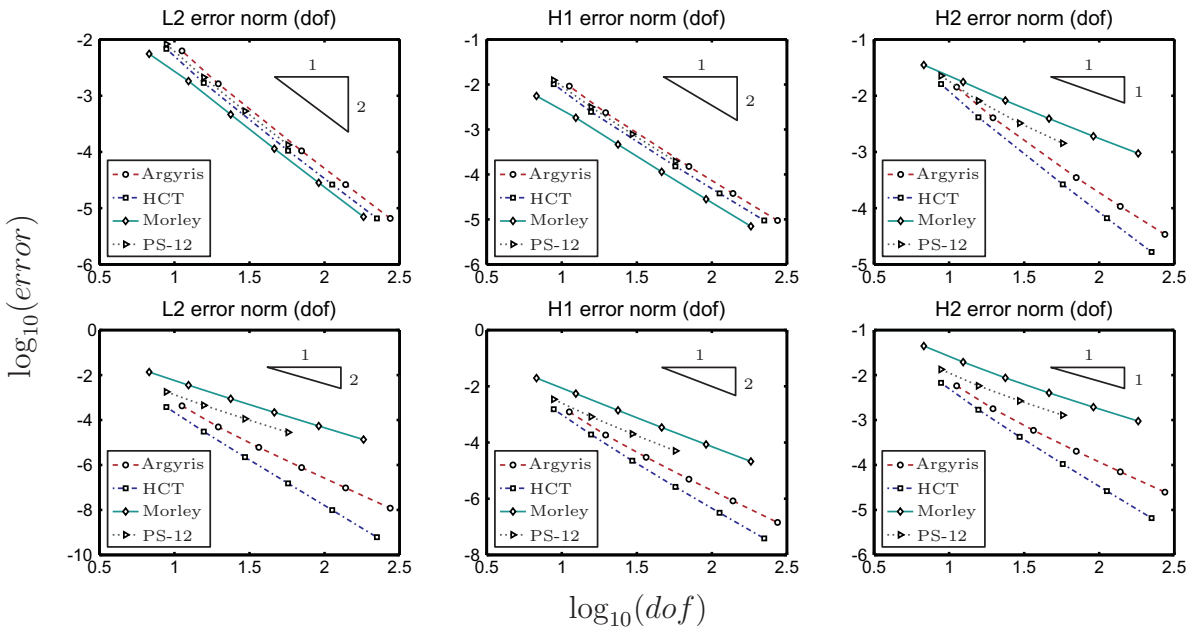


Figure 8.6: Convergence diagrams for the different linear approximations of the boundary. (Top): Linear interpolation of the geometry, (Bottom): Area preserving approximation of the geometry.

	L^2 error norm	H^1 error norm	H^2 error norm
Argyris	3.15	2.71	1.61
Bell	3.34	2.90	1.75
HCT	4.07	3.20	2.08
HCT-R	2.16	2.15	1.21
PS-12	2.14	2.16	1.16
PS-12-R	2.17	2.17	1.21
PS-6 (C^1)	2.11	2.11	1.13
PS-6 (d)	2.18	2.18	1.20
CSD	0.03	0.05	0.01
Zienk.	2.02	1.92	0.99
Mor	2.07	2.07	1.12
NEM	2.58	2.42	1.10
BFS (mo)	4.09	3.24	2.17
BFS (pp)	4.32	3.38	2.23
BFS (no)	2.50	2.43	1.18

Table 8.1: Rates of convergence for the different element methods.

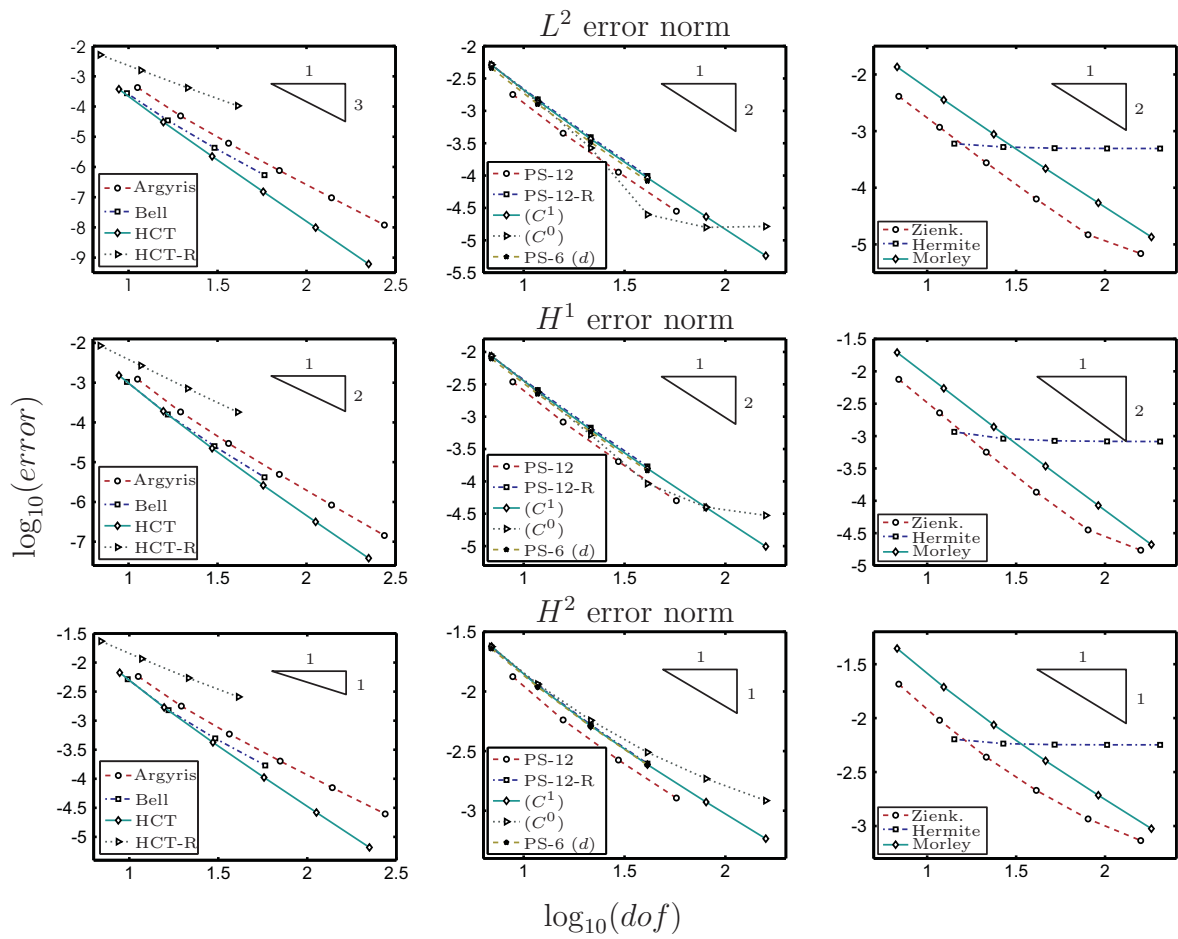


Figure 8.7: Convergence diagrams for the different subparametric methods.

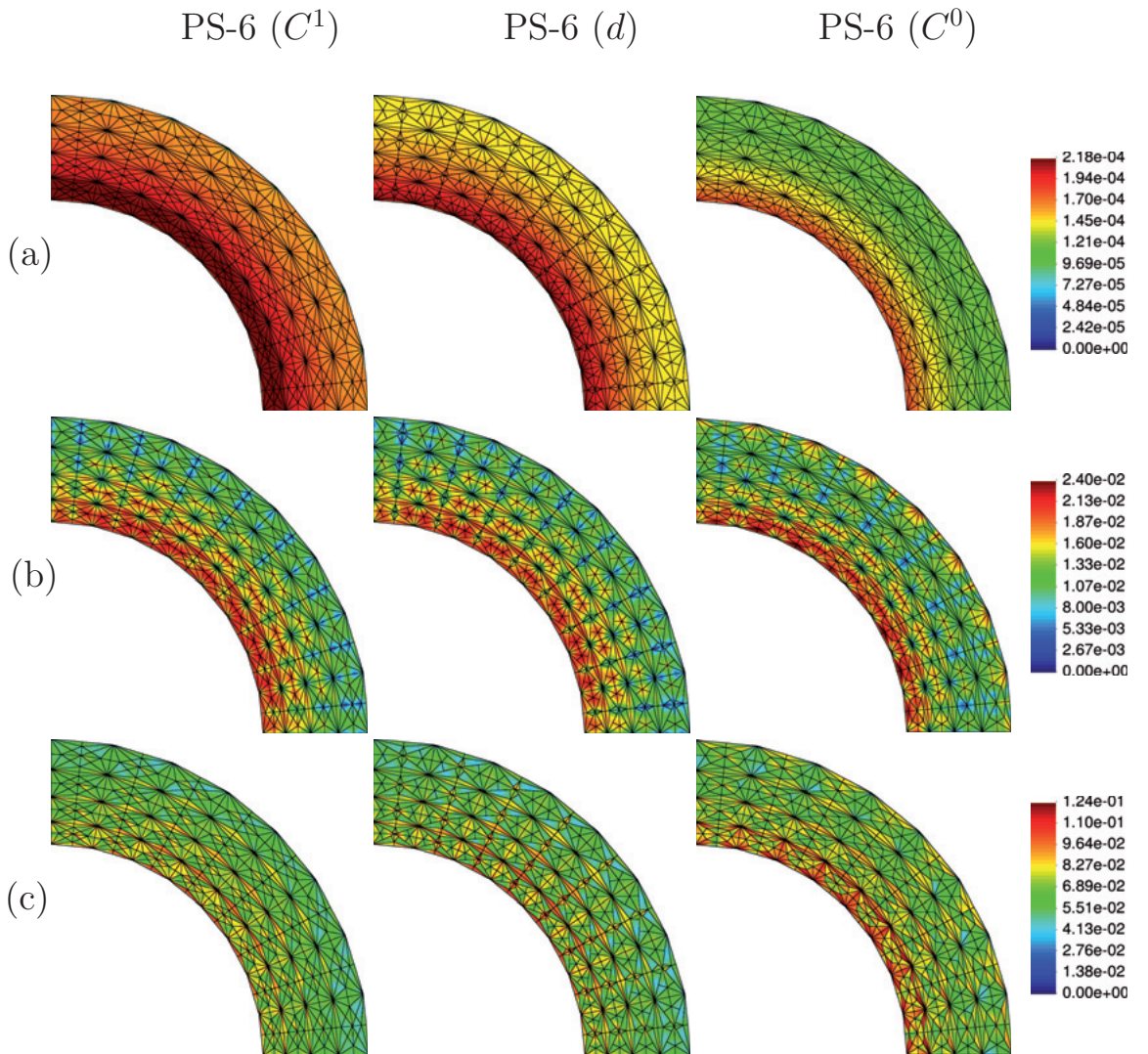


Figure 8.8: Powell-Sabin 6 split elements. Comparison of the Frobenius norm of (a) local displacement, (b) strain and (c) strain gradient error.

Numerical results of the Isogeometric Analysis In the second part of this example, the numerical behavior of the isogeometric analysis for the application to the thick hollow cylinder is observed. Within this investigation, several additional aspects such as the influence of the polynomial as well as the order of continuity can easily be observed. Furthermore, the influence of the geometry approximation cancels out due to the exact approximation of the geometry. The comparison of the IGA to the subparametric HCT element with similar number of degrees of freedom is presented in figure 8.12. Within this example, it can be observed, that the local error of the IGA is only dependent on the approximation of the deformation in radial direction and in contrast to the HCT element, no change in direction of the circular geometry can be observed.

In the following, the geometry is changed slightly, i.e. the ratio of the inner to outer radius is set to $r/R = 0.1$. The material parameters are chosen as $\lambda = 7000$, $\mu = 3000$ and $l = 0.2R$, together with the coefficients $a_3 = \frac{1}{2}l^2\lambda$ and $a_5 = l^2\mu$.

In a first numerical investigation, the rate of convergence for different degrees of the

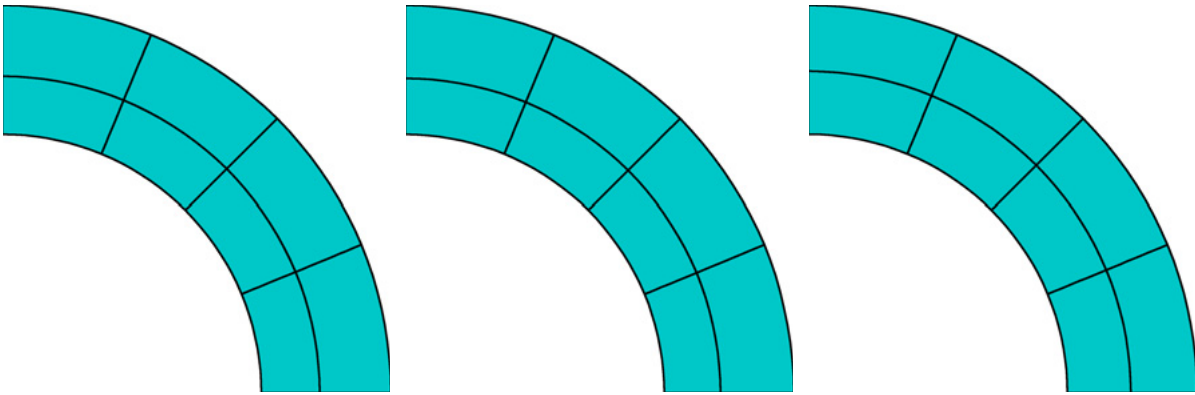


Figure 8.9: Comparison of the different results, obtained by the mesh construction algorithms. (Left): Direct mesh construction. (Center): Least-square fit. (Right): G-optimization.

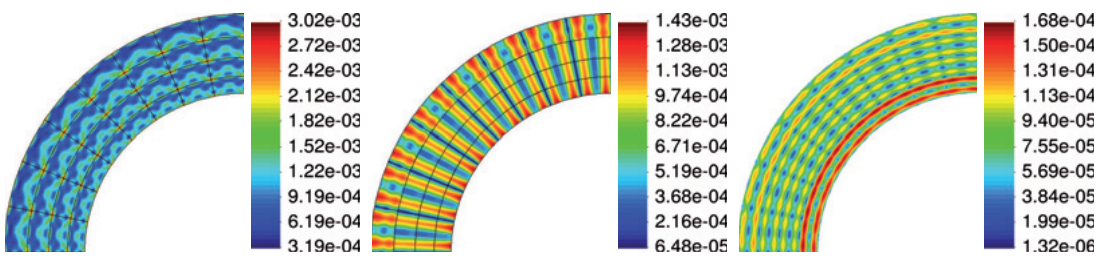


Figure 8.10: Contour plot of the local error $\|\mathbf{F}^h - \mathbf{F}^{ref}\|_2$. (Left): Direct mesh construction. (Center): Least-square fit. (Right): G-optimization.

polynomial within a C^1 continuous setting is investigated. In figure 8.13, the convergence diagrams for the isogeometric analysis can be observed. Clearly, the expected results of increased rates of convergence for higher polynomial orders can be observed. Additionally, compare to table 8.2, where the rates of convergence are computed by a least square fit to the diagrams.

The next investigation is the influence of an increase of continuity for the approximation

	P2	P3	P4	P5	P6	P7	P8
L^2 rate	1.48	2.96	4.21	5.01	5.38	5.59	6.10
H^1 rate	1.36	2.27	3.09	3.80	4.16	4.77	4.89

Table 8.2: Convergence rates for the IGA with continuity C^1 . The rates are computed by the linear regression line, approximating the values, presented in figure 8.13.

of the solution. Therefore, the maximal possible continuity of C^{k-1} has been chosen. In figure 8.14, the results are illustrated for polynomial degrees of $k \in \{2, 4, 6, 8\}$. The rates of convergence for $k \in \{2, 3, \dots, 8\}$, computed by a linear recursion are given in table 8.3. At last, the convergence behavior for two selected degrees of the rational functions, p_4 and p_6 are compared by the use of different degrees of continuity, see figure 8.15 and table 8.4. It can be observed that for the presented example, an increase of continuity and the resulting reduction of the total number of degrees of freedoms, comes along with only a

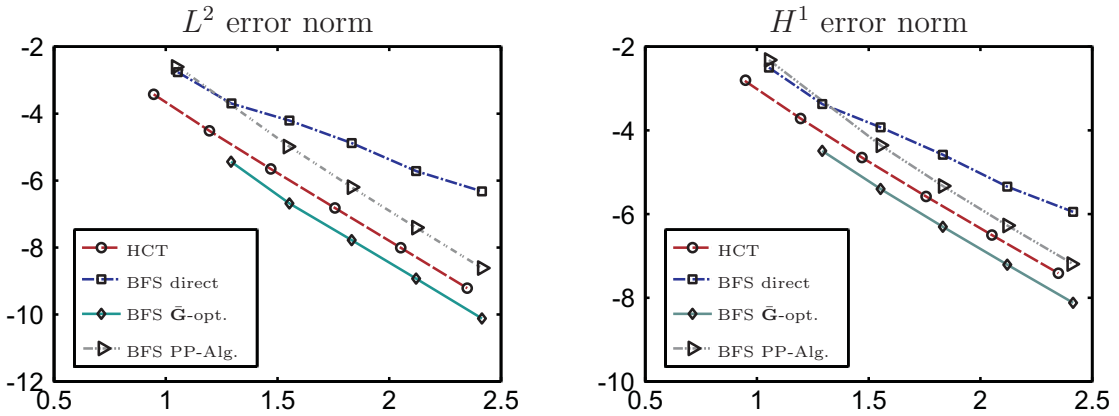


Figure 8.11: Convergence rates for the different mesh construction algorithms.

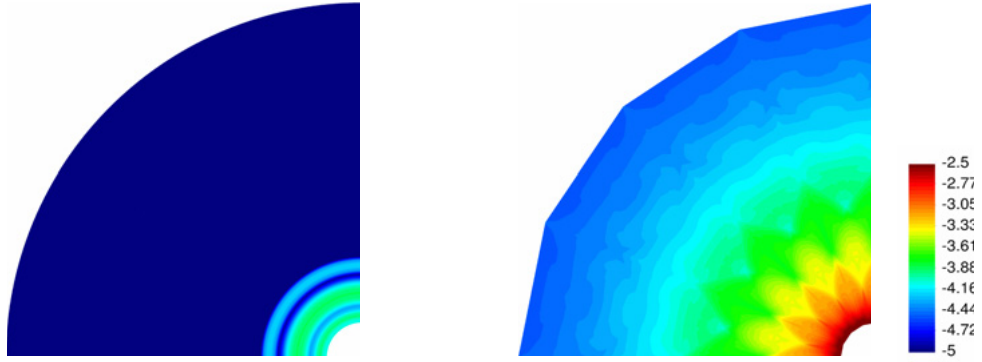


Figure 8.12: Comparison of the local error distribution of the isogeometric analysis and the HCT elements.

slight increase of the rate of convergence and a more efficient use of the global degrees of freedom. But those results have to be taken with care, since the analytical solution of the thick hollow cylinder example is C^∞ and thus very smooth. In general, it is possible that there exists an optimal level of continuity.

	P2	P3	P4	P5	P6	P7	P8
L^2 rate	1.48	3.82	6.03	7.56	9.42	10.31	13.15
H^1 rate	1.36	2.91	4.37	5.74	7.38	8.55	10.81

Table 8.3: Convergence rates for the IGA with continuity C^{k-1} . The rates are computed by the linear regression line, approximating the values, presented in figure 8.14.

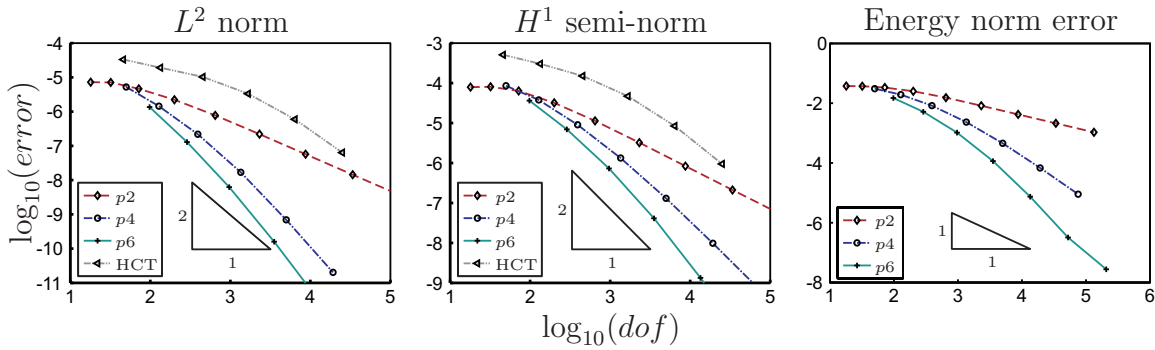


Figure 8.13: Convergence of the IGA with C^1 continuous shape functions and different polynomial degrees k . Different errors are plotted with respect to the logarithm of the total number of degrees of freedom.

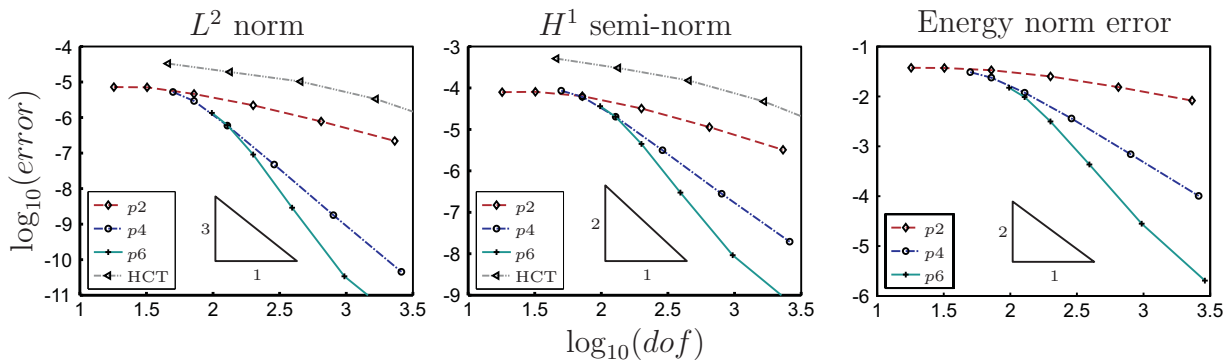


Figure 8.14: Convergence of the IGA with C^{k-1} continuous shape functions and different polynomial degrees k . Different errors are plotted with respect to the logarithm of the total number of degrees of freedom.

	C^1	C^2	C^3	C^4	C^5
$p4:$	4.21	4.61	6.03		
$p6:$	5.38	5.78	6.34	6.75	9.42

Table 8.4: Convergence rates for the IGA with varying continuity. The rates are computed by the linear regression line, approximating the values, presented in figure 8.15.

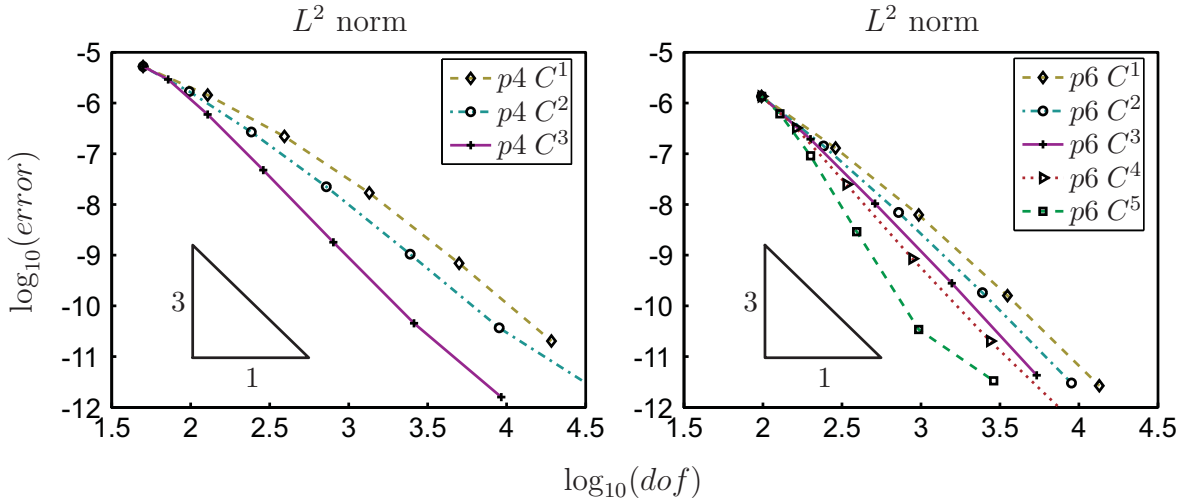


Figure 8.15: Convergence of the IGA for the polynomial degrees $k = 4$ and $k = 6$ and different orders of continuity. The errors are plotted with respect to the logarithm of the total number of degrees of freedom. (Left): L^2 error norm in log10 scale for $k = 4$. (Right): L^2 error norm in log10 scale for $k = 6$.

8.2 Gradient elasticity at finite strains

Similar investigations as in the previous section can be done for nonlinear gradient elasticity. The additional difficulty for the use of nonlinear models is that no analytical solution exists and therefore, the comparison of the different methods has to be done with the use of a numerical reference solution. This choice is quite tricky, since it is never completely clear, how much of the error is due to the wrong reference solution and what is the effect of the computed numerical results.

8.2.1 Inhomogeneous compression test

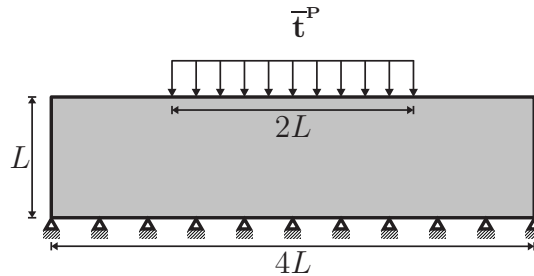


Figure 8.16: Geometry and loading description of the inhomogeneous compression test.

In subsection 8.1.2, it is demonstrated that the approximation of the geometry highly influences the rate of convergence for the different finite element discretizations. There-

fore, a new test for the analysis for extremely inhomogeneous states of deformations is presented. It is motivated by the inhomogeneous compression test presented in [178], but with slight changes of the geometrical boundary conditions.

We want to mention that the use of pressure boundary conditions is necessary to achieve good solutions. In a first attempt, compare [97] and [99], the rigid flat punch example as presented in [138] or more recently in [120] has been applied to gradient elasticity. However, due to the abrupt end of the boundary conditions, a singularity at the boundary of the flat punch occurred in the strain gradient values and dominated the convergence behavior. Therefore, all of the finite elements have demonstrated similar rates of convergence. Comparable results occur at the cracked specimen in subsection 8.2.3.

Here, a nonlinear material model with material Young's modulus of $200kN/mm^2$ and Poisson's ratio of 0.3 has been chosen together with $l=0.1L$. The geometry and loading conditions are presented in figure 8.16.

In a first comparison, the local strain error of four different elements with similar number

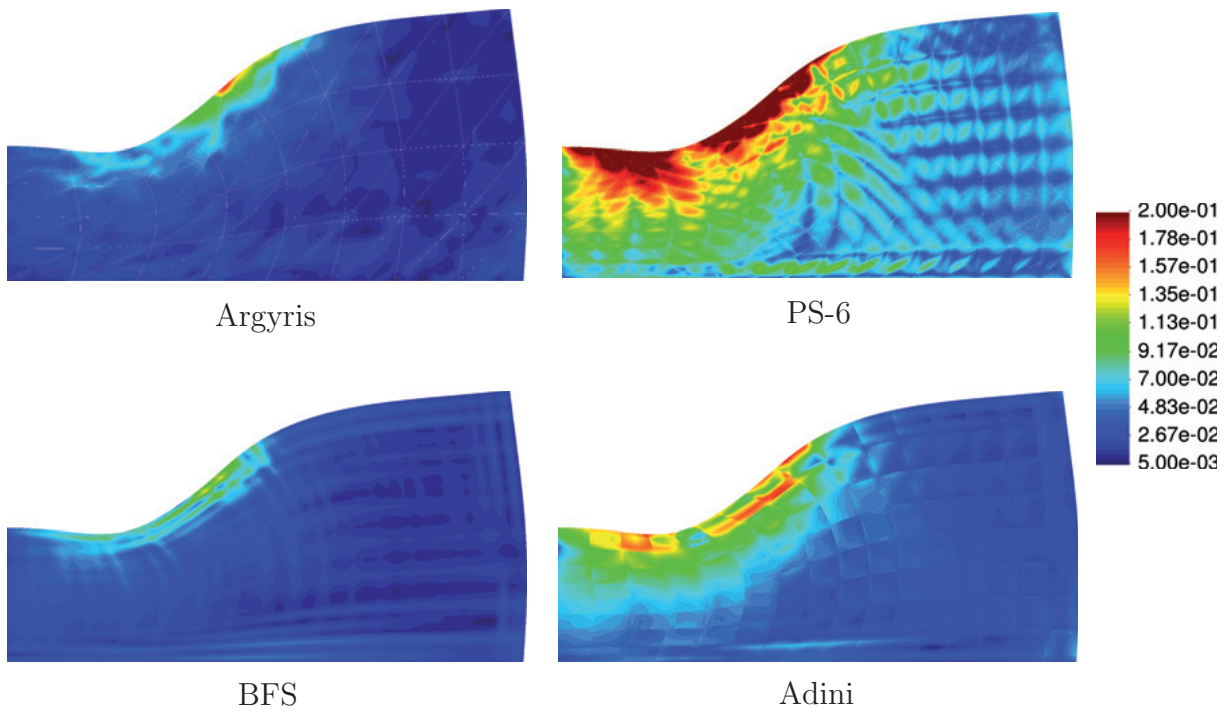


Figure 8.17: Local error distribution of $\| \mathbf{F}^h - \mathbf{F}^r \|_2$. Nodof: Argyris 756, PS6 918, BFS 1224 and Adini 918.

of degrees of freedom is presented in figure 8.17. Therein it is possible to see that for the Argyris and BFS element, the highest values of the error is located at the boundary of the applied load whereas for the Adini and the PS-6 (C^1) element, the strains at the position of the highest displacement are not captured optimally.

Additionally, the rates of convergence are provided in table 8.5 and the convergence diagrams are given in figure 8.2.1 and figure 8.2.1. The main result, obtained within this example, is that for an exact representation of the geometry, together with a smooth solution, the Argyris and Bell elements show the best performance. They are even better than the BFS element. This result was not achieved in subsection 8.1.2. In the THC

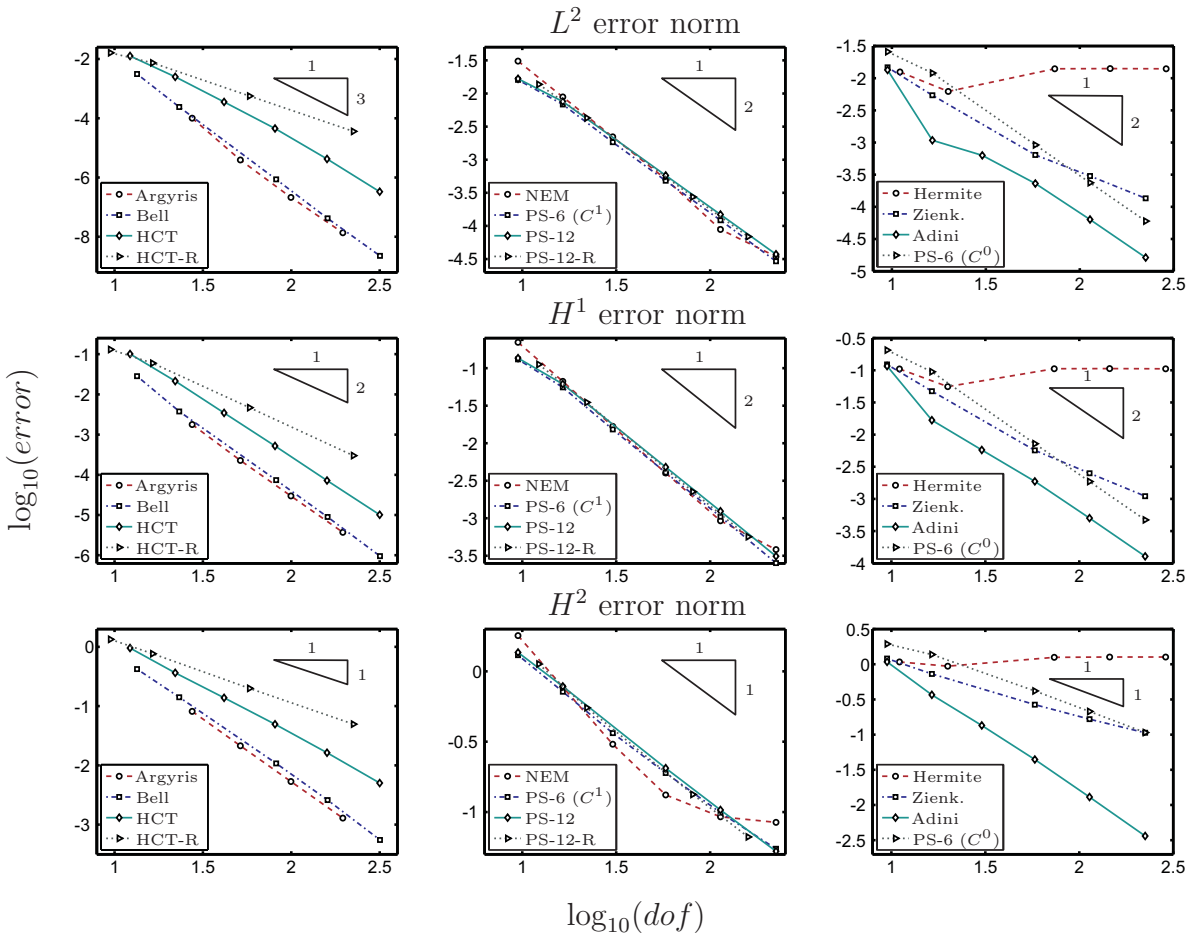


Figure 8.18: Convergence diagrams for the inhomogeneous compression test.

example, the rates of convergence as well as the absolute error were better for the HCT element and the BFS element. The current result demonstrates that the former solution is really caused by the insufficient linear approximation of a curved boundary.

An additional outcome of this numerical test is that the C^* elements do not show sufficient convergence behavior. The Morley element fails completely, the Hermite triangle is not convergent and the Zienkiewicz as well as the Adini element fail in the direct comparison to the C^1 elements, see figures 8.18 and 8.2.1 as well as table 8.5.

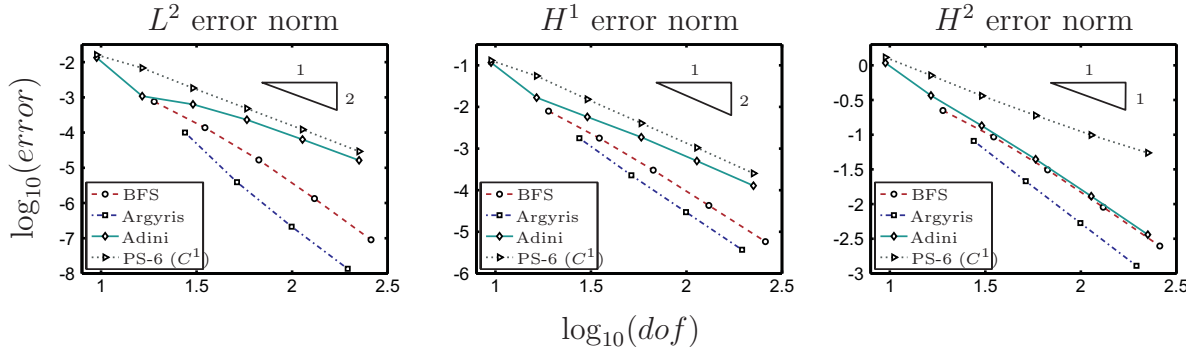


Figure 8.19: Convergence rates for the inhomogeneous compression test

	L^2 error norm	H^1 error norm	H^2 error norm
Argyris	4.24	3.09	2.11
Bell	4.44	3.16	2.12
HCT	3.35	2.88	1.61
HCT-R	2.04	2.02	1.05
PS-12	2.09	2.09	1.07
PS-12-R	2.03	2.02	1.03
PS-6 (C^1)	2.08	2.06	0.98
PS-6 (d)	2.03	2.03	0.98
Zienkiewicz	1.40	1.44	0.74
Adini	1.64	1.86	1.77
BFS	3.64	2.86	1.80
NEM	2.26	2.23	1.40

Table 8.5: Convergence rates for the inhomogeneous compression test.

8.2.2 Plate with hole example

In the second nonlinear numerical example a stress concentration problem is considered, similar to a problem in [186] or [122]. A rectangular specimen with length $3L$ and width L and a hole with radius $0.5L$ is clamped on the right hand side in horizontal direction and stretched by $u_1 = 3L$ to 100% elongation. Due to symmetry reasons only one quarter of the plate is simulated. A detailed description of the geometry and the loading conditions is presented in figure 8.20. Young's modulus of 200 kN/mm^2 and a Poisson's ratio of 0.3 are used. The parameter for the internal length scale is related to the size of the specimens and is defined as $l = L$.

In this example, the circular hole makes the construction of an isoparametric mesh for the BFS element difficult and can result in poorly designed elements. Therefore, the various mesh construction algorithms of subsection 5.4.4 are compared to each other. In figure 8.21 the L^2 , H^1 and H^2 error norms are presented for the refinement of differently constructed isoparametric meshes, respectively. It is obvious that the \bar{G} -optimization algorithm reveals

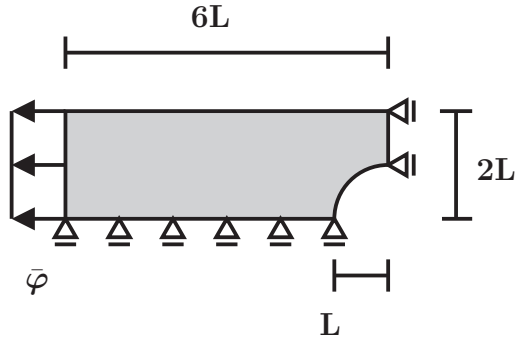


Figure 8.20: Geometry and loading description for the nonlinear plate with whole example.

a much better absolute error together with an improved rate of convergence. The non-smooth progression of the error norms are induced by the mesh optimization algorithm. By the use of the different mesh construction algorithm, the refined meshes are not nested. Here, the second observation is that the total error is composed of significantly different

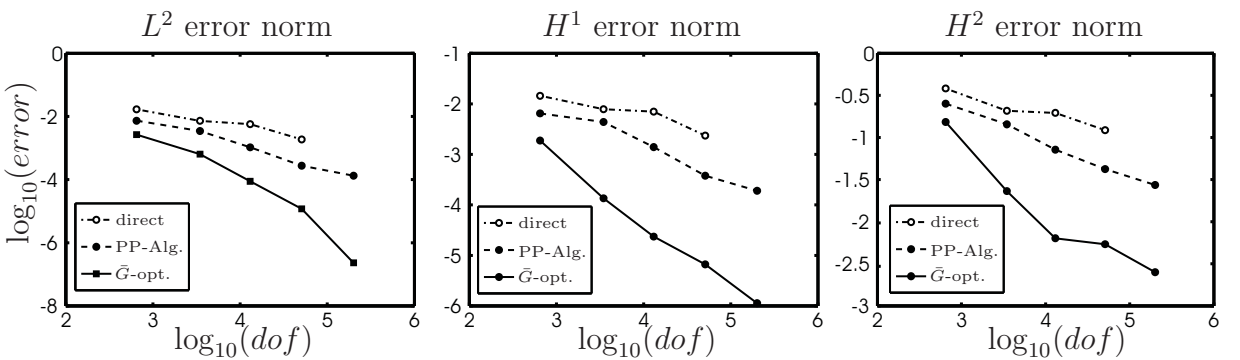


Figure 8.21: Comparison of the different mesh construction algorithms.

local error distributions for the various numerical methods. The local errors of the BFS, HCT and Argyris elements, together with the NEM are displayed in figures 8.22 and 8.23. For the comparison, the values of the local error of the deformation gradient \mathbf{F} and the strain gradient \mathbf{G} are presented in terms of the Frobenius norm. For the Argyris and the HCT element the highest errors of the deformation gradient arise in strongly deformed regions. The main part of the error of the strain gradient \mathbf{G} is located at the hole, where the geometry is approximated by a linear interpolation. The NEM shows a spurious error distribution. The major error for the BFS element results from the missing C^1 continuity of the geometry at the upper left corner. However, this error becomes negligible for finer meshes and does not influence the positive performance of the BFS element.

In figure 8.24, the relative error norms and semi-norms for the different numerical methods are shown. The rates of convergence and the absolute errors show only minor differences between the four numerical schemes, if the L^2 and H^1 norms are considered.

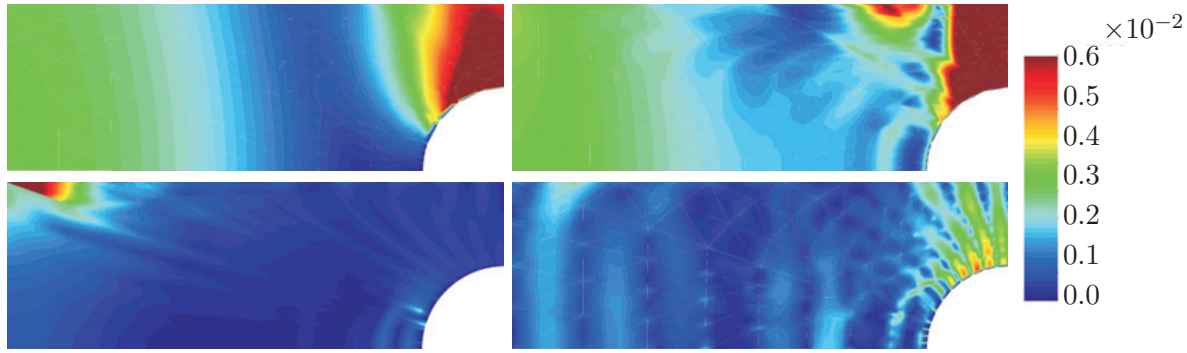


Figure 8.22: Frobenius norm of local error $\|\mathbf{F}^{ref} - \mathbf{F}^h\|_F$ for the plate with hole. (Upper left): Argyris. (Upper right): HCT element. (Bottom left): BFS element with $\bar{\mathbf{G}}$ -optimization. (Bottom right): NEM.

Only the H^2 norm reveals some difference in the rates of convergence. This result is very much similar to the result of the THC example with linear interpolation of the boundary, compare to figure 8.6. Only the BFS element and the NEM have a slight advantage over the triangular elements.

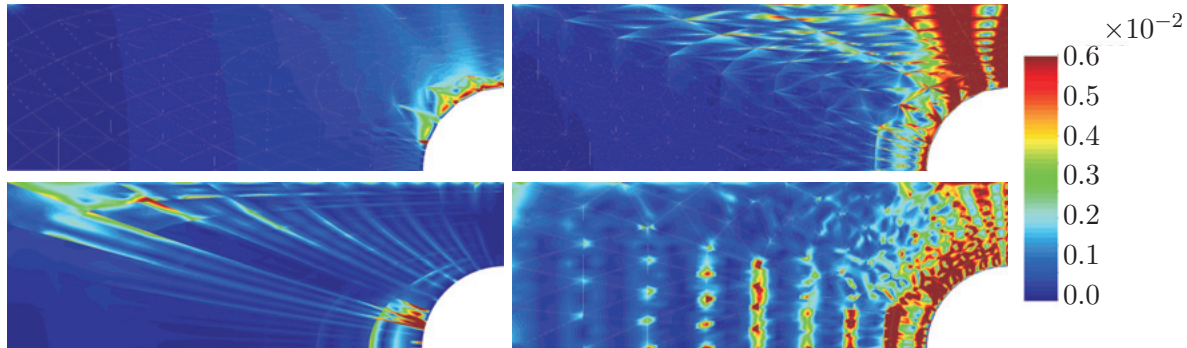
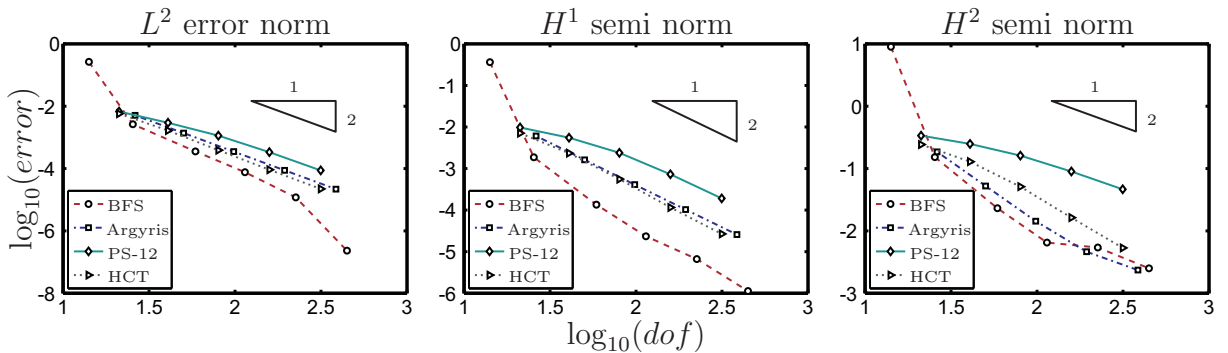


Figure 8.23: Frobenius norm of local error $\|\mathbf{G}^{ref} - \mathbf{G}^h\|_F$ for the plate with hole. (Upper left): Argyris. (Upper right): HCT element. (Bottom left): BFS element with $\bar{\mathbf{G}}$ -optimization. (Bottom right): NEM.

	L^2 error norm	H^1 error norm	H^2 error norm
NEM	2.15	2.05	0.73
Argyris	2.03	2.03	1.54
BFS	3.10	2.53	1.38
HCT	2.11	2.20	1.57
Adini	0.23	0.31	0.39
Bell	2.09	2.08	1.58
HCT-R	1.91	1.74	0.91
Morley	2.54	2.05	1.00
PS-12	1.73	1.65	0.82
PS-12-R	1.67	1.53	0.77
PS-6 (C^1)	1.19	1.09	1.09
PS-6 (C^0)	1.29	1.17	1.17

Table 8.6: Convergence rates for the plate with hole example.**Figure 8.24:** Convergence diagrams for the plate with hole example.

8.2.3 Cracked specimen

This example is chosen, to demonstrate the limits of the presented numerical methods for the application to gradient continua.

The major advantage of the application of generalized continua is the introduction of size effects. Additionally, in case of a strain gradient continuum, the strain field is not singular at the crack tip. However, it is well known that the singularity is shifted to the strain gradient and thus resulting in similar problems.

Several publications, considering the asymptotical crack-tip solutions are [10, 211–214] and [110] for the treatment of mode-III crack problems. The cases of mode-I and mode-II cracks were treated more recently in [90, 185] or [116, 117].

Further publications, with focus on the numerical aspects are [224] and [14], where mixed finite elements are used. A numerical analysis, based on the boundary element method is due to Karlis et al. [133, 134].

The geometry and loading for the last example are described in figure 8.25. An elongation to 150% is applied. The compressible Neo-Hookean model is used together with a quadratic

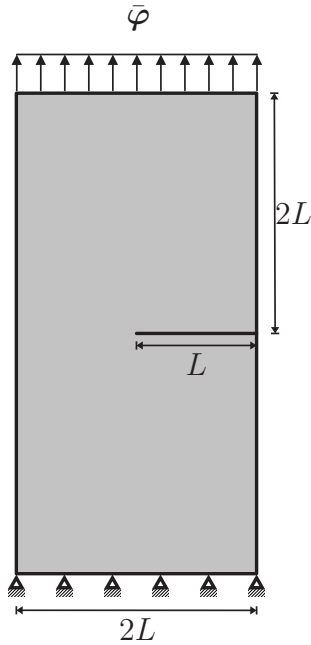


Figure 8.25: Geometry and loading description of the cracked specimen.

dependence of the energy density on the strain gradient with $a_4 = \mu l^2$.

In the convergence diagrams, plotted in figure 8.27, it can be observed that the convergence rates are far away from their optimal values. This is due to the fact that the rates are only governed by the mesh refinement. Since the geometry is approximated exactly, this effect is caused by the singularity of the exact solution.

The local error distribution of the deformation map φ , the deformation gradient \mathbf{F} and the strain gradient \mathbf{G} under mesh refinement for the HCT element is presented in figure 8.26. It can nicely be observed that the error in all of the three presented results is mainly caused by the singularity at the crack tip, rather than the effect of the element. The error is computed by comparison to a numerical reference solution. A nice additional result is presented in figure 8.28. Therein, the local error $\|\mathbf{G}^h - \mathbf{G}^{ref}\|$ is plotted on the set of triangles around the crack tip, showing similar results for all three refinement levels, though the size of the elements is significantly different, due to the different zoom factors. For this example, the numerical behavior of the elements can only be explained by the singularity at the crack tip. Even so, the first order strains are bounded, the strain gradient is still showing a singularity and thus, the applied numerical methods are not suited to capture the relevant effects of the method.

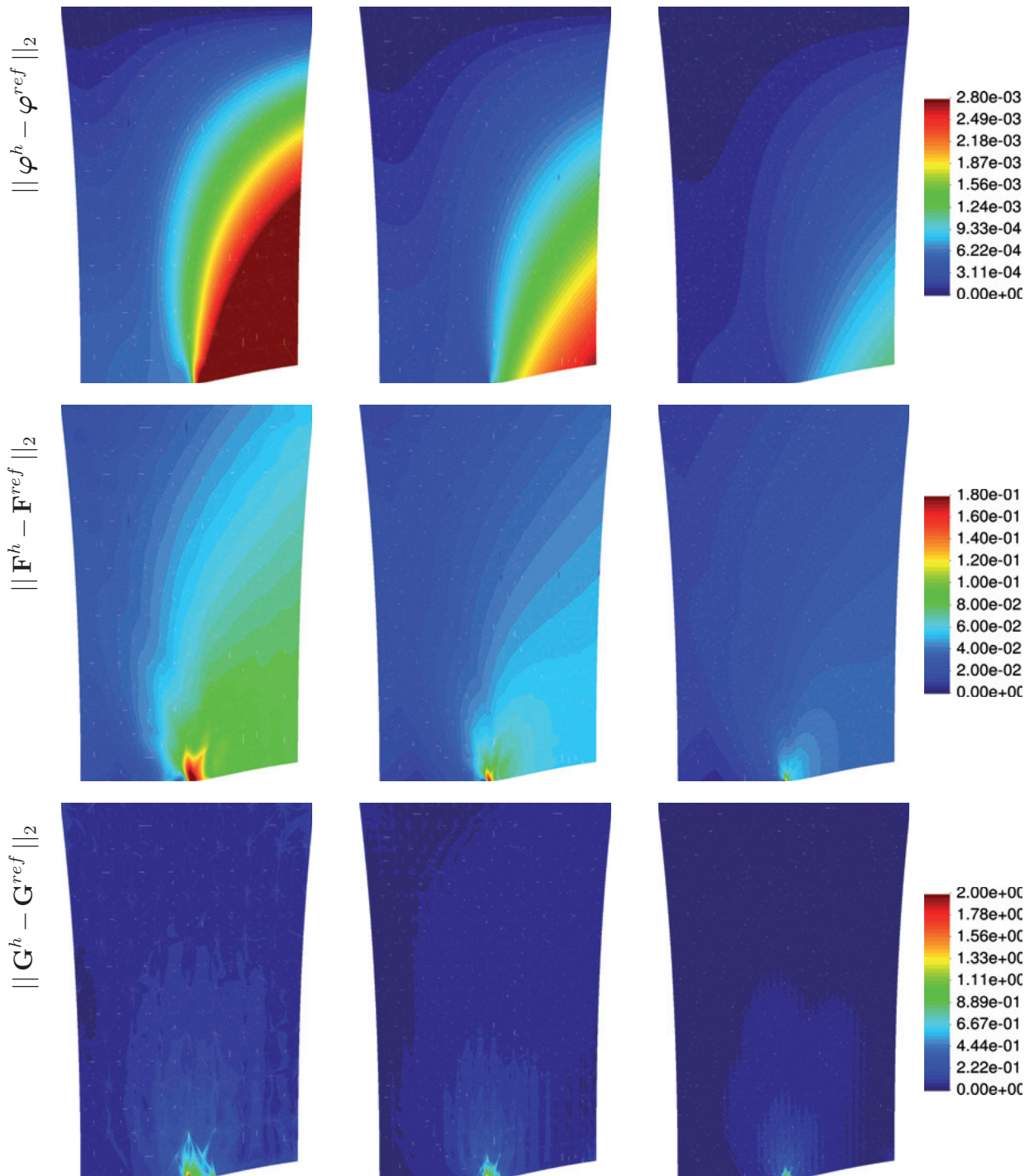


Figure 8.26: Local error behavior of the cracked specimen under h -refinement, computed with the HCT element and a numerical reference solution based on the BFS element. (Left): Discretization with 8×8 rectangular cells including 4 elements. (Center): 16×16 cells, (Right): 32×32 cells.

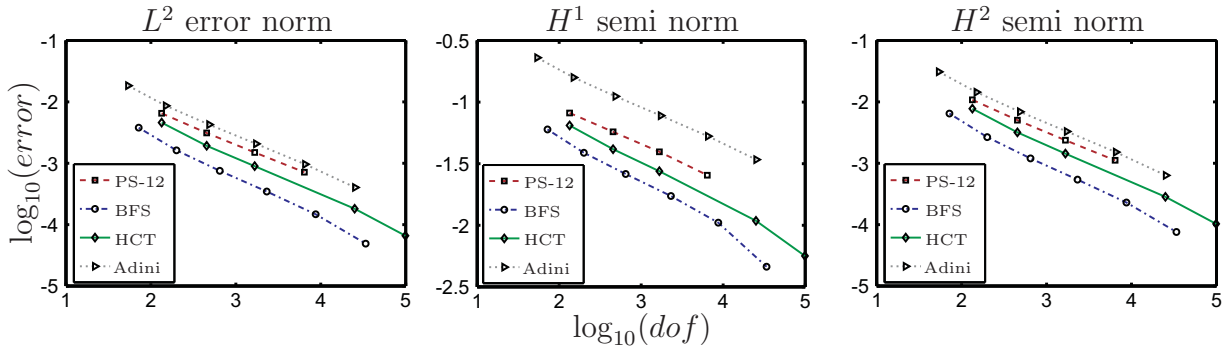


Figure 8.27: Convergence diagrams for the cracked specimen.

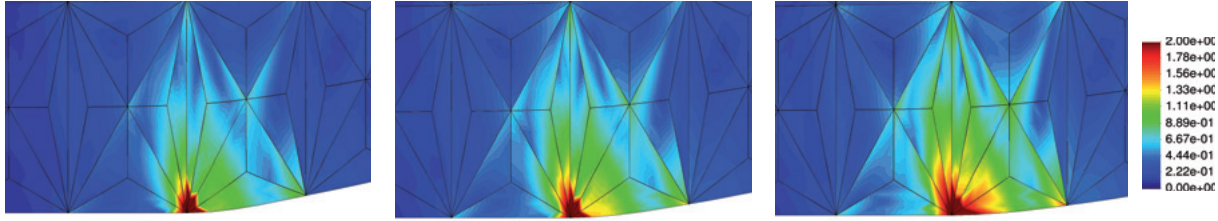


Figure 8.28: Local error at the elements around the crack tip, computed with the HCT element. The different size of the elements caused by different zoom factors (compare to figure 8.26) is not visible. (Left): Discretization with 8×8 rectangular cells including 4 elements. (Center): 16×16 cells, (Right): 32×32 cells.

8.3 Conclusions

The conclusions of this chapter can be concentrated in the following results. The first is that the C^* elements are not worth to be used, when compared to the other C^1 continuous elements. In all of the numerical examples they either failed or have shown inferior numerical behavior. Second, the use of higher order polynomials can improve the rates of convergence, e.g. see the comparison of the IGA in subsection 8.1.2 of the inhomogeneous compression test, presented in subsection 8.2.1, but this is only valid if the boundary is approximated sufficiently. With the use of the linear approximation of a curved boundary, the HCT element has always demonstrated superior behavior to the Argyris element with higher polynomial order, i.e. compare to the results of subsections 8.1.2 and 8.2.2.

By considering the numerical results as well as the restrictions of the methods, the following suggestions can be given for the choice of the numerical method:

Since the IGA as well as the BFS element are restricted in the approximation of the geometry, unstructured objects should be treated with the use of the subparametric triangular elements or the NEM. Otherwise the BFS element and the IGA have demonstrated their superiority in the previous sections. However, one additional aspect has to be consid-

ered. A good subparametric triangular mesh can be better than a poor isoparametric approximation, see figure 8.11.

9 The Bogner-Fox-Schmidt element with incompressible material behavior

Numerical solution schemes for the application to large deformations have to show good performance, in order to be acceptable for practical use. Many of the existing schemes are suitable for the application to a large variety of problems. However, they often collapse at the limit of incompressibility.

Incompressible or nearly incompressible material behavior is a common property of polymer materials. To treat this special problem, a three field variational principle is used, which has first been presented in [189]. This is also known as the mixed Jacobian-pressure formulation. An overview on different mixed approaches can be found in the publications of [51] or [178]. In the latter, a comprehensive review on the enhanced strain method is presented. Additionally, a nice introduction from the engineering point of view can be found in the monograph of Hughes [128]. The mathematical background for its application to the finite element method is given in [50].

Motivated by its excellent performance, see chapter 8, the BFS element is chosen for an exemplarily investigation of the performance of C^1 continuous finite elements at the limit of incompressibility.

This chapter is structured as follows: In section 9.1 a short introduction to the locking mechanism within the finite element method is presented. This is followed by the introduction of a variational three field formulation, see section 9.2.

The numerical treatment of the three field formulation is discussed in section 9.3. Therefore, the additional approximation fields are presented in section 9.4 and the chapter closes with a numerical evaluation of the mixed elements in section 9.5.

9.1 The principle of volumetric locking

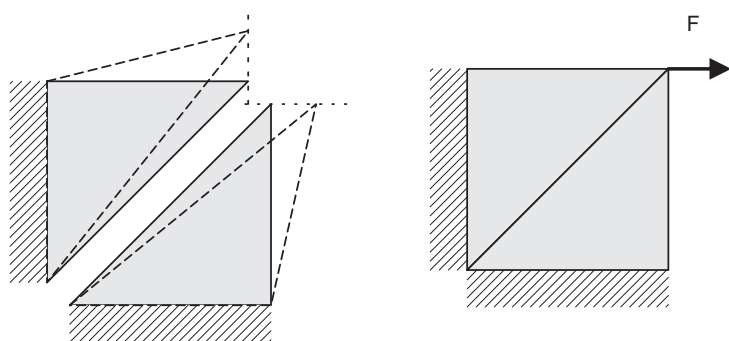


Figure 9.1: Locking example: The force in the right picture does not cause any deformation of the system due to the incompressibility constraint.

The simplest example to explain why the finite element method fails at incompressible material behavior is given in figure 9.1. Due to the constant volume condition, each of the linear elements is restricted to the deformation indicated by the dotted lines. However, by combining both elements in one geometry, any deformation of the mesh would either cause a change in the volume of one of the elements or violate the Dirichlet boundary conditions. Therefore the combination of the two linear elements prevents any deformation of the structure and thus results in an unphysical infinite stiffness.

An additional explanation for the unacceptable performance of standard finite elements is found if the eigenmodes of the elements are analyzed. Consider a 2d bilinear finite element for the approximation of the displacement. This element has eight degrees of freedom, the vertical and horizontal displacements at the nodes. By evaluating the eigenvectors of the discrete problem $\mathbf{Ku} = \mathbf{f}$, one obtains the characteristic deformations of this element. Neglecting the rigid body motions, there are five degrees of freedom left for the deformation. However, three of these deformations violate the incompressibility criterion, due to local changes in the volume, see figure 9.2.

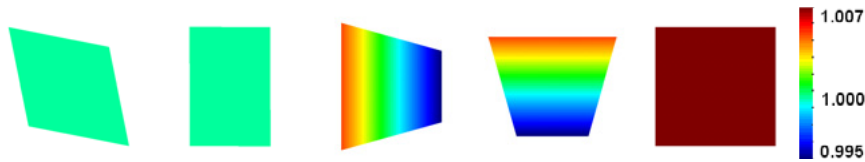


Figure 9.2: Eigenmodes of a bilinear finite element and contour plot of the determinant of the Jacobian. The rigid body motion modes are neglected.

By the previous argumentation, one could claim that for the bicubic Bogner-Fox-Schmidt element with its 32 degrees of freedom and thus 29 relevant eigenmodes, if the rigid body deformations are neglected, there should be enough possible deformations left for a satisfying numerical behavior. Anyhow, we will demonstrate that the single field formulations shows a remarkably higher error than the presented mixed formulations, if the material behavior is nearly incompressible.

9.2 Three-field formulation

An efficient variational principle for modeling nearly incompressible material response is the Simo-Taylor-Pister variational principle (Simo et. al. [189]), which is also known as the mixed Jacobian-pressure formulation. Thereby, besides the deformation map φ , two additional fields are introduced, i.e. the pressure field p (used as a Lagrange parameter) and the independent variable θ (for an approximation of the Jacobian $\det \mathbf{F}$). The free energy density of the three field formulation W_0^{3f} is then defined as

$$W_0^{3f} := W_{vol}(\theta) + p[\det \mathbf{F} - \theta] + W_{dev}(\bar{\mathbf{F}}), \quad (9.1)$$

where the volumetric part W_{vol} and the deviatoric W_{dev} of the free energy density are treated independently. The quantity $\bar{\mathbf{F}}$ in (9.1) denotes the deviatoric part of the deformation gradient, defined by

$$\bar{\mathbf{F}} := \det \mathbf{F}^{-\frac{1}{n}} \mathbf{F}. \quad (9.2)$$

9.2.1 Weak form of the equation

For the introduction of the three field formulation (9.1) to gradient elasticity, we start with the additive split of the internal energy density, presented in (2.36). For sake of simplicity, the three field formulation is only replacing $W^F(\mathbf{F})$ and thus, the internal energy Π^{int} of the system is given by

$$\Pi^{int} = \int_{\mathcal{B}_0} W_0^{3f} + W^G \, dV. \quad (9.3)$$

The external potential energy is equal to the single field formulation, i.e.

$$\Pi^{ext} = - \int_{\mathcal{B}_0} \mathbf{b} \cdot \boldsymbol{\varphi} \, dV - \int_{\mathcal{B}_0^P} \bar{\mathbf{t}}^P \cdot \boldsymbol{\varphi} \, dA + \int_{\mathcal{B}_0^Q} \bar{\mathbf{t}}^Q \cdot \nabla_x^N \boldsymbol{\varphi} \, dA, \quad (9.4)$$

To achieve the state of equilibrium, the variations of the total potential energy $\Pi = \Pi^{int} + \Pi^{ext}$ with respect to all variables have to vanish. By inserting (9.1) in (9.3) and the use of (9.4), the following three sets of equations have to be solved

$$\begin{aligned} \delta_{\boldsymbol{\varphi}} \Pi(\boldsymbol{\varphi}, p, \theta) &= \delta_{\boldsymbol{\varphi}} \Pi^{int}(\boldsymbol{\varphi}, p, \theta) - \delta_{\boldsymbol{\varphi}} \Pi^{ext}(\boldsymbol{\varphi}) \\ &= \int_{\mathcal{B}_0} \left[\mathbf{P}_{dev} : \delta \mathbf{F} + p \frac{\partial \det \mathbf{F}}{\partial \mathbf{F}} : \delta \mathbf{F} + \mathbf{Q} : \delta \mathbf{G} \right] \, dV - D_{\delta \boldsymbol{\varphi}} \Pi^{ext}(\boldsymbol{\varphi}) \\ &= 0. \end{aligned} \quad (9.5)$$

$$\delta_p \Pi(\boldsymbol{\varphi}, p, \theta) = \int_{\mathcal{B}_0} [\det \mathbf{F} - \theta] \delta p \, dV = 0 \quad (9.6)$$

as well as

$$\delta_{\theta} \Pi(\boldsymbol{\varphi}, p, \theta) = \int_{\mathcal{B}_0} \left[-p + \frac{\partial W_{vol}(\theta)}{\partial \theta} \right] \delta \theta \, dV = 0. \quad (9.7)$$

Here, the deviatoric part of the first Piola-Kirchoff stress tensor \mathbf{P}_{dev} in (9.5) is defined by the derivative of the deviatoric part of the free energy density with respect to the deformation gradient, i.e.

$$\mathbf{P}_{dev} := \frac{\partial W_{dev}(\bar{\mathbf{F}})}{\partial \mathbf{F}}. \quad (9.8)$$

The complete stress tensor \mathbf{P} is obtained by

$$\mathbf{P} = \mathbf{P}_{dev} + p \det \mathbf{F} \mathbf{F}^{-T}, \quad (9.9)$$

where the latter term is given by inserting the derivative of the determinant $\det \mathbf{F}$ with respect to \mathbf{F} into the variation of the internal energy in (9.5).

9.2.2 Incompressible Neo-Hookean model

For the incompressible Neo-Hookean model, the internal elastic energy density is decomposed into the volumetric and deviatoric part. The volumetric term describes the change

of internal energy induced by a change of the volume, whereas the deviatoric part describes the response of the body under isochoric deformations. Assuming an additive split, they can be treated separately, i.e.

$$W(\mathbf{F}) = W_{vol}(J) + W_{dev}(\bar{\mathbf{F}}), \quad (9.10)$$

where J denotes the determinant of the deformation gradient \mathbf{F} which describes the local volume change, i.e. see (2.4). Again $\bar{\mathbf{F}}$ denotes the deviatoric part of the deformation gradient, defined in (9.2).

By replacing the deformation gradient in the original definition of the Neo-Hookean model with its deviatoric part $\bar{\mathbf{F}}$, i.e. see (2.33), only the part being directly dependent on the deformation gradient is left and the deviatoric part of the energy density is resulting in,

$$W_{dev}(\bar{\mathbf{F}}) = \frac{1}{2}\mu[\bar{\mathbf{F}} : \bar{\mathbf{F}} - n]. \quad (9.11)$$

The corresponding deviatoric part of the Piola stress is therefore derived to

$$\mathbf{P}_{dev} = \frac{\partial W_{dev}}{\partial \mathbf{F}} = \mu J^{-\frac{2}{n}} \left[\mathbf{F} - \frac{1}{n}[\mathbf{F} : \mathbf{F}] \mathbf{F}^{-T} \right] \quad (9.12)$$

and the tangent operator is a result of straightforward computations,

$$\frac{\partial \mathbf{P}_{dev}^T}{\partial \mathbf{F}} = \mu J^{-\frac{2}{n}} \left[\mathbf{I}_2 \otimes \mathbf{I}_2 - \frac{2}{n} [\mathbf{F}^{-1} \otimes \mathbf{F} + \mathbf{F}^T \otimes \mathbf{F}^{-T}] + \frac{1}{n}[\mathbf{F} : \mathbf{F}] [\mathbf{F}^{-1} \bar{\otimes} \mathbf{F}^{-T} + \mathbf{F}^{-1} \otimes \mathbf{F}^{-T}] \right]. \quad (9.13)$$

9.2.3 Volumetric part of the internal energy

For the volumetric response, an additional term is introduced. Here, the simple quadratic formulation, solely dependent on the compression modulus κ , is used

$$W_{vol}(\bar{J}) = \frac{1}{2}\kappa[\bar{J} - 1]^2. \quad (9.14)$$

In (9.14) the quantity \bar{J} can either represent the determinant of the deformation gradient $\det \mathbf{F}$ or alternatively, the additional field θ .

In case of $\bar{J} = \det \mathbf{F}$, the corresponding stress tensor and tangent operator are

$$\mathbf{P}_{vol} = \kappa[J - 1]J \mathbf{F}^{-T} \quad (9.15)$$

and

$$\frac{\partial \mathbf{P}_{vol}^T}{\partial \mathbf{F}} = \kappa[2J - 1]J \mathbf{F}^{-1} \otimes \mathbf{F}^{-T} - \kappa[J - 1]J \mathbf{F}^{-1} \bar{\otimes} \mathbf{F}^{-T}. \quad (9.16)$$

In the second case, if \bar{J} is representing the additional field θ , the derivative is a scalar function and therefore, the computation of the derivatives is left to the reader.

At this point, the only non-trivial part missing for the computation of the tangent operators is the part with the Lagrange multiplier $p[\theta - J]$. Its derivative with respect to \mathbf{F} is given by

$$\mathbf{P}_{vol}(\mathbf{F}, p) = -pJ \mathbf{F}^{-T} \quad (9.17)$$

and

$$\frac{\partial \mathbf{P}_{vol}^T}{\partial \mathbf{F}} = pJ [\mathbf{F}^{-1} \bar{\otimes} \mathbf{F}^{-T} - \mathbf{F}^{-1} \otimes \mathbf{F}^{-T}]. \quad (9.18)$$

9.3 Incompressible material behavior: Discretization and linearization

In the context of a mixed three field formulation, the elliptic boundary value problem of elasticity transforms into a saddle point problem. For the computation of the variational problem of section 9.2 it is therefore not expedient to use arbitrary finite element subspaces for the approximation of φ , p and θ . For example, the well known Q1P0 element leads to spurious pressure modes under certain configurations. A sufficient condition to guarantee the convergence of the finite element method for mixed problems is the so-called LBB or inf-sup condition, i.e. see Babuska [22] or Brezzi [49]. It can be proven for linear elasticity that finite element spaces fulfilling this condition are converging to the unique solution. Therefore it is at least guaranteed, that the linear system in each step of the Newton iteration leads to correct results. For a comprehensive overview on the topic, the interested reader is referred to book of Brezzi and Fortin [50].

9.3.1 Pressure approximation

For the approximation of the deformation map φ , the formulation presented in (3.7) is used. In case of the discrete pressure approximation and the approximation of the additional field θ , the following definition are used,

$$p^h = \sum_{\mathcal{L}} p_L N_L \quad \text{and} \quad \theta^h = \sum_{\mathcal{L}} \theta_L N_L, \quad (9.19)$$

where \mathcal{L} is the set of nodes, where the additional approximation fields are defined. In (9.19), it is assumed that both fields are approximated similar.

9.3.2 Discrete weak equations

Using the definitions given by (9.19), the discretized form of equations (9.5), (9.6) and (9.7) results in the following residuals:

$$\begin{aligned} \mathbf{R}_I^\varphi := & \int_{\mathcal{B}_0} [[\mathbf{P}_{dev}(\varphi^h) + p \det \mathbf{F} \mathbf{F}^{-T}] \cdot \nabla_{\mathbf{x}} \Psi_I] + \mathbf{Q} \cdot \nabla_{\mathbf{x}}^2 \Psi_I \, dV \\ & - \int_{\partial \mathcal{B}_0^P} \bar{\mathbf{t}}^P \Psi_I \, dA + \int_{\mathcal{B}_0^Q} \bar{\mathbf{t}}^Q \cdot \nabla_{\mathbf{x}}^N \Psi_I \, dA - \int_{\mathcal{B}_0} \mathbf{b} \Psi_I \, dV = \mathbf{0}, \end{aligned} \quad (9.20)$$

which is the discretized form of (9.5) and the additional terms

$$R_J^p = \int_{\mathcal{B}_0} [\det \mathbf{F} - \theta] N_J^p \, dV \quad (9.21)$$

$$R_J^\theta = \int_{\mathcal{B}_0} \left[-p + \frac{\partial W_{vol}(\theta)}{\partial \theta} \right] N_J^\theta \, dV. \quad (9.22)$$

9.3.3 Linearized discrete weak equations

The nonlinear system of equations presented in (9.20) can efficiently be solved by a Newton-Raphson scheme. To this end, the linearizations of the residuals are required. This can as well be written as

$$\mathbf{R}_I^{k+1} = \mathbf{R}_I^k + \Delta\mathbf{R}_I = \mathbf{0}, \quad (9.23)$$

whereas the iteration increment $\Delta\mathbf{R}_I$ is given by

$$\Delta\mathbf{R}_I = \frac{\partial\mathbf{R}_I}{\partial\mathbf{a}_J} \cdot \Delta\mathbf{a}_J = \mathbf{K}_{IJ} \cdot \Delta\mathbf{a}_J \quad (9.24)$$

and the incremental update of the nodal variables is calculated by

$$\mathbf{K}_{IJ} \cdot \Delta\mathbf{a}_J = -\mathbf{R}_I^k. \quad (9.25)$$

The stiffness matrix \mathbf{K} reads

$$\mathbf{K} = \begin{pmatrix} \mathbf{K}^{\varphi\varphi} & \mathbf{K}^{\varphi p} & \mathbf{K}^{\varphi\theta} \\ \mathbf{K}^{p\varphi} & \mathbf{K}^{pp} & \mathbf{K}^{p\theta} \\ \mathbf{K}^{\theta\varphi} & \mathbf{K}^{\theta p} & \mathbf{K}^{\theta\theta} \end{pmatrix}, \quad (9.26)$$

whereas $\mathbf{K}^{\varphi\varphi}$ is given by

$$\begin{aligned} \mathbf{K}_{IJ}^{\varphi\varphi} &= \int_{\mathcal{B}_0} \nabla_{\mathbf{x}} \Psi_I \cdot \frac{\partial \mathbf{P}_{dev}^T}{\partial \mathbf{F}} \cdot \nabla_{\mathbf{x}} \Psi_J + \nabla_{\mathbf{x}}^S \Psi_I : \frac{\partial \mathbf{Q}^T}{\partial \mathbf{G}} : \nabla_{\mathbf{x}}^S \Psi_J \, dV \\ &\quad + \int_{\mathcal{B}_0} p \det \mathbf{F} \nabla_{\mathbf{x}} \Psi_I \cdot [\mathbf{F}^{-1} \otimes \mathbf{F}^{-T} - \mathbf{F}^{-1} \bar{\otimes} \mathbf{F}^{-T}] \cdot \Psi_J \, dV. \end{aligned} \quad (9.27)$$

The remaining components in equation (9.26) are derived to

$$\begin{aligned} \mathbf{K}_{IJ}^{\varphi p} &= \int_{\mathcal{B}_0} \nabla_{\mathbf{x}} \Psi_I \cdot [\det \mathbf{F} \mathbf{F}^{-1}] N_J^p \, dV \\ \mathbf{K}_{IJ}^{\varphi\theta} &= 0 \end{aligned} \quad (9.28)$$

and

$$\begin{aligned} K_{IJ}^{pp} &= 0 \\ K_{IJ}^{p\theta} &= - \int_{\mathcal{B}_0} N_I^p N_J^\theta \, dV \\ K_{IJ}^{\theta\theta} &= \int_{\mathcal{B}_0} N_I^\theta \frac{\partial^2 W_{vol}}{\partial \theta^2} N_J^\theta \, dV. \end{aligned} \quad (9.29)$$

9.4 The BFS element in a mixed formulation

Within this section, the different settings for the mixed finite element description are presented. The small filled dots are denoting the additional approximation fields. In all elements the additional field representing the Lagrange parameter p and the additional field θ are approximated by the same set of functions.

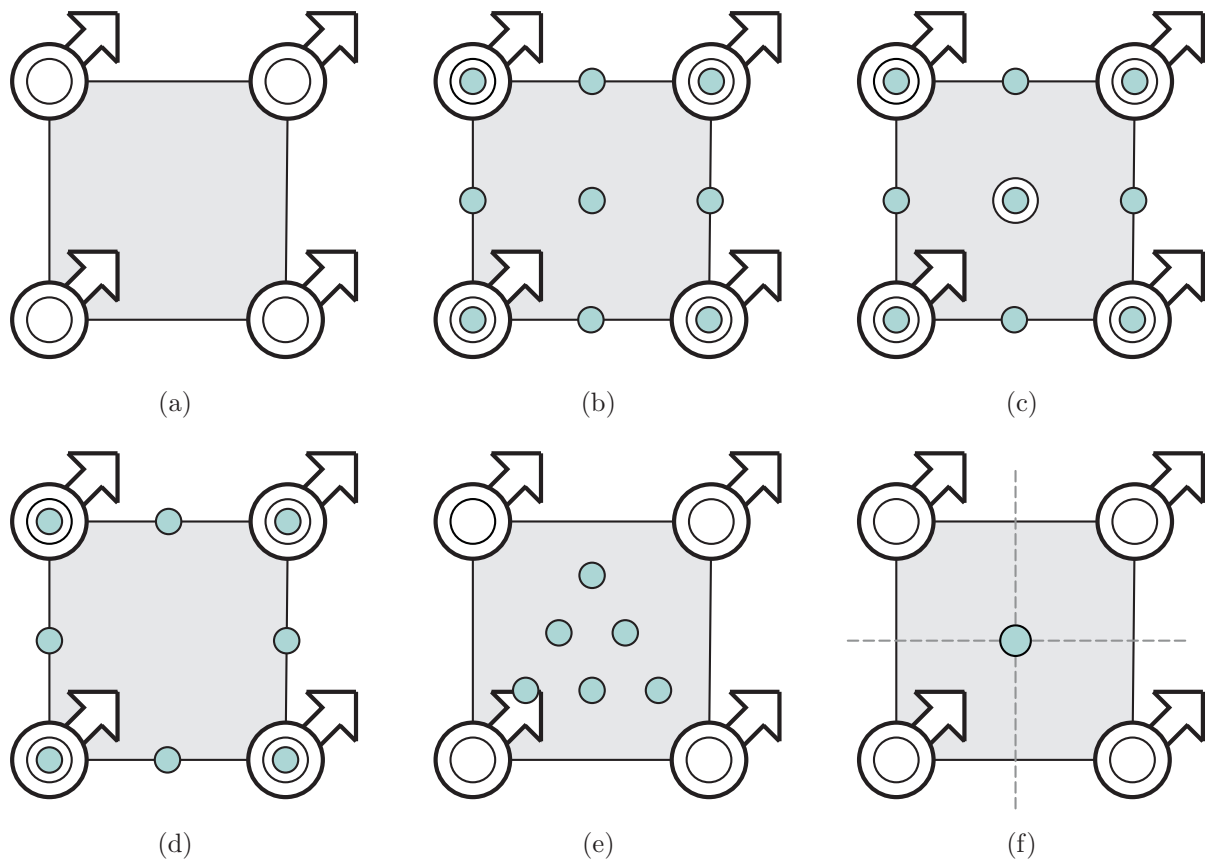


Figure 9.3: Different mixed approximations for the BFS element. (a) Original element (b) $BFS/Q2$ (c) $BFS^+/Q2$ (d) $BFS/S2$ (e) $BFS/P2$ and (f) $BFS/B2$.

Motivated by the classical mixed displacement pressure elements, the polynomial order of the additional fields has been chosen to be quadratic. In detail, a biquadratic interpolation of the additional variables has been used in the elements, presented in subfigure 9.3(b) and 9.3(c). Within the formulation of the latter element, additionally the displacement field has been enriched by a quartic bubble function, with no influence on the boundary deformation or deformation gradient. Those element will simply be denoted $Q2$ and $Q2^+$. Additionally continuous quadratic Serendipity ($S2$) functions as well as simple quadratic interpolants ($P2$) have been applied to approximate p and θ , compare to subfigures 9.3(d) and 9.3(e). In a last trial, the approximation of the fields p and θ is done by a quadratic C^1 continuous B-spline interpolant, see subfigure 9.3(f). Therefore, only one degree of freedom per element exists, the remaining part of the polynomial space is governed by the continuity conditions. A comprehensive introduction to the quadratic B-spline elements can be found in [179]. Unfortunately, it turns out that the approximation of the pressure is not accurate enough and thus, unphysical oscillations of the Jacobian $\det \mathbf{F}$ arise.

9.5 Numerical validation for the Boltzmann continuum

The previously described mixed formulations for the BFS element are compared to the single field formulation. The geometry of the numerical test is closely related to the geom-

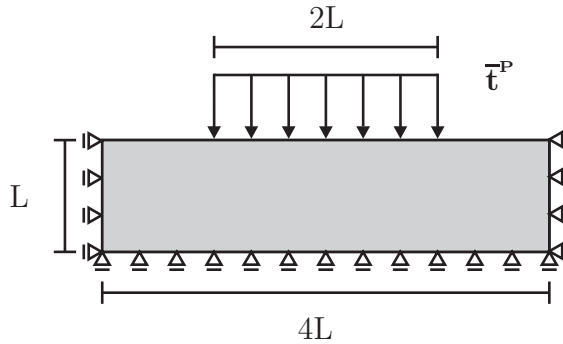


Figure 9.4: Geometry description of the punch example.

etry of the well known rigid flat punch example, [120]. Only the prescribed displacement is replaced by an external pressure \bar{t}^P , compare to figure 9.4.

A classical Boltzmann continuum has been chosen together with the incompressible Neo-Hookean material model and a quadratic expression for the volumetric part, see section 9.2.3. The chosen material parameters are $E = 10^5$, $\nu = 0.3$ and $\kappa = 10^{10}$. The errors are computed by comparison to a numerical solution with much more degrees of freedom based on the Serendipity pressure approximation.

Usually, if the effects of locking are analyzed, the displacement of a single point is compared with different finite element formulations. For the cubic Hermite elements, the displacement at the centerpoint does not vary significantly. Moreover, the vertical displacement at the center of the applied pressure is higher for the single field than for the mixed formulations, see figure 9.5. Thus, a qualified judgment on the performance of the different element formulation has to be related to the performance in terms of the L^2 or H^1 error norms.

It can be observed in figure 9.7 and figure 9.8, that the maximal and the average errors in the displacements are significantly less for the mixed formulations than for the standard element. An additional indicator for the superiority of some of the mixed formulations is the plot of the field \bar{J} in figure 9.6. Therein, oscillation behavior for the single field, as well as for the P2 and B2 elements can be observed. A further disadvantage of the single field formulation is that the applied load has to be subdivided into a significantly larger amount of load steps. This is necessary in order to be in the range of the convergence of the Newton scheme. Those three results demonstrate the necessity of mixed displacement-pressure approximations for the C^1 continuous BFS element.

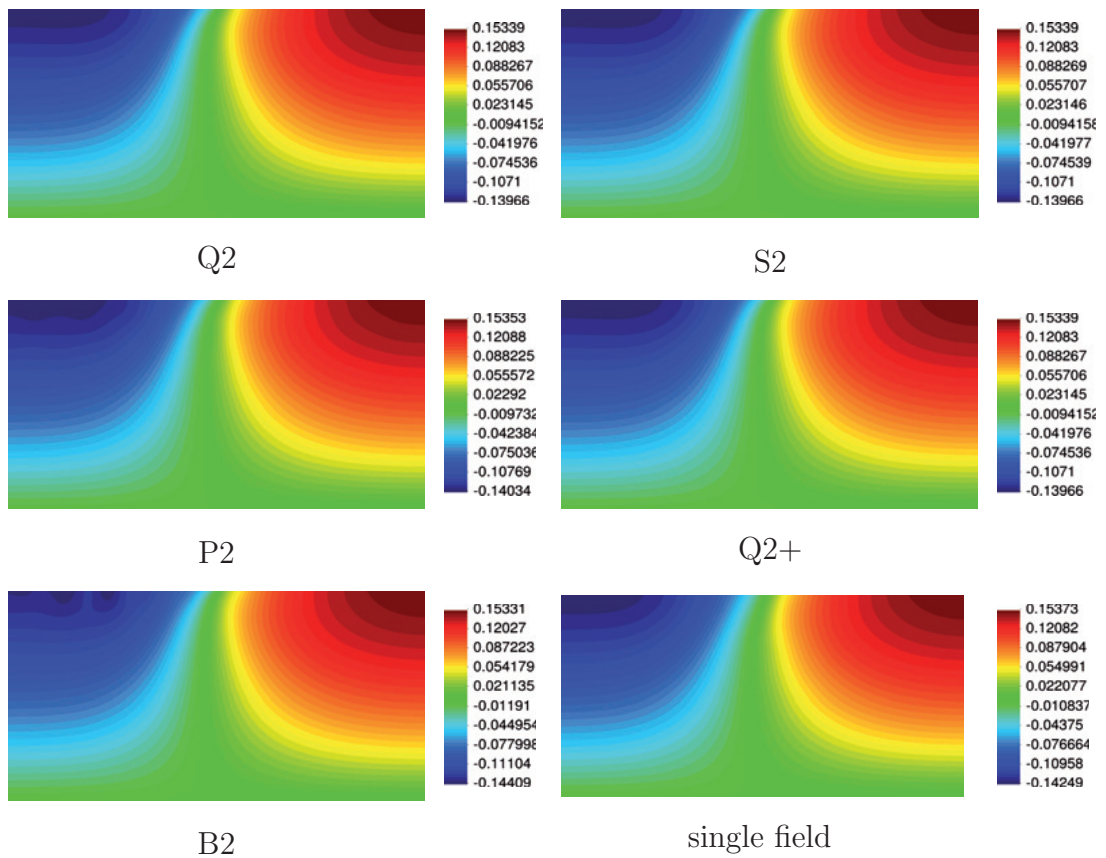


Figure 9.5: Comparison of the horizontal displacement of the different element formulations. The scales are showing the maximal, as well as the minimal values for the horizontal displacement.

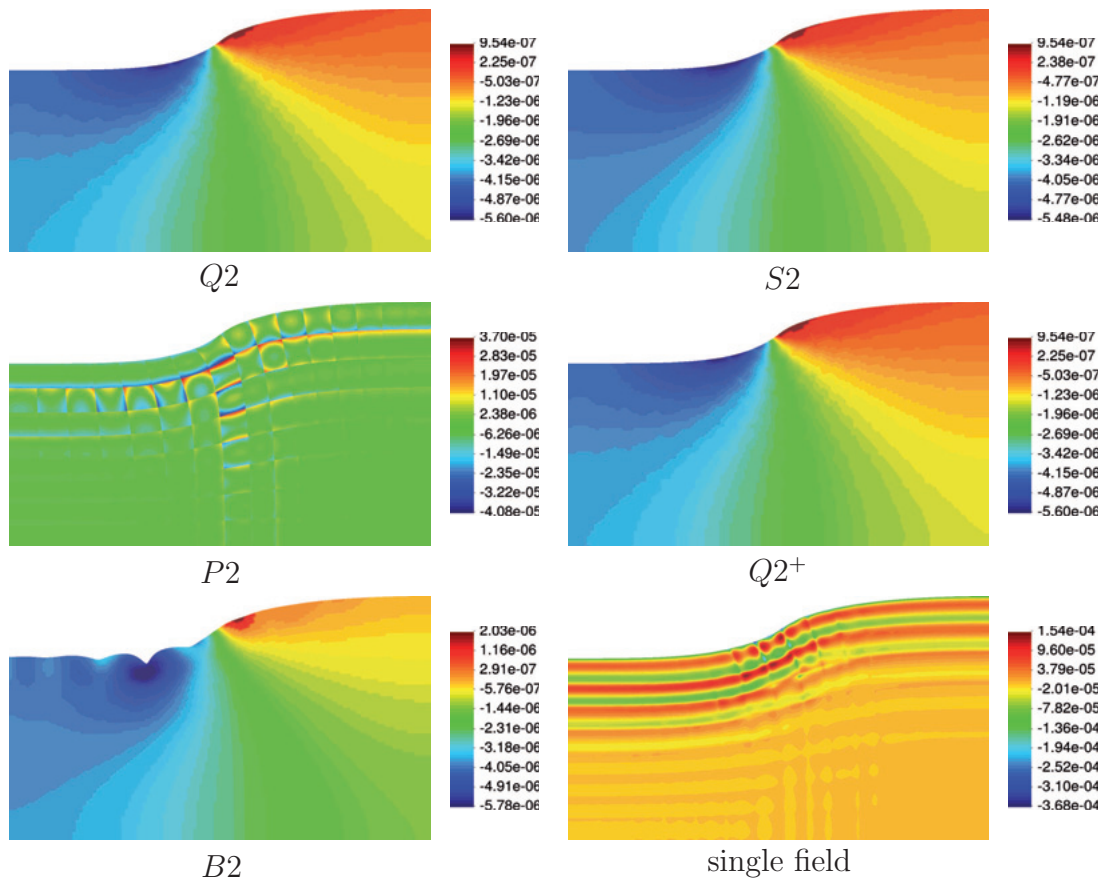
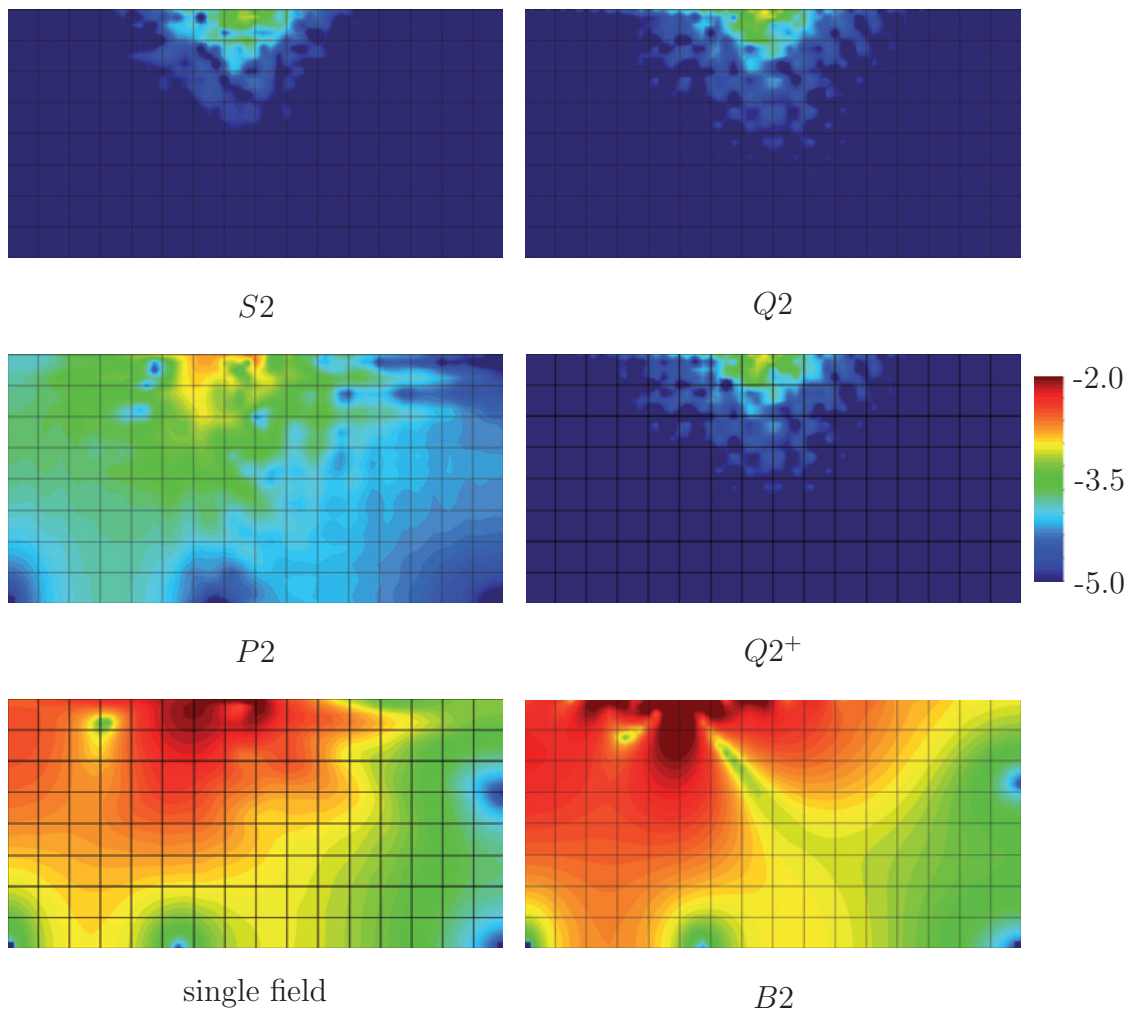
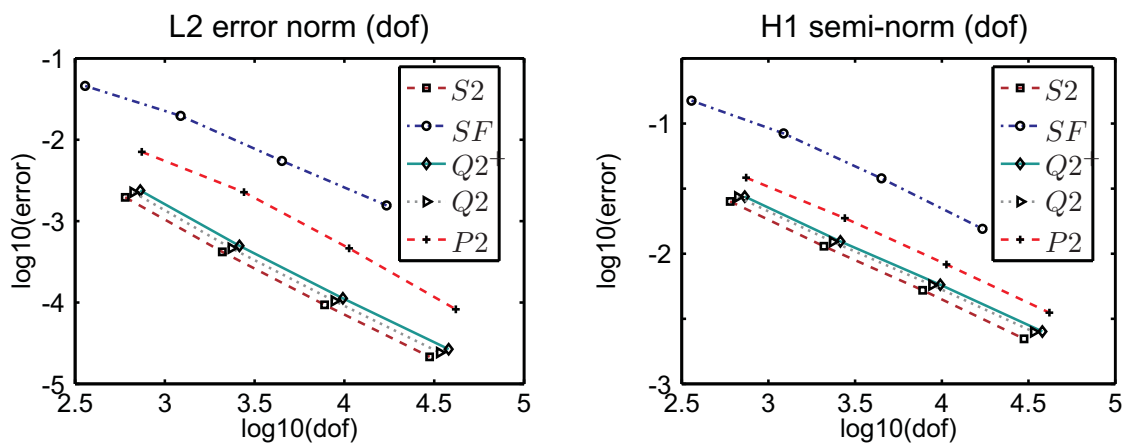


Figure 9.6: Approximation of the field \bar{J} as defined in subsection 9.2.3. The plot is performed on the deformed configuration. \bar{J} is either representing the additional field θ in case of a three-field formulation or the additional field $\det \mathbf{F}$.

**Figure 9.7:** Local error of the displacement in logarithmic scale.**Figure 9.8:** Convergence of the different approximation methods.

9.6 Numerical validation for the strain gradient continuum

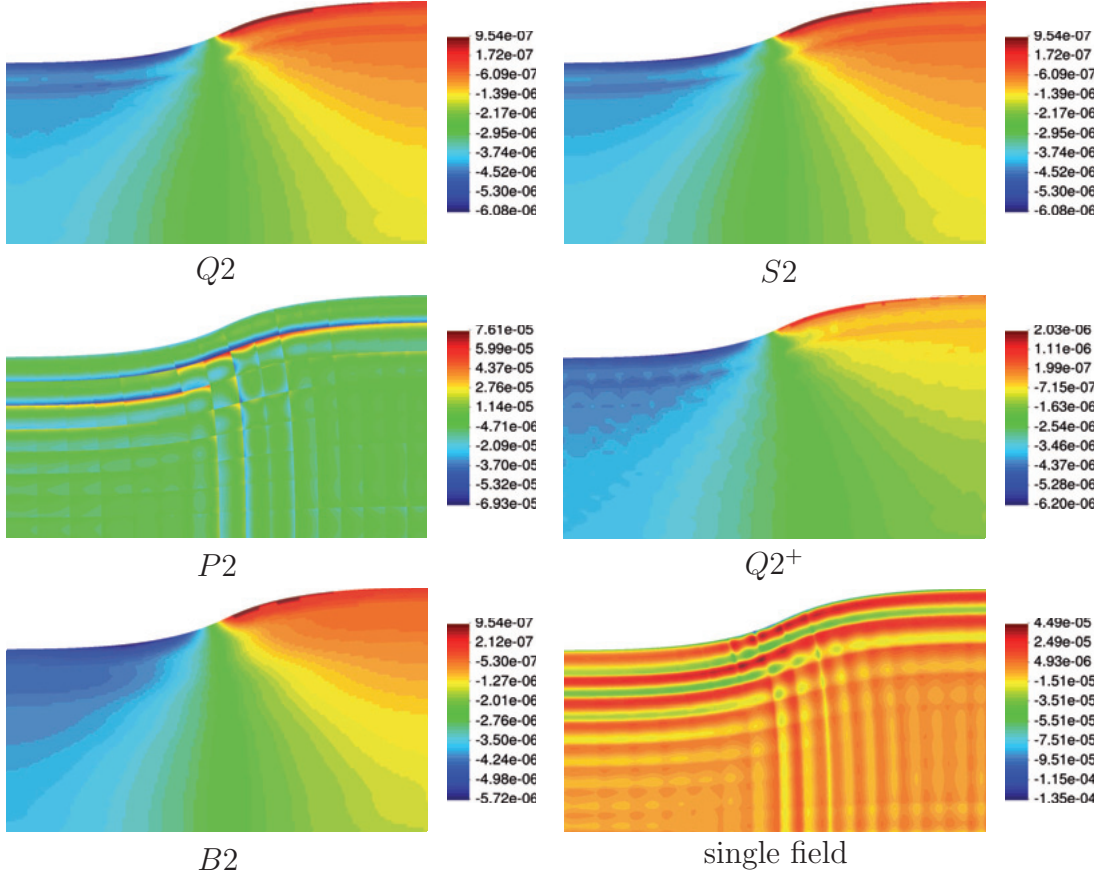


Figure 9.9: Approximation of the field \bar{J} as defined in subsection 9.2.3. The plot is performed on the deformed configuration. \bar{J} is either representing the additional field θ in case of a three-field formulation or the additional field $\det \mathbf{F}$.

For the validation of the mixed formulation for the strain gradient continuum, the same test is used, again. The only difference is that the additional strain energy

$$W^G(\mathbf{G}) = \mu l^2 \mathbf{G} : \mathbf{G}, \quad (9.30)$$

with $l = 0.1$ is added to the potential energy. The contour plots of the additional field θ on the deformed configuration is presented in figure 9.9. Furthermore, in figure 9.10, the local displacement error distribution is presented. The convergence diagrams are presented in figure 9.11. By the comparison with the previous section, several results are obtained. First, the BFS-B2 element is stabilized by the introduction of the strain energy part and the oscillatory behavior of the displacement has vanished. The most interesting result is that the rate of convergence of the single field is now better than that of the mixed element formulations. However, the absolute error is still better for the mixed BFS-Q2 and the BFS-S2 elements. The different results within the last two sections could be explained by the fact that the strain gradient was not split up into a volumetric and deviatoric part. This could cause a punishment of the slight variations of the deformation gradient which

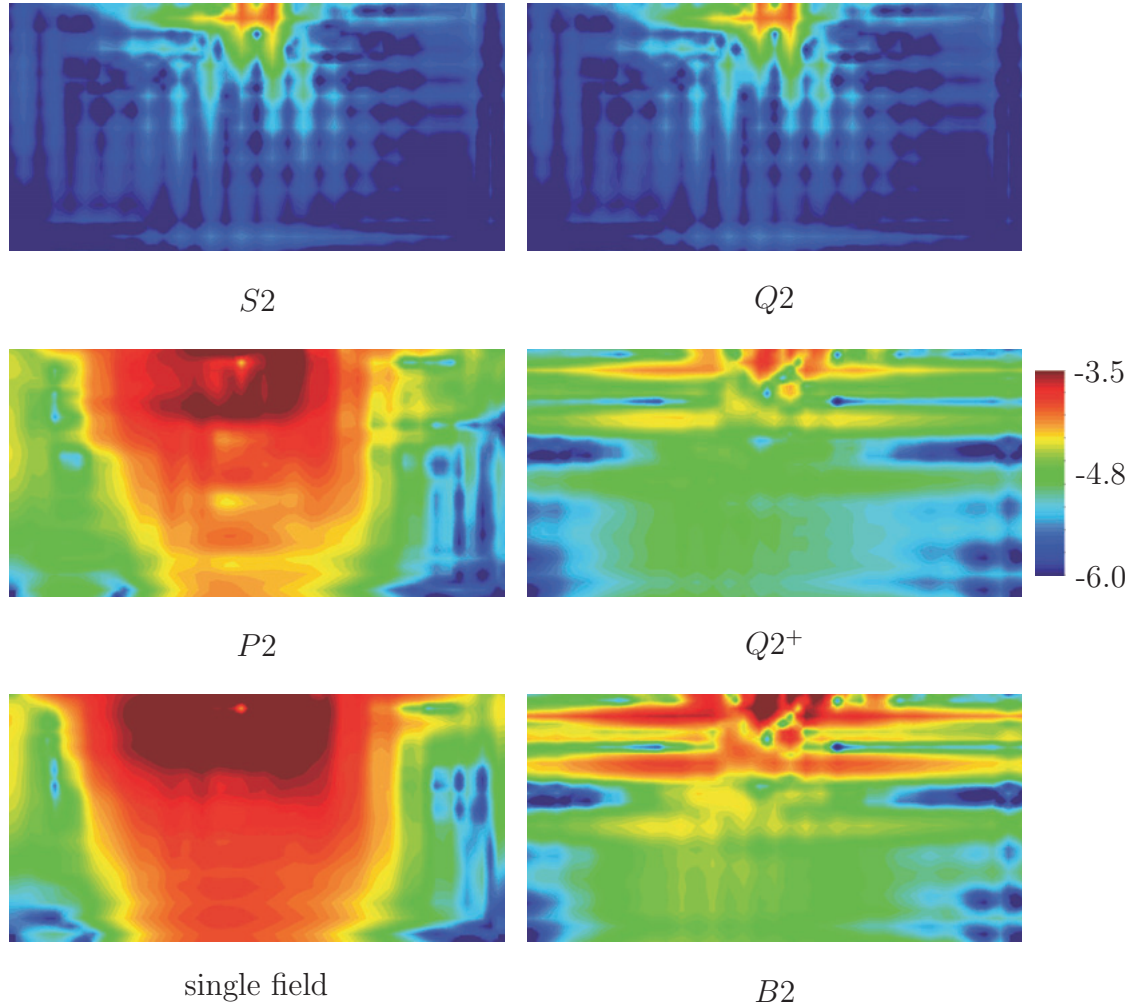


Figure 9.10: Local error of the displacement in logarithmic scale.

are responsible for the better performance of the mixed displacement-pressure elements. A possible split of the strain energy $W^{\mathbf{G}}(\mathbf{G})$ could be

$$W^{\mathbf{G}}(\mathbf{F}, \mathbf{G}) = W_{dev}^{\mathbf{G}}(\bar{\mathbf{G}}) + W_{vol}^{\mathbf{G}}(\nabla_{\mathbf{x}} \det \mathbf{F}), \quad (9.31)$$

where by the definition $\bar{\mathbf{G}} := \nabla_{\mathbf{x}} \bar{\mathbf{F}}$ and the use of $\nabla_{\mathbf{x}} \det \mathbf{F}$ an implicit dependency of $W^{\mathbf{G}}$ on the deformation gradient itself is induced. Therefore, the simplification as presented in subsection 2.4.2 can not be used, thus complicating the constitutive equations significantly. The verification of the split of the strain gradient energy as proposed in (9.31) is left for future work.

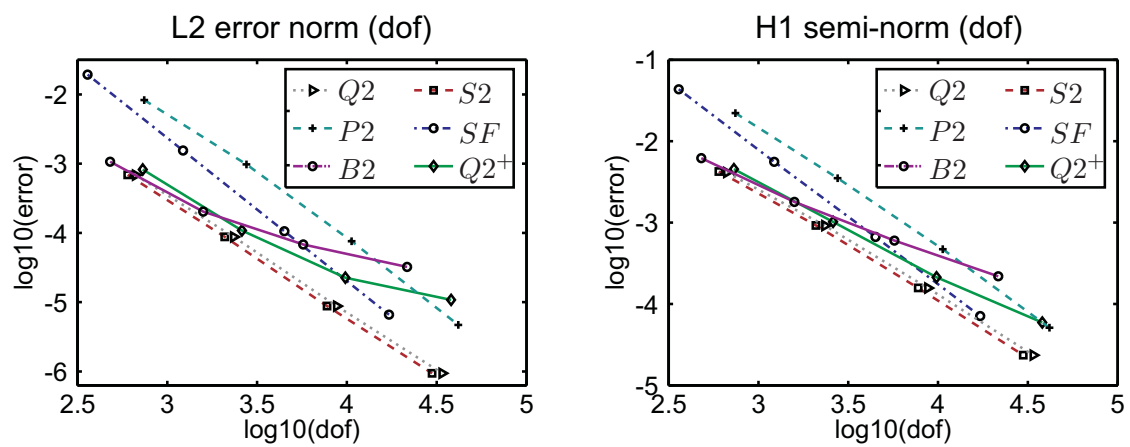


Figure 9.11: Convergence of the different approximation methods for the test with the strain gradient continuum.

10 Cahn-Hilliard equation

An additional fourth order problem, where C^1 continuous discretization methods are necessary is the Cahn-Hilliard equation. The Cahn-Hilliard equation is a nonlinear fourth order partial differential equation, describing phase separation of binary mixtures. In this chapter, we present an application of the natural element method (NEM) to the Cahn-Hilliard equation. As described in chapter 7, the NEM can be used in its original C^0 continuous form with the Sibson or Laplace interpolant or a smoothing algorithm can be used to achieve Farin's C^1 interpolant. Here, both possibilities are used for the application to the Cahn-Hilliard equations. Therefore, the numerical solutions requires either a two field formulation with C^0 continuous shape functions or a higher order C^1 continuous approximation to solve the fourth order equation directly. The C^1 NEM, based on Farin's interpolant is used for the direct treatment of the second order derivatives, occurring in the weak form of the fourth order partial differential equations. Additionally, the classical C^0 continuous Sibson interpolant is applied to the set of two coupled second order equations. It is demonstrated that both methods provide similar results, however, the C^1 continuous version needs fewer degrees of freedom to capture the contour of the phase boundaries.

10.1 Introduction

The Cahn-Hilliard equation is a mathematical description of the kinematics and morphology evolution of phase separation. Typical examples of phase separation include multiphase fluid flow [52, 91], image processing [81], mineral exsolution and growth [146], biological applications [135] and polymer science [223], to mention just a few.

In phase separation or spinodal decomposition, a binary mixture of two components moves against the concentration gradients and forms components pure in each phase. This effect is driven by the gradients of the chemical potential. The whole process is governed by two energies, a local configurational energy and a nonlocal surface energy. The local configurational energy is a function of the concentrations, whereas the surface energy depends on the concentration gradients.

Starting with a homogeneous mixture, the spinodal decomposition can be classified into two stages. The initial stage of the phase separation minimizes the configurational energy by driving the local concentration into the two local minima of the energy potential that are associated with the pure phases. The second stage, which can be identified to be equivalent to Ostwald ripening [166], minimizes the surface energy by reducing the number of pure phase regions.

The numerical solution of the Cahn-Hilliard equation is extremely challenging. Firstly, because of multiple reasons, the initial phase separation and the minimization of the surface energy takes place at different time scales. Secondly, the configurational energy is a highly nonlinear function of the concentration. And third, the most critical point is that the Cahn-Hilliard equation is a fourth order partial differential equation. These three difficulties result in the necessity of adaptive time stepping schemes and the requirement

of iterative solutions within each of the time steps. The treatment of the fourth order gradients of the concentration requires either C^1 continuous approximation schemes or the decomposition of the partial differential equation into two second order equations. Both methods have shown to be applicable for the solution of the Cahn-Hilliard equation, i.e. see [112, 176, 195] for C^1 continuous approximation schemes, [220] for the application to the discontinuous Galerkin method or [86, 146, 210] for application of the operator decomposition.

In this chapter, a comparison of the direct solution based on the C^1 natural element method and an equation decomposition, treated with the C^0 NEM based on Sibson's interpolant is presented. It is mainly based on [101].

We start with a review of the Cahn-Hilliard equation in section 10.2, the decomposition of the Cahn-Hilliard equation into two second order equations is revisited in section 10.3. This is followed by section 10.4, introducing the weak forms of the equations. For temporal discretization, a generalized trapezoidal method is discussed in section 10.5. This is followed by the introduction of the discrete residuals and stiffness matrices in section 10.6 and a short presentation of the practical application of periodic boundary conditions is presented in section 10.7. The contribution closes with a numerical example and discussion of the results in section 10.8.

10.2 Governing equations

We consider a binary mixture of two constituents with c and $1 - c$ as their respective concentrations. The concentration c satisfies $0 \leq c \leq 1$. Pure phases are obtained for $c = 0$ and $c = 1$. Let $\mathcal{B} \subset \mathbb{R}^d$, $d = 1, 2$ or 3 be an open, simply connected domain. The Cahn-Hilliard equation describes the evolution of the concentration \dot{c} by the following diffusion equation,

$$\dot{c} = -\nabla \cdot \mathbf{j} \quad \text{with} \quad \mathbf{j} = -M\nabla\mu. \quad (10.1)$$

Here, the flux of the concentration \mathbf{j} is driven by the gradients of the chemical potential $\nabla\mu$ weighted by the mobility $M > 0$.

The chemical potential μ is the variational derivative of the free energy density Ψ^c , $\mu = \delta_c(\Psi^c)$. For the Cahn-Hilliard equation, the free energy density

$$\Psi^c = \Psi^{con}(c) + \Psi^{sur}(\nabla c), \quad (10.2)$$

is decomposed into the configurational energy, parameterized in terms of the local concentration c and the surface term $\Psi^{sur}(\nabla c)$, parameterized in the concentration gradient. The configurational energy is assumed to have the symmetric form

$$\Psi^{con} = RT [c \log(c) + [1 - c] \log(1 - c) + 2\theta c[1 - c]]. \quad (10.3)$$

In (10.3) R is the gas constant, T the absolute temperature in Kelvin and $\theta = T_c/T$ the dimensionless ratio between the critical and the absolute temperature. The critical temperature T_c is the lowest temperature at which the two phases attain the same composition. The contribution of the configurational energy to the chemical potential will be denoted as

$$\mu_c = \delta_c \Psi^{con}. \quad (10.4)$$

$\Psi^{sur}(\nabla c)$, denotes the surface energy parameterized in terms of the concentration gradient ∇c . Here a quadratic function is used for the interface energy expression

$$\Psi^{sur} = \frac{1}{2}\lambda||\nabla c||^2, \quad (10.5)$$

where the parameter λ is related to an internal length scale l as $\lambda = l^2 RT$. Its contributions to the chemical potential takes the following explicit representation

$$-\nabla \cdot (\delta_{\nabla c} \Psi^{sur}) = -\lambda \Delta c. \quad (10.6)$$

By inserting (10.4) and (10.6) in (10.1), we obtain the typical fourth order Cahn-Hilliard equation

$$\dot{c} = \nabla \cdot (M \nabla (\mu_c - \lambda \Delta c)). \quad (10.7)$$

To achieve the initial boundary value problem, the boundary $\Gamma = \partial \mathcal{B}$ of the domain with an outward unit normal \mathbf{N} is considered. Here, it is assumed that the boundary is sufficiently smooth. The boundary is composed of two complementary parts $\Gamma = \Gamma_c \cup \Gamma_t = \Gamma_g \cup \Gamma_q$ on which either Dirichlet or Neumann boundary conditions are prescribed. The strong form of the problem is stated as follows:

Find $c : \mathcal{B} \times (0, \mathcal{T}) \rightarrow \mathbb{R}$ such that

$$\dot{c} = \nabla \cdot (M \nabla (\mu_c - \lambda \Delta c)) \text{ in } \mathcal{B} \times (0, \mathcal{T}) \quad (10.8)$$

satisfying the initial value

$$c(x, 0) = c_0(x) \text{ in } \mathcal{B} \quad (10.9)$$

subject to the following boundary conditions

$$\begin{array}{lll} c = \bar{c} & \text{on } \Gamma_c \times (0, \mathcal{T}) & \text{or} & M \nabla (\mu_c - \lambda \Delta c) \cdot \mathbf{N} = \bar{t} & \text{on } \Gamma_t \times (0, \mathcal{T}) \\ \nabla c \cdot \mathbf{N} = \bar{g} & \text{on } \Gamma_g \times (0, \mathcal{T}) & \text{or} & M \lambda \Delta c = \bar{q} & \text{on } \Gamma_q \times (0, \mathcal{T}). \end{array} \quad (10.10)$$

In (10.10), the boundary conditions are represented in a general form. The upper row constitute the Dirichlet boundary conditions on the concentration and the first order Neumann boundary conditions. The second row of (10.10) represents the remaining set of boundary conditions. In this contribution, either homogeneous Neumann or periodic Dirichlet boundary conditions are used.

Remark 10.1 Mobility:

In most physical applications, the mobility M is assumed as $M = Dc[1 - c]/[RT]$, where D is the diffusivity which has units of length²/time. The above relationship for the mobility restricts the diffusion process primarily to the interfacial zones and is commonly referred to as degenerate mobility. To simplify the equations, the mobility is often approximated to be constant $M = D/[RT]$.

10.3 Decomposition of the diffusion equation

To avoid the difficulty of the fourth order diffusion equation, the non-local concentration field

$$\bar{c} = c + \kappa \Delta c \quad (10.11)$$

is introduced. Accordingly, the surface part of the chemical potential

$$-\nabla \lambda \Delta c = -\gamma \nabla(\bar{c} - c) \quad (10.12)$$

can be expressed in terms of the local concentration field c and the nonlocal concentration field \bar{c} . The new parameters κ and γ are introduced as decomposition of the parameter λ by $\gamma = \lambda/\kappa$. In principle, this decomposition can be chosen arbitrarily. Here the concrete value is used for scaling of the numerical equations, occurring in section 10.6.

By inserting (10.12) into the original form of the Cahn-Hilliard equation (10.7), the single fourth order partial differential equation is thus replaced by the set of two second order equations

$$\begin{aligned} \dot{c} &= \nabla \cdot (M \nabla(\mu_c + \gamma[c - \bar{c}])) \\ \bar{c} &= c + \kappa \Delta c. \end{aligned} \quad (10.13)$$

10.4 Weak form of the Cahn-Hilliard equation

The weak form of equation (10.7) and (10.13) is achieved by multiplication with the test functions w and \bar{w} and integrating over the domain \mathcal{B} . By application of integration by parts, symmetric equations are derived. The result of the fourth order equation (10.7) is given by

$$\begin{aligned} &\int_{\mathcal{B}} w \dot{c} + \Delta w M \lambda \Delta c + \nabla w \cdot [M \nabla \mu_c + \nabla M \lambda \Delta c] \, dV \\ &- \int_{\Gamma} w M \nabla(\mu_c - \lambda \Delta c) \cdot \mathbf{N} - M \lambda \Delta_c \nabla w \cdot \mathbf{N} \, dA \doteq 0. \end{aligned} \quad (10.14)$$

The weak form of (10.13) results in the set of two equations

$$\begin{aligned} &\int_{\mathcal{B}} \dot{c} w + \nabla w \cdot [M \nabla \cdot [\mu_c + \gamma[c - \bar{c}]]] \, dV - \int_{\Gamma} w M \nabla \mu \cdot \mathbf{N} \, dA \doteq 0 \\ &\int_{\mathcal{B}} w [\bar{c} - c] + \nabla \bar{w} \cdot \kappa \nabla c \, dV - \int_{\Gamma} \bar{w} \lambda^2 \nabla c \cdot \mathbf{N} \, dA \doteq 0. \end{aligned} \quad (10.15)$$

In contrast to (10.14), where second order derivatives are occurring, (10.15) only contains first derivatives in the resulting expressions.

10.5 Time integration

To discretize the residual equations (10.15) and (10.14) in time, the generalized trapezoidal method is used. To this end, the time interval $(0, \tau)$ is partitioned into discrete strictly

positive subintervals $[t_n, t_{n+1}]$ with current increment $\Delta t = t_{n+1} - t_n$. From here on, the index \circ_{n+1} is omitted for sake of transparency.

The starting point is the known concentration c_n , at the beginning of the current time step Δt . The generalized trapezoidal method is used for the update of the concentration in time, according to the concentration functional $\Pi_B(c, w)$, defined by

$$\begin{aligned}\Pi_B(c, w) := & \int_B \Delta w M \lambda \Delta c + \nabla w \cdot [M \nabla \mu_c + \nabla M \lambda \Delta c] \, dV \\ & - \int_{\Gamma} w M \nabla(\mu_c - \lambda \Delta c) \cdot \mathbf{N} + M \lambda \Delta c \nabla w \cdot \mathbf{N} \, dA\end{aligned}\quad (10.16)$$

or the corresponding expression for the two field problem

$$\begin{aligned}\Pi_B^c(c, w) := & \int_B \nabla w \cdot [M \nabla \cdot [\mu_c + \gamma[c - \bar{c}]]] \, dV \\ & - \int_{\Gamma} M \nabla \mu \cdot \mathbf{N} \, dA\end{aligned}\quad (10.17)$$

In a semi-discretized form, using the generalized trapezoidal method, we write

$$R_{n,\alpha}(c, w) = \int_B \frac{1}{\Delta t} w [c - c_n] \, dV + \alpha \Delta t \Pi_B(c, w) + [1 - \alpha] \Delta t \Pi_B(c_n, w) \doteq 0. \quad (10.18)$$

10.6 Stiffness matrices

By introducing the C^1 continuous interpolation functions in the semi-discretized form (10.18), the discrete residuals are

$$R_{n,\alpha}(c, N_I^1) = \int_B N_I^1 \frac{1}{\Delta t} [c - c_n] \, dV + \alpha \Pi_B(c, N_I^1) + [1 - \alpha] \Pi_B(c_n, N_I^1) \doteq 0. \quad (10.19)$$

For the solution of the highly-nonlinear discrete residual equations (10.19), the Newton-Raphson method is used,

$$R_{n,\alpha}^{k+1} = R_{n,\alpha}^k + dR_{n,\alpha} \doteq 0 \quad \text{with} \quad dR_I = \sum_{J=1}^{3m} K_{IJ} dc_J. \quad (10.20)$$

The corresponding iteration matrix takes the following explicit representation:

$$\begin{aligned}K_{IJ} = & \int_B N_I^1 \frac{1}{\Delta t} N_J^1 \\ & + \alpha \left[\int_B \Delta N_I^1 \lambda [M \Delta \partial_c M N_J^1] \, dV \right. \\ & + \int_B \nabla N_I^1 \cdot [\nabla \mu_c \partial_c M N_J^1 + M \partial_c \mu_c \nabla N_J^1] \, dV \\ & + \int_B \nabla N_I^1 \cdot [\lambda [\Delta c \partial_c M \nabla N_J^1 + \nabla M \Delta N_J^1]] \, dV \\ & \left. + \int_B \nabla N_I^1 \cdot [\lambda \Delta c \partial_c^2 M \nabla c N_J^1 + M \partial_c^2 \mu_c \nabla c N_J^1] \, dV \right].\end{aligned}\quad (10.21)$$

For the mixed form, the two sets of residual equations are identified as follows:

$$\begin{aligned} R_{n,\alpha}^c &= \int_{\mathcal{B}} N_I^0 \frac{c - c^n}{\Delta t} dV + \alpha \Pi_{\mathcal{B}}(c, N_I^0) + [1 - \alpha] \Pi_{\mathcal{B}}(c_n, N_I^0) \doteq 0 \\ R^{\bar{c}} &= N_J^0 [\bar{c} - c] + \nabla N_J^0 \kappa \nabla c \doteq 0 \end{aligned} \quad (10.22)$$

with the following iteration matrices

$$\begin{aligned} K_{IK}^{cc} &= \int_{\mathcal{B}} N_I^0 \frac{1}{\Delta t} N_K^0 dV \\ &\quad + \int_{\mathcal{B}} \nabla N_I^0 \cdot [M \partial_c \mu_c + \gamma] \nabla N_K^0 dV \\ &\quad + \int_{\mathcal{B}} \nabla N_I^0 \cdot [\partial_c M \nabla [\mu_c + \gamma[c - \bar{c}]]] N_K^0 dV \\ &\quad + \int_{\mathcal{B}} \nabla N_I^0 \cdot [M \partial_c \nabla c \mu_c] N_K^0 dV \\ K_{IL}^{c\bar{c}} &= - \int_{\mathcal{B}} \nabla N_I^0 \cdot M \gamma \nabla N_L^0 dV \\ K_{JK}^{\bar{c}c} &= - \int_{\mathcal{B}} N_J^0 N_K^0 + \nabla N_J \cdot \kappa \nabla N_K^0 dV \\ K_{IL}^{\bar{c}\bar{c}} &= \int_{\mathcal{B}} N_J^0 N_L^0 dV. \end{aligned} \quad (10.23)$$

10.7 Periodic boundary conditions

At this point, either C^1 continuous finite elements, as presented in chapter 5 or the isogeometric analysis of chapter 6 can be used for the application of the discretized equation (10.22). Here, Farins C^1 interpolant (see subsection 7.3.1) is used. The behavior of the C^1 Farin interpolant along the boundary of the domain is identical to a 1d cubic Hermite interpolation, see section 4.1.2. Unfortunately, this statement is not valid for the normal derivatives of the function. Due to this reason, for exact application of C^1 continuous boundary conditions either the bubble functions $6(\lambda_1 \lambda_2 \lambda_3)$ have to be rearranged at the boundary, such that the normal derivative is linear between two boundary nodes or the Voronoi cells have to be computed directly on the periodic topology. In this contribution, the latter has been chosen.

Considering a periodic box with width l_1 and height l_2 , the distance on the modulo space $\mathbb{R}/l_1\mathbb{R} \times \mathbb{R}/l_2\mathbb{R}$ is given by

$$d(\mathbf{x}, \mathbf{y}) := \left[\sum_i [\min \{|x_i - y_i|, l_1 - |x_i - y_i|\}]^2 \right]^{\frac{1}{2}} \quad (10.24)$$

and the periodicity is a simple consequence of the definition of the Sibson interpolant. The resulting periodic boundary box is illustrated in figure 10.1(a).

10.8 Computational results

Here, the solution for the C^0 NEM with Sibson's interpolant of subsection 7.2.3 and the C^1 NEM of subsection 7.3.1 are compared. A periodic unit square domain with length $l_1 = 20$

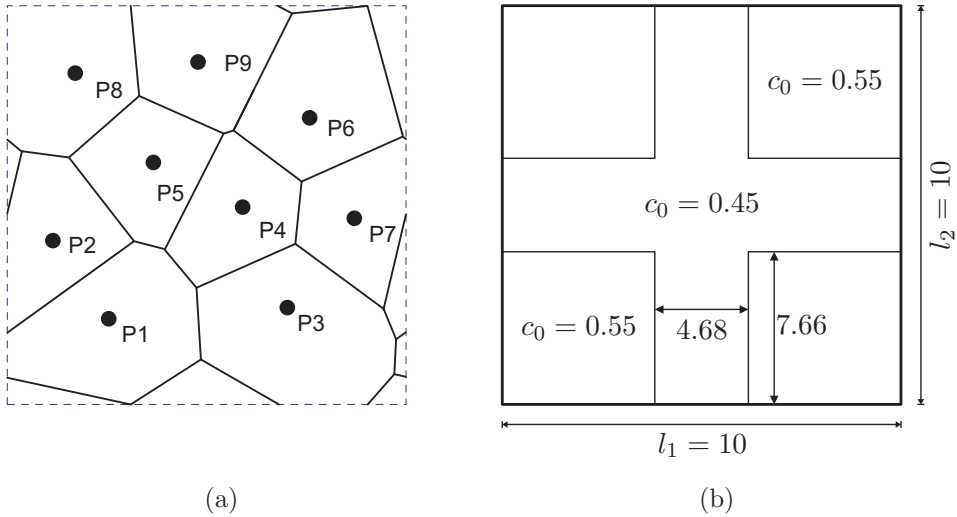


Figure 10.1: (a) Voronoi cells on periodic domain. (b) Initial concentration of the presented numerical example.

and $l_2 = 20$ has been used. For the comparison of the results, the initial concentration is given by

$$c_0(\mathbf{x}) = \begin{cases} 0.55 & \text{for } \min_i(x_i) \leq 2.34 \\ 0.45 & \text{for } \min_i(x_i) > 2.34. \end{cases} \quad (10.25)$$

This is illustrated in figure 10.1(b). The computations are performed with degenerate mobility and the dimensionless material parameters: $D = 2$, $RT = 2000$, $\theta = 1.1$ and $\lambda = 500$. An initial time step of $\Delta t = 10 \times 10^{-3}$ is considered. Figure 10.2 illustrates the behavior of the internal energies for different discretizations. The fine discretizations have 200, 1250 and 5000 degrees of freedom in case of the C^0 continuous discretization and 192, 1200 and 7500 in case of the C^1 continuous results. To be able to see any difference in the contour plots of the concentration for the comparison of the results of the C^0 and C^1 continuous approximation, in figure 10.3, the coarsest meshes is used. It contains 64 points in case of the C^1 solution and 100 points for the C^0 continuous solution. By the presented example, it is shown that both, the C^1 as well as the C^0 continuous discretization methods lead to similar results. For the coarse solution, the C^1 continuous discretization delivers smoother concentration profiles, compare figure 10.3. However, even more important, the C^1 continuous discretization demonstrates faster convergence in the energy plot, see figure 10.2 for details. Especially to reach the energy level of the semi-stable solution after phase separation, the C^0 continuous discretization method needs a much higher total number of degrees of freedom. Additionally, the initial behavior for the C^1 NEM is similar for the medium and fine concentrations, whereas it is still varying a lot in case of the C^0 NEM. Therefore, we propose to choose the C^1 continuous discretization whenever possible. Nevertheless, one single example is definitely not enough and further investigations on the behavior of the two different types are necessary. Additionally, those results have to be compared to different numerical schemes such as the finite element method or the isogeometric analysis, presented in chapter 5 and chapter 6.

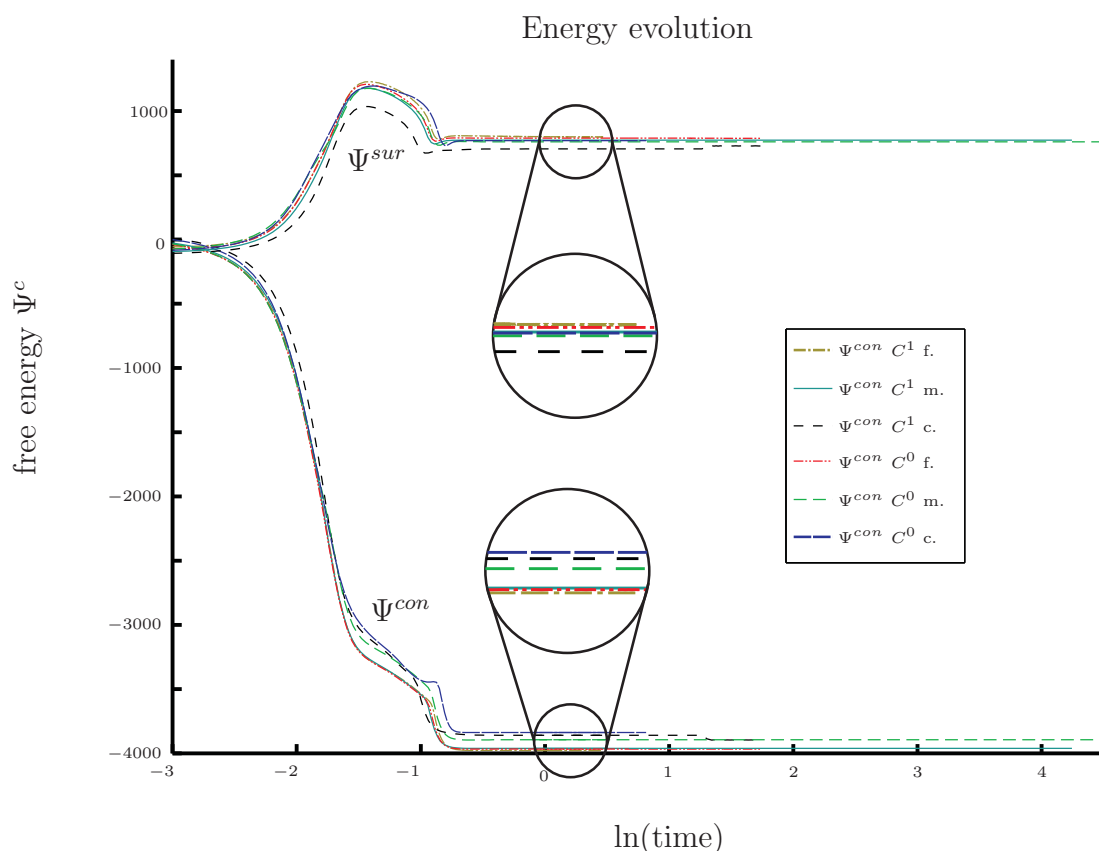


Figure 10.2: Energy evolution whithin the phase separation processes.

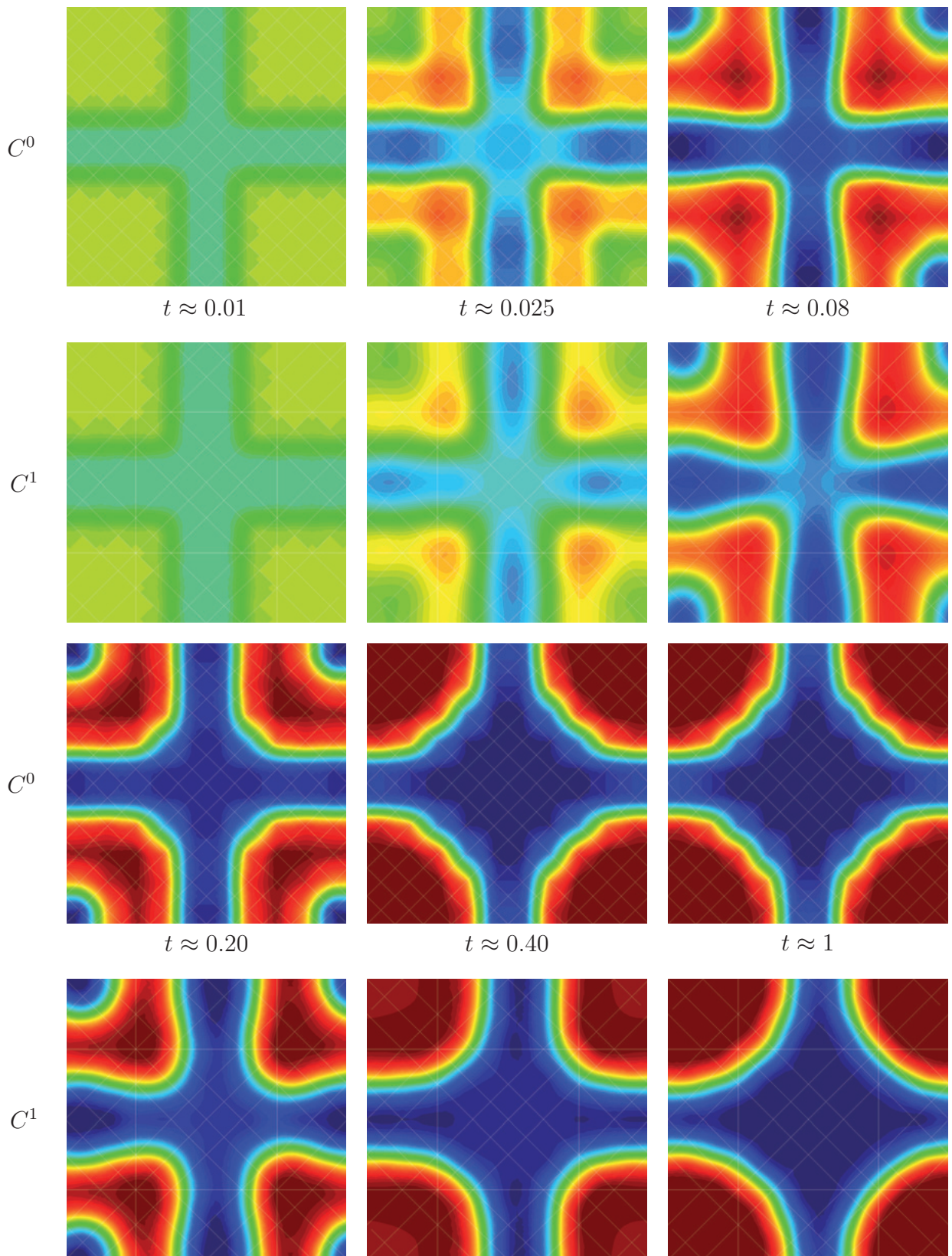


Figure 10.3: Evolution of concentration for a coarse mesh. Comparison of C^1 and C^0 NEM.

11 Conclusion

11.1 Summary

The main objective of this work is the systematic investigation of different C^1 continuous numerical methods for the application to gradient elasticity. Therefore, in the first chapters 2 and 3, the underlying equations are derived. In chapter 4 the basic principles of the use of control points, for the construction of C^1 continuous finite element shape functions are presented.

This is followed by the explicit computation of several C^1 continuous finite element shape functions in chapter 5 and the additional presentation of the isogeometric analysis, chapter 6, and the natural element method, chapter 7. The main part of this work closes with a numerical comparison of the methods, presented in chapter 8.

Besides the major topic of the comparison of the numerical methods, performed in the first part, two additional aspects are considered, namely the investigation of the BFS element at the incompressible limit, see chapter 9 and the application of the NEM to the Cahn-Hilliard equation in chapter 10.

11.2 Main contribution

A brief summary of new contributions and results is presented within this section. The main contributions of chapter 5 is the most extensive computation of subparametric C^* and C^1 continuous shape functions in a unified representation, by means of the Bernstein-Bézier representation given in chapter 4. These results are presented in sections 5.2 and 5.3. Within this framework, two new variations of the PS-6 split element are proposed in subsection 5.3.5, one of them is showing similar convergence behavior like the original C^1 continuous version, but without the complicated nonlocal construction of the split of the macroelement.

Furthermore, the Bézier representation is used to describe the local construction of isoparametric C^1 continuous finite elements, in section 5.4. This is followed by the introduction of a new and simple mesh construction, and a linear mesh optimization algorithm in subsections 5.4.5.2 and 5.4.5.3. It is demonstrated in chapter 8 that the mesh optimization algorithm can improve the results of the existing mesh construction algorithm, proposed by [169] and used in [234] by 90%. Here, we want to point out that the general principle of the C^1 continuous mesh construction is presented in appendix C, where it is applied to the triangular Bell element. Up to our knowledge, this is additionally the first time where unstructured isoparametric triangular elements are used to solve problems of numerical analysis.

In chapter 6, a short introduction to the isogeometric analysis is presented. Since, it is applied to gradient elasticity for the first time, special aspects such as gradient and

symmetry boundary conditions are discussed in section 6.3.

Chapter 7 deals with the application of the C^1 continuous natural element method for the application to gradient elasticity. Therein two new aspects are explored. The first is the investigation of the performance of a numerical integration, based on a triangulation of the Voronoi cells, see subsection 7.4.2 and second, in subsection 7.4.3 the possible influence of additional bubble functions on the performance of the natural element method is analyzed.

The major part of this work is the presentation of an extensive numerical comparison of several C^1 continuous methods within the application to gradient elasticity. Therefore, in chapter 8, the performance of the methods is compared using several numerical examples. To get a relation to the underlying mathematical theory, this work introduced the measurement of the errors based on the L^2 , H^1 and H^2 Sobolev norms for both, the linear and nonlinear gradient elasticity. The first major result is the identification of the strong influence of the boundary approximation of the linear, subparametric elements. In subsection 8.1.2, it is observed that a linear interpolation of the boundary is dramatically reducing the rate of convergence, as well as the absolute error for all subparametric elements. The error can be significantly decreased, if a linear, area preserving approximation of the boundary is applied. In the second part of chapter 5, i.e. section 8.2, the application of the numerical schemes to nonlinear gradient elasticity is investigated. To get rid of the undesired effect of the boundary approximation, a new benchmark example, the inhomogeneous compression test is proposed in subsection 8.2.1. An additional result is the failure of the Morley element within the framework of finite strain.

Two additional problems have been studied within this work. In chapter 9 the behavior of the BFS element at the incompressible limit is examined. In this process new, mixed finite elements are proposed. In the last chapter (chapter 10), the Cahn-Hilliard equation is solved with the use of the natural element method. Therefore, Farin's C^1 interpolant is compared to the Sibson interpolant with a split of the partial differential equation. Based on a computational example, it is demonstrated that the use of C^1 continuous shape functions is superior to the use of C^0 continuous functions with a set of two equation.

11.3 Outlook

Here, a brief overview on the methods, which desire further investigations, but could not be taken into account within this contribution are listed below.

Boundary approximation As demonstrated in the results of chapter 8, some more work should be done within the right approximation of the boundary. Therefore, an investigation of a least square fit of the subparametric as well as the isoparametric finite elements should be investigated further. Especially, since the use of isoparametric triangular elements as presented in appendix C, introduces second order derivatives for the interpolation of the geometry boundary. Thus, the complexity of the boundary interpolation is drastically increased.

Furthermore, an interesting aspect could be the consideration of boundary patches, as introduced by [54] and used in the works of Bernadou et al. [31,33] for the exact represen-

tation of the geometry of shells. Further developments are presented in [175], where the boundary patches are improved, such that essential boundary conditions can be applied exactly.

An additional treatment could be the use of weight function for the representation of the geometry together with the use of simple B-splines for the construction of C^1 continuous shape functions. An excellent description of the method is given in the textbook of Höllig [127].

Extension to three dimensions An extension to three dimensions is absolutely necessary. This is already initiated by the work of [167], but further existing C^1 continuous numerical methods have to be tested. This could be the three dimensional extension of the NEM and the IGA, which seems to be straightforward. Furthermore tetrahedral subparametric elements as presented in [221], [5], [184] or [8] should be considered.

Due to the complex structure of the tetrahedral C^1 continuous finite elements in three dimensions and the problems concerning the geometrical restriction of the IGA, caused by difficulties in the combination of several patches, three-dimensional C^* elements could be interesting. Possible examples are the element of Ženíšek [231] where the shape functions are only C^1 at the nodal points and the extension of the Morley triangle, recently presented in [163].

More finite elements Since there is such a huge number of different element formulations, we restricted ourselves to the class of fully polynomial shape functions. The maybe earliest approach where singular element shape functions are used for the construction of C^1 interpolants is due to Irons [132]. The reader with special interest in rational shape functions is referred to Peano [168]. Those elements have not been considered in this thesis, but would be very interesting for future works.

A further restriction of this contribution is that only the elements of one kind with minimal polynomial order and continuity are considered. Extensions to higher order continuity (C^r , $r \geq 2$) are given in [230] and [182] for fully polynomial shape functions or [180] for macroelements, where additionally an excellent explanation for the use of Bernstein-Bézier patches is presented. Additional references are [6, 147] for the extension of the HCT element and [7, 148, 183] for the Powell-Sabin type elements.

Additional numerical formulations Despite the small number of elements and numerical methods, presented in this work, there is a large variety of additional approaches, which should be considered. These are mixed formulations as presented in [122, 232, 233] and [111], the discontinuous Galerkin method, used in [87, 155, 219]) or Discrete Kirchhoff elements, see [58, 138, 216] and [190]. However, a comparison of their performance with respect to each other or C^1 continuous finite element methods is still missing for most of them.

Furthermore, a comparison of the moving least square method of [17], the meshless local Petrov-Galerkin approach of [203] and the subdivision methods, introduced in [61] and [62] needs further research concerning their performance for the application to gradient elasticity.

A Notation

Throughout this work, the used notations are presented in the following. All scalar quantities are denoted by standard symbols. Vectors and tensors of second and third order are denoted by bold symbols. Tangent operators are labeled by double lines.

- **Tensor notation:**

$$\begin{aligned}
 \mathbf{a} &= a_i \mathbf{e}_i \\
 \mathbf{A} &= A_{ij} \mathbf{e}_i \otimes \mathbf{e}_j \\
 \mathbf{B} &= B_{ijk} \mathbf{e}_i \otimes \mathbf{e}_j \otimes \mathbf{e}_k \\
 \mathbf{A} &= A_{ijkl} \mathbf{e}_i \otimes \mathbf{e}_j \otimes \mathbf{e}_k \otimes \mathbf{e}_l \\
 \mathbf{B} &= B_{ijklmn} \mathbf{e}_i \otimes \mathbf{e}_j \otimes \mathbf{e}_k \otimes \mathbf{e}_l \otimes \mathbf{e}_m \otimes \mathbf{e}_n.
 \end{aligned} \tag{A.1}$$

- **Inner products:**

$$\begin{aligned}
 \mathbf{A} \cdot \mathbf{C} &= A_{ij} C_{jk} \mathbf{e}_i \otimes \mathbf{e}_k \\
 \mathbf{A} : \mathbf{C} &= A_{ij} C_{ij} \\
 \mathbf{B} : \mathbf{D} &= B_{ijk} D_{ijk}.
 \end{aligned}$$

- **Dyadic products for second-order tensors:**

$$\begin{aligned}
 \mathbf{A} \otimes \mathbf{B} &= A_{ij} B_{kl} \mathbf{e}_i \otimes \mathbf{e}_j \otimes \mathbf{e}_k \otimes \mathbf{e}_l \\
 \mathbf{A} \bar{\otimes} \mathbf{B} &= A_{ik} B_{jl} \mathbf{e}_i \otimes \mathbf{e}_j \otimes \mathbf{e}_k \otimes \mathbf{e}_l \\
 \mathbf{A} \underline{\otimes} \mathbf{B} &= A_{il} B_{jk} \mathbf{e}_i \otimes \mathbf{e}_j \otimes \mathbf{e}_k \otimes \mathbf{e}_l
 \end{aligned}$$

- **Identity tensors:**

$$\begin{aligned}
 \mathbf{I}_2 &\text{ identity tensor of second order} \\
 \mathbb{I}_4 &= \mathbf{I}_2 \bar{\otimes} \mathbf{I}_2 \text{ identity tensor of fourth order}
 \end{aligned}$$

- **Transposition:**

$$\begin{aligned}
 \mathbf{A}^T &= A_{ji} \mathbf{e}_i \otimes \mathbf{e}_j \\
 \mathbf{B}^T &= B_{kji} \mathbf{e}_i \otimes \mathbf{e}_j \otimes \mathbf{e}_k
 \end{aligned}$$

- **Multi index**

Let $\alpha \in \mathbb{N}^k$ denote a multi-index with the following definitions

$$|\alpha| = \sum_{i=1}^k \alpha_i, \quad \lambda^\alpha = \prod_{i=1}^k [\lambda_i]^{\alpha_i} \quad \text{and} \quad \binom{n}{\alpha} = \frac{n!}{\alpha!}. \quad (\text{A.2})$$

- **Differential operators**

$$\begin{aligned}\nabla_{\mathbf{x}} \mathbf{a} &= \frac{\partial a_i}{\partial X_j} \mathbf{e}_i \otimes \mathbf{e}_j \\ \nabla_{\mathbf{x}}^2 \mathbf{a} &= \frac{\partial^2 a_i}{\partial X_j \partial X_k} \mathbf{e}_i \otimes \mathbf{e}_j \otimes \mathbf{e}_k \\ \Delta \mathbf{a} &= \frac{\partial^2 a_i}{\partial X_j \partial X_j} \mathbf{e}_i\end{aligned}$$

- **Differential operators on the surface**

$$\nabla_{\mathbf{x}}^S \mathbf{a} = \nabla_{\mathbf{x}} \mathbf{a} \cdot (\mathbf{I} - \mathbf{N} \otimes \mathbf{N})$$

$$\nabla_{\mathbf{x}}^N \mathbf{a} = \nabla_{\mathbf{x}} \mathbf{a} \cdot \mathbf{N}$$

$$\text{Div}^s \mathbf{a} = \nabla_{\mathbf{x}} \mathbf{a} : (\mathbf{I} - \mathbf{N} \otimes \mathbf{N})$$

B Strain gradient elasticity

Within this chapter, the derivation of gradient elasticity is done in a more detailed way. For the interested reader, an excellent overview on the underlying mathematical theorems can be found in Steinmann [193].

Starting with variation of the internal energy density, some mathematical transformations have to be done to identify the local form of the partial differential equation as well as the expressions for the boundary tractions.

Using integration by parts, the variation of the internal energy can be transformed in the following way,

$$\begin{aligned}
\int_{\mathcal{B}_0} \mathbf{P} : \delta \mathbf{F} + \mathbf{Q} : \delta \mathbf{G} \, dV &= \int_{\mathcal{B}_0} \operatorname{Div} (\mathbf{P}^T \cdot \delta \boldsymbol{\varphi}) - \operatorname{Div} \mathbf{P} \cdot \delta \boldsymbol{\varphi} \, dV \\
&\quad + \int_{\mathcal{B}_0} \operatorname{Div} (\nabla_{\mathbf{x}} \delta \boldsymbol{\varphi} : \mathbf{Q}) - \operatorname{Div} \mathbf{Q} : \nabla_{\mathbf{x}} \delta \boldsymbol{\varphi} \, dV \\
&= \int_{\mathcal{B}_0} \operatorname{Div} (\mathbf{P}^T \cdot \delta \boldsymbol{\varphi}) - \operatorname{Div} \mathbf{P} \cdot \delta \boldsymbol{\varphi} \, dV \\
&\quad + \int_{\mathcal{B}_0} \operatorname{Div} (\nabla_{\mathbf{x}} \delta \boldsymbol{\varphi} : \mathbf{Q}) \, dV \\
&\quad - \int_{\mathcal{B}_0} \operatorname{Div} (\delta \boldsymbol{\varphi} \cdot \operatorname{Div} \mathbf{Q}) + \operatorname{Div} (\operatorname{Div} \mathbf{Q}) \cdot \delta \boldsymbol{\varphi} \, dV. \tag{B.1}
\end{aligned}$$

Applying the Gauss divergence theorem on the results of equation (B.1), it results in:

$$\begin{aligned}
\int_{\mathcal{B}_0} \mathbf{P} : \delta \mathbf{F} + \mathbf{Q} : \delta \mathbf{G} \, dV &= \int_{\mathcal{B}_0} \delta \boldsymbol{\varphi} \cdot \operatorname{Div} (\operatorname{Div} \mathbf{Q} - \mathbf{P}) \, dV \\
&\quad + \int_{\partial \mathcal{B}_0} \delta \boldsymbol{\varphi} \cdot [\mathbf{P} - \operatorname{Div} \mathbf{Q}] \cdot \mathbf{N} + \nabla_{\mathbf{x}} \delta \boldsymbol{\varphi} : [\mathbf{Q} \cdot \mathbf{N}] \, dA. \tag{B.2}
\end{aligned}$$

In the last summand of (B.2), the expression $\nabla_{\mathbf{x}} \delta \boldsymbol{\varphi}$ inherits some dependence on the displacement $\delta \boldsymbol{\varphi}$ of the surface of the domain. Therefore it is desirable, to decompose the expression into two independent parts in order to identify the independent higher order Dirichlet boundary conditions:

$$\begin{aligned}
\nabla_{\mathbf{x}}(\bullet) &= \nabla_{\mathbf{x}}(\bullet) \cdot (\mathbf{I} - \mathbf{N} \otimes \mathbf{N}) + \nabla_{\mathbf{x}}(\bullet) \cdot (\mathbf{N} \otimes \mathbf{N}) \\
&=: \nabla_{\mathbf{x}}^S(\bullet) + \nabla_{\mathbf{x}}^N(\bullet) \otimes \mathbf{N}. \tag{B.3}
\end{aligned}$$

With this definition, the last part of (B.2) can be transformed to

$$\int_{\partial \mathcal{B}_0} \nabla_{\mathbf{x}} \delta \boldsymbol{\varphi} : [\mathbf{Q} \cdot \mathbf{N}] \, dA = \int_{\partial \mathcal{B}_0} [\nabla_{\mathbf{x}}^N \delta \boldsymbol{\varphi} \cdot [\mathbf{Q} : [\mathbf{N} \otimes \mathbf{N}]] + \nabla_{\mathbf{x}}^S \delta \boldsymbol{\varphi} : [\mathbf{Q} \cdot \mathbf{N}]] \, dA, \tag{B.4}$$

where the first part is independent from the boundary values of $\delta \boldsymbol{\varphi}$.

The following surface divergence theorem will be used to transform the latter part such

that only $\delta \boldsymbol{\varphi}$ will be left. It requires that the surface $\partial\mathcal{B}_0$ can be subdivided into a finite number of C^1 continuous patches \mathcal{S}_0^J ,

$$\int_{\mathcal{S}_0^J} \nabla_{\mathbf{x}}^s(\bullet) - \text{Div}^s \mathbf{N}[(\bullet) \cdot \mathbf{N}] \, dA = \int_{\partial\mathcal{S}_0^J} (\bullet) \cdot \mathbf{M} \, dS, \quad (\text{B.5})$$

where \mathbf{M} is the unit external normal to the boundary of the surface patch, with the property $\mathbf{N} \cdot \mathbf{M} = 0$. \mathbf{M} is clearly lying at the tangent plane of $\partial\mathcal{B}_0$. The last term in (B.4) therefore results in

$$\int_{\partial\mathcal{B}_0} \nabla_{\mathbf{x}}^s \delta \boldsymbol{\varphi} : [\mathbf{Q} \cdot \mathbf{N}] \, dA = \sum_J \left[\int_{\mathcal{S}_0^J} \delta \boldsymbol{\varphi} \cdot [\text{Div}^s \mathbf{N} \mathbf{Q} : [\mathbf{N} \otimes \mathbf{N}]] \, dA + \int_{\partial\mathcal{S}_0^J} \delta \boldsymbol{\varphi} \mathbf{Q} : [\mathbf{M} \otimes \mathbf{N}] \, dS \right]. \quad (\text{B.6})$$

The total problem can therefore be rewritten as

$$\begin{aligned} & \int_{\mathcal{B}_0} \mathbf{P} : \delta \mathbf{F} + \mathbf{Q} : \delta \mathbf{G} \, dV \\ &= \int_{\mathcal{B}_0} \delta \boldsymbol{\varphi} \cdot \text{Div}(\text{Div} \mathbf{Q} - \mathbf{P}) \, dV \\ &+ \int_{\partial\mathcal{B}_0} \delta \boldsymbol{\varphi} \cdot [\mathbf{P} - \text{Div} \mathbf{Q}] \cdot \mathbf{N} + \nabla_{\mathbf{x}}^N \delta \boldsymbol{\varphi} \cdot [\mathbf{Q} : [\mathbf{N} \otimes \mathbf{N}]] \, dA \\ &+ \sum_J \left[\int_{\mathcal{S}_0^J} \delta \boldsymbol{\varphi} \text{Div}^s \mathbf{N} \mathbf{Q} : [\mathbf{N} \otimes \mathbf{N}] \, dA + \int_{\partial\mathcal{S}_0^J} \delta \boldsymbol{\varphi} \mathbf{Q} : [\mathbf{M} \otimes \mathbf{N}] \, dS \right] \\ &= \int_{\mathcal{B}_0} \delta \boldsymbol{\varphi} \cdot \text{Div}(\text{Div} \mathbf{Q} - \mathbf{P}) \, dV \\ &+ \int_{\partial\mathcal{B}_0} \delta \boldsymbol{\varphi} \cdot [\mathbf{P} - \text{Div} \mathbf{Q}] \cdot \mathbf{N} + \nabla_{\mathbf{x}}^N \delta \boldsymbol{\varphi} \cdot [\mathbf{Q} : [\mathbf{N} \otimes \mathbf{N}]] \, dA \\ &+ \int_{\partial\mathcal{B}_0} \delta \boldsymbol{\varphi} \text{Div}^s \mathbf{N} \mathbf{Q} : [\mathbf{N} \otimes \mathbf{N}] \, dA + \sum_J \left[\int_{\partial\mathcal{S}_0^J} \delta \boldsymbol{\varphi} \mathbf{Q} : [\mathbf{M} \otimes \mathbf{N}] \, dS \right]. \end{aligned} \quad (\text{B.7})$$

Introducing the body force \mathbf{b} , as direct consequence of (B.7), the local form of the boundary value problem holds

$$\text{Div}(\mathbf{P} - \text{Div}(\mathbf{Q})) = -\mathbf{b}. \quad (\text{B.8})$$

For the description of the Neumann boundary conditions, the definition of the tractions

$$\mathbf{t}^P := [\mathbf{P} - \text{Div} \mathbf{Q}] \cdot \mathbf{N} + [\text{Div}^s \mathbf{N}] \mathbf{Q} : [\mathbf{N} \otimes \mathbf{N}] - \text{Div}^s [\mathbf{Q} \cdot \mathbf{N}]^T \quad (\text{B.9})$$

$$\mathbf{t}^Q := \mathbf{Q} : [\mathbf{N} \otimes \mathbf{N}] \quad \text{and} \quad (\text{B.10})$$

$$\mathbf{t}^E := \mathbf{Q} : [\mathbf{M} \otimes \mathbf{N}] \quad (\text{B.11})$$

is used.

Remark B.1 (Simplification for smooth boundaries:) *If inhomogeneous Neumann boundary conditions are only applied at smooth surfaces, the term \mathbf{t}^E in (B.11) can be omitted. This is done in chapter 2.*

C Isoparametric C^1 -continuous triangular elements

Within this appendix, it will be demonstrated that the principle to construct C^1 continuous isoparametric finite elements as presented in section 5.4.1 can additionally be applied to triangular elements. Here, the Bell element as presented in subsection 5.3.2 is used, together with the \bar{G} mesh optimization of subsection 5.4.5.3.

In contrast to their quadrilateral counterpart, the geometry of triangular elements is in general much more flexible since the mesh is not restricted to exactly four elements for each interior node. It only has to be verified that the sum of the angles at each node is 360.

In the following part of the appendix, first a set of equations is presented for the derivation of the angles of the triangular elements. The computation of the interior angles is necessary to define the intermediate configuration, compare to figure 5.11. This is followed by a short description of the construction of the isoparametric geometry and some numerical examples in section C.2.

C.1 Construction of the shape of the triangles

To be able to construct the intermediate configuration, where the element shape functions are defined, the shape of the triangles has to be fixed. This can be achieved by the construction of the internal angles. For the computation of the internal angles, we establish a suitable system of equations.

Let β_I^J the the angle of the element J at node I . For sake of simplicity we define $\beta_I^J := 0$ if the node I is not involved in element J . By β_i^j , $j = 1, 2, 3$, be the local nodal index is denoted. To be able to guarantee that the mapping φ between two different intermediate configurations is affine linear, the angles have to fullfill the following properties:

The angular sum of each triangle has to fulfill

$$\sum_I \beta_I^J = \sum_{i=1}^3 \beta_i^J = \pi. \quad (\text{C.1})$$

and additionally, the angular sum at each node has to satisfy one of the following equations:

$$\sum_J \beta_I^J \begin{cases} = 2\pi & \text{if } I \in \mathcal{I}_i \text{ is an interior node,} \\ = \pi & \text{if } I \in \mathcal{I}_s \text{ is a boundary node at a smooth boundary,} \\ < \pi & \text{if } I \in \mathcal{I}_c \text{ is a outer corner node, and} \\ > \pi & \text{if } I \in \mathcal{I}_n \text{ is at a nook.} \end{cases} \quad (\text{C.2})$$

There is no unique solution fulfilling the conditions defined in (C.1) and (C.2). Therefore, the following functional is introduced, where the previous conditions are verified by

Lagrange parameters.

$$\begin{aligned}
\bar{\Pi}(\boldsymbol{\beta}) := & \sum_J p_J \left[\sum_i \beta_i^J - \pi \right] + \sum_{I \in \mathcal{I}_i} p_I^i \left[\sum_J \beta_I^J - 2\pi \right] + \sum_{I \in \mathcal{I}_s} p_I^s \left[\sum_J \beta_I^J - \pi \right] \\
& + k_1 \sum_{I \in \mathcal{I}_i} \sum_J \left[\beta_I^J - \frac{2\pi}{\sum_J \text{sign}(\beta_I^J)} \right]^2 \\
& + k_2 \sum_{I \in \mathcal{I}_s} \sum_J \left[\beta_I^J - \frac{\pi}{\sum_J \text{sign}(\beta_I^J)} \right]^2 \\
& + k_3 \sum_{I \in \mathcal{I}_c} \sum_J \left[\beta_I^J - \frac{\pi}{2 \sum_J \text{sign}(\beta_I^J)} \right]^2 \\
& + k_4 \sum_{I \in \mathcal{I}_n} \sum_J \left[\beta_I^J - \frac{3\pi}{2 \sum_J \text{sign}(\beta_I^J)} \right]^2 \\
& + \sum_J \sum_i \log(\beta_i^J).
\end{aligned} \tag{C.3}$$

Within (C.3), the values k_1, \dots, k_4 are similar to material parameters, stating how important the condition is within the angle construction and the last summand $\sum_J \sum_i \log(\beta_i^J)$ is to guarantee the strict positivity of each angle.

Remark C.1 (Lagrange parameters) *Alternatively to the Lagrange parameter description, it would be possible to relate the angles to each other. However, for sake of simplicity this relation has been used. Additionally, it is in general not always possible to have smooth boundaries, wherever it is desired. In such a case, $\sum_{I \in \mathcal{I}_s} p_I^s [\sum_J \beta_I^J - \pi]$ of equation (C.3) can be replaced by*

$$\sum_{I \in \mathcal{I}_s} \kappa_I^s \left[\sum_J \beta_I^J - \pi \right]^2. \tag{C.4}$$

For $\kappa \rightarrow \infty$, the best possible smoothness is achieved.

The minimization of the nonlinear equation (C.3) is done with the use of a Newton scheme. For sake of simplicity, the indices I and J are combined, and all non-existing quantities are removed. For this purpose, the residual vectors together with the angle stiffness matrices have to be derived. By \mathcal{K}_i denotes the index set for the nodes adjacent to an internal angle, \mathcal{K}_c those of a corner angle, etc. \mathcal{K}_j is defined to be the three angles related to an element J . Using these definitions, the resulting system of equations has to be solved

$$R_{I \in \mathcal{I}_i} = p_J + p_I^i + 2k_2 \left[\beta_I^J - \frac{2\pi}{\sum_J \text{sign}(\beta_I^J)} \right] + k_5 \frac{1}{\beta_I^J} = 0 \quad \text{for } (I, J) \in \mathcal{K}_i \tag{C.5}$$

$$R_{I \in \mathcal{I}_s} = p_J + p_I^s + 2k_2 \left[\beta_I^J - \frac{\pi}{\sum_J \text{sign}(\beta_I^J)} \right] + k_5 \frac{1}{\beta_I^J} = 0 \quad \text{for } (I, J) \in \mathcal{K}_s \tag{C.6}$$

$$R_{I \in \mathcal{I}_c} = p_J + 2k_2 \left[\beta_I^J - \frac{\pi}{2 \sum_J \text{sign}(\beta_I^J)} \right] + k_5 \frac{1}{\beta_I^J} = 0 \quad \text{for } (I, J) \in \mathcal{K}_c \tag{C.7}$$

$$R_{I \in \mathcal{I}_n} = p_J + 2k_2 \left[\beta_I^J - \frac{3\pi}{2 \sum_J \text{sign}(\beta_I^J)} \right] + k_5 \frac{1}{\beta_I^J} = 0 \quad \text{for } (I, J) \in \mathcal{K}_n \tag{C.8}$$

together with the residual equations for the Lagrange parameters

$$R_J^r = \sum_{i=1}^3 \beta_i^J - \pi = 0 \quad (\text{C.9})$$

$$R_{I_i}^r = \sum_{I \in \mathcal{I}_i} \beta_I^J - 2\pi = 0 \quad (\text{C.10})$$

$$R_{I_s}^r = \sum_{I \in \mathcal{I}_c} \beta_I^J - \pi = 0. \quad (\text{C.11})$$

If the angles of the triangular elements are known, the only work left is the construction of the linear subparametric elements in the intermediate configuration $\bar{\xi}(\xi)$. Therefore, one edge of one element has to be fixed and the remaining parts of the geometry are a direct consequence of the shapes of the elements. Then, the linear geometry can be used to define the Bézier coefficients of the shape functions for the geometry approximation. To construct the isoparametric geometry representation, it is possible to make use of the principle, presented in subsection 5.4.5.3, and the starting point that the shape functions that interpolate the primal unknowns, are related to a fixed set of element nodes. For the following application of the \bar{G} -optimization, the boundary nodes are fixed, together with the description of the boundary tangent $\partial_{t_{\bar{x}i}} \mathbf{X}$. For the value $\partial_{t_{\bar{\xi}}}^2 \mathbf{X}$, which is influencing the shape of the boundary, is separated into two cases. If the boundary is described by a straight line, the value is set to zero. Otherwise, it is left free for the \bar{G} -optimization.

Remark C.2 (Numerical stability) *Unfortunately, the use of the Lagrange parameters results in a non optimally conditioned system of equations. Hence, the equations in (C.1) and (C.2) are only satisfied up to a small numerical error. This becomes relevant for the construction of the intermediate configuration. Thereby, either the element shape can not exactly be recovered or problems are caused within the assembly of the elements at one node.*

C.2 Numerical examples

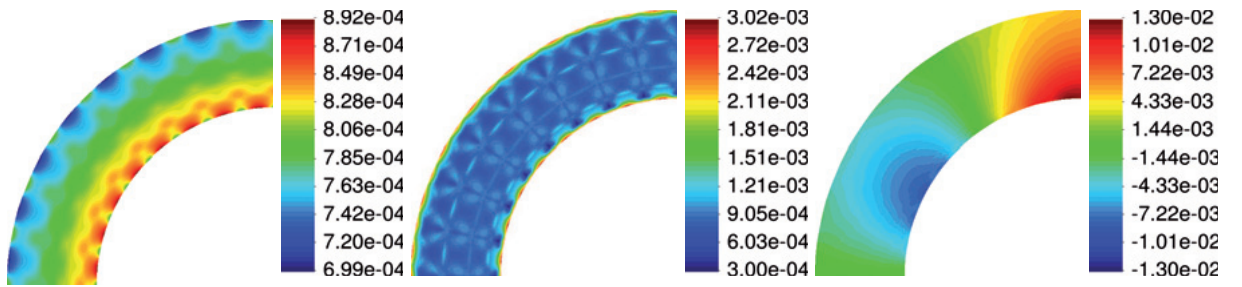


Figure C.1: Example of the hollow cylinder under external pressure. (Left): $\|\mathbf{u}^h - \mathbf{u}^a\|_2$, (Center): $\|\boldsymbol{\epsilon}^h - \boldsymbol{\epsilon}^a\|_2$ and (Right): κ_{112} .

Within this section, three numerical examples are used to demonstrate the practicability of the presented principle for the application to isoparametric triangular elements.

In a first example, the thick hollow cylinder as presented in section 8.1.2 is applied. In figure C.1, the values of the relative local error for the displacements (left), strains (center) and the value κ_{xxx} (right) are presented. It can be observed that the interpolation is obviously C^1 continuous and additionally provides reasonable solutions.

The second numerical example is for the demonstration of the mesh quality, archived

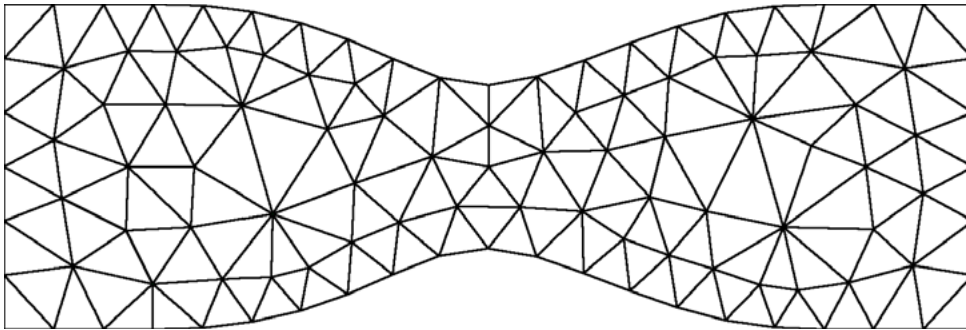


Figure C.2: Original linear mesh for the geometry construction of the notched specimen.

by the previously presented procedure for the description of the element shape. The example is a notched specimen. For the description of the linear reference geometry, an unstructured, homogeneous mesh is used. In figure C.3, it can be observed that due to the use of the connectivity, given by the linear reference mesh, compare to figure C.2, the element concentration is preserved without fixing the nodal positions. Furthermore, a nice approximation of the boundary as well as a smooth strain distribution can be observed.

And third, to demonstrate that the principle can as well be applied to more complex geometries, half the geometry of the plate with hole is discretized. Again, the nice distribution of the mesh can be observed, see figure C.4. Only some problems occur within the mesh construction at the semicircular boundary of the hole.

C.3 Conclusion

Within this chapter, we have presented a new algorithm for the construction of isoparametric triangular elements. The good thing is that it works and provides nice C^1 continuous results. The drawback of the method is the fact that a good approximation of the boundary is difficult especially for the quintic Bell element. We believe that the application of the fully quintic Argyris element or the HCT element within the algorithm can improve the results. Furthermore, we have to mention, that within the last example, small discontinuities of the strains occurred due to errors within the construction of the element angles by the use of Lagrange parameters. This is solved, if the high dependencies of the angles are directly taken into account.

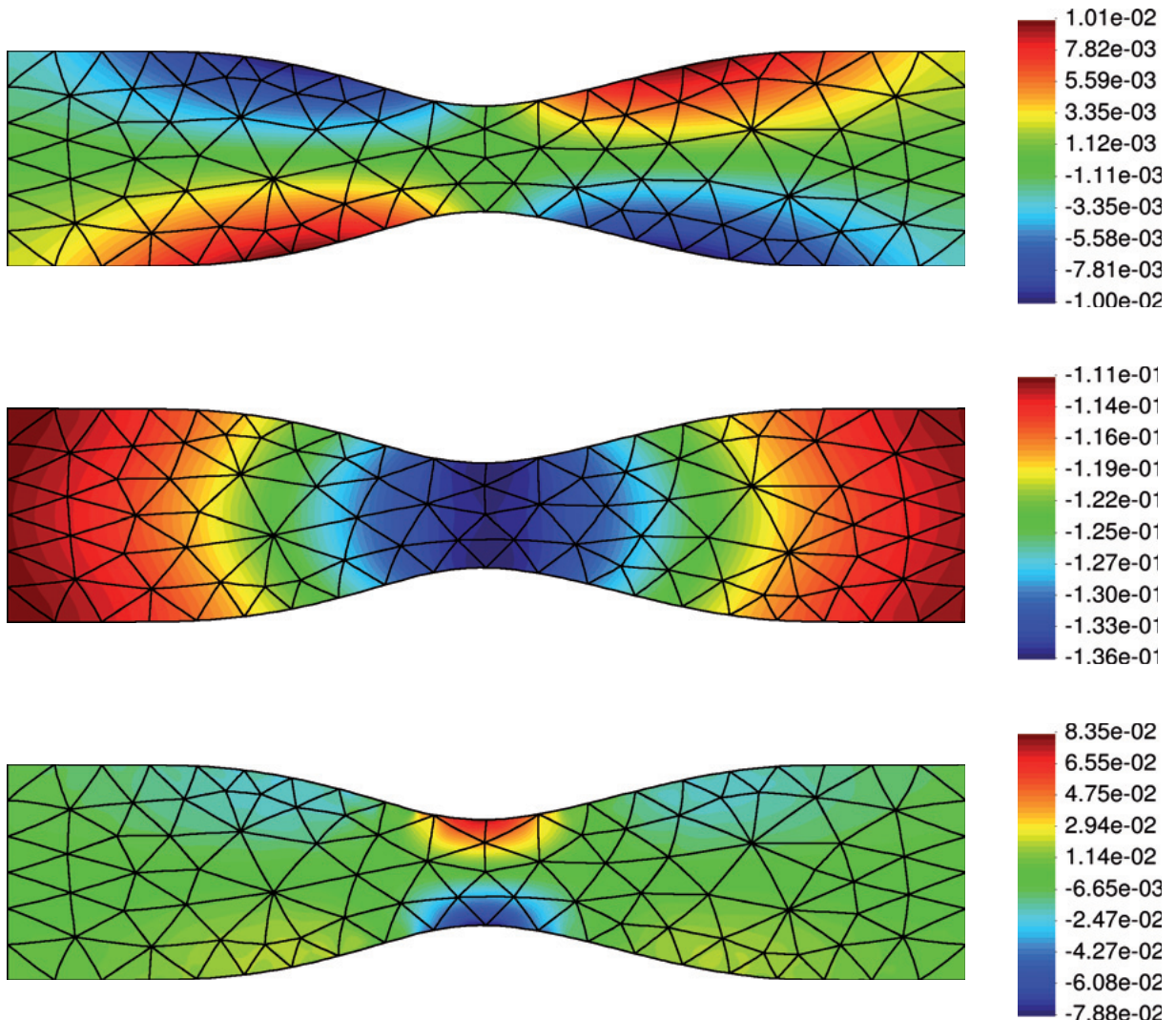


Figure C.3: Example of a notched specimen under 50% elongation. Contour plots of: Top: F_{xy} Center: F_{yy} and bottom G_{xyx} .

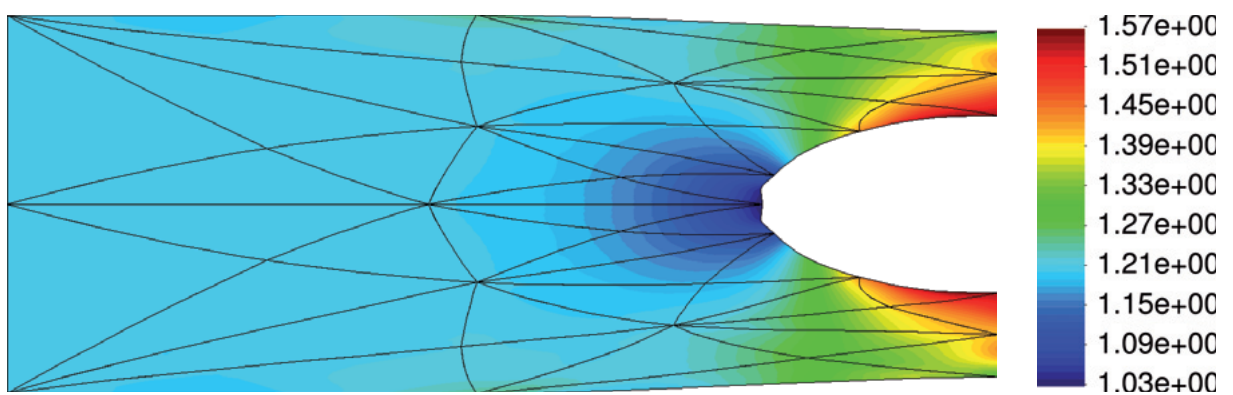


Figure C.4: Plate with hole example of subsection 8.2.2. Contour plot of F_{yy} .

Bibliography

- [1] A. Adini and R. Clough. Analysis of plate bending by the finite element method. *NSF Report G.7337*, 1961.
- [2] E. Aifantis. Higher order gradients and size effects. In A. Carpinteri, editor, *Size-scale effects in the failure mechanisms of materials and structures*. 1996.
- [3] E. Aifantis. Strain gradient interpretation of size effects. *International Journal of Fracture*, 95:299–314, 1999.
- [4] E. Aifantis. On scale invariance in anisotropic plasticity, gradient plasticity and gradient elasticity. *International Journal of Engineering Science*, 47:1089–1099, 2009.
- [5] P. Alfeld. A trivariate Clough-Tocher scheme for tetrahedral data. *Computer Aided Geometric Design*, 1:169–181, 1984.
- [6] P. Alfeld and L. Schumaker. Smooth macro-elements based on Clough-Tocher triangle splits. *Numerische Mathematik*, 90:597–616, 2002.
- [7] P. Alfeld and L. Schumaker. Smooth macro-elements based on Powell-Sabin triangle splits. *Advances in Computational Mathematics*, 16:29–46, 2002.
- [8] P. Alfeld and T. Sorokina. Two tetrahedral C^1 cubic macro elements. *Journal of Approximation Theory*, 157:53–69, 2009.
- [9] H. Alt. *Lineare Funktionalanalysis*. Springer, 2002.
- [10] S. Altan and E. Aifantis. On the structure of the mode-III crack-tip in gradient elasticity. *Scripta Metallurgica*, 26:319–324, 1992.
- [11] J. Altenbach and H. Altenbach. *Einfuehrung in die Kontinuumsmechanik*. B. G. Teubner, 1994.
- [12] E. Amanatidou and N. Aravas. Mixed finite element formulations of strain-gradient elastic problems. *Computer Methods in Applied Mechanics and Engineering*, 191:1723–1751, 2002.
- [13] N. Amenta, M. Bern, and M. Kamvysselis. A new Voronoi-based surface reconstruction algorithm. *Proceedings of SIGGRAPH*, 98:415–421, 1998.
- [14] N. Aravas and A. Giannakopoulos. Plane asymptotic crack-tip solutions in gradient elasticity. *International Journal of Solids and Structures*, 46:4478–4503, 2009.
- [15] J. Argyris and I. Fried. The TUBA family of elements for the matrix displacement method. *The Aeronautical Journal*, 72:701–709, 1968.

- [16] E. Arruda and M. Boyce. A three-dimensional constitutive model for the large stretch behavior of rubber elastic materials. *Journal of the Mechanics and Physics of Solids*, 41(2):389–412, 1993.
- [17] H. Askes and E. Aifantis. Numerical modeling of size effects with gradient elasticity-formulation, meshless discretization and examples. *International Journal of Fracture*, 117:347–358, 2002.
- [18] H. Askes, T. Bennett, and E. Aifantis. A new formulation and C^0 -implementation of dynamically consistent gradient elasticity. *International Journal for Numerical Methods in Engineering*, 72:111–126, 2007.
- [19] H. Askes and M. Gutiérrez. Implicit gradient elasticity. *International Journal for Numerical Methods in Engineering*, 67:400–416, 2006.
- [20] F. Auricchio, L. Beirao da Veiga, A. Buffa, C. Lovadina, A. Reali, and G. Sangalli. A fully locking-free isogeometric approach for plane linear elasticity problems: A steam function formulation. *Computer Methods in Applied Mechanics and Engineering*, 197:160–172, 2007.
- [21] F. Auricchio, L. Beirao da Veiga, C. Lovadina, and A. Reali. The importance of the exact satisfaction of the incompressibility constraint in nonlinear elasticity: mixed FEMs versus NURBS-based approximations. *Computer Methods in Applied Mechanics and Engineering*, 199:314–323, 2010.
- [22] I. Babuška. The finite element method with Lagrangian multipliers. *Numerische Mathematik*, 20:179–192, 1973.
- [23] Z. Bazant. Size effects. *International Journal of Solids and Structures*, 37:69–80, 2000.
- [24] G. Bazeley, Y. Cheung, B. Irons, and O. Zienkiewicz. Triangular elements in plates bending conforming and non-conforming solutions. *Proceedings of the Conference on Matrix Methods in Structural Mechanics*, pages 547–576, 1965.
- [25] Y. Bazilevs, L. Beirão de Veiga, J. Cottrell, T. Hughes, and G. Sangalli. Isogeometric analysis: approximation, stability and error estimates for h-refined meshes. *Mathematical Models and Methods in Applied Sciences*, 16(7):1031–1090, 2005.
- [26] Y. Bazilevs, V. Calo, J. Cottrell, J. Evans, T. Hughes, S. Lipton, M. Scott, and T. Sederberg. Isogeometric analysis using T-splines. *Computer Methods in Applied Mechanics and Engineering*, 199:229–263, 2010.
- [27] Y. Bazilevs, V. Calo, Y. Zhang, and T. Hughes. Isogeometric fluid-structure interaction analysis with applications to arterial blood flow. *Computational Mechanics*, 38:310–322, 2006.
- [28] V. Belikov, V. Ivanov, V. Kontorovich, S. Korytnik, and A. Semenov. The non-Sibsonian interpolation: A new method of interpolation of the values of a function on

- an arbitrary set of points. *Computational Mathematics and Mathematical Physics*, 37(1):9–15, 1997.
- [29] K. Bell. A refined triangular plate bending finite element. *International Journal for Numerical Methods in Engineering*, 1:101–122, 1969.
- [30] P. Bergan. Finite elements based on energy orthogonal functions. *International Journal for Numerical Methods in Engineering*, 15:1541–1555, 1980.
- [31] M. Bernadou. C^1 -curved finite elements and applications to plate and shell problems. *Journal of Computational and Applied Mathematics*, 50:133–144, 1994.
- [32] M. Bernadou and J. Boisserie. *The Finite Element Method in Thin Shell Theory: Application to Arch Dam Simulations*. Birkhaeuser, 1982.
- [33] M. Bernadou and J. Boisserie. Curved finite elements of class C^1 : Implementation and numerical experiments part 1: Construction and numerical tests of the interpolation properties. *Rapports de Recherche*, 1718:1–50, 1992.
- [34] M. Bernadou and K. Hassan. Basis functions for general Hsieh-Clough-Tocher triangles, complete or reduced. *Short Communications*, pages 784–789, 1981.
- [35] B. Bigdeli and D. Kelly. C^* -convergence in the finite element method. *International Journal for Numerical Methods in Engineering*, 40:4405–4425, 1997.
- [36] B. Bigdeli and D. Kelly. Convergence of the C^* family of finite elements and problems associated with forcing continuity of the derivatives at the nodes. *Structural Engineering and Mechanics*, 7(6):561–573, 1999.
- [37] T. Bobach. *Natural Neighbor Interpolation and Critical assessment and new contributions*. PhD thesis, TU Kaiserslautern, 2008.
- [38] T. Bobach, M. Bertram, and G. Umlauf. Comparison of Voronoi based scattered data interpolation schemes. In *Proceedings: Visualization, Imaging and Image Processing*, 45:342–348, 2006.
- [39] T. Bobach, A. Constantiniu, P. Steinmann, and G. Umlauf. Geometric properties of the adaptive Delaunay tessellation. In *Proceedings of the 7th international Conference on Mathematical Methods for Curves and Surfaces*. 2008.
- [40] T. Bobach and G. Umlauf. Natural neighbor concepts in scattered data interpolation and discrete function approximation. 2008.
- [41] F. Bogner, R. Fox, and L. Schmidt. The generation of inter-element-compatible stiffness and mass matrices by the use of interpolation formulas. *Matrix Methods in Structural Mechanics*, pages 397–443, 1965.
- [42] W. Böhm, G. Farin, and J. Kahmann. A survey of curve and surface methods in cagd. *Computer Aided Geometric Design*, 1:1–60, 1984.

- [43] J. Bonet and R. Wood. *Nonlinear Continuum Mechanics for Finite Element Analysis*. Cambridge University Press, 2008.
- [44] A. Bowyer. Computing Dirichlet tessellations. *The Computer Journal*, 24(2):162–166, 1981.
- [45] C. Bradley, A. Pullan, and P. Hunter. Geometric modeling of the human torso using cubic Hermite elements. *Annals of Biomedical Engineering*, 25:96–111, 1997.
- [46] D. Braes. *Finite Elemente*. Springer, 1992.
- [47] J. Braun and M. Sambridge. A numerical method for solving partial differential equations on highly irregular evolving grids. *Nature*, 376, 1995.
- [48] S. Brenner. Two-level additive Schwarz preconditioners for plate elements. *Wuhan University Journal of Natural Sciences*, 1(3,4):658–667, 1996.
- [49] F. Brezzi. On the existence uniqueness and approximation of saddle-point problems arising from Lagrangian multipliers. *Revue Francaise d'Automatique, d'Informatique et de Recherche Opérationnelle*, 129, 1974.
- [50] F. Brezzi and F. M. *Mixed and hybrid finite element methods*. Springer, 1991.
- [51] U. Brink and E. Stein. On some mixed finite element methods for incompressible and nearly incompressible finite elements. *Computational Mechanics*, 19(13-16):105–119, 1996.
- [52] J. Cahn. Free energy of a non uniform system II: thermodynamic basis. *Jurnal of Chemical Physics*, 30:1121–1124, 1959.
- [53] B. Calvo, M. Martinez, and M. Doblaré. On solving large strain hyperelastic problems with the natural elemen method. *International Journal for Numerical Methods in Engineering*, 62:159–185, 2005.
- [54] C. Caramanlian. A conforming solution to curved plate bending problems. *International Journal for Numerical Methods in Engineering*, 17:879–907, 1981.
- [55] J. Chen, C. Wu, S. Yoon, and Y. You. A stabilized conforming nodal integration for Galerkin mesh-free methods. *International Journal for Numerical Methods in Engineering*, 50, 2001.
- [56] J. Chen, S. Yoon, and C. Wu. Non-linear version of stabilized conforming nodal integration for Galerkin mesh-free methods. *International Journal for Numerical Methods in Engineering*, 53:2587–2615, 2002.
- [57] Y. Cheung, I. King, and O. Zienkiewicz. Slab bridges with arbitrary shape und support conditions. *Proceedings - Institution of Civil Engineers*, 40:9–36, 1968.
- [58] Y. Cheung and C. Wanji. Refined nine-parameter triangular thin plate bending element by using refined direct stiffness method. *International Journal for Numerical Methods in Engineering*, 38:283–298, 1995.

- [59] P. Ciarlet. *The finite element analysis for elliptic problems*. North-Holland, 1978.
- [60] P. Ciarlet and J. Lions. *Handbook of numerical analyis, Volume 2*. Elsevier, 1991.
- [61] F. Cirak, M. Ortiz, and P. Schröder. Subdivision surfaces: A new paradigm for thin-shell finite-element analysis. *International Journal for Numerical Methods in Engineering*, 47:2039–2072, 2000.
- [62] F. Cirak, M. Ortiz, and P. Schröder. Fully C^1 -conforming subdivision elements for finite deformation thin-shell analysis. *International Journal for Numerical Methods in Engineering*, 51:813–833, 2001.
- [63] R. Clough and J. Tocher. Finite element stiffness matrices for analysis of plate bending. *Matrix Methods in Structural Mechanics*, pages 515–545, 1965.
- [64] A. Constantiniu, P. Steinmann, T. Bobach, G. Farin, and G. Umlauf. The adaptive Delaunay tessellation: A neighborhood covering meshing technique. *Computational Mechanics*, 42:655–670, 2008.
- [65] E. Cosserat and F. Cosserat. *Théorie des corps déformables*. Hermann, 1909.
- [66] J. Cottrell, T. Hughes, and Y. Bazilevs. *Isogeometric analysis*. Wiley, 2009.
- [67] J. Cottrell, T. Hughes, and A. Reali. Studies of refinement and continuity in isogeometric structural analysis. *Computer Methods in Applied Mechanics and Engineering*, 196:4160–4183, 2007.
- [68] J. Cottrell, A. Reali, Y. Bazilevs, and T. Hughes. Isogeometric analysis of structural vibrations. *Computer Methods in Applied Mechanics and Engineering*, 195:5257–5296, 2005.
- [69] M. Cox. The numerical evaluation of B-splines. *Technical Report, National Physics Laboratroy, DNAC 4*, 1971.
- [70] E. Cueto, B. Calvo, and M. Doblaré. Modeling three-dimensional piece-wise homogeneous domains using the alpha-shape-based natural element method. *International Journal for Numerical Methods in Engineering*, 54:871–897, 2002.
- [71] E. Cueto, J. Cegonino, B. Calvo, and M. Doblaré. On the imposition of essential boundary conditions in natural neighbour Galerkin methods. *Communications in Applied Numerical Methods*, 19:361–376, 2003.
- [72] E. Cueto, M. Doblaré, and L. Garcia. Imposing essential boundary conditions in the natural element method by means of density-scaled alpha-shapes. *International Journal for Numerical Methods in Engineering*, 49:519–546, 2000.
- [73] E. Cueto, N. Sukumar, B. Calvo, J. Cegonino, and M. Doblaré. Overview and recent advances in natural neighbour Galerkin methods. *Archives of Computational Methods in Engineering*, 10(4):307–384, 2003.

- [74] W. Dahmen. On multivariate B-splines. *SIAM Journal for Numerical Analysis*, 17(2):179–191, 1980.
- [75] S. Dasgupta and D. Sengupta. Higher-order triangular plate bending element revised. *International Journal for Numerical Methods in Engineering*, 30:419–430, 1990.
- [76] C. de Boor. On calculation with B-splines. *Journal of Approximation Theory*, 6A:50–62, 1972.
- [77] C. de Boor, K. Höllig, and M. Sabin. High accuracy geometric Hermite interpolation. *Computer Aided Geometric Design*, 4:269–278, 1987.
- [78] R. de Borst and J. Pamin. A gradient plasticity approach to finite element predictions of soil instability. *Archives of Mechanics*, 47(9):353–377, 1995.
- [79] R. de Borst and J. Pamin. Some novel developments in finite element procedures for gradient-dependent plasticity. *International Journal for Numerical Methods in Engineering*, 39:2477–2505, 1996.
- [80] P. deCasteljau. Courbes et surfaces à poles. *André Citroën Automobiles SA, Paris*, 1963.
- [81] I. Dolcetta, S. Vita, and R. March. Area preserving curve shortening flows: from phase transitions to image processing. *Interfaces Free Boundaries*, 4(4):325–343, 2002.
- [82] R. Echter and M. Bischoff. Numerical efficiency, locking and unlocking of NURBS finite elements. *Computer Methods in Applied Mechanics and Engineering*, 199:374–382, 2010.
- [83] A. El-Zafrany and R. A. Cookson. Derivation of Lagrangian and Hermitian shape functions for quadrilateral elements. *International Journal for Numerical Methods in Engineering*, 23:1939–1958, 1986.
- [84] A. El-Zafrany and R. A. Cookson. Derivation of Lagrangian and Hermitian shape functions for triangular elements. *International Journal for Numerical Methods in Engineering*, 23:275–285, 1986.
- [85] A. Elias-Zuniga. A non-Gaussian network model for rubber elasticity. *Polymer*, 47:907–914, 2006.
- [86] C. Elliott and D. French. A non-conforming finite element method for the two-dimensional Cahn-Hilliard equation. *SIAM Journal for Numerical Analysis*, 26(4):884–903, 1989.
- [87] G. Engel, K. Garikipati, T. Hughes, M. Larson, L. Mazzei, and R. Taylor. Continuous/discontinuous finite element approximations of fourth-order elliptic problems in structural and continuum mechanics with applications to thin beams and plates, and strain gradient elasticity. *Computer Methods in Applied Mechanics and Engineering*, 191:3669–3750, 2002.

- [88] A. Eringen. *Microcontinuum Field Theories I: Foundations and Solids: 1*. Springer, 1999.
- [89] A. Eringen and E. Suhubi. Nonlinear theory of simple microelastic solids i. *International Journal of Engineering Science*, 2(2):189–203, 1964.
- [90] G. Exadaktylos. Gradient elasticity with surface energy: mode-I crack problem. *International Journal of Solids and Structures*, 35:421–426, 1998.
- [91] F. Falk. Cahn-Hilliard theory and irreversible thermodynamics. *Journal of Non-Equilibrium Thermodynamics*, 17(1):53–65, 1992.
- [92] G. Farin. A modified Clough-Tocher interpolant. *Computer Aided Geometric Design*, 2:19–27, 1985.
- [93] G. Farin. Triangular Bernstein-Bézier patches. *Computer Aided Geometric Design*, 3(2):83–127, 1986.
- [94] G. Farin. Surfaces over Dirichlet tessellations. *Computer Aided Geometric Design*, 7:281–292, 1990.
- [95] G. Farin. *Curves and surfaces for CAGD*. Morgan Kaufmann, 2002.
- [96] P. Fischer, M. Klassen, J. Mergheim, P. Steinmann, and R. Müller. Isogeometric analysis of gradient elasticity. *Computational Mechanics*, 47:325–334, 2011.
- [97] P. Fischer, J. Mergheim, and P. Steinmann. C^1 continuous discretization of gradient elasticity. In *Proceedings in Applied Mathematics and Mechanics*. 2010.
- [98] P. Fischer, J. Mergheim, and P. Steinmann. C^1 discretizations for the application to gradient elasticity. In G. Maugin and A. Metrikine, editors, *Mechanics of Generalized Continua*, chapter 29, pages 279–286. 2010.
- [99] P. Fischer, J. Mergheim, and P. Steinmann. On the C^1 continuous discretization of nonlinear gradient elasticity: a comparison of nem and fem based on Bernstein-Bézier patches. *International Journal for Numerical Methods in Engineering*, 82(10):1282–1307, 2010.
- [100] P. Fischer, J. Mergheim, and P. Steinmann. Direct evaluation of nonlinear gradient elasticity in 2d with C^1 continuous discretization methods. In *Proceedings in Applied Mathematics and Mechanics*. 2011.
- [101] P. Fischer, A. Rajagopal, E. Kuhl, and P. Steinmann. Cahn-Hilliard generalized diffusion modeling using the natural element method. In H. Altenbach, G. Maugin, and V. Erofeev, editors, *Mechanics of Generalized Continua*, chapter 16, pages 326–336. 2011.
- [102] N. Fleck, G. Muller, M. Ashby, and J. Hutchinson. Strain gradient effects in plasticity: Theory and experiment. *Acta Metallurgica et Materialia*, 42:475–487, 1994.

- [103] P. Flory. *Statistical mechanics of chain molecules*. Hanser, 1989.
- [104] P. Flory and J. Rehner. Statistical mechanics of cross-linked polymer networks I. rubberlike elasticity. *The Journal of Chemical Physics*, 11:512–520, 1943.
- [105] S. Forest and J.-M. Cardona. Thermoelasticity of second-grade media. In G. Maugin, R. Drouot, and F. Sideroff, editors, *Continuum Thermodynamics*, pages 163–176. 2000.
- [106] B. Fraeijs de Veubeke. A conforming finite element for plate bending. *International Journal for Solids and Structures*, 4:95–108, 1968.
- [107] E. Frind. An isoparametric Hermitian element for the solution of field problems. *International Journal for Numerical Methods in Engineering*, 11:945–962, 1977.
- [108] G. Galimbert and V. Pereyra. Solving confluent Vandermonde systems of Hermite type. *Numerische Mathematik*, 18:72, 1971.
- [109] A. Gent. A new constitutive relation for rubber. *Rubber Chemistry and Technology*, 69(1):59–61, 1993.
- [110] H. Georgiadis. The mode III crack problem in micro-structured solids governed by dipolar gradient elasticity: static and dynamic analysis. *Journal of Applied Mechanics*, 70:517–530, 2003.
- [111] A. Giannakopoulos and K. Stamoulis. Structural analysis of gradient elastic components. *International Journal of Solids and Structures*, 44:3440–3451, 2007.
- [112] H. Gomez, V. Calo, Y. Bazilevs, and T. Hughes. Isogeometric analysis of the Cahn-Hilliard phase-field model. *Computer Methods in Applied Mechanics and Engineering*, 197:4333–4352, 2008.
- [113] D. Gonzalez, E. Cueto, and M. Doblaré. Volumetric locking in natural neighbour Galerkin methods. *International Journal for Numerical Methods in Engineering*, 61:611–632, 2004.
- [114] D. Gonzalez, E. Cueto, and M. Doblaré. Higher-order natural element methods: Towards an isogeometric meshless method. *International Journal for Numerical Methods in Engineering*, 2007.
- [115] D. Gonzalez, E. Cueto, M. Martinez, and M. Doblaré. Numerical integration in natural neighbour Galerkin methods. *International Journal for Numerical Methods in Engineering*, 60:2077–2104, 2004.
- [116] C. Gentzelou and H. Georgiadis. Uniqueness for plane crack problems in dipolar gradient elasticity and in couple-stress elasticity. *International Journal for Solids and Structures*, 42:6226–6244, 2005.
- [117] C. Gentzelou and H. Georgiadis. Balance laws and energy release rates for cracks in dipolar gradient elasticity. *International Journal of Solids and Structures*, 45:551–567, 2008.

- [118] C. Großmann and H.-G. Roos. *Numerische Behandlung partieller Differentialgleichungen*. B. G. Teubner, 2005.
- [119] H. Hahn. *Methode der finiten Elemente in der Festigkeitslehre*. Akademische Verlagsgesellschaft, 1975.
- [120] P. Hauret, E. Kuhl, and M. Ortiz. Diamond elements: A finite-element/discrete-mechanics approximation scheme with guaranteed optimal convergence in incompressible elasticity. *International Journal for Numerical Methods in Engineering*, 72(3):253–294, 2007.
- [121] E. Hellinger. Die allgemeinen Ansätze der Mechanik. In F. Klein and K. Wagner, editors, *Encyklopädie der Mathematischen Wissenschaften*, pages 602–694. 1914.
- [122] C. Hirschberger, E. Kuhl, and P. Steinmann. On deformational and configurational mechanics for micromorphic hyperelasticity theory and computation. *Computational Methods in Applied Mechanics and Engineering*, 196:4027–4044, 2007.
- [123] H. Hiyoshi. Stable computation of natural neighbor interpolation. *International Journal of Computational Geometry and Applications*, 2006.
- [124] H. Hiyoshi and K. Sugihara. Two generalizations of an interpolant based on Voronoi diagrams. *International Journal of Shape Modeling*, 5(2):219–231, 1999.
- [125] H. Hiyoshi and K. Sugihara. An interpolant based on line segment Voronoi diagrams. *JCDCG and LNCS 1763*, 98:119–128, 2000.
- [126] H. Hiyoshi and K. Sugihara. Improving continuity of Voronoi-based interpolation over Delaunay spheres. *Computational Geometry*, 22:167–183, 2002.
- [127] K. Hoellig. *Finite element methods with B-splines*. SIAM, 2003.
- [128] T. Hughes. *The finite element method*. Prentice-Hall, 1987.
- [129] T. Hughes, J. Cottrell, and Y. Bazilevs. Isogeometric analysis: CAD, finite elements, NURBS, exact geometry and mesh refinement. *Computer Methods in Applied Mechanics and Engineering*, 194:4135–4195, 2005.
- [130] T. Hughes, A. Reali, and G. Sangalli. Duality and unified analysis of discrete approximations in structural dynamics and wave propagation: Comparison of p-method finite elements with k-method NURBS. *Computer Methods in Applied Mechanics and Engineering*, 197:4104–4124, 2008.
- [131] T. Hughes, A. Reali, and G. Sangalli. Efficient quadrature for NURBS-based isogeometric analysis. *Computer Methods in Applied Mechanics and Engineering*, 199:301–313, 2010.
- [132] B. Irons. A conforming quartic triangular element for plate bending. *International Journal for Numerical Methods in Engineering*, 1:29–45, 1969.

- [133] G. Karlis, S. Tsinopoulos, D. Polyzos, and D. Beskos. Boundary element analysis of mode I and mixed mode (I and II) crack problems of 2-d gradient elasticity. *Computer Methods in Applied Mechanics and Engineering*, 196:5092–5103, 2007.
- [134] G. Karlis, S. Tsinopoulos, D. Polyzos, and D. Beskos. 2d and 3d boundary element analysis of mode-I cracks in gradient elasticity. *Computer Modeling in Engineering Sciences*, 28:189–207, 2008.
- [135] E. Khain and L. Sander. Generalized Cahn-Hilliard equation for biological applications. *Physical Review Letters E*, 77(5):1–7, 2008.
- [136] J. Kiendl, Y. Bazilevs, M. Hsu, R. Wüchner, and K.-U. Bletzinger. The bending strip method for isogeometric analysis of kirchhoff-love shell structures comprised of multiple patches. *Computer Methods in Applied Mechanics and Engineering*, 199:2403–2416, 2010.
- [137] J. Kiendl, K. Bletzinger, J. Linhard, and R. Wüchner. Isogeometric shell analysis with kirchhoff-love elements. *Computer Methods in Applied Mechanics and Engineering*, 198:3902–3914, 2009.
- [138] F. Kikuchi. On a finite element scheme based on the discrete krchhoff assumption. *Numerical Mathematics*, 24:211–231, 1975.
- [139] H. Kim, Y. Seo, and S. Youn. Isogeometric ananlysis for trimmed cad surfaces. *Computer Methods in Applied Mechanics and Engineering*, 198:2982–2995, 2009.
- [140] N. Kirchner and P. Steinmann. On the material setting of gradient hyperelasticity. *Math. Mech. Solid*, 12:3875–3895, 2005.
- [141] N. Kirchner and P. Steinmann. A unifying treatise on variational principles for gradient and micro-morphic continua. *Philosophical Magazine*, 85:3975–3895, 2005.
- [142] M. Klassen. Analyse und anwendung der rationalen B-spline finite element methode in 2d. Master's thesis, TU Kaiserslautern, 2009.
- [143] W. Koiter. Couple-stress in the theory of elasticity I. *Proceedings of the Royal Netherlands Academy of Arts and Sciences (B)*, 67:17–29, 1964.
- [144] W. Koiter. Couple-stress in the theory of elasticity II. *Proceedings of the Royal Netherlands Academy of Arts and Sciences (B)*, 67:30–44, 1964.
- [145] E. Kuhl, A. Menzel, and K. Garikipati. On the convexity of transversely isotropic chain network models. *Philosophical Magazine*, 86(21-22):3241–3258, 2006.
- [146] E. Kuhl and D. Schmid. Computational modeling of mineral unmixing and growth-an application of the Cahn-Hilliard equation. *Computational Mechanics*, 39:439–451, 2007.
- [147] M. Laghchim-Lahlou and P. Sablonnière. Triangular finite elements of HCT type and class C^p . *Advances in Computational Mathematics*, 2:101–122, 1994.

- [148] M. Laghchim-Lahlou and P. Sablonnière. C^r -finite elements of Powell-Sabin type on the three direction mesh. *Advances in Computational Mathematics*, 6:191–206, 1996.
- [149] M.-J. Lai and L. Schumaker. *Spline functions on triangulations*. Cambridge University Press, 2007.
- [150] J. Lassèvre. An analytical expression and an algorithm for the volume of a convex polyhedron in \mathbb{R}^n . *Journal of Optimization Theory and Applications*, 39(3):363–377, 1983.
- [151] J. Lyness and D. Jespersen. Moderate degree symmetric quadrature rules for the triangle. *Journal of the Institute of Mathematics and its Applications*, 15:19–32, 1975.
- [152] J. E. Marsden and T. J. R. Hughes. *Mathematical foundations of elasticity*. Prentice-Hall, 1983.
- [153] G. Maugin. Generalized continuum mechanics: What do we mean by that? In G. Maugin and A. Metrikine, editors, *Mechanics of Generalized Continua*, chapter 1, pages 3–13. 2010.
- [154] G. Maugin and A. Metrikine. *Mechanics of Generalized Continua*. Springer, 2010.
- [155] A. McBride and B. Reddy. A discontinuous Galerkin formulation for gradient plasticity at finite strains. *Computer Methods in Applied Mechanics and Engineering*, 198:1805–1820, 2009.
- [156] R. Melosh. Basis of derivation of matrices for the direct stiffness method. *AIAAJ*, 1:1631–1637, 1963.
- [157] C. Miehe and S. Göktepe. A micro-macro approach to rubber-like materials. part II: The micro-sphere model of finite rubber viscoelasticity. *Journal of the Mechanics and Physics of Solids*, 53:2231–2258, 2005.
- [158] C. Miehe, S. Göktepe, and F. Lulei. A micro-macro approach to rubber-like materials part I: the non-affine micro-sphere model of rubber elasticity. *Journal of the Mechanics and Physics of Solids*, 52:2617–2660, 2004.
- [159] R. Mindlin. Influence of couple-stresses on stress concentrations. *Experimental Mechanics*, 3:1–7, 1963.
- [160] R. Mindlin. Micro-structure in linear elasticity. *Archive for rational Mechanics and Analysis*, 16(1):51–78, 1964.
- [161] R. Mindlin. Second gradient of strain and surface-tension in linear elasticity. *International Journal of Solids and Structures*, 1:417–438, 1965.
- [162] R. Mindlin and H. Tiersten. Effects of couple-stresses in linear elasticity. *Archive for rational Mechanics and Analysis*, 11:415–448, 1962.

- [163] W. Ming and J. Xu. The Morley element for fourth order elliptic equations in any dimensions. *Numerical Mathematics*, 103:155–169, 2006.
- [164] L. Morley. The constant-moment plate-bending element. *The Journal of Strain Analysis for Engineering Design*, 6(1):20–24, 1971.
- [165] R. Ogden. Large deformation isotropic elasticity - on the correlation of theory and experiment for incompressible rubberlike solids. *Proceedings of the Royal Society of London. Series A, Mathematical and Physical Sciences*, 326(1567):565–584, 1972.
- [166] W. Ostwald. ber die vermeintliche isometrie des roten und gelben quecksilberoxyds und die oberflächenspannung fester körper. *Z Phys Chem*, 6A:495–503, 1900.
- [167] S. Papanicolopoulos, A. Zervos, and I. Vardoulakis. A three-dimensional C^1 finite element for gradient elasticity. *International Journal for Numerical Methods in Engineering*, 77:1396–1415, 2009.
- [168] A. Peano. Conforming approximations for Kirchhoff plates and shells. *International Journal for Numerical Methods in Engineering*, 14:1273–1291, 1979.
- [169] J. Petera and J. Pittman. Isoparametric Hermite elements. *International Journal for Numerical Methods in Engineering*, 37:3489–3519, 1994.
- [170] L. Piegl and W. Tiller. *The NURBS book*. Springer, 1997.
- [171] B. Piper. Properties of local coordinates based on Dirichlet tessellations. *Computing Suppl.*, 8:227–239, 1993.
- [172] M. Powell and M. Sabin. Piecewise quadratic approximations on triangles. *ACM Trans. Math. Software*, 3:316325, 1977.
- [173] H. Prautzsch. A round trip to B-splines via de casteljau. *ACM Transactions on Graphics*, 8(3):243–254, 1989.
- [174] H. Prautzsch, W. Böhm, and M. Paluszny. *Bézier and B-spline techniques*. Springer, 2002.
- [175] G. Qing and L. Li. A note on C^1 -curved finite element. *Computer Methods in Applied Mechanics and Engineering*, 129:107–114, 1996.
- [176] A. Rajagopal, P. Fischer, E. Kuhl, and P. Steinmann. Natural element analysis of the Cahn-Hilliard phase-field model. *Computational Mechanics*, 46:471–493, 2010.
- [177] A. Rajagopal, M. Scherer, P. Steinmann, and N. Sukumar. Smooth conformal alpha - nem for gradient elasticity. *Int. J. of Structural Changes in Solids - Mechanics and Applications*, 1, 2009.
- [178] S. Reese and P. Wriggers. A stabilization technique to avoid hourgassing in finite elasticity. *International Journal for Numerical Methods in Engineering*, 48:79–109, 2000.

- [179] M. Sabin. *Spline Finite Elements*. PhD thesis, Leeds University, 1997.
- [180] P. Sablonnière. Bernstein-Bézier methods for the construction of bivariate spline approximants. *Computer Aided Geometric Design*, 2:29–36, 1985.
- [181] I. Schoenberg. On spline functions. In O. Sischa, editor, *Inequalities*, pages 255–291. 1967.
- [182] L. Schumaker. On super splines and finite elements. *SIAM Journal for Numerical Analysis*, 26:997–1005, 1989.
- [183] L. Schumaker and T. Sorokina. Smooth macro-elements on Powell-Sabin-12 splits. *Mathematics of Computation*, 75(254):711–726, 2005.
- [184] L. Schumaker, T. Sorokina, and A. Worsey. A C^1 quadratic trivariate macro-element space defined over arbitrary tetrahedral partitions. *Journal of Approximation Theory*, 158:126–142, 2008.
- [185] M. Shi, Y. Huang, and K. Hwang. Fracture in a higher-order elastic continuum. *Journal of the Mechanics and Physics of Solids*, 48:2513–2538, 2000.
- [186] J. Shu and C. Barlow. Strain gradient effects on microscopic strain field in a metal matrix composite. *International Journal of Plasticity*, 16:563–591, 2000.
- [187] J. Shu, W. King, and N. Fleck. Finite elements for materials with strain gradient effects. *International Journal for Numerical Methods in Engineering*, 44:373–391, 1999.
- [188] R. Sibson. A vector identity for the Dirichlet tessellation. *Mathematical Proceedings of the Cambridge Philosophical Society*, 87:151–153, 1980.
- [189] J. Simo, R. Taylor, and K. Pister. Variational and projection methods for the volume constraint in finite deformation elasto-plasticity. *Computer Methods in Applied Mechanics and Engineering*, 51:177–208, 1985.
- [190] A. Soh and W. Chen. Finite element formulations of strain gradient theory for microstructures and the C0-1 patch test. *International Journal for Numerical Methods in Engineering*, 61:433–454, 2004.
- [191] B. Specht. Modified shape functions for the three-node plate bending element passing the patch test. *International Journal for Numerical Methods in Engineering*, 26:705–715, 1988.
- [192] E. Stärk. *Mehrfach differenzierbare Bézier-Kurven und Bézier-Flächen*. PhD thesis, TU Braunschweig, 1976.
- [193] P. Steinmann. On boundary potential energies in deformational and configurational mechanics. *Journal of the Mechanics and Physics of Solids*, 56:772–800, 2008.
- [194] R. Stogner and G. Carey. C^1 macroelements in adaptive finite element methods. *International Journal for Numerical Methods in Engineering*, 70:1076–1095, 2007.

- [195] R. Stogner, G. Carey, and B. Murray. Approximation of Cahn-Hilliard diffuse interface models using parallel adaptive mesh refinement and coarsening with C^1 elements. *International Journal for Numerical Methods in Engineering*, 76:636–661, 2008.
- [196] G. Strang and G. Fix. *An analysis of the finite element method*. Prentice-Hall, 1973.
- [197] N. Sukumar. *The Natural Element Method in Solid Mechanics*. PhD thesis, Northwestern University, 1998.
- [198] N. Sukumar and B. Moran. C^1 natural neighbor interpolant for partial differential equations. *Numerical Methods for Partial Differential Equations*, 15:417–447, 1999.
- [199] N. Sukumar, B. Moran, and T. Belytschko. The natural element method in solid mechanics. *International Journal for Numerical Methods in Engineering*, 43:839–887, 1998.
- [200] N. Sukumar, B. Moran, A. Semenov, and V. Belikov. Natural neighbour Galerkin methods. *International Journal for Numerical Methods in Engineering*, 50:1–27, 2001.
- [201] N. Sukumar and A. Tabarraei. Conforming polygonal finite elements. *International Journal for Numerical Methods in Engineering*, 61:2045–2066, 2004.
- [202] R. Sunyk and P. Steinmann. On higher gradients in continuum-atomistic modeling. *International Journal of Solids and Structures*, 40:6877–6896, 2003.
- [203] Z. Tang, S. Shen, and S. Atluri. Analysis of materials with strain-gradient effects: A meshless local Petrov-Galerkin(mlpg) approach, with nodal displacements only. *CMES-Computer Modeling in Engineering and Sciences*, 4(2):177–196, 2003.
- [204] R. Toupin. Elastic materials with couple-stresses. *Archive for rational Mechanics and Analysis*, 11(26):385–411, 1962.
- [205] R. Toupin. Theory of elasticity with couple-stress. *Archive for rational Mechanics and Analysis*, 11:85–112, 1964.
- [206] L. Treloar. *The Physics of Rubber Elasticity*. Clarendon Press, 1975.
- [207] L. Treloar. The mechanics of rubber elasticity. *Proceedings of the Royal Society of London. Series A, Mathematical and Physical Sciences*, 351(1666):301–330, 1976.
- [208] L. Treloar and G. Riding. A non-Gaussian theory for rubber in biaxial strain.I. mechanical properties. *Proceedings of the Royal Society of London. Series A, Mathematical and Physical Sciences*, 369(1737):261–280, 1979.
- [209] C. Truesdell and W. Noll. *The non-linear field theories of mechanics*. Springer, 1965.

- [210] R. Ubachs, R. Schreurs, and M. Geers. A nonlocal diffuse interface model for microstructure evolution in tin-lead solder. *Journal of the Mechanics and Physics of Solids*, 52(8):1763–1792, 2004.
- [211] D. Unger and E. Aifantis. The asymptotic solution of gradient elasticity for mode III. *International Journal of Fracture*, 71:27–32, 1995.
- [212] D. Unger and E. Aifantis. Strain gradient elasticity theory for anti-plane shear cracks. part i: oscillatory displacements. *Theoretical and Applied Fracture Mechanics*, 34:243–252, 2000.
- [213] D. Unger and E. Aifantis. Strain gradient elasticity theory for anti-plane shear cracks. part II: monotonic displacements. *Theoretical and Applied Fracture Mechanics*, 34:253–265, 2000.
- [214] I. Vardoulakis, G. Exadaktylos, and E. Aifantis. Gradient elasticity with surface energy: mode-III crack problem. *International Journal of Solids and Structures*, 33:4531–4559, 1996.
- [215] D. Wang and J. Xuan. An improved NURBS-based isogeometric analysis with enhanced treatment of essential boundary conditions. *Computer Methods in Applied Mechanics and Engineering*, 199:2425–2436, 2010.
- [216] C. Wanji and Y. Cheung. Refined quadrilateral discrete Kirchhoff thin plate bending element. *International Journal for Numerical Methods in Engineering*, 40:3937–3953, 1997.
- [217] D. Watson. Computing the n-dimensional Delaunay tessellation with application to Voronoi polytopes. *The Computer Journal*, 24(2):167–172, 1981.
- [218] D. Watson. Nngridr. an implementation of natural neighbor interpolation. 1994.
- [219] G. Wells, K. Garikipati, and L. Molari. A discontinuous Galerkin formulation for a strain gradient-dependent damage model. *Computer Methods in Applied Mechanics and Engineering*, 193:3633–3645, 2004.
- [220] G. Wells, E. Kuhl, and K. Garikipati. A discontinuous Galerkin method for Cahn-Hilliard equation. *Journal of Computational Physics*, 218:860–877, 2006.
- [221] A. Worsey and G. Farin. An n-dimensional Clough-Tocher interpolant. *Constructive Approximation*, 3:99–110, 1987.
- [222] P. Wriggers. *Nichtlineare Finite Elemente*. Springer, 2001.
- [223] X. Wu and Y. Dzénis. Phase-field modeling of the formation of lamellar nanostructures in diblock copolymer thin film under inplanar electric field. *Physical Review Letters E*, 77(3,4):1–10, 2008.
- [224] Z. Xia and J. Hutchinson. Crack tip fields in strain gradient plasticity. *Journal of the Mechanics and Physics of Solids*, 44(10):1621–1648, 1996.

- [225] J. Yoo, B. Moran, and J.-S. Chen. Stabilized conforming nodal integration in the natural-element method. *International Journal for Numerical Methods in Engineering*, 60:861–890, 2004.
- [226] J. Yvonnet, V. P., and F. Chinesta. Bubble and Hermite natural element approximations. In M. Griebel and M. Schweitzer, editors, *Meshfree Methods for Partial Differential Equations III*, chapter 17, pages 283–298. 2007.
- [227] J. Yvonnet, D. Ryckelynck, P. Lorong, and F. Chinesta. A new extension of the natural element method for non-convex and discontinuous problems: the constrained natural element method (C-nem). *International Journal for Numerical Methods in Engineering*, 60:1451–1474, 2004.
- [228] J. Yvonnet, P. Villon, and F. Chinesta. Natural element approximations involving bubbles for treating mechanical models in incompressible media. *International Journal for Numerical Methods in Engineering*, 66:1125–1152, 2006.
- [229] B. Zeaiter. *Eine C₁-stetige Rekonstruktion der Randgeometrie für die Kontaktbehandlung mit der Finiten Element Methode*. PhD thesis, Universität Hannover, 2006.
- [230] A. Zeníšek. Interpolation polynomials on the triangle. *Numerische Mathematik*, 15:283–296, 1970.
- [231] A. Zeníšek and J. Hoderová-Zlámalová. Semiregular Hermite finite elements. *Applications of Mathematics*, 46(4):295–315, 2001.
- [232] A. Zervos, P. Papanastasiou, and I. Vardoulakis. A finite element displacement formulation for gradient elastoplasticity. *International Journal for Numerical Methods in Engineering*, 50:1369–1388, 2001.
- [233] A. Zervos, P. Papanastasiou, and I. Vardoulakis. Modelling of localization and scale effect in thick-walled cylinders with gradient elastoplasticity. *International Journal of Solids and Structures*, 38:5081–5095, 2001.
- [234] A. Zervos, S. Papanicolopoulos, and I. Vardoulakis. Two finite-element discretizations for gradient elasticity. *Journal of Engineering Mechanics*, 135(3):203–213, 2009.
- [235] A. Zervos, I. Vardoulakis, and P. Papanastasiou. Influence of nonassociativity on localization and failure in geomechanics based on gradient elastoplasticity. *International Journal of Geomechanics*, 7(1):63–74, 2007.
- [236] Y. Zhang, Y. Bazilevs, S. Goswami, C. Bajaj, and T. Hughes. Patient-specific vascular NURBS modeling for isogeometric analysis of blood flow. *Computer Methods in Applied Mechanics and Engineering*, 196:2943–2959, 2007.
- [237] H. Zhu, H. Zbib, and E. Aifantis. Strain gradients and continuum modeling of size effect in metal matrix composites. *Acta Mechanica*, 121:165–176, 1997.

- [238] O. Zienkiewicz and Y. Cheung. The finite element method for analysis of elastic isotropic and orthotropic slabs. *Proceedings - Institution of Civil Engineers*, 28:471–488, 1964.
- [239] O. Zienkiewicz and R. Taylor. *The finite element method volume 2: Solid mechanics*. Butterworth Heinemann, 2000.

bereits veröffentlicht wurden:

1. Geisler, J.: Numerische und experimentelle Untersuchungen zum dynamischen Verhalten von Strukturen mit Fügestellen
2010, Band 1
2. Hossain, M.: Modelling and Computation of Polymer Curing
2010, Band 2
3. Görke, D.: Experimentelle und numerische Untersuchung des Normal- und Tangentialkontaktverhaltens rauer metallischer Oberflächen
2010, Band 3
4. Constantiniu, A.: A Hybrid Nodal-Element-Based Discretization Method
2010, Band 4
5. Scherer, M.: Regularizing Constraints for Mesh and Shape Optimization Problems
2011, Band 5
6. Fischer, P.: C^1 Continuous Methods in Computational Gradient Elasticity
2011, Band 6